INVESTIGATION OF RESIDUAL STRESSES IN THE LASER MELTING OF METAL POWDERS IN ADDITIVE LAYER MANUFACTURING

Ibiye Aseibichin Roberts

A thesis submitted in partial fulfilment of the requirements of the University of Wolverhampton for the degree of Doctor of Philosophy

September 2012

This work or any part thereof has not previously been presented in any form to the University or to any other body whether for the purposes of assessment, publication or for any other purpose (unless otherwise indicated). Save for any express acknowledgments, references and/or bibliographies cited in the work, I confirm that the intellectual content of the work is the result of my own efforts and of no other person.

Signature ……

Date ……

Abstract

Laser Melting (LM) is an Additive Layer Manufacturing (ALM) process used to produce three-dimensional parts from metal powders by fusing the material in a layer-by-layer manner controlled by a CAD model. During LM, rapid temperature cycles and steep temperature gradients occur in the scanned layers. Temperature gradients induce thermal stresses which remain in the part upon completion of the process (i.e. residual stresses). These residual stresses can be detrimental to the functionality and structural integrity of the built parts.

The work presented in this thesis developed a finite element model for the purpose of investigating the development of the thermal and residual stresses in the laser melting of metal powders. ANSYS Mechanical software was utilised in performing coupled thermal-structural field analyses. The temperature history was predicted by modelling the interaction of the moving laser heat source with the metal powders and base platform. An innovative 'element birth and death' technique was employed to simulate the addition of layers with time. Temperature dependent material properties and strain hardening effects were also considered. The temperature field results were then used for the structural field analysis to predict the residual stresses and displacements. Experiments involving laser melting Ti-6Al-4V powder on a steel platform were performed. Surface topography analyses using a laser scanning confocal microscope were carried out to validate the numerically predicted displacements against surface measurements. The results showed that the material strain hardening model had a direct effect on the accuracy of the predicted displacement results.

Using the numerical model, parametric studies were carried out to investigate the effects of a number of process variables on the magnitude of the residual stresses in the built layers. The studies showed that: (i) the average residual stresses increased with the number of melted powder layers, (ii) increasing the chamber temperature to 300°C halved the longitudinal stresses. At 300°C, compressive stresses appeared on the Ti64 surface layer, (iii) reducing the raster length from 1 mm to 0.5 mm reduced the average longitudinal stress in the top layer by 51 MPa ($0.04\sigma_y$), (iv) reducing the laser scan speed from 1200 mm/s to 800 mm/s increased the longitudinal stress by 57 MPa ($0.05\sigma_y$) but reduced the transverse stress by 46 MPa ($0.04\sigma_y$).

Acknowledgements

My greatest thanks go to my director of studies Dr. Chang Jiang Wang. His guidance in achieving the set goals was crucial to the successful completion of this project. Special thanks go to Prof. Kevin Kibble and Dr. Mark Stanford (my other supervisors) for their immense input throughout the course of study. Many thanks also to the department's technicians – Iain Lyall, Colin Durnall and Chris Chew for their prompt intervention and assistance in realising the experiments.

I would also thank Prof. Diane Mynors for her input and self-determination that inspired me in many parts of the project and more importantly for the financial assistance provided. Thanks to Jon Rackley for his tremendous assistance. I aspire to match his enthusiasm, professionalism and all-round good nature.

Last and most important of all, I would like to thank my family, especially my Dad and Mum for their strong belief in me, encouraging words and timely support. Thank you.

Nomenclature

ALM	Additive Layer Manufacturing
LM/SLM	Laser Melting/Selective Laser Melting
SLS	Selective Laser Sintering
DMLS	Direct Metal Laser Sintering
RP	Rapid Prototyping
RM	Rapid Manufacturing
HAZ	Heat Affected Zone

I	laser irradiance	(W/m^2)
P	laser power	(W)
r	radial distance	(m)
D	beam diameter	(m)
v	scan speed	(m/s)
h_l	powder layer height	(m)
r_l	raster length	(m)
m	mass	(kg)
ρ	density	(kg/m^3)
ρ_r	relative density	dimensionless
V	volume	(m^3)
g	gravitational acceleration	(m/s^2)
L	latent heat of fusion per unit volume	(J/m^3)
α	absorptance	(unitless)
T	temperature	(°C)
h	convective heat coefficient	($W/m^2.K$)
Q	heat energy quantity	(J)
k	thermal conductivity	(W/m.K)
ΔH	enthalpy change per unit volume	(J/m^3)
ε	strain	dimensionless
β	thermal expansion coefficient	(1/K)
σ	stress	(N/m^2)

Table of Contents

List of Figures

List of Tables

1 Introduction

1.1 Background

The keys to maintaining competitiveness in most design and manufacturing industries are quality, productivity, reduced costs, customer satisfaction and responsiveness in bringing new products to the market place (Noorani, 2006). Since the late 1980s, Additive Layer Manufacturing (ALM) technologies such as Stereolithography Apparatus (SLA) and Selective Laser Sintering (SLS) have been developed and used in a wide range of applications in industry. It has been shown that they can greatly accelerate the product development process (i.e. providing quick prototypes) when used logically in combination with other conventional manufacturing technologies (Behrendt and Shellabear, 1995).

The emergence of ALM technologies has revolutionised the world of product development and new product introduction. In the last decade, Rapid Prototyping (RP) has firmly positioned itself in the product development cycle. According to Terry Wohler's report (Wohlers, 2006), there has been an increasing adoption of the technology since its commercialisation.

The first applications for RP were mostly for the fabrication of prototypes made from polymers to be used as communication or inspection aids. The capability of quickly turning over physical parts from CAD models shortened the product development steps. Currently, components made by ALM techniques are no longer used only as visualisation tools or for assembly testing (Santos *et al*, 2006), but increasingly as final production parts. As a collection of technologies, ALM aids in reducing costs within the product development cycle by facilitating design improvements early in the process, where changes are less expensive.

1.2 Problem Statement

The Department of Engineering in the University of Wolverhampton is in possession of a number of laser-based ALM systems – DTM Sinterstation 2500plus Selective Laser Sintering machine, EOSINT M250 Xtended, and EOSINT M270 Xtended Direct Metal Laser Melting machine. The advantages of laser-based ALM processes are widely

recognised, but certain properties have been restraining their wide acceptance in industry. Since acquisition, the department has been addressing and improving upon some technological issues associated with the process operation and part properties. These include the build orientation, overhang and support structures, surface finish, warping and distortion, part shrinkage, accuracy of builds, final material properties and wear characteristics.

Laser Melting (LM) of metal powders can be used interchangeably with Selective Laser Melting (SLM) as they are one and the same process. However, the term 'Selective' can be misleading because the process fully melts the powder material rather than selectively melting phases or partially melting the powder mixture as in Selective Laser Sintering (SLS). The distinctions are made clearer in the literature review in Chapter 2.

Laser melting of metal powders is characterised by multiple modes of heat and mass transfer, and chemical reactions that make the process very complex. Although the laser melting process has been applied to a broad range of powders, some of the scientific and technical aspects of the effects of processing parameters on the thermal and stress field changes during the process are not fully understood. Obtaining appropriate process parameters via trial and error in the laser melting process is expensive and inefficient as evidenced in statistical studies by Raghunath and Pandey (2007) and Yang *et al* (2002), where they used the Taguchi method (i.e. an orthogonal analysis method used in the design of experiments) to predict the influence of process parameters on parts built from laser sintering of duraform polyamide blocks.

Owing to the relatively high speeds at which LM occurs, deposition of new powder layers and subsequent melting, phenomena like shrinkage and solidification lead to the development of thermal and residual stresses. These residual stresses are known to cause dimensional inaccuracies, warping and part failure during both the building and post-processing stages. It is, therefore, desirable that residual stresses are minimised with appropriate process parameter selection for the materials used in the LM process.

With advances in computing capabilities, the Finite Element Method (FEM) has become an effective tool for predicting and assessing stresses in physical systems. The numerical method approach not only provides improved three-dimensional residual stress field information, which is difficult to obtain by measurements, but also allows parametric studies to support strategic process variable selection and optimisation.

Modelling the Laser Melting (LM) process required a good level of understanding of applied sciences – computational heat transfer, science and mechanics of materials, plasticity of metals, numerical modelling and lasers. The challenges include the addition of multiple powder layers with time, accurate representation of material properties, and translation of the process quantities for parametric studies.

1.3 Aims and Objectives of Research

In this thesis, an investigation into the effects of process and material variables on the residual stress distributions in the laser melting of Ti64 powder is dicussed and reported. The ultimate goal is to augment with practical experience and minimise the need for cost intensive experimental fabrication for the purpose of understanding the effects of process parameters.

The main objective is to develop a validated numerical model for use as a parametric tool in studying the effects of process variables. This was achieved through:

- Development of a generic three-dimensional numerical model.
- Validation of the numerical model from known geometric analysis information and from surface displacement experiments.
- Single response variable studies on the effect of process parameters on the residual stress distributions.

1.4 Structure of the Thesis

This thesis is divided into eight chapters with contents as described below:

Chapter 1 states the research problem and the objectives of this work

Chapter 2 presents the literature review of relevant work in the subject area regarding the development of residual stresses in laser-based ALM processes. It introduces the laser melting process variables, theoretical background of the process, physical processes involved, factors affecting the level of residual stresses, limitations of models from previous and current research works, and description of the method adopted in this work. It identifies how this work contributes to the subject area.

Chapter 3 focuses on an in-depth research of the temperature dependent material thermal and mechanical properties as well as relevant physical and strain hardening models. Measurement of powder and solid material properties are also presented here.

Chapter 4 deals with the development of the three-dimensional finite element model using ANSYS Mechanical software. It describes the building blocks of the thermal and structural field analysis and the method of analysis. The logic and workflow framework of the layer-by-layer simulation model are presented.

Chapter 5 describes the laser scanning confocal microscopy experiments conducted to validate and refine the layer-by-layer finite element model. Surface displacement results from the simulation model are validated against the surface topography measurements in this section.

Chapter 6 explores the capabilities of the numerical model in terms of transient temperature, stress and displacement distributions predicted by post-processing the thermal and stress field results from the validated simulation models. It draws initial findings and highlights the applicability of the developed model to other aspects of laser processing of materials.

Chapter 7 presents the parametric studies involving the effect of the process variables on the magnitude and distribution of residual stresses in the layers built by the LM process as well as potential areas for further research.

Chapter 8 summarises the main findings of this work, the extent to which the aims and objectives are met and the contribution to knowledge.

References and appendices follow after Chapter 8

1.5 Original Contribution to Knowledge

The original contributions of this thesis to the body of knowledge are:

- Development of a fully parametric three-dimensional numerical model to study the temperature and stress fields in laser melting of metal powders.
- Novel use of the ‘element birth and death’ simulation technique
- Unique understanding of the thermal and mechanical aspects of the laser melting process involving metal powders.

- Characteristics of residual stresses in laser melting of metal powders.
- The influence of the process parameters on the distribution of residual stresses in laser melting of metal powders.
- Augmentation of practical knowledge in the selection of process variables for the laser melting of metal powders.

2 Literature Review and Methodology

2.1 Introduction

This chapter presents the basis for the work described in this thesis. It focuses on ALM parts produced by laser sintering or laser melting of powders. The background theory of the laser melting process, heat transfer equations and thermal stresses are discussed. Current research (experimental and analytical) relating to the study of residual stresses are presented. Application of the finite element method in predicting the thermal and stress fields by previous researchers is also discussed.

2.2 Additive Layer Manufacturing

ALM refers to a collection of technologies that build prototypes, tooling and final production parts from three-dimensional CAD models in a layerwise manner. Raw data can be compiled from Computed Tomography (CT), Magnetic Resonance Imaging (MRI), or data from three-dimensional scanning systems, while the parts can be realised from liquid, powder or sheet materials (Wohlers, 2006). The roots of ALM technologies can be dated back to the 1890s when topography and photosculpture were the known means of replicating objects (Noorani, 2006). In the last half century, advances in lasers and optics, material science, and material handling led to the development of ALM technologies that evolved over time into the mainstream market. These technologies offer advantages in many applications compared to conventional fabrication methods. Parts can be manufactured irrespective of geometric complexity and without the need for detailed machine set-up. In addition, parts can be built from multiple materials, composites, or graded in a controlled manner to achieve the desired properties (Yakovlev *et al*, 2005).

Rapid manufacturing using ALM is becoming a cost effective alternative for new products, giving design flexibility and scope to manufacture parts that cannot be made by conventional manufacturing processes. It is also an attractive option when product volumes are relatively low. Some industrialists argue that rapid manufacturing should not just be attributed to ALM technologies alone, but should include conventional machining processes and CAD/CAM operations to form a complementary set of

processes (Morris-Technologies, 2007). It is worthy of note that the capabilities of ALM are different from conventional manufacturing processes like moulding, casting, and machining and there are still challenges to the adoption of ALM in industry; for example, limitations in terms of build speed, available materials, surface finish attainable and the accuracy of parts.

2.3 ALM Systems

ALM systems can be categorised into three groups, based on the form of the starting material used – liquid-based, solid-based, and powder-based systems (Noorani, 2006).

2.3.1 Liquid-Based Systems

In liquid-based ALM systems, parts are built from a photosensitive liquid or resin that solidifies when sufficiently exposed to ultra-violet light usually in the form of a laser beam. This idea was first invented in the 1950s by Munz, who patented a method of building with photoemulsion using projected light (Behrendt and Shellabear, 1995). Solidification occurs as a result of polymerisation or curing of the resin. The building is done layer-by-layer, with each layer scanned by an optical system. The layer thickness from which the part is built is controlled by an elevation mechanism. The two main types of liquid-based systems are Stereolithography Apparatus (SLA) and Solid Object Ultra-Violet Plotter (Noorani, 2006).

2.3.2 Solid-Based Systems

These are based on additive layer-wise building of three-dimensional geometries by bonding solid or semi-solid materials together utilising phase changes or other physical bonding techniques. The main types of solid-based systems include Fused Deposition Modelling (FDM), Laminated Object Manufacturing (LOM), 3D Printing (3DP), Multi-jet Modelling and Selective Adhesive Hot Passing (SAHP) (Noorani, 2006).

2.3.3 Powder-Based Systems

These systems are based on fusing powder particles in successive layers by either sintering or melting using laser energy. The main types of powder-based systems include Selective Laser Sintering (SLS), Direct Metal Laser Sintering (DMLS), Laser

Melting (LM), Laser cusing, 3D Laser Cladding (Santos *et al*, 2006) and Electron Beam Manufacturing (EBM) (ARCAM, 2010).

2.4 Laser Technology in ALM Systems

According to Crafer and Oakley (1993), lasers were discovered in 1960, and are arguably the most important of all light sources. They have vast industrial applications ranging from engineering, medical to food processing. Many active materials used as lasers have been commercialised while others are still being developed. Each laser type has its own properties of wavelength and operating parameters.

In terms of method of operation, lasers can be classified as either:

- continuous wave lasers, or
- pulsed lasers

In continuous wave lasers, the output of the laser is relatively constant and does not vary with time. Pulsed lasers as the name suggests are characterised by periodic pulse trains of the laser energy (Crafer and Oakley, 1993) and the peak power of the laser is governed by the pulse frequency (Morgan *et al*, 2001). Pulsed lasers can be further divided into Q-switched, mode-locked, and pumped lasers. Further classification can also be done with respect to the state of the generating material and or process from which they are produced. These include gas lasers, solid-state lasers, chemical lasers, excimer lasers and semi-conductor lasers.

In laser-based ALM systems, two types of lasers are predominantly used – Neodymium-doped Yttrium Aluminium Garnet laser (Nd:YAG) and CO_2 lasers.

Table 2.1 gives a summary of the classification of the different lasers. The applicability of lasers in ALM depends on their heating ability and interaction with the powder material. This will be dealt with in more detail in Section 2.10.

Table 2.1: Classification of Lasers (Das, 1991)

Gas lasers			
Gas used	Wavelength range	Excitation	Comments
He–Ne	3.39 μm 0.6328 μm (0.543 μm) 1.15 μm	Electrical	Pulsed
CO_2	10.6 μm (9.17–10.91 μm) 9.6 μm	Electrical highest efficiency and power	CW/pulsed
Ar^+	0.4880 μm 458 514	Electrical	CW
Nitrogen	0.337 μm	High power	Pulsed
Far infrared different gases	40 μm–1.2 mm	CO_2 pumped	CW and pulsed
Kr^+	0.675 μm 0.647 μm 0.58 μm	Electrical	
Xe	2.02 μm	Electrical	
He–Se	24 visible lines		
He–Cd	0.442 μm 0.325 μm	Electrical	CW
Other lasers			
Type	Wavelength range	Excitation	Comments
Ruby	0.7 μm	Optical flash lamp	Pulsed
Nd^{3+} : YAG	1.06 μm 0.53 (using doubler)	Optical flash lamp	Pulsed and CW
Junction lasers			
GaAs	0.8 μm	Electrical	CW/pulsed
InP	0.9 μm		
InAs	3.1 μm		
GaInAsP	1.5 μm		
Organic dye dye solvent	0.217–0.96 μm	Optical laser pumped	CW/pulsed shortest width $\sim 10^{-15}$
Excimer laser			
KrF	0.248 μm	Electrical/optical	Pulsed
KrCl	0.222 μm		
ArF	0.193 μm		
XeF	0.351 μm		
XeCl	0.308 μm		
Ar_2^*			
K_2^*			
Metal vapor laser			
gold and copper	0.628 μm UV–IR	Electrical	CW

2.5 Laser-based ALM using Metal Powders

Laser-based ALM processes that use metal powders as the initial material utilise the thermal energy provided by a laser to melt and fuse the particles together. The heating of the metal powders is accompanied by state changes that result in either liquid phase sintering or full melting followed by consolidation.

The main trademarked laser-based ALM processes that use metal powders are:

- Selective Laser Sintering (3D Systems)
- Laser Melting/Direct Metal Laser Sintering(DMLS) (MTT Technologies, EOS GmbH)
- Direct Metal Deposition (POM Group)
- Laser cusing (ES Technologies, Concept Laser Technologies)

The trend in laser-based ALM processes has historically been determined by the speed of laser processing. High-power lasers imply faster processing times, and the introduction of powerful electron beam lasers is holding promise with respect to replacing the current Nd:YAG and CO_2 lasers (Zaeh *et al*, 2008). Electron Beam Manufacturing (ARCAM, 2010) is a growing ALM process, and because it fully melts the metal powders in a vacuum chamber at elevated temperatures, it has strong similarities with the laser melting process.

2.6 Laser Sintering and Melting of Metal Powders

The mechanisms of laser sintering and melting have been discussed in the works of Tolochko *et al* (2003), Tolochko *et al* (2004), Klocke *et al* (2003) and Simchi (2006). The consensus is that the material is in powder form, and that the solidifying process is a thermally-induced state change rather than a chemical reaction. First, a thin layer of powder is spread onto a build platform and simultaneously levelled or compacted to the required thickness (Behrendt and Shellabear, 1995). In other methods, the powder is delivered through a nozzle onto a substrate (Pinkerton and Li, 2004). A CO_2 or Nd:YAG laser emitting in the infra-red spectrum heats the powder material at its focus, causing localised fusing which binds the individual grains of powder together. The laser beam scans the powder surface at an appropriate speed, heating the surface according to the desired scanning pattern and part profile. In principle, almost any fusible material can be used, but it has to be available with suitable surface and packing characteristics as well as optical and thermal properties matched to the laser radiation (TRUMPF, 2007).

During the manufacture of metal parts by SLS, the powder used is coated with polymeric binders which have lower melting temperatures than the base metal powder.

This is referred to as the indirect process. The binder material is melted by the laser beam, causing the powder particles to be joined giving what is termed as a 'green' part. The parts made by the indirect process are porous in most cases and still include the binders at this stage. The parts must be debonded and infiltrated to improve their mechanical properties (Shiomi *et al*, 1999). Furnace sintering is one method of achieving this.

The direct process creates solids from powder in a single operation. The metal powders without a binder are heated by the laser beam and melted or liquid sintered, hence debonding is not necessary. The direct process offers the possibility of making more accurate components than the indirect process through better control of shrinkage (Shiomi *et al*, 1999 and Wang *et al*, 2002). Laser melting processes use a much higher power density laser, which enables full melting of the powders used to take place. Therefore, the built parts have densities very close to the solid material (Santos *et al*, 2006).

2.7 Residual Stresses in Laser Melting of Metal Powders

Residual stresses are self-equilibrating internal stresses existing in a free body which has no external forces or constraints on its boundaries. They are those stresses that would exist if all external loads were removed.

According to Masubuchi (1980), residual stresses can be classified according to the mechanism which produces them:

- those produced by structural mismatching, and
- those produced by uneven distribution of non-elastic strains.

Residual stresses can also be classified according to the scale on which they occur:

- Type 1, σ^{I}: those that vary over large distances and evident in dimensional variations and can result in large deformations of the part. They are also referred to as macro-residual stresses.
- Type 2, σ^{II}: those that occur due to the formation of different phases in the material.

- Type 3, σ^{III}: those that occur as a result of dislocations at atomic scale, often referred to as micro-residual stresses.

The Type 3 residual stresses are beyond the scope of this work, hence, this work will deal mainly with the Type 1 and Type 2 residual stresses.

Understanding residual stresses generated through the LM of metal powders is required before finding ways to minimise them. However, accurate prediction of the residual stresses and distortions induced in laser melting processes has proved to be a challenge because of the localised high temperatures, rapid temperature cycles and a moving laser heat source.

2.7.1 Origin and Development of Stresses in LM of Metal Powders

The LM process utilises the heating effect of a laser beam on a powder surface. The powder absorbs a fraction of the energy flux from the laser. This is converted to heat via electronic interactions with the atoms on the surface of the powder, causing the lattice vibrations to increase and consequently raising the temperature of the powder material (Ready, 1971). If the absorbed energy is high enough, the powder can be melted or even vapourised (El-Ghany, 2006), the latter is not suitable for the LM process in consideration. Laser-based manufacturing processes (like laser welding and laser bending) are known to induce large amounts of residual stresses, due to the large temperature gradients which are inherent in these processes (Mercelis and Kruth, 2006). These residual stresses have been found to cause distortions, cracks, and delamination in SLS and LM parts in studies by Karalekas and Rapti (2002). Fig. 2.1 shows two Ti64 blocks produced by the laser melting process. It shows extensive stress crack lines around the blind holes and edges which are believed to be caused by residual stresses induced by the LM process.

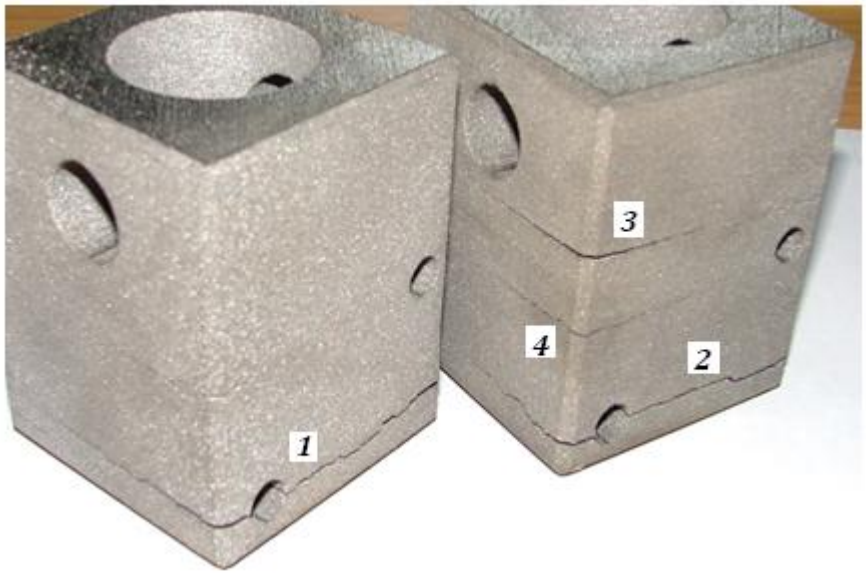

Fig. 2.1: Stress cracking around features in two Ti64 parts

Residual stresses in LM of metal powders are a consequence of non-uniformities in the thermal expansion or contraction between the different materials or states of the same material. According to Koric and Thomas (2008), thermal strains arise from volume changes caused by both temperature differences and phase transformations, including solidification and solid-state phase changes between crystalline structures.

Temperature differences in the irradiated region produce transient thermal strains at different surface and depth locations. When the heat source is removed, the material cools and contracts more than the area surrounding it and consequently generates residual stresses.

Mercelis and Kruth (2006) described the development of residual stresses using a similar Temperature Gradient Mechanism (TGM), in which thermal expansion and contraction of the material during the heating and cooling phases following laser interaction induce steep temperature gradients around the irradiated region. The heated material and surrounding solid material are analogous to a structural mismatch scenario which effectively restrains the movement of the heated metal as it changes state. During cooling, an overall contraction (i.e. tensile state) occur in the irradiated region, while for the surrounding material, an overall expansion (i.e. compressive state) occurs (Li *et al*, 2004). The shrinkage of the molten material (in the case of the powder material) during cooling induces compressive stresses in the material underneath that is within the influence of the temperature gradient as Fig. 2.2 illustrates (Kruth *et al*, 2004).

From this review, it can be seen that the residual stresses in the laser melting process are the accumulation of the quenching stresses arising from the solidification of the deposited layers and the thermal stresses due to the mismatch between the thermal expansions and stiffnesses of the different materials and or different states of the same material.

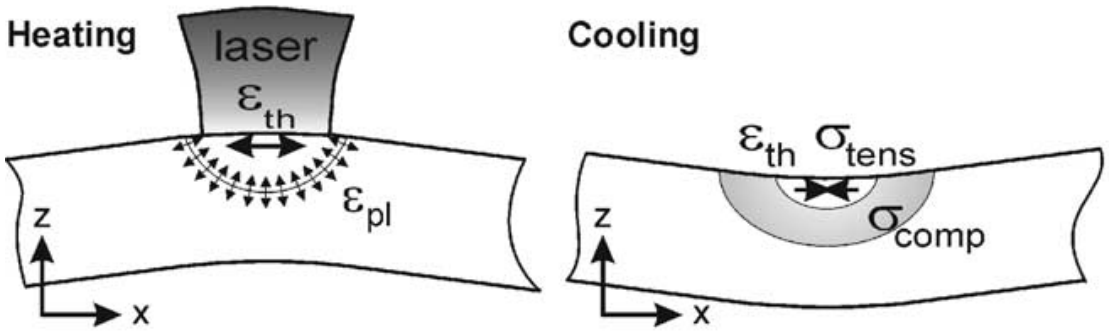

Fig. 2.2: Temperature gradient mechanism (Kruth *et al*, 2004)

2.7.2 Investigation of Residual Stresses in Laser-based ALM

There are a number of similarities between residual stresses developed in a multi-pass welding process and the laser melting process – both processes involve the heating of deposited material in a layer-by-layer manner. Although the former has been greatly researched in-depth, the investigation of residual stresses in LM of metal powders has not. A relatively small number of researchers have in the past investigated the residual stresses associated with ALM parts both experimentally and numerically.

Measuring the stresses directly in the built layers is a huge challenge using conventional stress measurement methods. This is because to employ techniques like X-ray or neutron diffraction, image correlation or strain gauge methods, the initial state of the layers and the final state of the fused layers have to be known (i.e. the spatial relationship in the unloaded and stressed positions) (Masubuchi, 1980). This is extremely difficult to achieve with the LM process as the fusion of the particles is entirely random. Shiomi *et al* (2004) performed experiments on SLS of a chrome molybdenum steel powder blend to study the effect of processing conditions on the residual stresses. They measured strain changes in the bottom of the build platform,

from which the residual stress changes were calculated assuming linear stress-strain relationships.

Karalekas and Rapti (2002) performed deep-hole drilling stress measurement tests on epoxy-based photopolymer (Somos 7110) discs built by SLA to investigate the effects of process parameters on the induced residual stresses. They found that the residual stresses had varying effects on the mechanical properties like the elastic modulus, tensile strength, and fatigue performance of the SLA discs. Although residual stresses are desired in certain applications (e.g. tempering glass to prevent crack growth), in most cases, they are unwanted. Loss of tolerance due to residual stress-induced warping is a major concern in laser-based ALM processes, particularly those which involve direct melting of powder metals (Li *et al*, 2000).

Beuth and Klingbeil (1996) and Klingbeil *et al* (2002) presented analytical and experimental studies for indirectly predicting the residual stresses developed in Solid Freeform Fabrication (SFF) which is also an ALM process. They investigated the delamination and warpage characteristics following deposition of layers. The method of layer deposition and preheat operation were found to limit the residual stresses. Mercelis and Kruth (2006) presented a theoretical and experimental study on residual stresses in stainless steel 316L SLS parts. They found that the number of layers added, base plate dimensions and yield strength of the added material influenced the magnitude of the residual stresses.

2.8 Parametric Investigation in Laser-based ALM

The parameters involved in the laser melting process can be categorised into three groups:

- Product Parameters: These are variables that are determined by the design of the part as well as the size and location of features on the part.

- Machine and Laser Parameters: These are dependent on the operational settings of the laser (i.e. the laser beam) and hardware of the machine. They are generally considered as those parameters that determine the amount of energy delivered to the surface.

- Material Parameters: These depend on the material characteristics – i.e. physical state, thermal and mechanical properties.

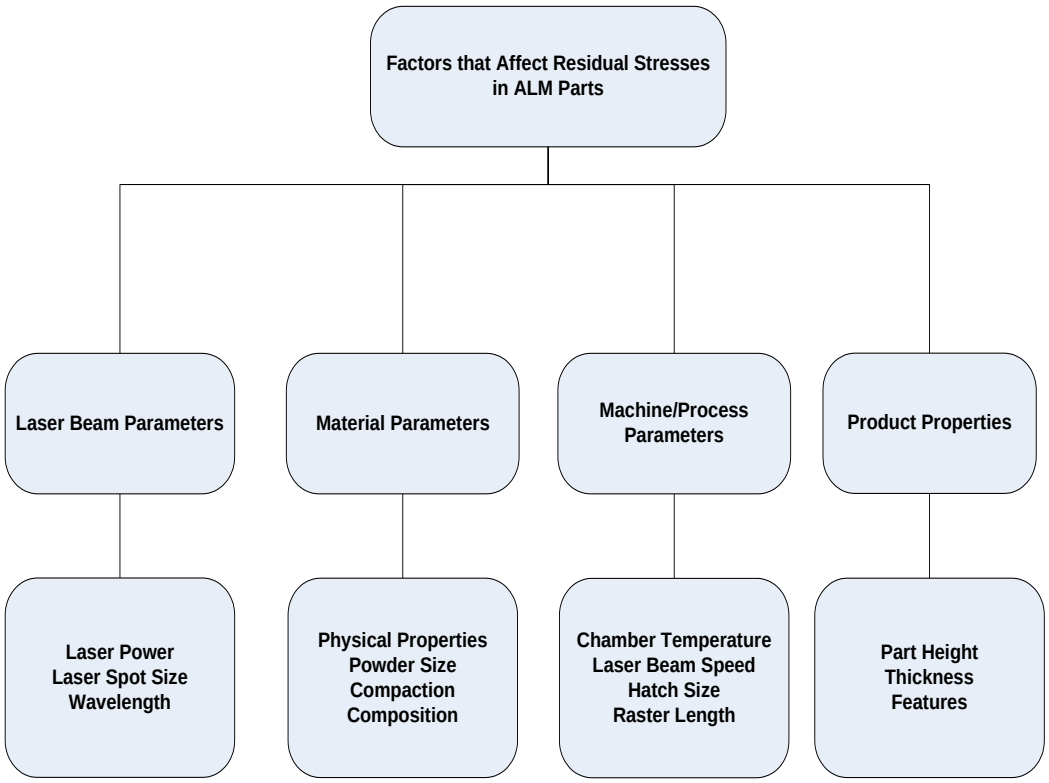

Fig. 2.3: Variables that affect the residual stresses in the laser melting process

A classification of these variables, which have been gathered from a number of experimental studies, is shown in Fig. 2.3 (Gusarov *et al*, 2007, Simchi and Pohl, 2003, Tolochko *et al*, 2003, Yadroitsev *et al*, 2007 and Tang *et al*, 2003).

- The laser power (for a continuous wave type laser) is normally a constant value measured at the powder bed surface. Due to losses in the beam generation system, it is normally lower than the laser generating system.

- The laser beam diameter, also referred to as the spot size, is also measured at the surface of the powder. With the aid of expanders and collimators, the beam diameter can be altered for different material applications.

- The scan speed is the rate at which the laser beam traverses the surface of the powder bed. The process build time is heavily dependent on the scan speed.

- The layer thickness is the depth of each newly spread powder layer. It is important that the laser energy is sufficient to penetrate and melt the entire layer to facilitate fusion with the substrate or a previous layer.

For the EOSINT M270 laser melting machine, EOS specifies the range of operating values for all process parameters according to material type. The operator is at liberty to modify these parameters based on experience to change certain physical attributes of the built parts to suit the application. However, the process variables interact with each other, and a change in one process variable may require alteration of another variable to produce a similar outcome.

The effects of some of the variables on the distribution and magnitude of residual stresses in built parts is the focus of this research in order to create a unique understanding of how they can be effectively selected for use in the laser melting of metal powders.

2.9 Laser Melting Process

The work in this thesis is focused on the EOSINT M270 laser melting machine. The process is shown schematically in Fig. 2.4.

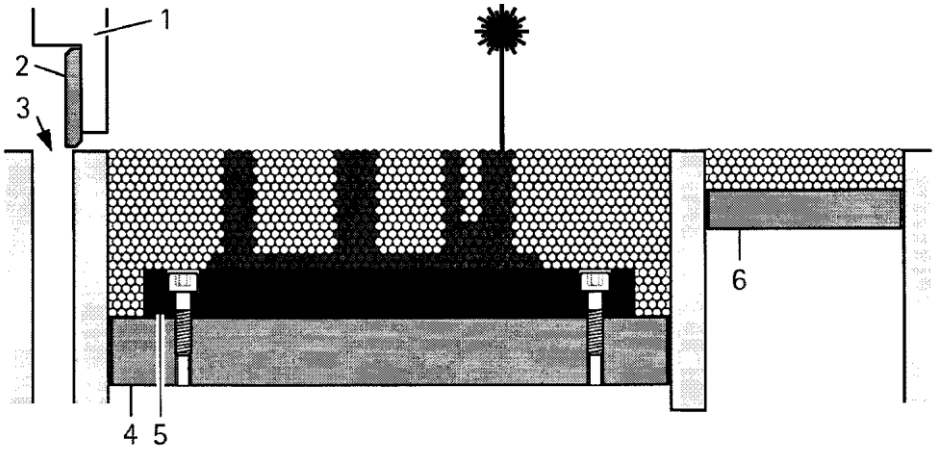

Fig. 2.4: Laser melting process operation (Electrical Optical Systems, 2005).

The heat input from the high power continuous wave Nd:YAG laser beam is highly localised on the irradiated region as the laser scans the surface of the powder bed in an enclosed argon atmosphere. Scanning refers to the application and movement of the

laser beam within a cross-section along defined paths with constant application of energy. Self-quenching occurs in the heated layer after exposure to the laser beam due to dissipation of heat to the surrounding bulk material. The heated molten material bonds to the platform or supporting structure as it solidifies. Following scan completion of the layer, the build platform is lowered by one layer thickness or by a defined depth. A new layer of metal powder is applied by means of a recoating mechanism and it is subsequently laser-scanned. The process is repeated until the part is complete, with each new layer being bonded to the previous layer (Electrical Optical Systems, 2005).

2.10 Laser Melting Process Mechanism

The complex physical phenomenon involved in laser melting of metal powders requires consideration in order to build an understanding of their mutual dependence. The mechanism comprises the laser interaction, material behaviour and the resulting physical processes governed by the selection of variables.

2.10.1 Laser-Material Interaction

Laser radiation is electromagnetic, occurring in the infra-red wavelength spectrum for the laser types used in laser melting. In all laser processing procedures, the irradiated material absorbs a part of the laser beam energy, a second part is reflected and a third part, known as transmission, penetrates the work piece without interaction. The absorption characteristics and absorption-reflection-transmission ratio depends on the type and nature of the material. It is important to note that there is minimal transmission in metals because of their high opacities (Das, 1991). Laser beam from the source incident on the material interacts with the surface particles on an atomic scale. Analyses by Crafer and Oakley (1993) show that most absorption occurs in a narrow surface layer a few atoms thick. According to Tolochko *et al* (2000), the surface layer is typically between 0.01 µm and 1 µm for dense opaque materials for the range of laser wavelengths of interest as given in Table 2.1.

In metals, the energy absorption mechanism is governed by the electrons in the crystal lattices gaining energy from interactions with the electric field caused by the laser (Ready, 1971). The heat generated diffuses into the surrounding bulk material by conduction. In the case of metal powders, the energy is deposited in a thin layer on the

surface of the individual powder grains, which is typically several nanometres (Fischer *et al*, 2004). The downstream energies depend on this important stage of the energy transformation.

2.10.2 Laser Absorptance of Metals and Metal Powders

Absorptance and absorptivity are terms used interchangeably to define the amount or fraction of radiation energy captured by an irradiated body. It is important to note that the term absorptance of a material as used in this work differs from the 'absorption coefficient'. Absorption coefficient has units of per unit length and describes the decay of the laser intensity with depth of penetration (Ready, 1971), while absorptance has no units.

Kruth *et al* (2003) distinguished two modes of laser energy absorption as intrinsic absorption (in solid materials) and incoupling absorptance (in powder materials). Tests performed in their work showed that the incoupling absorption was always greater than the intrinsic absorption. This was because the powder morphology (e.g. rough surface and packing structure) made it more absorbent to incident laser radiation. According to Taylor (2004), two types of interactions are possible in the material: radiative (or optical) and non-radiative absorption. In a radiative interaction, energy levels in the absorption layer are increased on laser application but fall back to a lower energy level with the release of another electromagnetic wave, while in a non-radiative interaction, heat is generated by energy transmission to the material's lattice structure (i.e. calorimetric absorption).

A number of factors have been found to influence the laser absorptance of metals. According to Frewin and Scott (1999) and Chen *et al* (2007), the absorptance of a material is a function of a number of variables such as the nature of the surface, level of oxidation, and surface temperature. Kruth *et al* (2003), in their work involving lasers and materials used in SLS, found that the absorptance of a material depended strongly on the physical state of the material and the wavelength of the laser. Table 2.2 lists the absorptance of some metal powders measured by Tolochko *et al* (2000). The absorptance is greater for the shorter wavelength Nd:YAG laser than the longer wavelength CO_2 laser. This favours the use of shorter wavelength Nd:YAG for laser melting applications. In the same study by Tolochko *et al* (2000), they also found that the laser absorptance of metal powders did not depend on the powder particle size.

Measurements carried out on single component 50-160 μm nickel alloy powders showed that the particle size had very little influence on the absorptance values.

Table 2.2: Optical absorptance for selected metal powders (Tolochko *et al*, 2000)

Powder Material	Absorptance	
	Nd:YAG (λ = 1.06 μm)	CO_2 (λ = 10.6 μm)
Fe	0.64	0.45
Cu	0.59	0.26
Ti	0.77	0.59

The techniques for measuring the absorptance of materials fall into calorimetric techniques, which measure the heating effect (BSI, 2004 and Gur and Pan, 2008), and radiometric techniques, which measure reflectivity (Tolochko *et al*, 2000). The definition and application of laser absorptance used for this work is limited to calorimetric absorption in which the heating effect is of paramount interest.

Some studies have taken the absorptivity of the material to be the same as its emissivity at a given wavelength assuming Kirchoff's law of radiative emission. Sih and Barlow (2004) used this assumption to predict the absorptance of alumina and iron powder beds to CO_2 lasers. Bergstrom *et al* (2007) conducted reflectance tests to determine the optical absorptance of commercial steels to Nd:YAG lasers at room temperature. In their study, they pointed out that although it was possible to accurately measure the absorptance at room temperature, it was extremely difficult to measure the absorptance of molten or turbulent surfaces during laser processing. In the determination of the absorptance using the calorimetric and radiometric methods, the dependence of material properties at elevated temperatures and heat losses to the surrounding medium are ignored (BSI, 2004).

In order to simplify laser energy absorption modelling, most researchers have assumed a constant value for the laser absorptance of the material. The assumption of a constant absorptance in the laser melting of metal powders is unlikely to be realistic because attenuation of the absorbed laser energy occurs as a result of powder cloud formation, scattering and changes to the surface and state of the material (Zaeh *et al*, 2008). This is

evident in experiments conducted by Taylor (2004), where the calorimetric absorptance decreased when a previously scanned track was rescanned. Values reported for stainless steel 314S-HC powder showed that the calorimetric absorptance varied from 21% for the first scan to about 5.4% for the fifth rescanning. Childs *et al* (2005) reported values of 36 ± 6% for the same material. Gur and Pan (2008) reported values for steel that were dependent on surface roughness. They reported values of 18% at 25 μm Ra and 8.5% at 1 μm Ra, indicating a reduction in the absorptance as the surface became smoother. This change in absorptance makes modelling the transient heat transfer problem for the laser melting of metal powders exceptionally challenging. Experimental measurements reported by Bass in Bertolotti (1983) gave estimates for the calorimetric absorptance to Nd:YAG lasers for most solid metals as 20% and proposed an absorptance of 10% when even a small degree of melting was involved. These values are conservative compared to the radiative absorptance values reported and will, therefore, be used for this work. A more conservative value for the powder absorptance to Nd:YAG lasers is 30% reported by Fischer *et al* (2003). This value has also been chosen for this work, the same as that used by Fu *et al* (2002) in laser cladding studies.

2.10.3 Material Solidification

The heating of metal powders above their melting temperature, and subsequent cooling, results in the flow and fusion of the molten material. This bonding mechanism in LM is markably different to that of SLS. In the sintering processes – Solid Phase Sintering (SPS) and Liquid Phase Sintering (LPS), a single-phase powder or mixture of powders is heated close to melting temperatures or above the melting temperature for one phase in the case of LPS (Thummler and Oberacker, 1993). The diffusion of the necks (i.e. aggregation of partially melted particles) and the rearrangement of the particles account for the reduction of porosity (i.e. densification) in SPS; whereas, in the case of LPS, the flow of binder material into the pores through capillary action results in densification as utilised in the copper infiltration into a steel matrix (Stewart *et al*, 1999).

Unlike SLS, LM is more difficult to control. The distinctive feature is that it is always accompanied by significant shrinkage due to the density change from bulk powder to liquid and finally to solid. The high laser energy input and the complete melting of particles lead to phenomena like balling and thermal stresses (Kruth *et al*, 2004). Fig. 2.5 shows the balling effect where following laser scanning, large spherical

droplets are formed on the surface of a powder bed. This occurs when the melt forms a spherical mass engulfing contiguous powder particles due to surface tension effects. The mechanism of balling has been investigated by Tolochko *et al* (2003) and Tolochko *et al* (2004). According to Rombouts *et al* (2006), balling occurred due to Rayleigh instability and Marangoni convection of the melt pool at high aspect ratios of the tracks (i.e. length-to-width ratio) which caused track fragmentation in an attempt to reduce its surface energy. It is known to be more severe in LM than in SLS (Gusarov *et al*, 2007), hence the difficulty in control. Appropriate selection of the LM process parameters can prevent the occurrence of balling (Simchi, 2006).

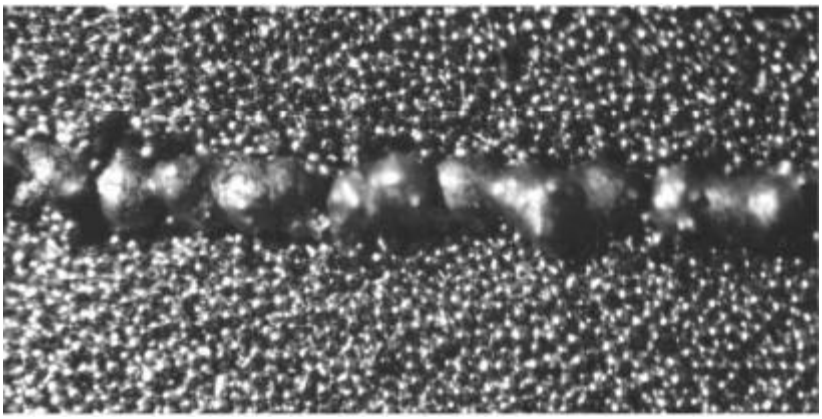

Fig. 2.5: Balling of an SLS powder track (Tolochko *et al*, 2004)

Yadroitsev *et al* (2007) conducted a series of experiments to investigate the relationship between the laser power, scanning speed and the stability of melted tracks in SLS of commercial austenitic stainless steel powder (Inox 90L). They concluded that the power-to-speed ratio or specific energy (*P/v*) was the main determining factor for stability (or bonding) of the melted tracks, the higher the *P/v* value the greater the bonding was in the tracks. However, studies by Schneider (1998) suggest that the specific energy alone is not a suitable parameter for explaining the quality of laser melting of powders onto substrates. It was found that below a certain value of specific energy, no fusion bonds were formed, whereas excessive diffusion of the irradiated material into the substrate became too large when the specific energy was above a certain level.

2.10.4 Laser Process Parameter Selection

The selection of laser power and scan speed (which effectively controls the exposure time) governs the type of laser processing achieved. Fig. 2.6 shows the relationship

between the laser process parameters and the resultant process. It can be seen that the different laser processes occur in clusters, and in some cases overlaps occur for the same set of process parameters. It is therefore, apparent that careful and strategic process parameter selection is vital to the successful implementation of a desired laser processing technique. Within each laser processing cluster, optimal parameters for processing particular materials can be found.

The material 'fusion' regime shown in Fig. 2.6 is the process of interest in this work. It can be seen that the fusion cluster is a small subset of 'cladding and alloying' which is itself a subset of the 'continuous operation' cluster. It shows that the small window of process variable selection available to operators to alter the physical properties of built parts requires a lot of experience. Parametric analysis and investigation can help enhance the knowledge of how residual stresses and displacements are influenced by the process variables.

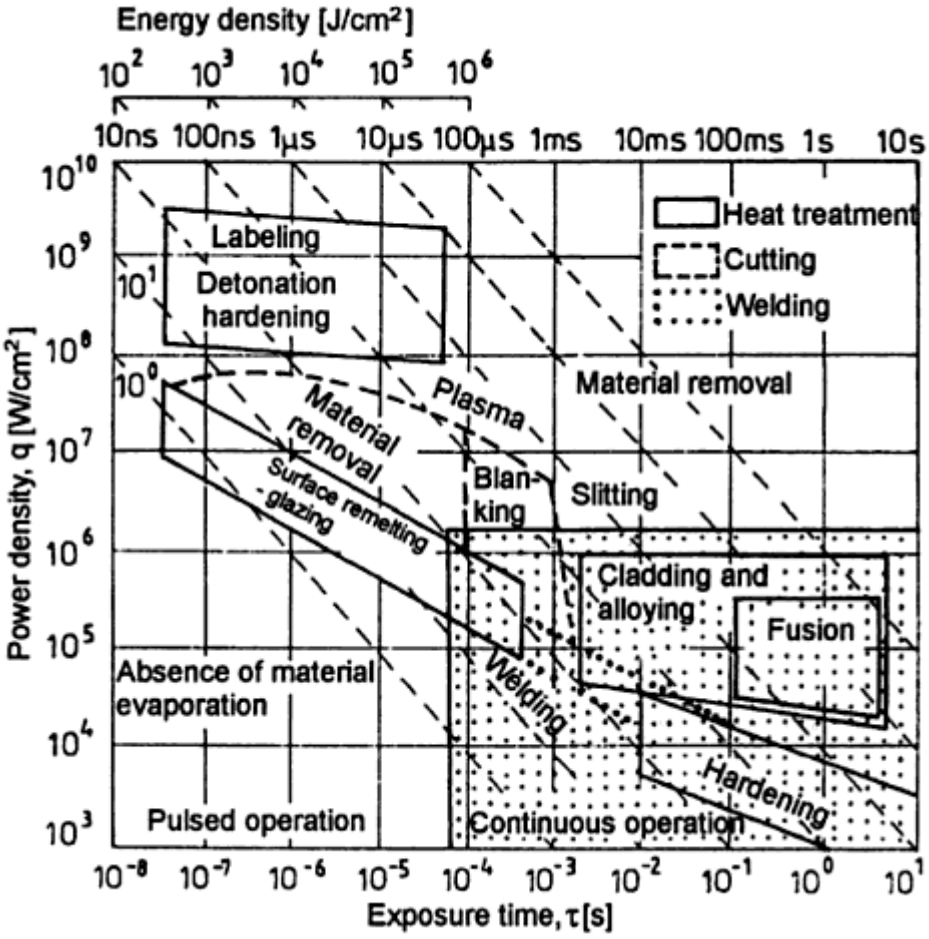

Fig. 2.6: Dependence of thermal processes on absorbed laser power density (Burakowski and Wierzchon, 1998)

2.11 Physical Thermodynamics and Numerical Modelling

When the laser beam irradiates the surface of the powder bed, its energy is transferred in several forms as illustrated in Fig. 2.7. The heat transfer associated with the laser melting process can be placed into three categories, namely:

- Energy Absorption
- Heat Dissipation
- Phase Transformation

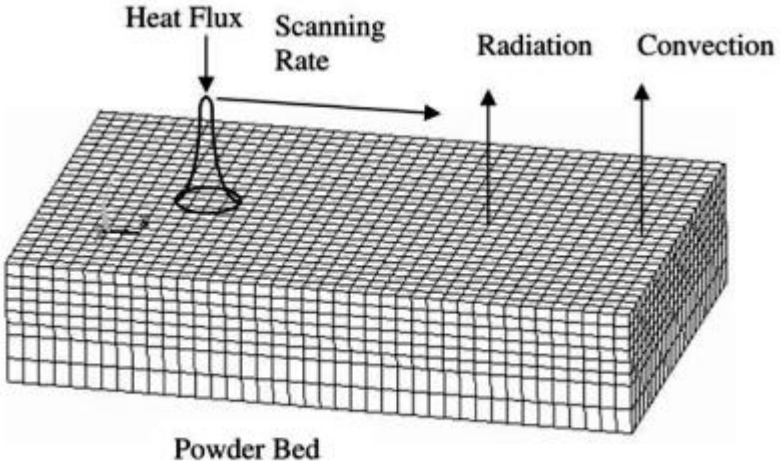

Fig. 2.7: Heat transfer during laser melting (Dai and Shaw, 2005)

A fraction of the energy determined by the absorptance is captured by the powder, while the remainder is reflected. The absorbed energy raises the temperature of the material up to and above its melting point while the rest is dissipated by either conduction to the surrounding material or lost from the surface to the atmosphere over time by convection or radiation.

The heat balance equation in the system during laser irradiation within a closed system in accordance with the first law of thermodynamics can be written as:

$$\vec{Q}_L = \vec{Q}_{CD} + \vec{Q}_{CV} + \vec{Q}_R + \vec{Q}_S \qquad \text{Eq. 2.1}$$

where Q_L is the laser irradiation heat, Q_R, Q_{CV}, Q_{CD} are the radiation, convection and conduction heat energy components between the powder bed and the environment respectively. Q_S is the heat changes associated with structural or phase transformations.

Badrossamay and Childs (2007) in studying the laser melting of stainless steel powders stated that the major source of heat loss through the powder bed is via conduction and contributions by convection and radiation are so small they can be neglected without any loss of accuracy. This study will consider the surface heat losses due to convection; however, the radiation component of the heat balance equation will not be considered.

Although the laser energy is converted into the other energy forms like visible light, Eq. 2.1 considers only the thermal energy components of the laser energy.

2.11.1 Laser Irradiation Models

Predicting the temperature field distribution resulting from laser irradiation in the laser melting of powders is an important step in determining the generated thermal stresses. A number of researchers have experimentally measured the temperatures during laser sintering. Gao *et al* (2007) measured the surface temperatures in the SLS of polystyrene powder using a non-contact infra-red thermograph. Fischer *et al* (2004) were able to measure the maximum temperatures achieved during the laser heating of titanium powder using a Raytheon infer-red camera. Jamal (2001) used experimentally determined temperatures from Infra-Red sensors as input for modelling the heating process in the SLS of polycarbonates. Other researchers have used theoretical models to predict the temperatures reached during laser heating of metals (Ready, 1971, Young, 1977 and Das, 1991). The theoretical models have been adapted in a number of laser heating temperature field analytical studies by Shen *et al* (2001), Majumdar and Xia (2007) and Jun Chang *et al* (1999). These models are idealised, treating the laser beam as a point source and assuming the material properties remain the same at elevated temperatures. The transient rapid temperature cycles that generate the thermal stresses are not fully captured by these methods. Therefore, numerical models which take into account the three-dimensional effects and treating the laser as a moving heat source would provide a unique understanding of the laser melting process.

2.11.2 Cylindrical Model

The cylindrical model assumes that the laser irradiation is constant at every point bounded by the spot area (Crafer and Oakley, 1993). The heat flux is simply defined as:

$$q_{CYL} = \frac{P}{\pi R^2} \qquad \text{Eq. 2.2}$$

where *P* is the laser power and *R* is the beam radius.

The cylindrical model is the basis of the analytical equations used for predicting the maximum achievable temperatures (Ready, 1971). Researchers like Shiomi *et al* (1999) and Bai *et al* (2006) used the cylindrical model for predicting the temperature field in laser sintering of metal and plastic powders respectively.

2.11.3 Gaussian Model

Laser beams are symmetric about their propagation direction and exhibit a radial pattern of irradiance. The Gaussian model is the most widely adopted irradiation model. It utilises the symmetrical distribution of laser irradiation across its field domain. It is important to note that while the laser intensity and irradiance have been used interchangeably in a number of studies, they are in actual fact two different quantities.

In the fundamental Gaussian mode, the maximum irradiance (power per unit area), I_o is at the centre of the beam and reduces exponentially outwards. All other values are usually written in terms of this maximum value. Fig. 2.8 shows the Gaussian profiles for the first three irradiation modes – TEM_{00}, TEM_{01} and, TEM_{10}.

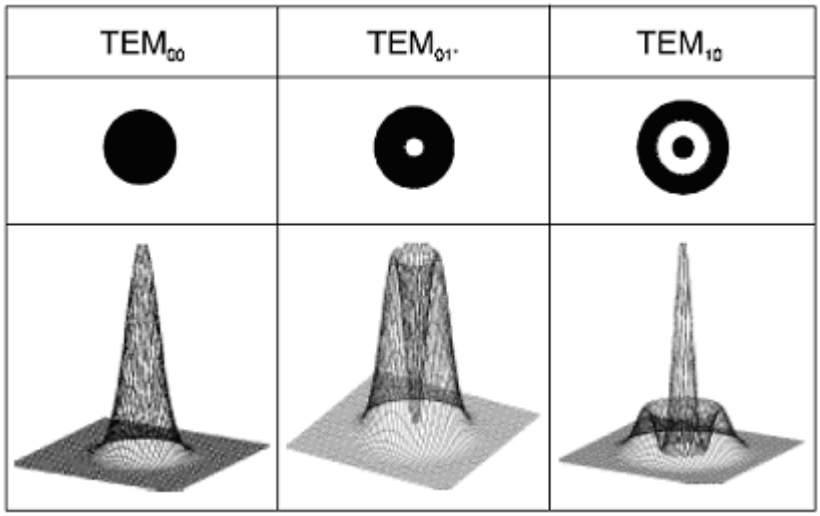

Fig. 2.8: Gaussian beam mode profiles (Ready, 1971)

The beam irradiance at any point on a diameter, *d* for the fundamental mode (TEM_{oo}) is defined as (Ready, 1971):

$$I(r) = I_o e^{-2r^2/R^2} \qquad \text{Eq. 2. 3}$$

where I_o is the maximum irradiance which occurs at the centre of the beam, *r* is the radial distance at an instance from the centre of the beam and *R* is the radius corresponding to the point where the laser irradiation diminishes to $1/e^2$ of its maximum value.

In the TEM_{oo} mode, the beam emitted from a laser begins as a perfect plane wave with a Gaussian transverse irradiance profile as shown in Fig. 2.9.

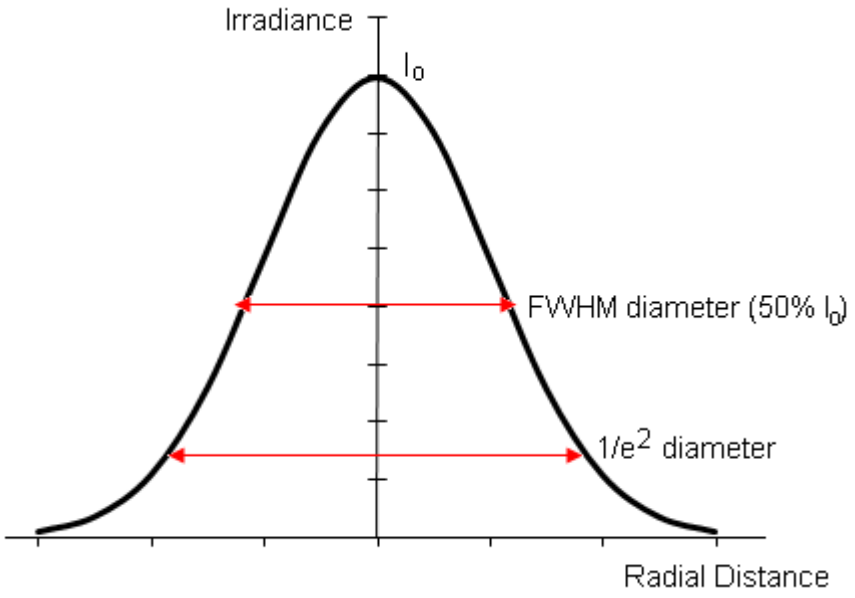

Fig. 2.9: Irradiance profile for Gaussian TEM_{00} mode

There are two commonly accepted definitions for the size or diameter of a laser beam. One definition is the diameter at which beam irradiance has fallen to $1/e^2$ (i.e. 13.5%) of its peak, and the other is the diameter at which the beam irradiance has fallen to 50% of its peak. The second definition is referred to as the Full Width at Half Maximum (FWHM) (Young, 1977). The $1/e^2$ definition is the generally accepted and is the measurement convention suggested in the British Standards (BSI, 2005). The unexpanded laser beam diameter of the Nd:YAG laser in the EOSINT M270 used for this work as quoted by the manufacturer was 80-100 µm (Electrical Optical Systems, 2005). The range for the beam diameter value is a result of the instrument sensitivity in registering low intensity values for distances greater than the $1/e^2$ distance. Also, changes in the position of the focused point and inclination of the scanning mirrors (for

systems that use mirrors) investigated by Wang (1999) contribute to this observation. The upper boundary beam diameter of 100 μm is used for the rest of this work.

A number of researchers have adopted the Gaussian model with varying degrees of success. Dai *et al* (2003) used the Gaussian irradiance distribution in predicting the temperature field of laser powder deposition of silicon carbide. In Dai and Shaw (2005), they expressed the heat flux distribution as:

$$q(r) = \frac{2P}{\pi R^2} e^{-2r^2/R^2} \qquad \text{Eq. 2.4}$$

$$\text{or} \qquad q(r) = 2e^{-2r^2/R^2} \frac{P}{\pi R^2} = 2e^{-2r^2/R^2} \times q_{CYL}$$

This definition is the same as that given by Ready (1971) for beam irradiance. Patil and Yadava (2007) also employed a similar Gaussian model (but with a higher constant value of 4.55 in place of 2 in Eq. 2.4) in the temperature distribution prediction in the laser sintering of a single layer of titanium powder.

It can be seen that the cylindrical model given in Eq. 2.2 holds true for the points at or close to the centre of the laser beam, but not the decay that occurs across the radial distance. It follows therefore that the cylindrical model as used by Shiomi *et al* (1999) and Bai *et al* (2006) would have resulted in an over-estimation of the heat energy transferred to the irradiated surface material.

In using the Gaussian model in a thermal numerical model, the generation of elements in the numerical should be done to accommodate the application of the heat flux to the nodal points of the influenced elements in a radial manner from the centre of the designated spot (i.e. using a cylindrical coordinate system). To mimic the movement of the laser heat source, the centre of the laser beam moves to a new position and the heat flux is applied according to the new radial points. The location and distribution of the nodal points in the numerical model are very important to use this method.

2.11.4 Modified Cylindrical Laser Heat Flux

The irradiation model adopted in this research is a hybrid between the cylindrical and Gaussian irradiation models. A numerical average of the Gaussian distribution is computed to represent an equivalent cylindrical heat flux density distribution. This numerical average can be expressed in integral form as follows:

From the cylindrical flux density distribution,

$$q = \frac{\overline{P}}{A} \qquad \text{Eq. 2.5}$$

$$q = \frac{1}{A}\int_S IdA = \alpha\frac{1}{\pi R^2}\int_0^R \frac{2P}{\pi R^2} e^{-2r^2/R^2}\ 2\pi r dr \qquad \text{Eq. 2.6}$$

where α is the absorptance of the surface to the laser

The expression $\int_o^R e^{-2r^2/R^2}\left(\frac{4r}{R^2}\right)dr$ is a definite integral and its value is:

$$\int_0^R e^{-2r^2/R^2}\left(\frac{4r}{R^2}\right)dr = \left[e^{-2r^2/R^2}\right]_0^R = 1 - e^{-2}$$

Therefore,

$$\overline{q} = \left(1-\frac{1}{e^2}\right)\alpha\frac{P}{\pi R^2} = 0.864\alpha\frac{P}{\pi R^2} \qquad \text{Eq. 2.7}$$

or $$\overline{q} = \left(1-\frac{1}{e^2}\right)\alpha\frac{P}{\pi R^2} = 0.864\alpha \times q_{CYL}$$

This approximation was used by Shi *et al* (2007) successfully in predicting the temperature field and plate deformation in laser bending analysis of thin steel plates. The results from their study for the bending angles agreed with experimentally measured angles.

2.11.5 Heat Transfer Equations

The temperature field involves a laser beam moving in the planar direction at a given speed. The different material states can be assumed to be semi-infinite continuous media that follow Fourier's law of heat conduction. According to Samarskii and Vabishchevich (1995), the heat transfer equation for an isotropic material is given as:

$$\rho C\left(\frac{\partial T}{\partial t} - v\frac{\partial T}{\partial x}\right) = \nabla\cdot(k\nabla T) + \dot{q} \qquad \text{Eq. 2.8}$$

where ρ is the density, C is the specific heat capacity, k is the thermal conductivity, v is the speed and the term $\dot{q}$ represents the rate at which heat is supplied to or lost from

the system. During the cooling stage, no external heat source exists but losses via convection continue.

The rapid movement of the laser beam in laser melting makes it a transient problem, which can be transformed into a quasi-steady state problem. The general energy balance equation for each step can be written as:

$$\rho C \frac{\partial T}{\partial t} = \nabla \cdot (k \nabla T) + \dot{q} \qquad \text{Eq. 2.9}$$

When the material changes state, latent heat due to melting or fusion is involved. This is a considerable amount of energy that ultimately influences the heat transfer dynamics. Dai and Shaw (2002) ignored this heat quantity in their study, while others like Patil and Yadava (2007) used a modified specific heat capacity to account for heat changes during state change.

Whereas researchers like Matsumoto *et al* (2002) used a temperature recovery method to account for latent heat changes with the solid-liquid transformation, the enthalpy change variant given in Eq. 2.11 is used in this work. This uses the enthalpy change method, here the energy changes within a particular material state can be captured as will be seen in Chapter 3.

The change in enthalpy (*dH*) is given as:

$$dH = C_p dT \qquad \text{Eq. 2.10}$$

It follows that:

$$\rho \frac{\partial H}{\partial t} = k\left(\frac{\partial^2 T}{\partial x^2} + \frac{\partial^2 T}{\partial y^2} + \frac{\partial^2 T}{\partial z^2}\right) + \dot{q} \qquad \text{Eq. 2.11}$$

With the above equations, most thermal processes can be described mathematically. Depending on the problem, additional terms must be included to reflect particular loads and boundary conditions.

The laser beam is treated as a moving heat source with a prescribed flux density, $\overline{q}$ on the material surface.

In the LM process, the parts are built in a chamber which is maintained at a uniform preheat temperature, T_O. The time dependent losses from the surface of the powder bed are convection, thermal radiation and material vapourisation. Vapourisation of metal

powders is a very important factor because plasma formation could occur over the powder surface which effectively absorbs all the laser radiation, thus shielding the powder and stopping the process (Schneider, 1998). For the LM process, the selection of laser power and scan speed makes it unlikely for vapourisation to occur. Material vapourisation, which is the driver in the laser ablation process, is beyond the scope of this work.

The surface convection heat loss is described using Newton's law of cooling as:

$$q_{conv} = -h(T - T_o) \qquad \text{Eq. 2.12}$$

Where q_{conv}, is the rate of cooling per unit area, and *h* is the convective heat transfer coefficient.

As laser melting of metal powders involves rapid localised melting and solidification, convective redistribution of heat within the molten pool is not as significant like it is in other processes where a liquid pool is permanent (Frewin and Scott, 1999). Convective flow of heat in the molten material is neglected.

2.12 Derivation of Thermal and Residual Stresses

The stress field generated during the LM of metal powders is characterised by several physical processes. These include microstructure evolution, porosity changes, molten pool effects and structural changes, all of which influence the development of thermal and residual stresses (Wang *et al*, 2002). The thermal history of the material in the scanned layers varies from point to point depending on the process parameters and exposure strategy. As a result, Costa *et al* (2005) suggested that the built part may present complex microstructures and mechanical properties, which are dependent on the processing and material conditions.

2.12.1 Thermal Elasto-Plastic Constitutive Model

Masubuchi (1980), in the analysis of solidification of weld materials, stated that the temperature dependence of the material properties (i.e. the yield stress and the plastic flow) is one of the most important elements in the analysis of thermal stresses.

For strain rate independent plasticity, the total strain can be expressed as:

$$\varepsilon = \varepsilon_{el} + \varepsilon_{ie} + \varepsilon_{th} \quad \text{Eq. 2.13}$$

where ε_{el}, ε_{ie} and ε_{th} are the elastic, inelastic and thermal strain components respectively.

The thermal component arises from volume changes caused by both temperature and phase changes. It can be expressed as:

$$\varepsilon_{th} = \beta \Delta T \quad \text{Eq. 2.14}$$

where β is the coefficient of thermal expansion (also temperature dependent).

The inelastic component depends in a complex manner on the temperature, strain hardening behaviour of the material and the temperature (Masubuchi, 1980). The flow rule describes the changing behaviour of the yield surface with progressive yielding, so that the conditions (i.e. stress states) for subsequent yielding can be established.

The elastic component can be derived as follows:

$$\varepsilon_{el} = \varepsilon - \varepsilon_{ie} - \varepsilon_{th} \quad \text{Eq. 2.15}$$

The stress field components are computed from elastic strains as follows (ANSYS10, 2007):

$$\{\sigma\} = [D]\{\varepsilon - \varepsilon_{ie} - \varepsilon_{th}\} \quad \text{Eq. 2.16}$$

where $[D]$ is the stress-strain matrix.

2.12.2 Laser-based ALM Process Numerical Simulation Models

This section reviews the works of researchers that have undertaken thermal and stress analyses on laser-based ALM processes like sintering, cladding, and melting using numerical models. Altan and Vazquez (1997) in a study of various metal forming and manufacturing processes, stated that numerical models were increasingly being applied to eliminate process defects that could be caused by residual stresses, as well as optimise process variables for best outputs. This knowledge is difficult to achieve experimentally because the required tests could be prohibitively costly and time-consuming.

2.12.3 Part Geometry Modelling

Depending on the complexity of the part geometry, the laser melting process can be represented as either a two-dimensional or three-dimensional problem. Until recently, a large number of the numerical studies of residual stresses in laser-based ALM processes were limited to idealised two-dimensional models with a number of approximations and assumptions. Shiomi *et al* (1999) used two-dimensional models for modelling the melting and solidification processes in the SLS of copper powder. Matsumoto *et al* (2002) used a plane stress two-dimensional model to analyse the SLS of a single layer on a powder bed. Jamal (2001) predicted the curl developed during the SLS of Laserite Polycarbonate Compound (LPC3000) using a plane strain finite element assumption to model the sintering of up to ten layers. The stress relaxation that occurred during cooling of the added layers was considered. Gan *et al* (2004) used a two-dimensional axisymmetrical finite element model to study laser plasma deposition of nickel-based alloy on an aluminium substrate. Sowdari and Majumdar (2010) recently used two-dimensional models to predict the molten pool characteristics of a single irradiated spot during the laser melting of aluminium.

According to Dong *et al* (2005), residual stresses in thermally processed parts exhibit strong three-dimensional features. Therefore, three-dimensional effects should be taken into account in both experimental measurements and numerical modelling. Two-dimensional idealisation can be a quick and in some cases an effective means of modelling the laser melting process. Jiang (2006) compared the characteristics of two-dimensional and three-dimensional models in the analysis of multi-pass butt welding. The results from both the two-dimensional and three-dimensional models agreed with published experimental results; however, the three-dimensional model provided a greater depth of understanding of the development and distribution of residual stresses in the multi-pass welding process. Dai *et al* (2003 and 2004) also used three-dimensional numerical models for predicting the distribution of residual stresses and shrinkage in the laser deposition of silicon carbide and dental porcelain.

2.12.4 Layer Deposition Modelling

The addition of powder material with time in laser-based ALM studies have presented challenges to previous researchers in creating three-dimensional models, restricting

most studies to modelling single tracks or single layer parts. For example, Branner *et al* (2008) modelled the scanning of separate scan tracks on a steel plate using three-dimensional considerations, while Matsumoto *et al* (2002) were able to model the deposition of a single layer of nickel-base powder using a two-dimensional plane stress model. In their work, they assumed that the shrinkage and change in geometry only affected the thickness of the layer. Analytical solutions have been used with limited success to predict the stresses for multiple layer addition. Mercelis and Kruth (2006) used a two-dimensional beam idealised approach to predict the variation of residual stresses for the addition of up to fifty layers of metal powder on a steel platform. A similar beam model theory was used by Shiomi *et al* (2004) to calculate the residual stresses in the SLS of a chrome-molybdenum-steel powder mixture (JIS SCM440). They used strain changes in the base platform that occurred when top layers of sintered material were milled off.

The challenge presented by the addition of multiple layers is addressed in this work by using an innovative simulation technique known as 'the element birth and death method'. The technique is discussed in Section 2.13.2.

2.12.5 Material Properties Modelling

Good knowledge of the temperature dependent thermal and mechanical properties of the material is a requirement for modelling the temperature and stress fields in the laser melting of metal powders. In representing the material properties for the range of operating temperatures, a number of researchers have used 'effective' values of material properties in their studies. The 'effective' value used in some cases is the average value of the material property over the temperature range and in other cases, it is merely value of the material property at room temperature. Although some positive conclusions were drawn from studies that used this assumption, they fell short of capturing the complex non-linearities in material state changes that occur in the laser process.

Kolossov *et al* (2004), in predicting the temperature field in the DMLS of titanium, assumed various effective values for the thermal conductivity. The results were significantly different from measurements for different values of thermal conductivities used, indicating the importance of temperature dependent values for accurate predictions. Costa *et al* (2005) and Dai and Shaw (2002) used temperature-dependent material properties with some success in modelling the laser deposition of metal

powders. In analysing the temperature distribution during laser enamelling of a grout material on ceramic tiles, Nisar *et al* (2003) used a numerical model that considered the non-linearity presented by phase and state changes but not volume changes due to solidification. The results from the simulation model showed some agreement with results from their temperature measurements.

In terms of the mechanical properties, studies by Branner *et al* (2008) in laser melting of titanium alloy showed that using only material properties in the elastic range in their model overestimated the residual stresses. Therefore, consideration of the non-linear mechanical behaviour is an essential component that should be taken into account.

2.13 Finite Element Modelling

Although it has become more feasible to conduct three-dimensional numerical simulations for the temperature and residual stress distributions in ALM processes, it was the finding of the author that a large number of previous studies were limited to relatively simple models, single spot locations and single tracks. As a result, the models were not representative enough of the process under investigation. Hence, this research sought to develop a more realistic finite element model as a tool to assess the influence of process variables on the magnitude and distribution of residual stresses in the laser melting of metal powders. Extensive research in the area of structural field modelling and measurement was needed in the following aspects:

(1) Three-dimensional numerical model to simulate the temperature field using temperature dependent material properties.

(2) Three-dimensional numerical model to simulate the structural powder-platform interaction during the laser melting process, including material yielding and strain hardening (i.e. plastic deformation in both deposited material and platform, where stresses potentially exceed the yield stress of the material of one of the components).

In this work, the heat transfer and structural field calculations were performed using ANSYS Mechanical finite element software (ANSYS10, 2007). ANSYS Mechanical provides a convenient means of numerically modelling the laser melting process. A system with an infinite number of unknowns (i.e. the response at every location in a system) is transformed into one that has a finite number of unknowns controlled by

elements of defined sizes. The system is solved using a problem dependent solution strategy.

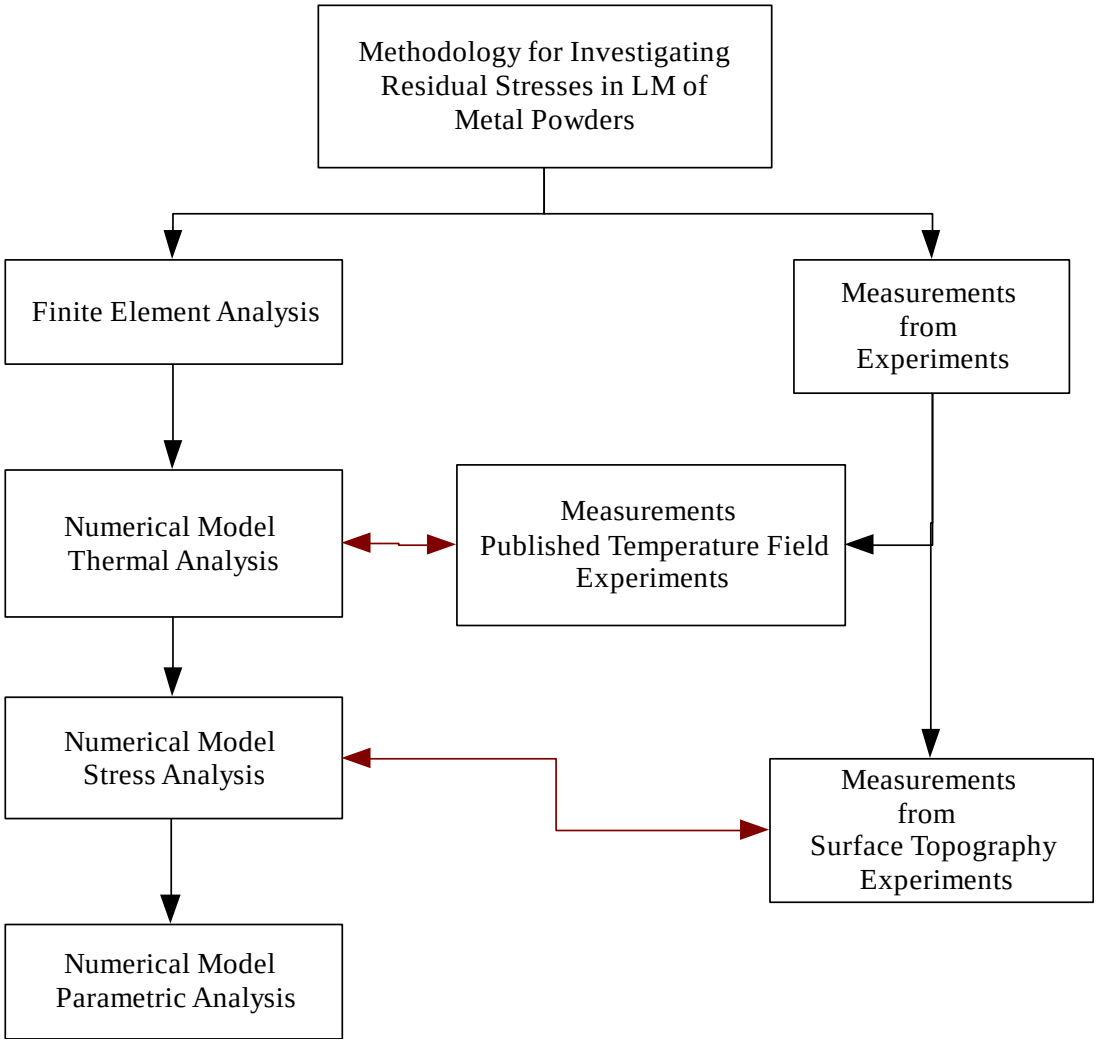

Fig. 2.10: Methodology flowchart

Fig. 2.10 illustrates the methodology flow chart. In the current work, prediction of the residual stress field in the laser melting of metal powders is the goal; hence, transient thermal-mechanical analysis is required.

The temperature field analysis can be validated against published experimental results, while validation of the structural field analysis can be carried out from the experimental measurements of the surface displacements induced by the laser melting of a defined number of powder layers on a platform. A close correlation between the numerical and experimental results would support the applicability of the thermal-mechanical numerical model for use in the parametric studies to study the effects of the process

variables on the magnitude and distribution of residual stresses in the laser melting of metal powders.

2.13.1 Coupled-Field Analysis

Coupled-field analysis is a combination of analyses from different engineering disciplines (referred to as physics fields) that interact in a global engineering problem; hence, it is often referred to as a multiphysics analysis (Adams and Askenazi, 1999). The mechanism of laser melting involves a number of closely related physical processes of which the thermal, fluid and mechanical fields are dominant. The LM process is, therefore, a complex multiphysics problem that involves coupling between thermal, metallurgical, fluid and mechanical fields. The overall heat transfer and structural field quantities are derived by solving a combination of the equation sets described earlier in Sections 2.11 and 2.12. More advanced modelling of the thermal-fluid-structural interaction would give a more realistic representation of the problem; however, the choice of coupled-field analysis is limited by the currently available element formulation capabilities. At present, no single commercially available element incorporates all of these capabilities. Therefore, this work focuses on the coupling between the thermal and mechanical fields.

Calculating the transient temperature field requires knowledge of thermal properties and heat transfer mechanism, while the stress field is governed by the thermal history and mechanical properties in each location. According to Koric and Thomas (2008), it is practically impossible to provide exact solutions for such a coupled field problem, hence numerical methods which provide approximate solutions are required.

When the results of one field analysis provide the loads and boundary conditions for another physics field, the analyses are said to be sequentially coupled (ANSYS10, 2007). Theoretically, during the laser melting process, the temperature field is thermodynamically coupled with the mechanical field because of the possible heat generation during plastic deformation. In the study of the thermal stresses in multi-pass welding by Jiang and Yahiaoui (2007), it was found that the temperature field introduced thermal strains in the structural field, but the structural strains were very small and had negligible effect on the temperature field. As in multi-pass welding, it is generally agreed that the heat caused by plastic straining of the material in laser melting is very small compared to the heat input from the laser source. Thus, the coupling is

sequential or one-way, in which the thermal history is the main driver of the transient stresses. Fully coupled thermal stress is required where the temperature and stress fields are mutually dependent, for example in large deformation forging processes. This type of analysis involves solving both the thermal and stress fields simultaneously (ANSYS10, 2007).

Fig. 2.11 illustrates the workflow diagram for the sequentially coupled-field analysis. The thermal analysis quantities $\{C\}$, $\{k\}$ and $\{q\}$ represent the capacitance matrix, conductance matrix, and the heat load vector respectively, while the stress analysis quantities $\{D\}$,$\{B\}$, and $\{M\}$ represent the stress-strain matrix, shape-function matrix and the mass matrix respectively.

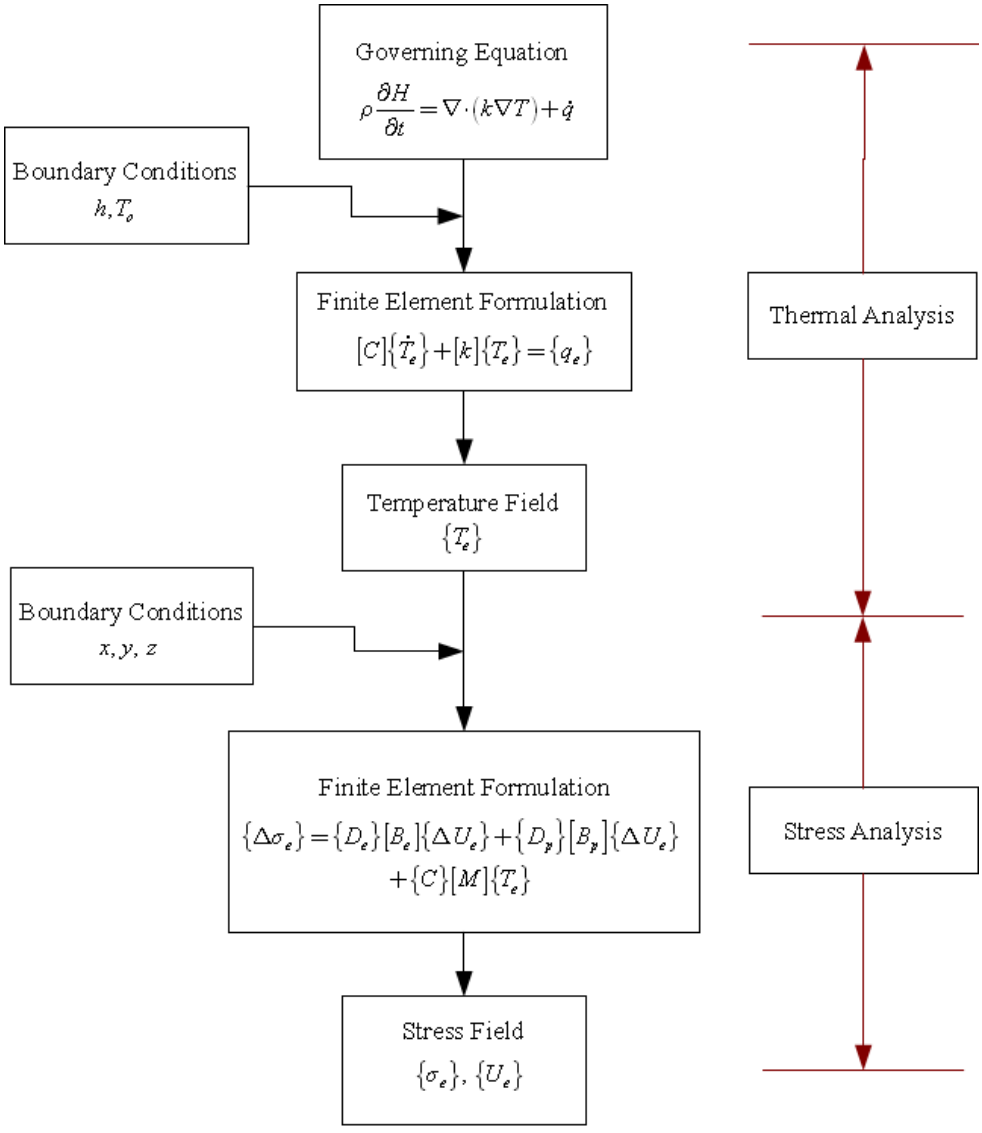

Fig. 2.11: Coupled-field analysis flow chart

This coupling method was employed by Dai and Shaw (2001) and Dai and Shaw (2002) for the simulation of distortions in laser-processed components. Jamal (2001) used a similar coupling method for predicting the curls produced in the laser sintering of polycarbonate powder. Shi *et al* (2007) also utilised this technique in predicting the deformation in laser bending of thin steel plates.

2.13.2 Element Birth and Death Technique

The deposition of powder material in layers with respect to time can be modelled using a technique known as 'element birth and death'. The procedure involves the activation of elements at the time points when they are required. To use this modelling technique in a top-bottom fashion, all elements would be created initially in the finite element model including those to be activated at later stages of the analysis. The method term 'death' does not remove elements to achieve element death, instead it deactivates them by multiplying their stiffness matrices by a very small value – typically 1×10^{-9} (ANSYS10, 2007). Similarly, when the elements are activated (i.e. 'born'), their stiffness coefficients return to the original values. This method was employed by Noorzaei *et al* (2006) and Jaafar *et al* (2007) in predicting the temperature fields in the layered construction of Roller Concrete Construction (RCC) dams. In Dong and Wei (2006), the birth and death method was used for the study of stress build-up during multi-pass welding. Further studies by Gan *et al* (2004) employed it in predicting the residual stresses in nickel-cobalt plasma sprayed coatings on a thin aluminium substrate, while Jamal (2001) used the technique in simulating the addition and laser sintering of ten layers of polycarbonate powder. The method has, however, not been applied in the layerwise scanning of metal powders on a platform as characterised by the laser melting process.

2.13.3 Material Strain Hardening Models

Strain hardening in metals may be defined as the increase in yield strength due to plastic deformation. According to Chakrabarty (2010), for strain hardening materials, the yield surface can evolve in space in one of three ways:

- Linear Isotropic hardening: the yield surface expands but its centre remains fixed in space

- Kinematic hardening: also referred to as multilinear isotropic hardening. In this case, both the yield surface and its centre translate in space but no expansion of the yield surface occurs.

- Mixed hardening: combination of isotropic and kinematic hardening characteristics. Extension of the kinematic hardening to include the expansion of the yield surface.

Fig. 2.12(a)-(c) shows the stress-strain curves for various idealised material plasticity models.

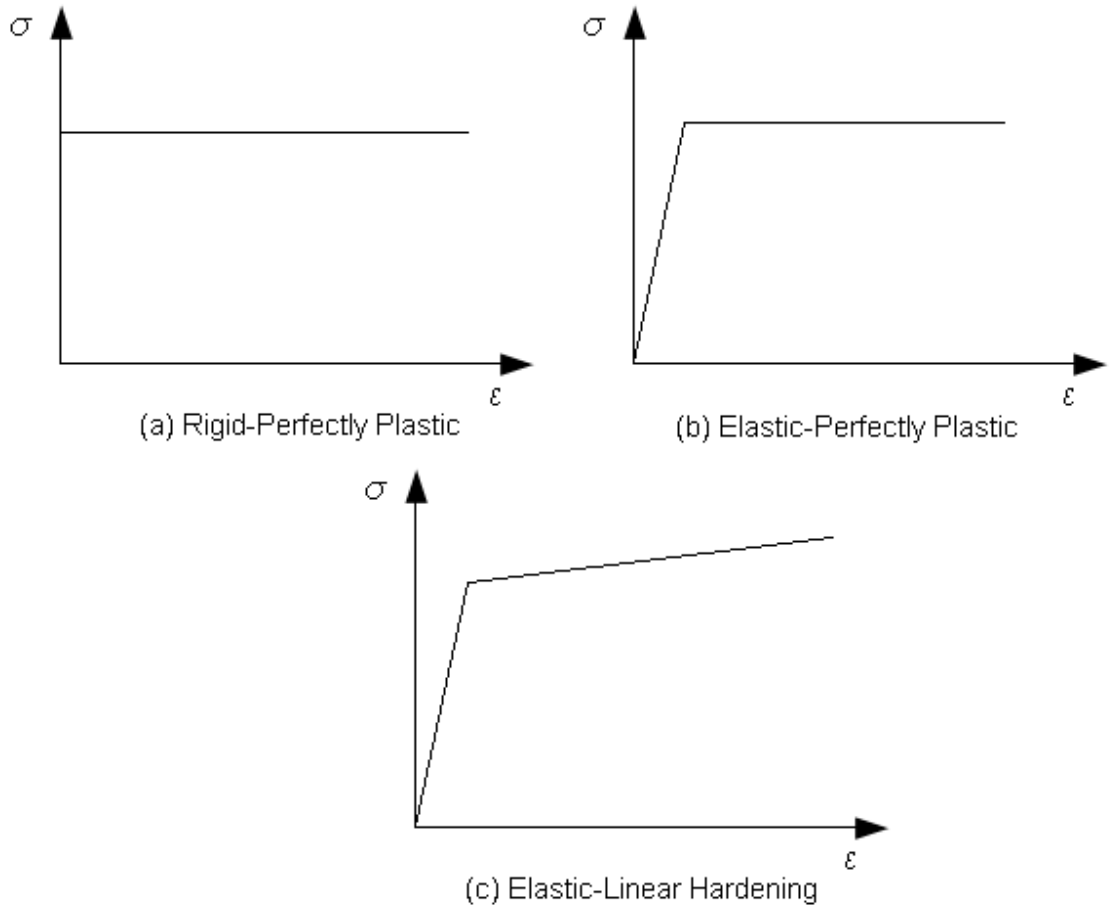

Fig. 2.12: Idealised material hardening models (Chakrabarty, 2010)

The isotropic hardening model and kinematic hardening models have been widely utilised in research work involving modelling material plasticity. While the isotropic hardening behaviour (Fig. 2.12(c)) is described by a linear strain hardening variation using the von Mises yield criterion with an associative flow rule, the kinematic hardening uses data points from stress-strain curves capturing the flow stress variation

with strain even at elevated temperatures. The material properties that define the isotropic hardening model are the yield strength and the slope of the stress-strain curve in the plastic regime.

2.13.4 Simulation Process Programming

In order to execute the finite element analysis, a robust interaction procedure with the analysis software was required. The Advanced Parametric Design Language (APDL) feature in ANSYS Mechanical software, which has strong similarities with FORTRAN programming language, provides this service and is utilised for running the vast repetitive parametric studies. It is important to mimic the step-by-step analogy of the LM building process in designing the simulation model program as well as capture the process and material variables of interest to investigate their effects on the residual stress distribution. This is described in detail in the numerical model development in Chapter 4.

2.14 Review Summary

This chapter has reviewed relevant laser-based additive layer manufacturing technologies. Laser-based ALM technologies can greatly accelerate the product development process when combined logically with other manufacturing processes (Behrendt and Shellabear, 1995). Since the late 1980s, stereolithography apparatus and laser sintering have been applied to many areas of industry. The technology has migrated from use for prototyping purposes to production of functional parts, while its material base has increased from a handful of research materials to commercially available ones.

The context in which lasers are considered in this research is limited to their heating characteristics and how they are adopted in ALM systems. Selective laser sintering and laser melting are leading commercial laser-based ALM processes that are applicable to metal powders. They have the potential to become an indispensable industrial tool. However, continuous process improvement and an improved understanding of the parametric effects on properties of built parts are required to promote their standing in industry.

The existence of residual stresses in laser-based ALM parts built from metal powders has been identified as a hindrance to the wide adoption of the technology in industry. Studies by previous researchers which have attempted to address the issue of residual stresses in SLS and LM have been reviewed. These included experimental studies carried out to investigate the effects of process parameters on the characteristics of built parts. Experimental methods, however, are known to be prohibitively costly and time consuming; hence, using analytical and numerical models prove to be an attractive option.

The origin and development mechanism of residual stresses were discussed, including the heat transfer process and the theoretical evaluation of residual stresses. The laser irradiation model, laser absorption and temperature dependence material properties were considered to be important components for the accurate modelling of the laser melting process.

The finite element method was introduced and its relevance to this research as an investigative tool has been outlined. Numerical analysis involving thermal and stress fields relating to laser-based ALM processes conducted by researchers in the subject area were reviewed in order to understand their scope, assumptions and limitations. It has been identified that the distinct non-linear characteristics (e.g. temperature-dependent material properties and moving laser source) as well as computation resource implications have been the major obstacles to the development of three-dimensional residual stress field models.

This work will focus on the development of a three-dimensional numerical thermal-mechanical model using innovative methods such as the ‘element birth and death’ technique and greater material properties representation to model the deposition and scanning of multiple layers of metal powder for use in studying the influence of process variables on the residual stress fields developed in the LM of metal powders.

3 Material Properties

3.1 Introduction

The distinct state changes that occur in the metal powders in a successful laser melting operation are powder-to-liquid-to-solid. Accurate representation and description of the material properties are essential to properly capture these changes in a numerical model. This chapter gathers relevant material data from published sources for modelling the laser melting process. Measurement tests were also conducted to determine certain material data.

3.2 Materials

The materials of interest in this work are pure titanium, titanium alloy (Ti64) and hot-rolled mild steel (BS970 070M20 equivalent to AISI 1015). The Ti64 powder and the steel plates were obtained from a local powder supplier and a steel supplier respectively for which specifications were obtained.

The chemical compositions for Ti64 and AISI 1015 used in this work are given in Table 3.1 and Table 3.2 (Mills, 2002 and Touloukian, 1977).

Table 3.1: Ti64 Composition (%mass)

Al	Fe	Ti	V	H	O_2 & N_2
5.5-6.7	0.03	90	3.5-4.5	0.0125	0.25

Table 3.2: AISI 1015 Composition (%mass)

Fe	C	Mn	P	S
99.20	0.18	0.60	0.040	0.050

3.3 Thermophysical Properties

Temperature dependent physical properties (i.e. thermal conductivity, enthalpy and density) were used in the transient thermal analysis as outlined in the heat transfer equations in Chapter 2. The use of temperature dependent thermal properties and latent heat considerations implies a non-linear thermal analysis. This section reviews the thermal properties of the solid materials. The thermophysical properties of the powder material are addressed in a later section.

3.3.1 Thermal Conductivity

The thermal conductivity is a property of the material which describes the rate at which heat is transferred through the material. The thermal conductivity for pure Ti (melting point = 1670°C) and Ti64 (melting point = 1650°C) are shown in Fig. 3.1. The values for AISI 1015 are listed in Table 3.6.

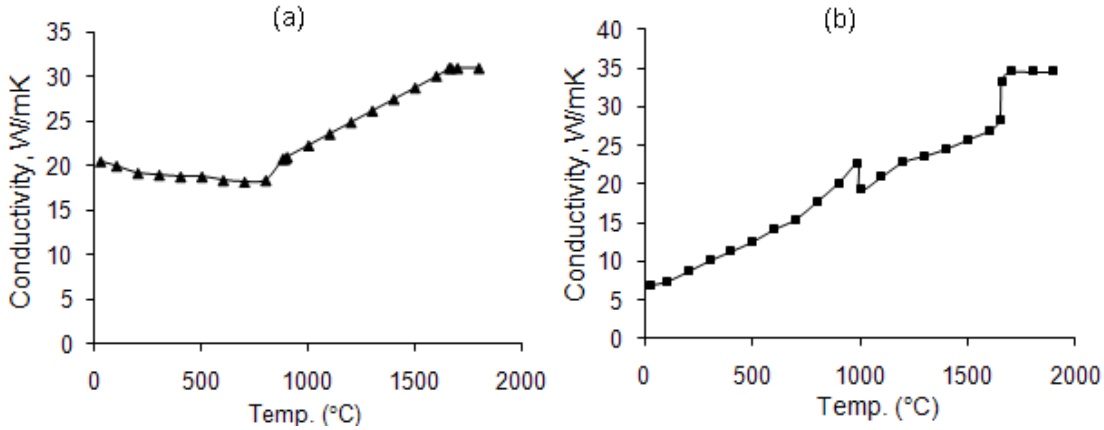

Fig. 3.1: Temperature dependence of thermal conductivity: (a) Pure Ti, (b) Ti64 (Mills, 2002)

An upper limit temperature of 2800°C is assumed for the analysis. This upper limit is less than the boiling point of titanium (i.e. 3260°C – Donachie, 1989) because vapourisation is not expected for the laser melting process being considered. The upper limit temperature was chosen considerably higher than what is physically achievable with the current laser scanning parameters as advised by EOS-GmbH (2005). For temperatures above the melting point, the thermal conductivity is assumed to vary in the same linear manner up to the upper limit temperature.

3.3.2 Enthalpy Change

Enthalpy is a measure of the heat energy content or internal energy of a system at a particular temperature. A change in temperature in the system causes a change in the enthalpy of the system. The specific heat capacity of a material at a given temperature is defined as the derivative of the enthalpy change with respect to temperature.

Fig. 3.2 shows the variation of enthalpy with temperature for pure titanium and Ti64. It shows noticeable enthalpy changes at the Ti α–β transition as well as the melting temperature which would not have been easily captured using the constant specific heat capacity method. The values for AISI 1015 are listed in Table 3.6.

The enthalpy data gives a latent heat of melting/fusion of 295 kJ/kg and 282 kJ/kg for Ti and Ti64 respectively. The latent heat of melting for steel was given as 247 kJ/kg (USDD, 1998).

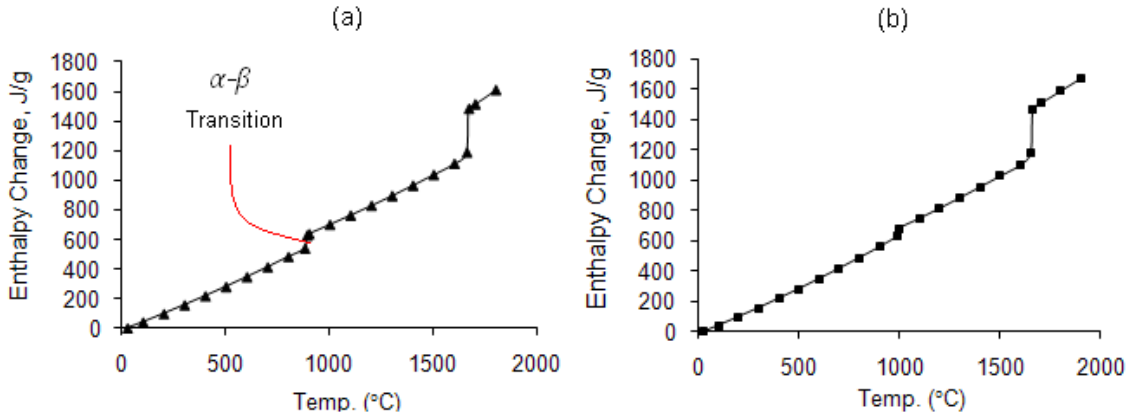

Fig. 3.2: Temperature dependence of enthalpy: (a) Pure Ti, (b) Ti64 (Mills, 2002)

Above the melting point and up to the upper limit temperature, the enthalpy change is assumed to vary linearly maintaining the same trend above the melting point.

3.3.3 Density

This is a physical quantity that describes the mass of a unit volume of a substance. It is a temperature dependent quantity and decreases with temperature for most materials.
Fig. 3.3 shows the variation of the density with temperature for Ti and Ti64. The values for AISI 1015 are listed in Table 3.6.

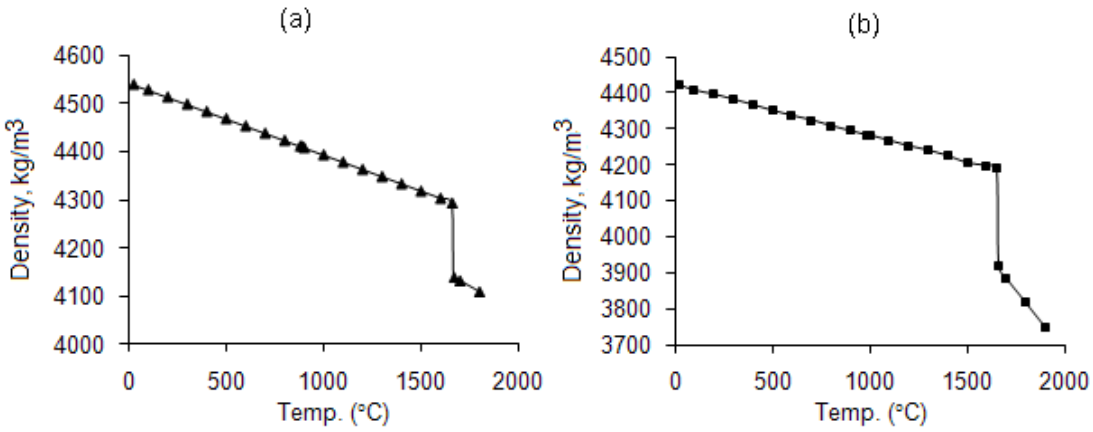

Fig. 3.3: Temperature dependence of density: (a) Pure Ti, (b) Ti64 (Mills, 2002)

For temperatures above the melting point, the density is assumed to vary linearly with temperature at the same rate after melting up to the analysis upper limit temperature.

3.4 Powder Metallurgy and Properties

In material forming processes involving metal powders, the properties of the starting powders determine to a great extent the properties of the final product. For example, the size distribution and shape of the powder particles has an effect on the powder's bulk density (Boivie, 2003). It is therefore essential to have an understanding of the metal powder properties in order to apply suitable methods for the quantitative characterisation of the relevant physical properties of the powder.

3.4.1 Powder Thermal Properties

The thermal conductivity of metal powders was found to be dependent in a complex manner on porosity (Thummler and Oberacker, 1993). Within the powder bed, two constituent phases can be identified (i.e. powder particles and gas pores). As a consequence, the conductivities of a material in its powder state and its solid state differ greatly as adjacent particles only make solid contact over small areas. Gusarov *et al* (2003) proposed that the effective thermal conductivity of the powder bed is strongly dependent on the linear contact distance between the particles. It follows that some form of convection and radiation heat transfer modes exist in addition to conduction. These heat transfer modes are adequately represented by the effective conductivity of the

powder. Some empirical relationships have been used to calculate the effective thermal conductivity of a powder bed (Thummler and Oberacker, 1993):

$$k = \frac{\rho_r k_s}{1 + \phi \frac{k_s}{k_g}} \qquad \text{Eq.3.1}$$

where k_g and k_s are thermal conductivities for the gas and solid respectively, ϕ is an empirical coefficient and ρ_r is the ratio of bulk density to that of the solid material.

These thermal conductivity quantities are themselves temperature dependent, thereby increasing the difficulty in establishing the actual temperature relationship for each quantity and consequently the effective thermal conductivity.

Experimental measurements carried out by Rombouts *et al* (2005) showed that the bulk or effective thermal conductivity of loose metal powders was largely controlled by the gas in the pores (determined by the size and morphology of the particles and the void fraction or bulk density) and was independent of material type. Thermal conductivity values reported for 10-50 µm metal powders ranged between 0.1-0.3 W/mK. Measurement tests performed by Taylor (2004) on stainless steel 316L powders agreed with their findings where the reported bulk thermal conductivities were between 0.08-0.25 W/mK. For this work, the value of the thermal conductivities for Ti and Ti64 powders were taken as 0.25 W/mK up to the melting temperatures in line with Taylor's measurements.

The enthalpy is controlled by the mass of a given composition. According to Tolochko *et al* (2003), the relationship between the enthalpy changes in the powder and solid states is given as:

$$\Delta H = \rho_r \Delta H_S \qquad \text{Eq. 3.2}$$

where ΔH_S is the change in enthalpy for the solid material and ρ_r is the ratio of bulk density to that of the solid material. Measurement of the powder bulk density is presented in Section 3.4.3.

3.4.2 Powder Compaction and Size Distribution

According to Thummler and Oberacker (1993), in sintering operations, the degree of compaction of the powders determines the packing density (i.e. bulk density) as well as the strength of the final formed part, while the fineness of powders (i.e. particle size distribution) determines its sinterability and meltability (Simchi, 2006). Most methods for particle size measurement yield a size-dependent property for the powder. This property in most cases is related to a linear dimension such as a sieve diameter, minimum aperture length through which the particle passes, or an equivalent spherical diameter.

The most widely used is the equivalent spherical diameter which is defined as the diameter of a sphere with the same characteristics as a corresponding particle (Thummler and Oberacker, 1993). The shape of the powder particles in most cases deviate significantly from the ideal geometries, therefore, a statistical distribution of the particle sizes is used to represent the size distribution of particles in the powder. The powder size of the Ti64 powder used in this work given by the material supplier was 20-30 µm and a minimum layer thickness of 30 µm was recommended by EOS-GmbH (2007).

3.4.3 Bulk Density Measurements for Ti64 powder

The bulk density as seen in Eq. 3.2 is a requirement for calculating the enthalpy of the powder phase at different temperature points from the solid material data.

The bulk density of the powder material was determined using a measuring cylinder and a high precision measurement scale. A 25.0 cm^3 cylinder was filled with loose powder and its mass determined. A calibrated Fisherbrand PS-200 digital measurement scale having an accuracy of 10 µg was used for this exercise.

The results of Ti64 powder mass-volume measurements were as follows:

Average powder mass, m_{pwd}	=	66.4866 g
Powder volume, V	=	25.0 cm^3
Calculated density, ρ_{pwd}	=	2659.5 kg/m^3

Room temperature solid density, ρ_s	=	4420 kg/m^3
Density ratio, ρ_r	=	0.602

The measurement gives a ratio of the powder bulk density relative to solid Ti64 of 60.2% at 25°C, which compared favourably with 64.6% for 30 µm diameter pure titanium powder reported by Fischer *et al* (2004). Niu and Chang (2000) stated that the typical estimate of the bulk density of steel powders is about 60% of the solid density. Measurements done by Abe *et al* (2001) on 75 µm diameter nickel-base alloy gave a value of 51%. This is expected because less packing is achieved with increasing powder particle size.

3.5 Convection Coefficient

From Chapter 2, the heat loss due to natural convection is described by:

$$q_{conv} = -h(T - T_O)$$

According to Bejan and Kraus (2003), the heat transfer coefficient is size-dependent and is given as:

$$h = \frac{kNu}{L} \qquad \text{Eq. 3.3}$$

where k is the thermal conductivity of the fluid, Nu is the Nusselt number and L is a characteristic length.

The Nusselt number is related in a complex manner to the Prandtl and Grashof numbers (which are other fluid parameters). Eq. 3.3 gives a useful relation as it shows that the convective coefficient is directly proportional to the thermal conductivity. Therefore, knowledge of the thermal conductivity can be used to deduce the convective coefficient.

Mardolcar *et al* (1986) measured the thermal conductivity of argon at different temperatures. They reported values of 0.018 W/mK at 35°C. Lemmon and Jacobsen (2004) provided formulations for calculating the thermal conductivities of argon and air which they validated against experimental data. They calculated values of 0.0178 W/mK and 0.0264 W/mK for argon and air respectively at 27°C.

Due to lack of available data for the convective heat transfer coefficient for argon, that of air is used in this work. According to Pope (1997), the convective coefficient of air varies between 5 W/m^{2}K and 20 W/m^{2}K at room temperature. Although the upper bound value is used initially, the effect of the convective coefficient is discussed in Chapter 7.

3.6 Thermo-Mechanical Properties

This section describes the material properties required to define the structural model. These consist of the elastic and non-linear mechanical properties at elevated temperatures.

3.6.1 Young's Modulus

This is a material property that represents the stiffness in the elastic range. As a general rule, the modulus of elasticity of metals decreases with increasing temperature. The variation of the elastic modulus with temperature for Ti64 and AISI 1015 are shown in Fig. 3.4.

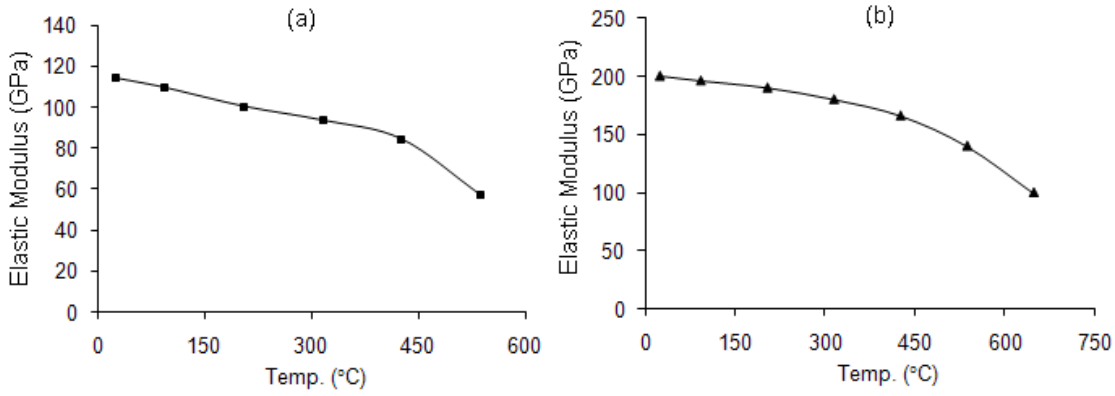

Fig. 3.4: Variation of Young's modulus with temperature (a) Annealed Ti64, (b) AISI 1015 (USDD, 1998)

It can be seen from Fig. 3.4 that the steel material loses more than half its stiffness at about 650°C, while Ti64 loses half its stiffness at about 540°C.

3.6.2 Yield Strength and Elasto-Plastic Constitutive Model

The stress-strain curve of a typical ductile metal exhibits a region beyond the proportionality limit where the material becomes plastic. A number of mathematical models have been developed to model the material behaviour in this plastic region (Chakrabarty, 2010). The linear isotropic and kinematic hardening models which are widely used for the analysis of plasticity in metals were introduced in Chapter 2.

The yield strength of the hot-rolled steel (AISI 1015) material at room temperature was corroborated by carrying out hardness tests. Vickers hardness tests were performed on cut-out samples of the steel material. The average hardness for the material was 143 H_V30. This corresponded to an ultimate tensile strength of 400 MPa using conversion charts and was in the range obtained in data sheets provided for the steel material (Wrekin Steels, 2009). The reported yield and ultimate tensile strengths were 255-290 MPa and 380-420 MPa respectively. The yield strength of the gas atomised Ti64 material was given as 1090 ± 70 MPa (EOS GmbH, 2007).

The reference room temperature yield strengths used in this work were taken as 255 MPa and 1090 MPa for the steel and Ti64 materials respectively.

The variation of the yield strength (tensile) at elevated temperatures of Ti64 and AISI 1015 are shown in Fig. 3.5. It can be seen that both Ti64 and AISI 1015 lose more than half their room temperature yield strengths at approximately 500°C.

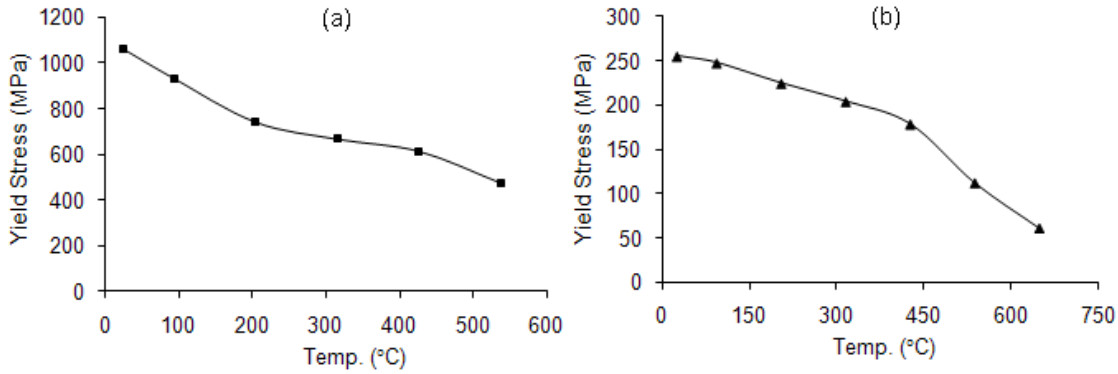

Fig. 3.5: Temperature dependence of yield strength (a) Annealed Ti64, (b) AISI 1015 (USDD, 1998)

High temperature yield strength curves from Corus (2010) generated by testing a series of small steel samples showed that most of the strength is lost at 800°C. This is taken as the *structural transition temperature* for the steel material for the analysis.

Fig. 3.6 and Fig. 3.8 show the true stress-strain curves at elevated temperatures for annealed Ti64 and steel. The stress-strain points and plastic tangent moduli were derived from the data for use in the kinematic hardening and isotropic hardening models respectively. The true stress-strains were obtained from the engineering stress-strain data using the relationships (Chakrabarty, 2010):

$$\varepsilon_{true} = \ln(1+\varepsilon_{eng})$$
$$\sigma_{true} = \sigma_{eng}(1+\varepsilon_{true}) \qquad \text{Eq. 4. 1}$$

The engineering stress-strain curves reported by USDD (1998) at elevated temperatures were derived using the Ramberg-Osgood formulation for describing the stress-strain curve in terms of three parameters (i.e. Young's modulus and two secant yield strengths). Comparison with the tensile and compressive data for aluminium alloy, stainless steel and carbon steel showed that the formula is adequate for these materials (Ramberg and Osgood, 1943). It was not stated if a high temperature extensometer was used in the measurement of the Young's moduli at these elevated temperatures.

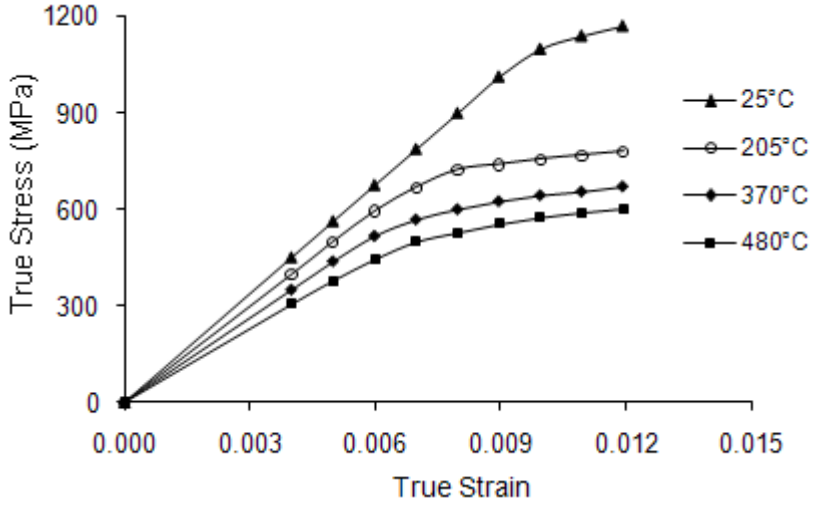

Fig. 3.6: Tensile stress-strain curves at elevated temperatures of annealed Ti64 (USDD, 1998)

Tensile tests performed at the University of Wolverhampton on the superplasticity of Ti64 alloy measured the stress-strain characterstics at temperatures up to 950°C. Results

at 1×10^{-3} s^{-1} strain rate for temperatures above 800°C are shown in Fig. 3.7. The stress-strain characteristic shows flow stress acitivity at these high temperatures. The decrease in strength can be seen as the temperature increases. The stress-strain properties for Ti64 for temperatures up to the melting point where it loses all its structural properties are obtained by extrapolation.

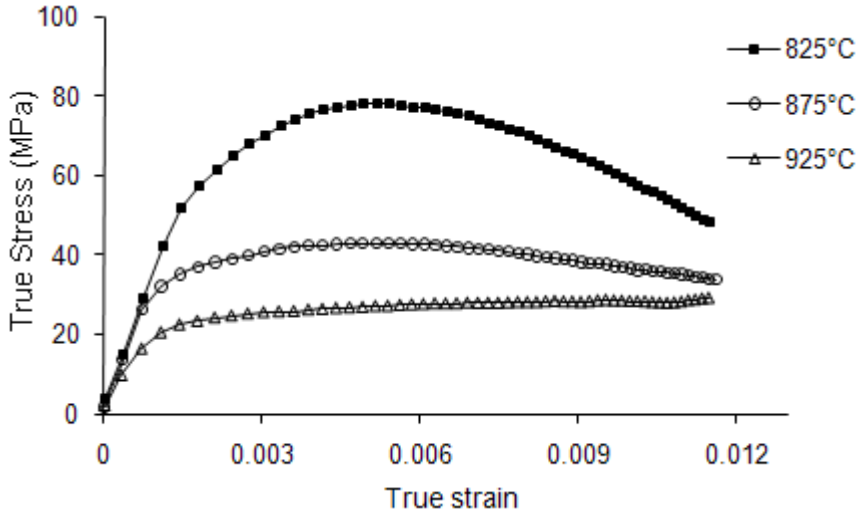

Fig. 3.7: High temperature tensile stress-strain curves of Ti64

Due to lack of available data for the high temperature stress-strain curves for AISI 1015, the high temperature properties are assumed to be similar to those of construction steel ASTM A36. Stress-strain curves for steel ASTM A36 have been published by FEMA (2010). The elemental compositions for both materials were similar with ASTM A36 having a slightly higher carbon content (0.26% C – CES, 2005).

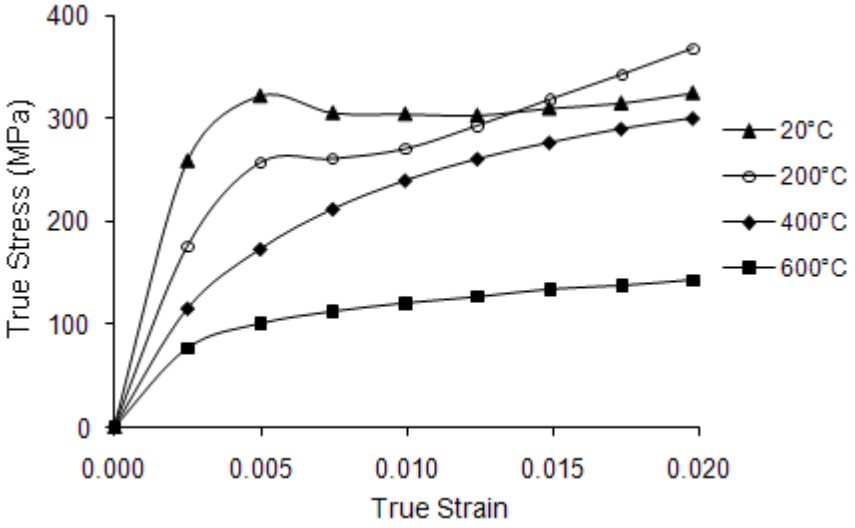

Fig. 3.8: Tensile stress-strain curves at elevated temperatures of ASTM A36 alloy (FEMA, 2010)

For the isotropic hardening model, the 0.2% proof stresses were determined graphically to represent the yield strengths at the given temperatures. The tangent moduli in the plastic region illustrated in Fig. 3.9 were also determined graphically from the stress-strain curves as follows:

$$E_{plastic} = \tan\theta_2$$
$$E_{elastic} = \tan\theta_1$$

Eq. 4. 2

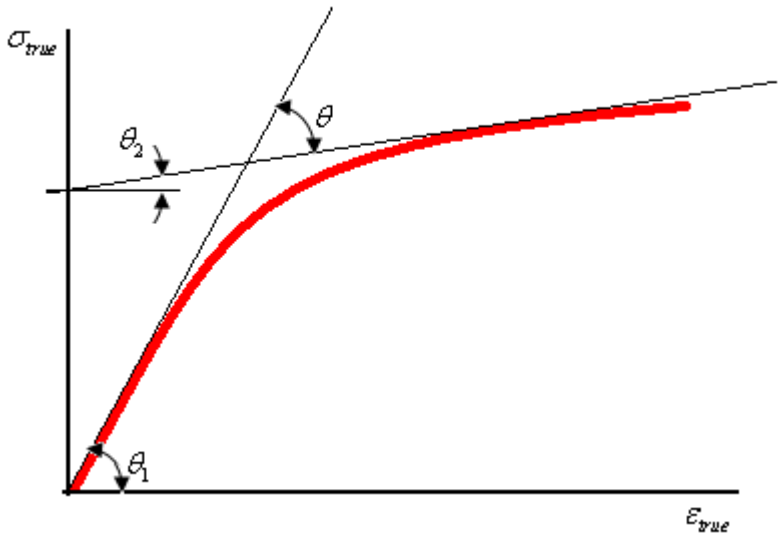

Fig. 3.9: Graphical determination of plastic tangent modulus

The stress-strain curve for the steel material shown in Fig. 3.8 shows the Yield Point Elongation (YPE) phenomenon at 25°C and 200°C where the load at the elastic limit suddenly drops from an upper yield point to a lower yield point, followed by an elongation of a few percent under approximately constant stress (Chakrabarty, 2010). The YPE characteristic becomes less pronounced with increasing temperature and eventually disappears at higher temperatures. The isotropic strain hardening model, which assumes a single linear tangent modulus value beyond the yield strength of the material, does not cater for this YPE non-linear characteristic. However, the kinematic (i.e. multilinear) strain hardening model which uses actual stress-strain points captures the YPE behaviour. The values for the tangent moduli are summarised in Table 3.3.

Table 3.3: Plastic tangent modulus at elevated temperatures

Temperature (°C)	Ti64 (GPa)	AISI 1015 (GPa)
25	6.31	5.51
200	-	8.79
205	5.52	-
370	5.01	-
400	-	7.27
480	4.76	-
600	-	4.74
825	3.48	-
875	2.11	-
950	1.67	-

3.6.3 Thermal Expansion Coefficient

The thermal expansion coefficient of most metals generally increases with temperature. Fig. 3.10 shows the temperature dependent thermal expansion coefficients for Ti64 and AISI 1015.

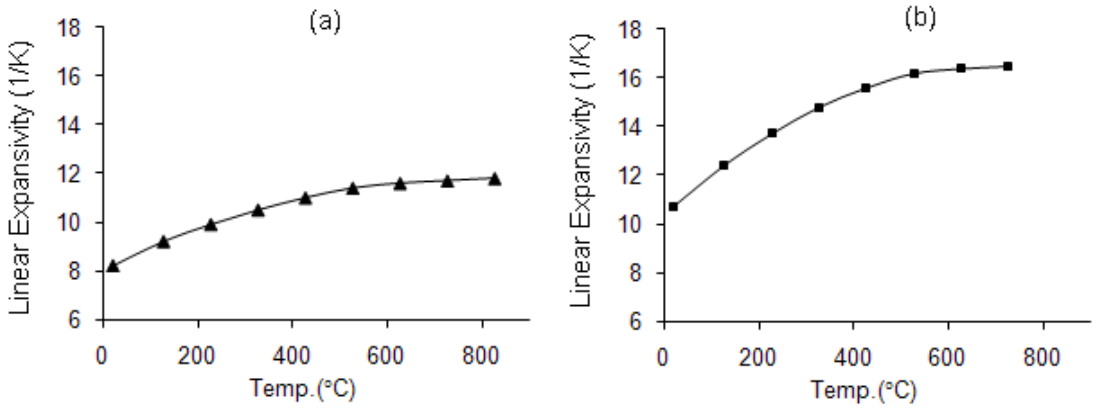

Fig. 3.10: Temperature dependence of thermal expansion coefficient (a) Ti64, (b) AISI 1015 (Touloukian, 1977)

For temperatures close to and above the melting temperature, the linear coefficient of thermal expansion can be derived from the volume expansion coefficient. For an isotropic material, the volume expansion coefficient is approximately three times the linear expansion coefficient (Bejan and Kraus, 2003). Experiments conducted by Li *et al* (2006) to measure the volume expansion coefficient of Ti64 using electrostatic levitation techniques reported a value of 6.05×10^{-5} K^{-1} near the melting point. This gives an approximate value of about 2.02×10^{-5} K^{-1} for the linear expansion coefficient. This shows a 68% increase in linear expansion coefficient as a result of the change in state.

3.6.4 Poisson's Ratio

This quantity determines the absolute value of the ratio between the transverse strain and the corresponding axial strain in the elastic range. For a fully plastic material, the Poisson's ratio is 0.5 (Chakrabarty, 2010). In the absence of high temperature data, the temperature dependence of the Poisson's ratio for Ti64 and AISI 1015 used in this study are assumed to vary linearly from their room temperature values (i.e. 0.342 and 0.28 respectively) to a maximum value of 0.49 at and above the structural transition temperature (i.e. 800°C for steel and 1650°C for Ti64) (Dai and Shaw, 2001).

3.7 Material Modelling Assumptions

It is important to note that it would be extremely difficult to achieve analytical or numerical solutions with all physical aspects incorporated into the model. Therefore, the following assumptions have been applied in this work.

- All material phases were assumed to be continuous homogeneous media.
- Intermediate material properties data were linearly interpolated between points outside the range of published data and up to the limit temperature of 2800°C.
- Creep and material viscoelastic effects were assumed to be negligible, due to the localised and rapid rate of solidification in the small irradiated regions.
- Although the steel material is known to lose both strength and stiffness above the *structural transition temperature* (i.e. 800°C), a small value of 0.1 GPa is assigned to both the elastic modulus and the plastic tangent modulus yield strength while a value of 1 MPa is assigned to the yield strength in order to avoid numerical errors in the form of zero matrices. The same values are applied to the Ti64 at its melting point.

3.8 Summary Tables of Material Properties

This section summarises the material properties used in the numerical model. Tables 3.4, 3.5 and 3.6 are used for the thermal analysis while Tables 3.7 and 3.8 are used for the structural analysis. The selected temperatures include the key transition temperatures and the analysis limit temperature. The properties for intermediate temperatures were obtained by extrapolation within ANSYS Mechanical software.

Table 3.4: Selected thermophysical properties of pure Titanium

Temperature	Density	Thermal Conductivity	Enthalpy Change
T (ºC)	ρ (kg/m^3)	k (W/m.K)	ΔH (J/g)
25	4420	7.0	0
100	4406	7.5	42
500	4350	12.6	284
1000	4282	19.3	684
1600	4198	27.0	1102
1650	4189	28.4	1184
1660	3920	33.4	1466
1900	3750	34.6	1674
2800	3138	34.6	2420

Table 3.5: Selected thermophysical properties of Ti64 alloy

T (ºC)	ρ (kg/m^3)	k (W/m.K)	ΔH (J/g)
25	4540	20.5	0
100	4529	20	40
500	4469	18.8	280
1000	4394	22.3	700
1600	4304	30.1	1112
1660	4294	31	1189
1670	4140	31	1484
1800	4110	31	1611
2800	3886	31	2565

Table 3.6: Selected thermophysical properties of AISI 1015

T (ºC)	ρ (kg/m^3)	k (W/m.K)	*ΔH (J/g)
25	7950	51.9	0
400	7785	49	225
800	7575	29.3	490
1480	7260	30	985
1500	6880	30	1232
1650	6725	30	1355
2100	6300	30	1710
2800	5630	30	2290

*Enthalpy change for AISI 1015 derived from specific heat capacities (Touloukian, 1977).

Table 3.7: Selected mechanical properties of Ti64 alloy

Temperature	Elastic Modulus	Yield Strength	Linear Expansivity Coefficient
T (°C)	E (GPa)	S (MPa)	α (1/ºC)
25	114	1061.0	8.2
100	109	933.7	9.2
200	100	742.7	9.9
315	93	668.4	10.5
430	84	615.4	11.0
540	57	477.5	11.4
1650	0.1	1.0	20.1
2800	0.1	1.0	20.1

Table 3.8: Selected mechanical properties of AISI 1015

T (°C)	E (GPa)	S (MPa)	α (1/ºC)
25	200	255.0	10.7
100	196	247.4	12.4
200	190	224.4	13.7
315	180	204.0	14.8
430	166	178.5	15.6
540	140	112.2	16.2
650	100	61.2	16.4
800	0.1	1.0	16.5
2800	0.1	1.0	28.1

3.9 Summary

Detailed temperature dependent material properties (i.e. thermal and mechanical) used in the numerical model have been presented in this chapter. Their importance in modelling the complex non-linear behaviours associated with the laser melting of metal powders have been discussed.

The derivation of the true stress-strain curves for defining linear isotropic and kinematic hardening models was described including material modelling assumptions that aid the simplification of the model.

4 Numerical Model Development

4.1 Introduction

This chapter deals with developing the simulation model for the laser melting of metal powders used in the experimental validation and parametric studies. The main thrust from this work was to develop a versatile three-dimensional computation model for predicting laser metling residual stresses on the basis of known material behaviour and laser melting process parameters. To embark from the outset on developing models and simulation techniques for a challenging geometry for which no experimental data exists for comparison could be deemed unacceptable. Consequently, it is pertinent to develop the technique using simple three-dimensional geometries for which both material data and some experimental results were available.

A number of validation analyses with published experimental data were carried out. Firstly, pilot temperature model simulations were performed and validated against experimental results of published work in predicting the maximum spot temperatures reached during laser scanning of a powder bed and in the direct laser heating of a steel plate. Secondly, a stress model simulation was performed to predict the transient and residual stresses produced by heating a three-bar structural mismatch system and validated against an analytical model. These initial studies then provided the basis for the development of the layer-by-layer numerical model for predicting the residual stresses in the laser melting of metal powders.

The development of the simulation model involved four key stages. These are:

- Predicting the maximum temperatures achieved,
- Capturing the temperature field history after laser heating,
- Calculating the transient stresses associated with the transient temperature fields, and
- Accumulating the thermal stresses and strains to obtain the final state of residual stresses.

ANSYS Mechanical software was used for pre-processing, solving and post-processing the results of the numerical model. The analysis program is capable of calculating the temperatures and stresses at nodal points at various times, which enables selection of different modes of presenting the results to assess the capability of the numerical model in predicting experimentally measurable quantities.

4.2 Spot Temperature Model (Case I: Pure Titanium Powder)

Experiments conducted by Fischer *et al* (2004) to measure the surface temperature during the laser scanning of a pure titanium powder bed were used to validate the temperature field model. The surface temperatures in their experiments were measured by a non-contact technique using a Raytheon radiance infra-red camera. In their experiment, a continuous wave 100 μm diameter Nd:YAG laser with an average power of 3 W at a scanning speed of 1 mm/s was used to heat the surface of a titanium powder bed. The powder height used in the tests was reported as 30 μm.

The theoretical laser heat flux of the focused beam on the surface of the powder bed was 1.28×10^8 W/m^2. Reference to the laser power density chart shown in Fig. 2.6 shows that this heat flux value lies in the alloying/cladding/fusion cluster and is, therefore, valid for the desired process.

4.2.1 Model Description and Solution Controls

The spot temperature model involves the transient thermal analysis of a laser heat source irradiating a single region equivalent to the laser beam diameter on the surface of the powder bed. The powder bed was assumed to be 0.5 mm deep; enough to prevent near field effects and also allow the heat flux to dissipate into the model. The ambient temperature was taken as 25°C. The absorptance to Nd:YAG laser was taken as 0.3 for the titanium powder (Fischer *et al*, 2003) and 0.1 when the material exceeded the melting point (Bertolotti, 1983).

The laser spot geometry is symmetrical about its centre; therefore, the model was further reduced by considering only a quadrant and applying symmetry boundary conditions to the symmetrical faces. It was taken that symmetrical planes and far-field

edges are impermeable to heat. This was done to improve accuracy and reduce solution time. Natural convection boundary conditions were applied to the exposed top surface.

The finite element model using SOLID70 thermal elements is shown in Fig. 4.1. SOLID70 elements have eight nodes with a single temperature degree of freedom at each node. The elements have three-dimensional thermal conduction capabilities and are applicable to steady-state and transient thermal analysis (ANSYS10, 2007). At regions around the laser spot, the element sizes were similar to those used in the spot so as to capture steep changes in temperature gradients. At regions away from the laser spot, however, the element sizes were coarser.

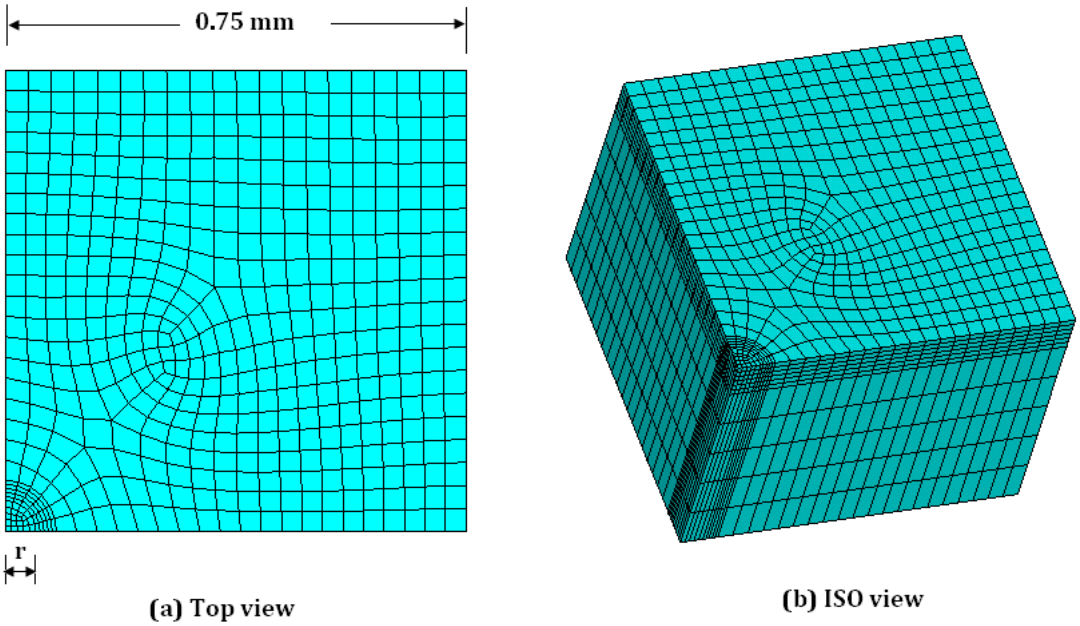

Fig. 4.1: Finite element mesh for spot temperature model

The beam-surface interaction time was defined as the time taken by the scanning laser beam to traverse one beam diameter (Dai and Shaw, 2005 and Gan *et al*, 2004). For the current case, the interaction time was 0.1 s. The heat flux was applied in time-step divisions and the state of the material is checked and updated for each time division until the irradiation time is reached. Ten time step divisions were chosen. The flow chart for the simulation program is shown in Fig. 4.2. The method of updating the material properties (thermal conductivity and density) depended on the nodal temperatures at the end of each iteration – a method similar to that employed by Dai and Shaw (2005).

The detection of state change was attributed to nodal temperatures. Hence, by determining the nodal temperatures at the end of each time-step division in the thermal analysis, the phase of the elements at that instant can be determined. Dai and Shaw (2005), in modelling the volume shrinkage in laser melting of dental porcelain, found that the criterion used to judge whether an element remained as powder or became liquid had discernable effects on the predicted temperature value as well as the temperature gradients. A criterion where the element was converted when its average nodal temperatures exceeded the melting temperature predicted higher maximum temperatures and larger laser-densified regions. However, the criterion which judged phase change based on the lowest nodal temperature yielded densified regions that agreed better with experiments. In this work, the second criterion was adopted. An element was converted (i.e. changes state from powder to liquid) if its lowest nodal temperature exceeded the melting point. This conversion was facilitated by generating a temporary element table for elements with nodal temperatures greater than the melting temperature. The material properties in that state [i.e. liquid, solid or powder (if not converted)] and temperature point were then updated, by extrapolation where necessary, for use in the next time-step division of the analysis. The shrinkage was captured by a reduction in thickness of the converted element(s) governed by the powder-solid density ratio measured in Chapter 3.

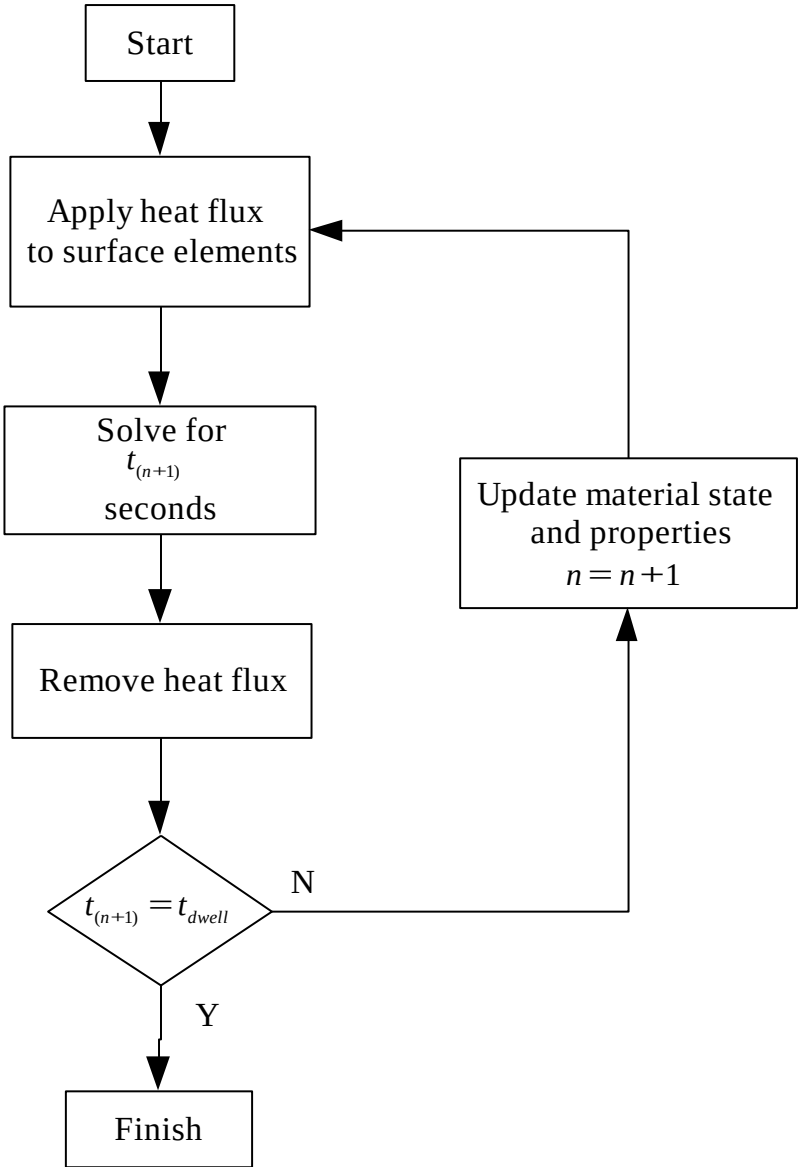

Fig. 4.2: Spot temperature analysis subroutine

Thermal properties of the material were given in accordance to the state of the element (i.e. powder, molten or solid) as discussed in Chapter 3. The spot temperature simulation program is given in Appendix 1.

4.2.2 Results and Discussion

Fig. 4.3 shows the reported experimental measurements for the temperature distribution on the surface of the powder bed. To aid comparison, circular contours corresponding to radial distances of 100 μm, 250 μm, 500 μm and 1000 μm are placed on the temperature plot about the presumed beam centre. The region of interest for the analysis is the marked quadrant (i.e. third quadrant). The region to the top-right of the image in Fig.

4.3 had been scanned by the moving laser and had consequently undergone some degree of sintering or densification. This solidified region has higher heat conductivity characteristics, conducting more heat away from the scanned region and thus explains the skewed temperature distribution plot.

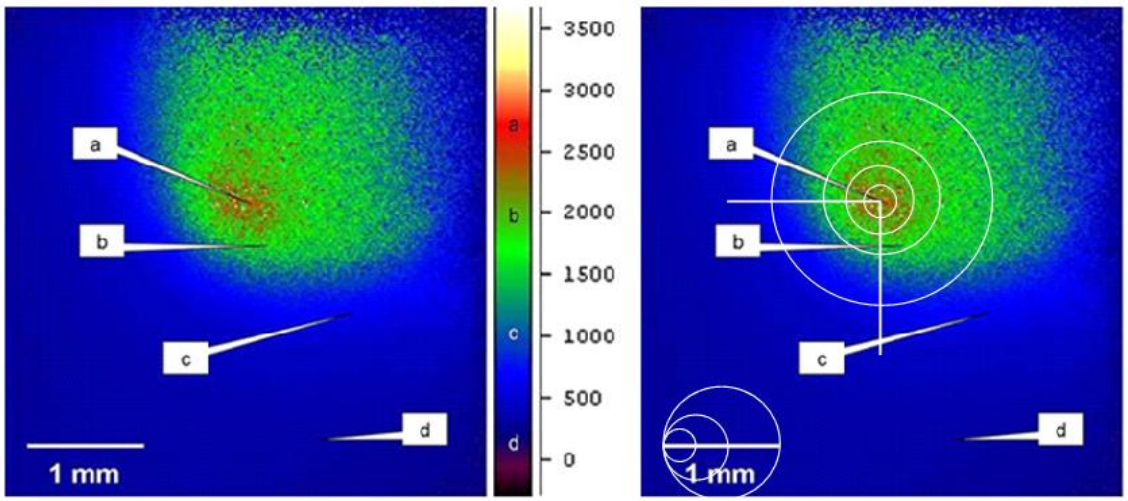

Fig. 4.3: Spot temperature distribution (T in Kelvin) (Fischer *et al*, 2004)

Fig. 4.4 shows the temperature distribution plot predicted by the simulation model after 0.1 s. The depth of melt predicted is 45 μm while the radius of the molten pool is 70 μm.

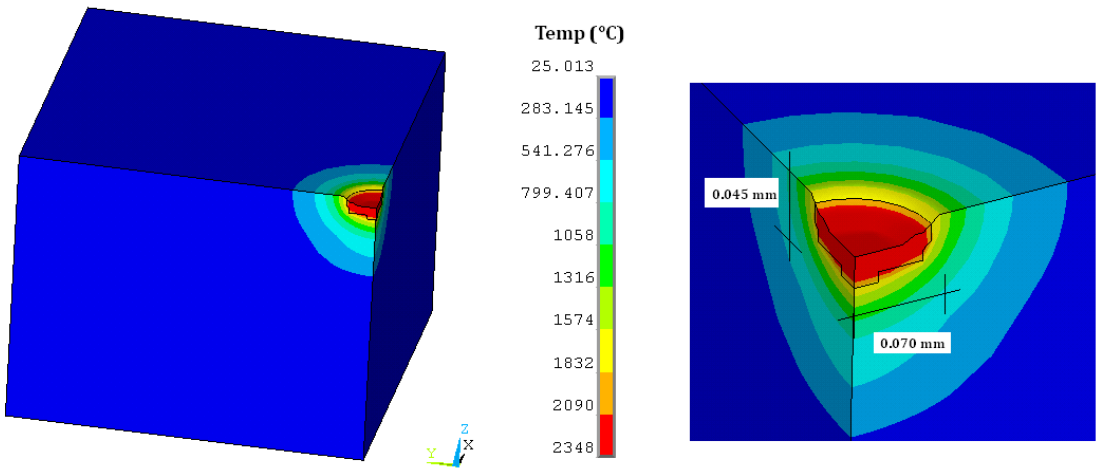

Fig. 4.4: Simulation temperature plot at t = 0.1 s

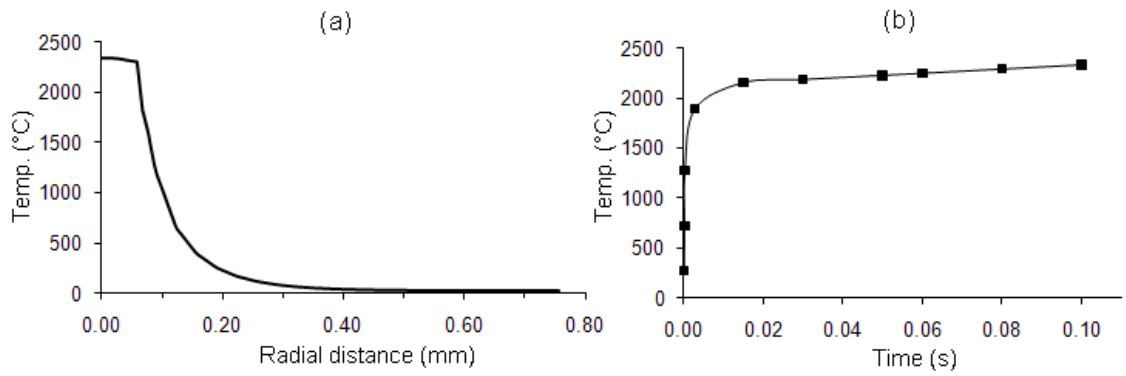

Fig. 4.5: (a) Temperature variation with radial distance from centre of laser beam, (b) Temperature history at laser beam centre

Fig. 4.5(a) shows the variation of temperature with radial distance obtained from the simulation model. It shows a region enclosed by the laser beam, $r < 50$ μm, where the temperature clearly exceeds the melting temperature (1670°C) in agreement with the experimental plot. The maximum temperature reported by Kolossov *et al* (2004) was 2400 ± 200°C, while the simulation model gives a value of 2348°C. Fig. 4.5(a) also shows a region 50 μm < r < 500 μm with a steep temperature gradient. This steep temperature drop, however, does not fully agree with that of the experiment. The experiment shows a more gradual decline in temperature outside the laser beam. The temperature field can be seen to approach that of the operating temperature for distances $r > 1000$ μm, while the numerical model predicts total dissipation for $r > 400$ μm. The discrepancies can be explained in terms of the laser irradiance model and the material assumptions. Although, the amount of heat energy in the enclosed region did not change, the modified cylindrical beam approximation was expected to underestimate the temperature at the centre of the spot. It is important to state at this point that the residual stresses as discussed in Section 2.7.1 are independent of the temperature path to melting. They only emerge during cooling and solidification after melting of the powder material has occurred.

The low conductivity surrounding unconverted powder bed accounts for the sharp drop in the temperature for regions just outside the beam radius. Fig. 4.5(b) shows the transient temperature at the centre of the spot. The steep rise in temperature (6.75×10^5 K/s) leading up to melting is hampered by the advent of the more conductive molten metal where the rate of heating drops to 2.08×10^3 K/s, more than a third of the initial rate. This more conductive molten material facilitates the conduction of heat into

the underlying as well as surrounding powder material. The shape of the molten region appears to be crescent and hemispherical, agreeing with the shape of scanned areas obtained in finite element analysis and experimental studies involving SLS of dental porcelain by Dai *et al* (2004).

The temperature contours around the spot and variation with radial distances show good agreement with the experiments for regions enclosed by the laser beam and the maximum temperature predicted is within 10% of the measured temperature from the experiment, giving confidence in the model for use in further temperature field analysis.

In finite element analyses, the accuracy of the computed results depends on the element size and the time increment used in simulations. Sensitivity to the element divisions in the irradiation region was performed by increasing the mesh divisions by one in the spot region to determine the suitability of the chosen mesh. The number of iterations for convergence increased but no noticeable difference in the temperature results was observed.

4.3 Spot Temperature Model (Case II: AISI 4142 Steel Plate)

Predicting the temperature for the direct irradiation of a steel plate surface is required for a control experiment which will be discussed in Chapter 5. Yilbas *et al* (1998) conducted experiments to measure the transient temperature variation and induced thermal stresses during the laser heating of a low-alloy steel plate (AISI 4142). A Nd:YAG pulsed laser of beam size 100 μm delivering 150 mJ in 1 ms pulses was used to irradiate the steel surface. Thermocouples inserted into the plate were used to measure the surface temperature just outside the irradiated spot.

4.3.1 Model Description and Solution Controls

The finite element model was similar to that used for the spot temperature simulation with the thickness of the steel plate maintained at 0.5 mm. Heat flux derived from the average laser power (given as the rate of energy delivery) per unit area was applied to the spot in equal time-step divisions as with the previous case until the irradiation time reached was similar to the workflow in Fig. 4.2. The absorptance value was taken as 0.2 for the solid material and 0.1 when the temperature of the material exceeded the melting

point (Bertolotti, 1983). The thermophysical properties of AISI 4140/AISI 4142 are similar to those of AISI 1015 at room temperature (Touloukian, 1977). However, the thermophysical properties at higher temperatures for low alloy steel AISI 4140 or AISI 4142 have not been widely published. According to ASM (1990), small variations in alloy content have negligible influence on these properties; therefore, the temperature dependent properties of AISI 1015 were used as representative values for this study. The melting point range for AISI 1015 is 1490-1520°C (CES, 2005). For the simulation model, this was set at 1490°C.

4.3.2 Results and Discussion

Fig. 4.6 compares the simulation results with the results published by Yilbas *et al* (1998).

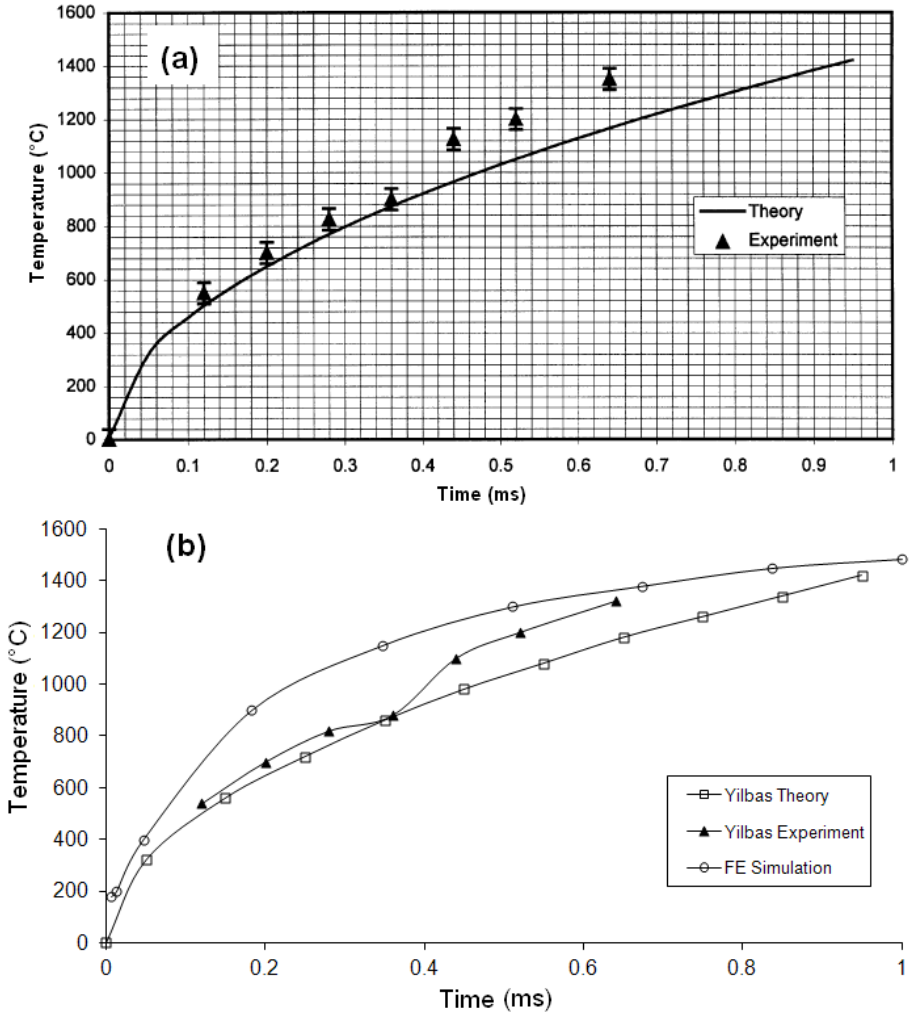

Fig. 4.6: (a) Experimental and theoretical surface temperature results (Yilbas *et al*, 1998), (b) Comparison of simulation temperature history

The results show that the temperature of the material is just below its melting point. The maximum temperature of 1485°C predicted by the numerical model compares well with 1420°C (after 0.95 ms) predicted by Yilbas' analytical model. Discrepancies in the rate of temperature rise can be seen between the experiment and simulation results. These can be attributed to the selected material properties and choice of laser irradiation model in the numerical model. In addition, the contact temperature measurement method using thermocouples measured the temperature at a small distance away from the irradiated region. In the experiment, the thermocouples were placed in drilled holes just below the surface of the plate. The measured temperatures relied on good contact with the specimen as well as conduction of heat through the material to the junctions of the thermocouples, which could have resulted in both a lag and attenuation of the actual spot temperatures.

The maximum temperature predicted as well as the reduced rate of temperature increase around and above 1200°C shows similarities with the experimental data points. Fig. 4.7 shows the temperature distribution for the quarter symmetry model. It shows high localised surface temperatures and steep temperature gradients with depth of plate.

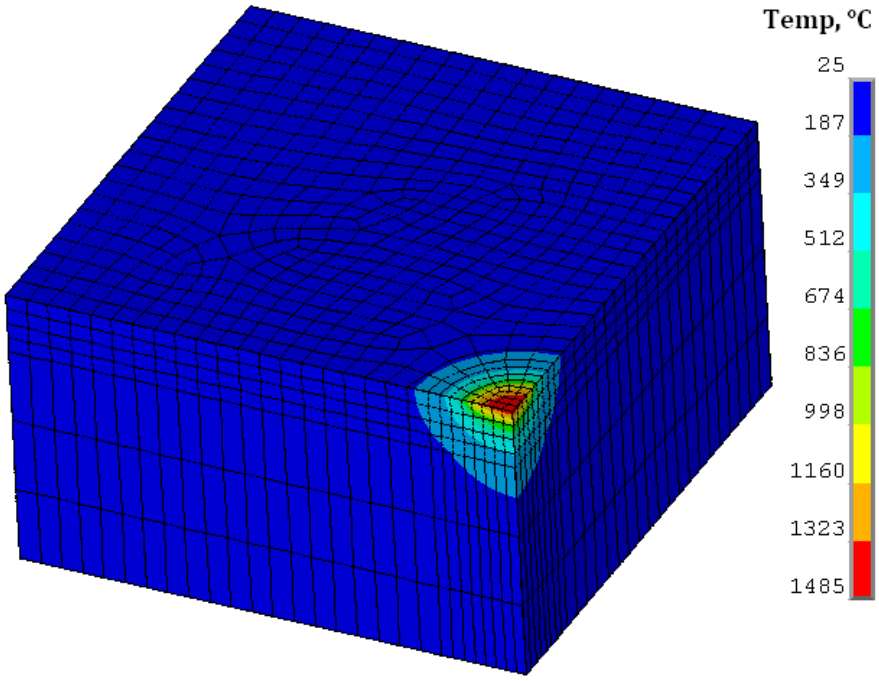

Fig. 4.7: Temperature distribution plot at t = 1 ms

Although the numerical model predicted different temperature paths with Yilbas' model and experiment the maximum spot temperature after laser scanning show good

agreement and highlights the strength of the numerical model in predicting the maximum achievable temperaures.

4.4 Thermal Elasto-Plastic Material Modelling

In this section, the thermal stress variation in a three-bar system is presented. It provides the basis for validating the linear isotropic and kinematic hardening models used for the stress analysis.

4.4.1 Model Description and Solution Controls

A structural mismatch problem involving three low-carbon steel bars fixed rigidly at one end and allowed to move alongside each other at the other end in the *xy*-plane was described in Masubuchi (1980). The middle bar was heated and then allowed to cool, producing thermal stresses as the side bars attempted to resist its deformation. Fig. 4.8 shows the arrangement for the problem. The temperature of the middle bar was raised uniformly from room temperature to 1100°F (593°C) and then allowed to cool down to room temperature by natural convection while the side bars were maintained at room temperature.

The bars are assumed to be identical, having dimensions of 10 mm × 5 mm × 100 mm and spaced 20 mm apart. The temperature cycle for the middle bar is shown in Fig. 4.8 (a). The uniform heating phase occurred in 6 s and the process end time was 750 s, enough to allow the system to cool down to room temperature.

The finite element model using 8-node brick elements SOLID70 and SOLID45 for the thermal and structural analyses is shown in Fig. 4.8(b). SOLID45 elements were used for the three-dimensional modelling of solid structures and are defined by eight nodes having three degrees of freedom at each node: translations in the nodal *x*, *y*, and *z* directions. The elements have plasticity, large deflection, and large strain capabilities (ANSYS10, 2007). A sequential coupled thermal-structural analysis was performed using the element switch feature in ANSYS Mechanical which converted the thermal elements (SOLID70) to the structural variant (SOLID45).

The nodal temperatures obtained from the thermal analysis were used as the input loads for the structural analysis. The temperature dependent physical and mechanical properties presented in Chapter 3 were used.

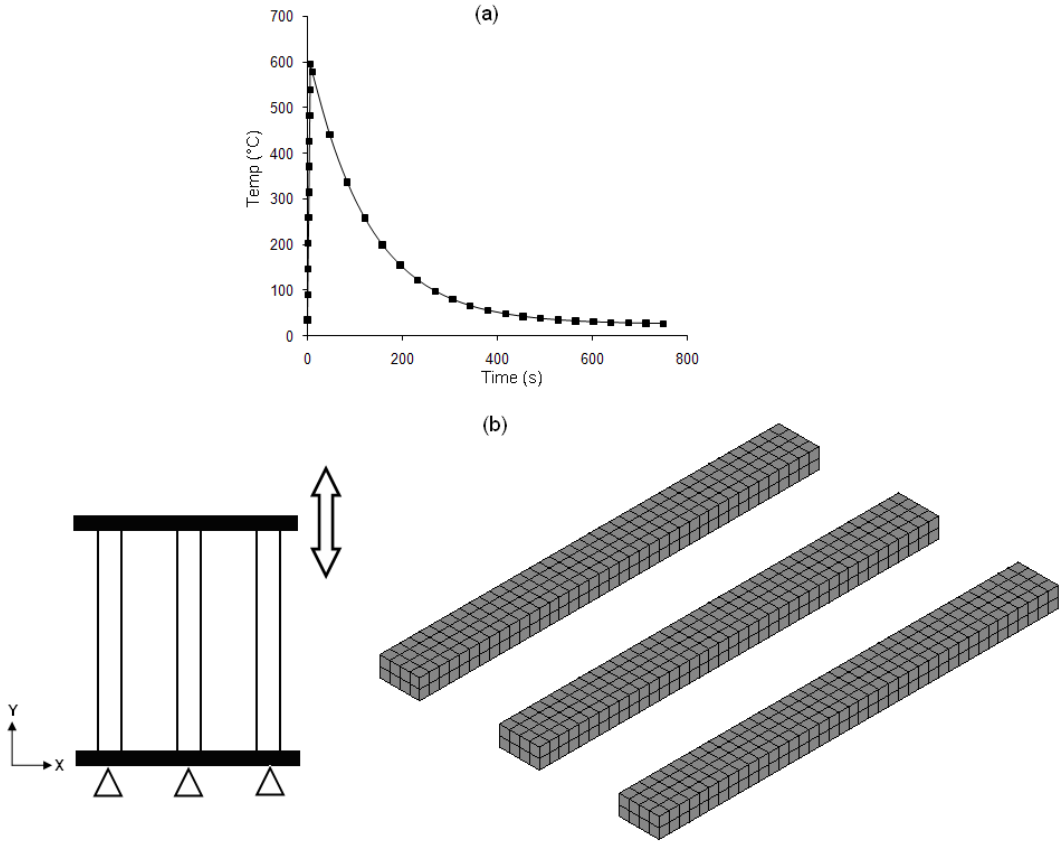

Fig. 4.8: (a) Middle bar temperature history (b) FE mesh of three-bar system

The nodal displacements at the expansion end were coupled using constraint equations to mimic the synchronised expansion. The time-step divisions used for the heating and cooling phases were 10 and 20 respectively. The two material strain hardening models (i.e. linear isotropic and kinematic) were used to study their relative influence on the stress history in the middle bar. Large deformation formulation was also considered.

4.4.2 Results and Discussion

Due to the mismatch between the thermal expansions between the middle bar and the two side bars, cooling caused non-uniform thermal contractions which resulted in the development of residual stresses. The axial stress distribution at the end time is shown in Fig. 4.9(a) for the isotropic hardening model. Ignoring end effects, the stress distribution result at the centre of the middle bar *P* gives a residual axial tensile stress of

269 MPa, showing some degree of strain hardening. The middle bar stress is found to be about twice the residual compressive stress in the side bars (126.6 MPa). This is expected as the two side bars are equally resisting the deformation of the middle bar. The two side bars are still elastic and would recover their deformation.

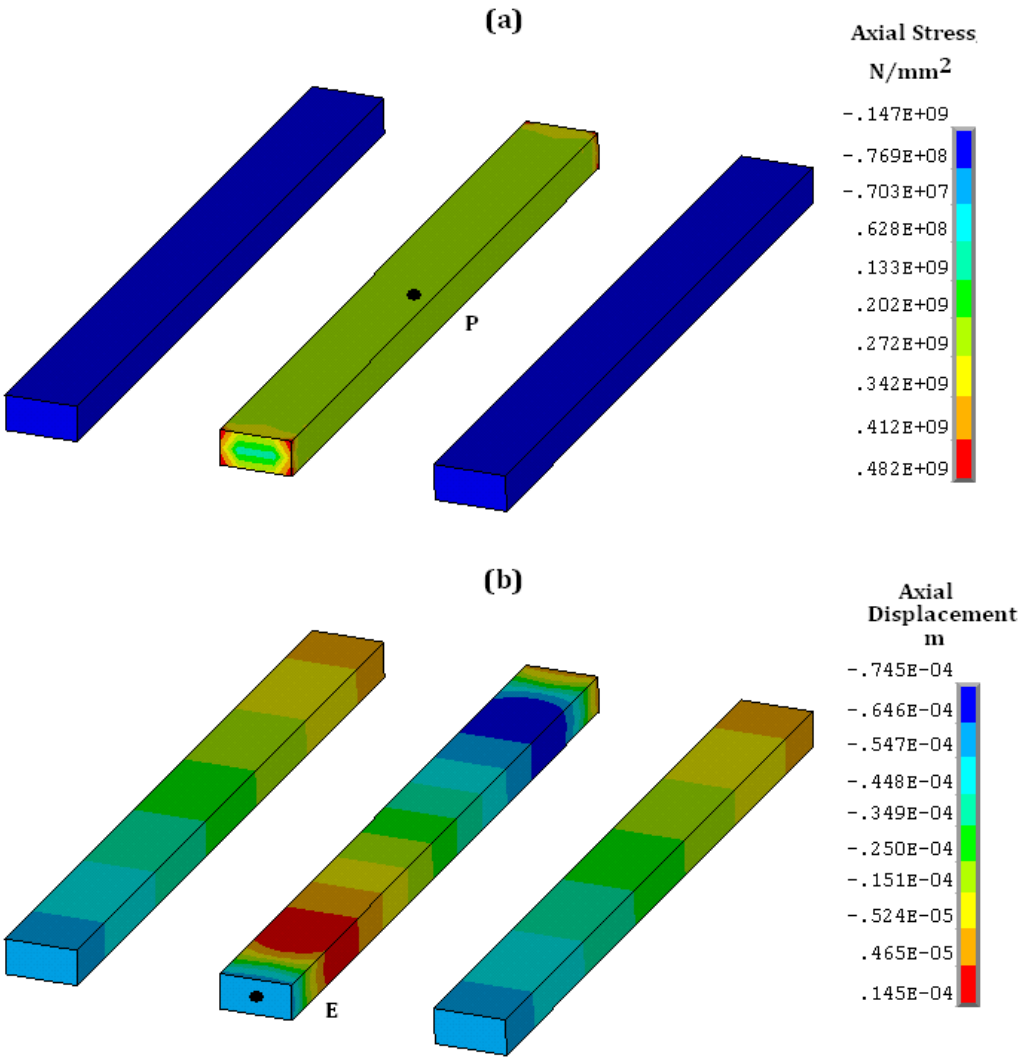

Fig. 4.9: (a) Axial stress distribution (b) Axial displacement plot

It can be seen in the stress-time variation plot in Fig. 4.10 that the stresses undergo a rapid transition from compression to tension at the start of the cooling stage. It shows that the middle bar remains in tension during the heating phase as a result of its expansion. The drop in tension observed half-way during the heating phase is as a result of the middle bar exceeding its yield strength at the elevated temperature. The flow stress characteristics become dominant beyond this point.

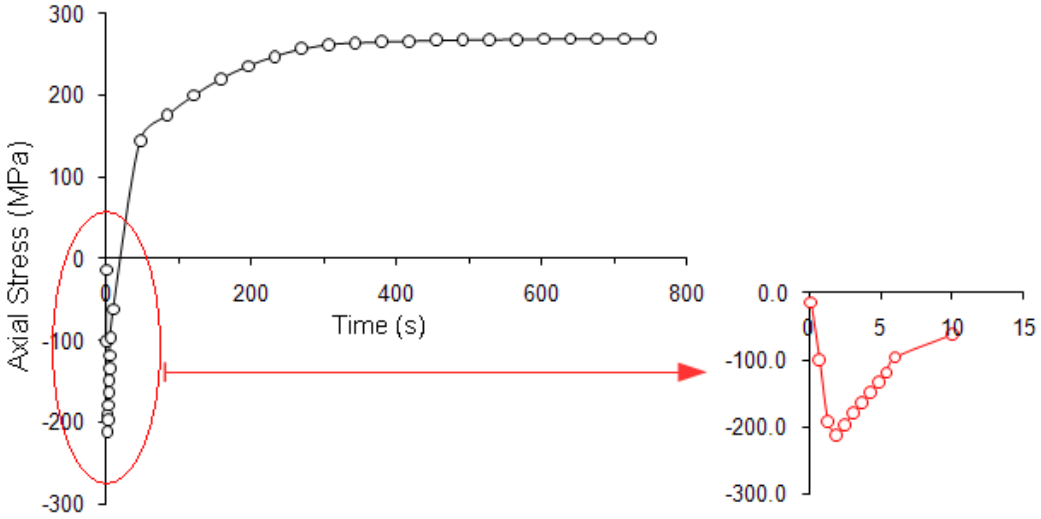

Fig. 4.10: Axial stress history

Fig. 4.11 compares the simulation models and the analytical stress-temperature histories. The plots show that the compressive stress in the middle bar increases with temperature approaching its yield stress at an elevated temperature (i.e. point *B*). The behaviour from this point onwards is characterised by plastic flow which is associated with an increase in elongation and a decrease in the compressive stress value seen in Fig. 4.10. At the end of the heating phase, the middle bar starts to contract and the stresses in it become tensile. The stresses quickly rise to the yield stress in tension at the elevated temperature (i.e. Point *D* in Fig. 4.11). Not all the deformation is recovered even though the side bars are not plastically deformed. The middle bar has a permanent extension of about 0.06 mm equivalent to elastic strains of 0.06% in the side bars.

The stress-temperature variation predicted by the analytical model and that predicted by the isotropic and kinematic simulation models show strong similarities. The residual stress at point *P* (centre node of middle bar in Fig. 4.9(a)) predicted by the analytical model was 242 MPa (i.e. 35 ksi) which compared well with 269 MPa (i.e. 39.0 ksi) for the linear isotropic hardening model and 263 MPa predicted by the linear kinematic hardening model. Investigation of the analytical model suggests that only yield strength dependence on temperature was considered but not strain hardening hence the 8.7% and 11.2% difference in axial residual stresses predicted by the the kinematic and isotropic models respectively. This study provides the required confidence on the thermal elasto-plastic model adopted for modelling the non-linear material behaviour.

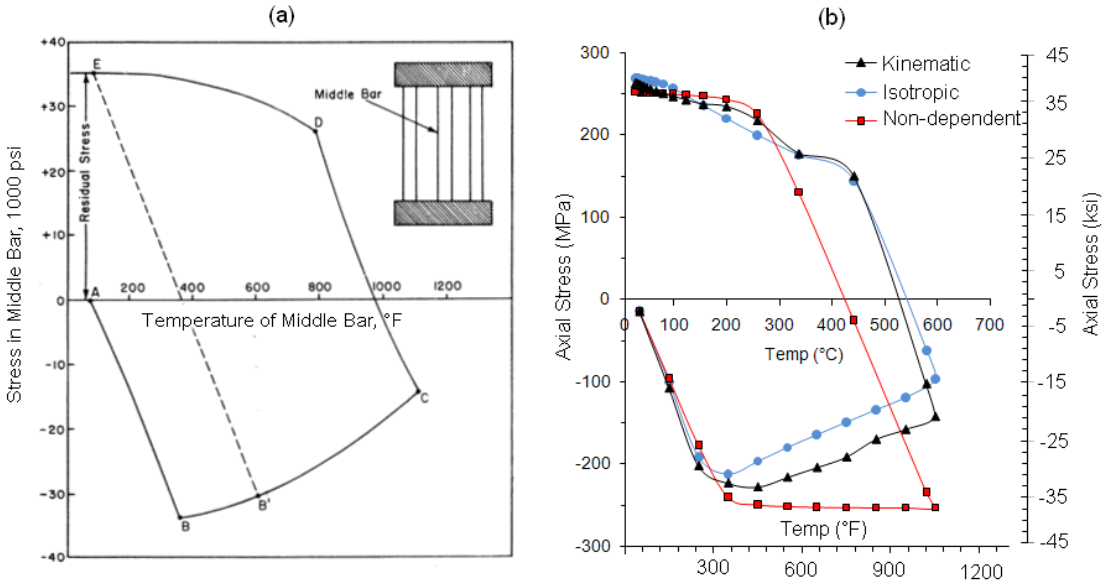

Fig. 4.11: (a) Analytical axial stress variation in middle bar (Masubuchi, 1980), (b) Simulation model axial stress variation with temperature

The temperature dependence of material properties at elevated temperatures and effect of the material model on the residual stress history was investigated by also considering an additional temperature non-dependent case (using room temperature properties). It can be seen in Fig. 4.11 that the material hardening model dictated the residual stress history in the middle bar. This is notable when the stress in the middle bar is compressive. The non-dependent model overestimates the compressive stresses in the heating phase but underestimates the tensile stresses during cooling. The opposite is observed with the isotropic model. It is interesting to note that all three models predicted similar final residual stresses in the middle bar.

Depending on the complexity of the problem, the kinematic hardening would require longer solution times. In this case, however, the solution times for both material strain hardening models were found to be comparable.

4.5 Layer-by-Layer Numerical Model

The analyses in the previous sections have laid the basis for the development of the layer-by-layer simulation model, building confidence on the thermal and mechanical simulation methods. The proposed simulation model mimics the laser melting process operation in terms of a moving laser heat source and material addition in powder layers as described in Chapter 2, capturing as many system variables as possible. By so doing,

they can be treated as reponse variables for which their relative effects on the level of residual stresses can be investigated via parametric simulation studies.

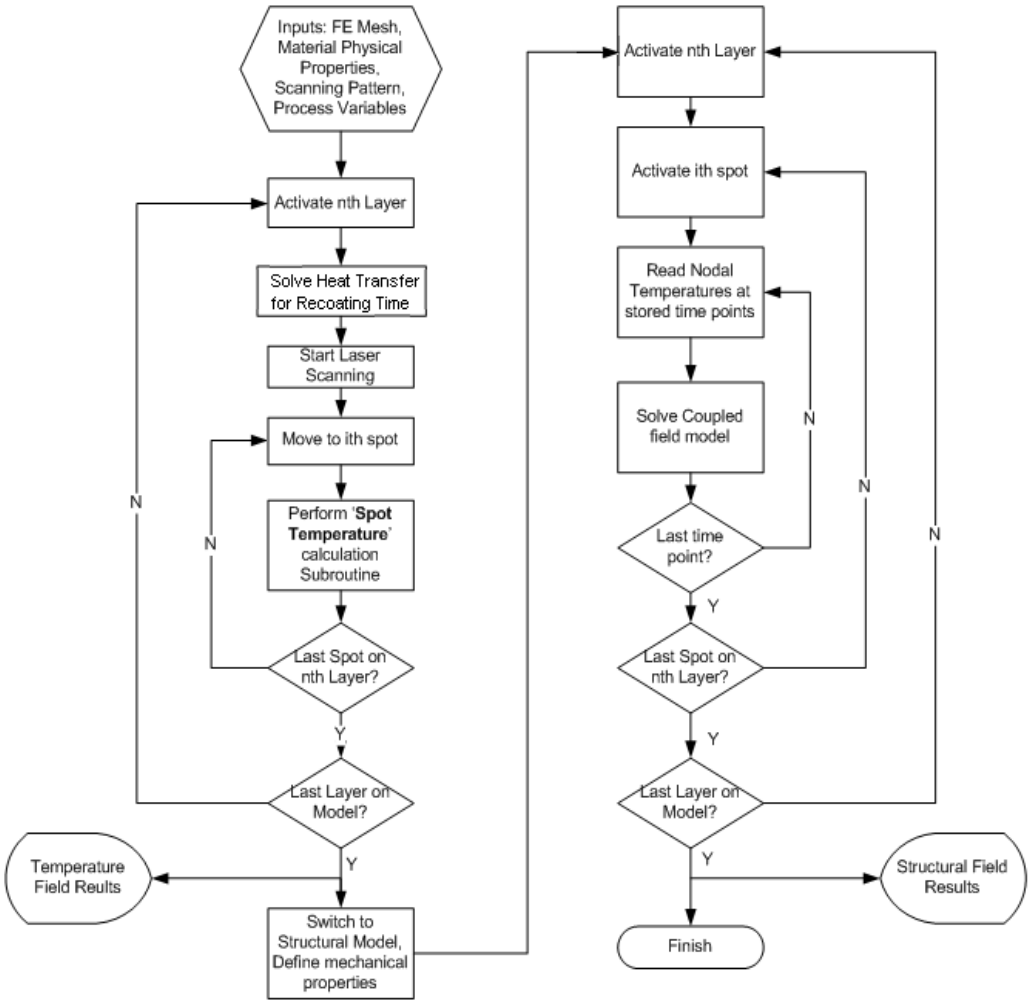

Fig. 4.12: Program flow chart for layer-by-layer model

Fig. 4.12 shows the simulation design framework used in the development of the model. The basic workflow is similar to that used by Dai and Shaw (2005) for the analysis of volume shrinkage during the laser sintering of dental porcelain. The program construction comprises two parts – thermal and structural parts. It is worth pointing out that although the thermal field occupies half of the design framework, it only accounted for about a quarter of the resources consumed in the simulation. Since residual stresses evolved during the cooling and solidification of the melted powder material, the bulk of the resources were channelled towards the structural analysis part of the model.

The process starts with the prediction of the temperature field after activating the first layer. Each layer consists of spot regions which are irradiated in steps by the moving

heat source according to the defined scanning pattern and governed by the geometric variables. The variables considered in the simulation program include the laser power, laser scanning speed, powder layer thickness, laser beam diameter, raster length, number of layers, preheat temperature (i.e. chamber temperature) and part dimensional variables. The dimensional variables include the dimensions of the scanned region and the thickness of the base platform. Fig. 4.13 illustrates the model geometry parameters. For computational simplicity, the raster length is taken as a whole number multiple of the laser beam diameter. Also, due to storage limitations (results required hundreds of gigabites of storage) the number of layers in this work is limited to five for the temperature field analysis and two for the structural analysis.

The numerical procedure is initiated by inputting the material and process quantities, followed by building the finite element mesh based on the input parameters and activation of the first layer. The stepping sequence begins at the starting spot and continues for all regions of the scanned layer before a new layer is activated according to the set recoating time. This process is repeated until the designated number of layers is reached. The results are stored in a thermal analysis file for post-processing and for subsequent use in the structural analysis.

The structural field analysis begins by switching all the deposited layer elements from the thermal to mechanical variant. The mechanical properties and the stored nodal temperature histories are used to calculate the stress field quantities for the activated layer regions. Activation of the irradiated regions is in the sequential manner dictated by the scanning pattern. This process is repeated until the specified number of layers is reached. Similarly, the results are stored in a structural analysis file for post-processing.

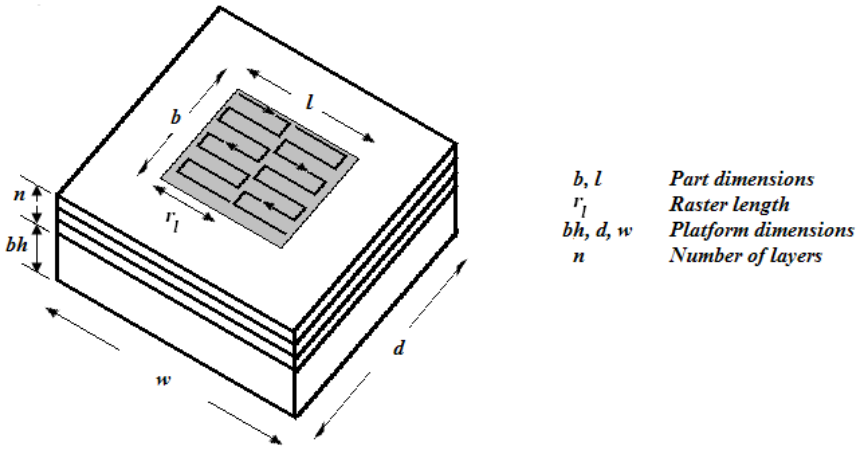

Fig. 4.13: Model geometry variables

4.5.1 Model Description and Boundary Conditions

The assumption of perfectly insulated walls at the boundaries of the scanned region was found to yield unacceptable results in laser sintering studies by Jamal (2001). Inclusion of the loose surrounding powder was therefore important in the thermal analysis as conduction was expected to occur between the side walls of the scanned layers and the unconverted powder. However, in order to reduce solution time and analysis file size, the unconverted loose powder elements were not included in the structural analysis, because they did not add to the stiffness or significantly constrain the solidified part compared to consolidation with the base platform or a previously solidified layer. Therefore, the input from the thermal model for the surrounding unconverted powder elements was not included in the structural analysis.

In the thermal analysis, the convection heat transfer boundary condition was applied to all exposed surface nodes apart from the current irradiated spot, simply because prescribed heat flux boundary conditions overwrite surface convection and vice versa. On completion of laser scanning, all surface nodes (including the irradiated region) were then subjected to convection heat transfer with a film coefficient of 20 W/m^2K for the duration of the cooling period, which was taken as 600 s. Compared to the irradiation time, the cooling time was much greater to allow the final effects to qualify as residual.

The recoating time refers to the time lapse between a new incoming layer and the previous one during which no laser melting occurs. During recoating, heat conduction between the scanned layer, the previous layer and the added layer is the dominant mode of heat transfer. The speed of recoating can be varied and must be matched to obtain a good spread of the powder in the layer. The recoating time used for this work was 8 s, which is the same as the setting on the EOSINT M270 machine.

The dead weights of the converted powder material and platform were taken into account by specifying a value for the acceleration due to gravity, $g = 9.81\ m/s^2$. Displacement boundary conditions (i.e. fixed) were applied to one end of the platform to represent a cantilevered system as will be described in Chapter 5.

4.5.2 Finite Element Model

Fig. 4.14 shows the finite element model using thermal 8-node brick (SOLID70) elements. The thermal elements were switched to the structural 8-node brick (SOLID45) variant for the structural field analysis. Element size divisions of 0.02 mm, 0.025 mm and 0.033 mm, which resulted in whole number divisions of the laser beam area, were used to investigate the suitability of the mesh.

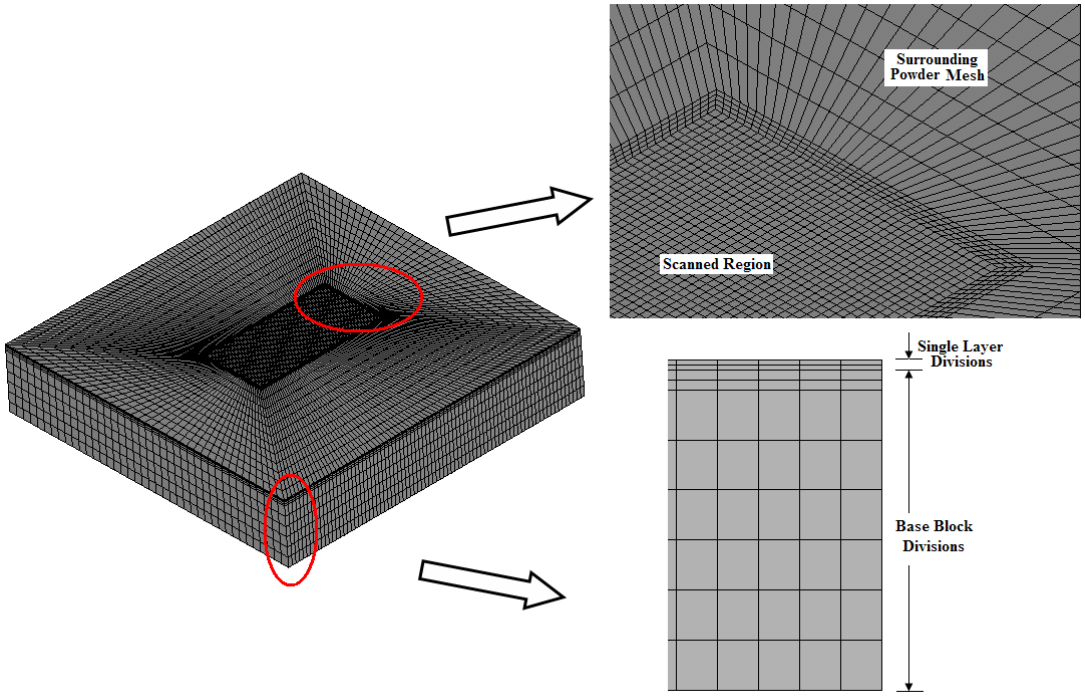

Fig. 4.14: Finite element mesh for layer-by-layer model

The mesh density was higher for the scanned layers and the immediate surrounding powder region but was made coarse away from the scanned region as seen in Fig. 4.14. The size of the surrounding region was set to at least 1 mm from the scanned region, large enough to prevent near field effects in the temperature field analysis.

4.5.3 Moving Heat Source

The realistic movement of the laser along the surface of the powder is continuous and an analytical solution for this would be very challenging. Some researchers like Gan *et al* (2004), Costa *et al* (2005) and Dai and Shaw (2005) circumvented this problem by employing a discrete method of representing the moving heat source. In the proposed

model, the heat source dwells on a spot for a time equal to the total irradiation time before moving to a new spot location defined by the laser scanning pattern. The method results in a step-wise movement of the laser heat source across the surface. Although, the resulting track shapes in the studies by Dai and Shaw (2001), Dai and Shaw (2002) and Dai and Shaw (2005) were not stated, the use of this method will result in the formation of lumped regions as opposed to smooth bell-shaped tracks of solidified material. This in itself will have an impact on the stress distributions in the scanned region. This is illustrated in Fig. 4.15. The step-wise method used here is an improvement on the generalised plane-strain model used by Klingbeil *et al* (2002) in the study involving laser-assisted deposition of stainless steel 308 powder on a low-carbon steel substrate, where entire rows of the raster scan were deposited at once.

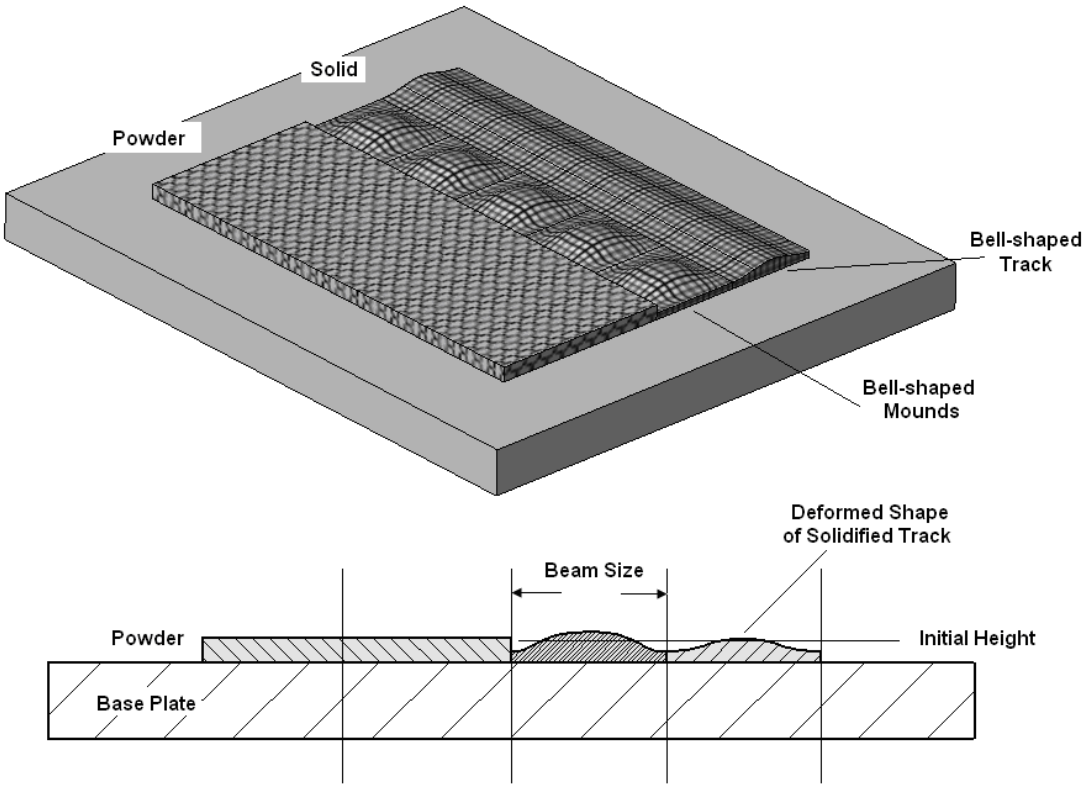

Fig. 4.15: Resulting track shapes

The raster method of scanning is performed in a traversing manner, from left to right and top to bottom as shown in Fig. 4.13. It is important to note that the laser spot starts with a circular profile at the edge of the part, but traces a rectangular path with width equivalent to the laser beam diameter as it moves along the raster. Therefore, by

ignoring end locations, the spots can be modelled as square regions with dimensions equivalent to the beam diameter.

In employing the element birth method, elements for each layer are activated with the chamber temperature as the initial condition in the thermal analysis, while they are activated strain-free for the structural analysis in accordance to the time they are scanned. In addition, the dead weights of the deactivated powder layer elements do not contribute to the weight of the system. It is important to emphasise that during the element birth stage, the elements at the bottom of the newly added layer share nodes with the elements at the top of the previous layer at the boundary. The shared nodes remain at the attained temperature while the remaining nodes of the newly added layer are activated at the chamber temperature.

4.5.4 Phase Change and Shrinkage Modelling

The material state monitoring process is the same as that described earlier in Section 4.2.1. In the thermal analysis, the change in density of the material is associated with a decrease in porosity and a proportional volume change (i.e. solidification shrinkage), thus, conserving the mass in the irradiated region. In such a case, to obtain an overall converged coupled-field solution, it is often necessary to update the finite element model mesh in the thermal model to coincide with the structural changes and recursively cycle between the thermal field solution and structural solution (ANSYS10, 2007). This work utilises a sequential coupling technique where the temperature field introduces thermal strains in the structural field, but not the other way round because the very small structural strains generally do not affect the temperature field. Therefore, the same mesh and time-step divisions can be used for both the thermal and stress analyses.

From the density measurements performed in Chapter 3, it is clear that when the powder material melts, there is a 40% decrease in volume from bulk density measurements. This shrinkage, as with the earlier pilot spot temperature simulation, was modelled by effecting changes to the volume for the converted elements by updating their surface nodal displacements (i.e. height locations) to reflect the volume change.

After laser heating of the first layer, the machine bed is lowered by a layer thickness followed by recoating of a second layer. It is important to note that as a result of the

shrinkage of the first layer, the new layers added will have thicknesses greater than the specified layer thickness.

4.5.5 Solution Controls

The thermal model was solved using an iterative solver, while the structural field was solved using a Pre-conditioned Conjugate gradient (PCG) solver with full transient and Newton-Raphson solution options suitable for large models (ANSYS10, 2007). The PCG solver has better performance for use with large non-linear problems compared to the SPARSE and FRONTAL solvers.

For the thermal analysis, the first iteration in the solution procedure solves the system equations at the starting temperature (i.e. chamber temperature), and subsequent iterations use temperatures from previous iterations to derive the thermal conductivity and enthalpy matrices. The iterative process continues until a converged solution is achieved. Similar to the heat transfer analysis, the numerical implementation of the quasi-static analysis for the structural analysis involves an incremental scheme with discrete time increments. The solution for a given time interval is obtained by using the solution at the previous time increment as an initial condition. The default convergence tolerance values (i.e. 0.10%) for both the thermal and stress field analyses were used. The accuracy of the structural field analysis in the high temperature stress gradient region was found to depend on the number of elements and sub-steps used in the structural analysis. This will be a subject for discussion in Chapter 5. The parametric simulation program is given in Appendix 2.

4.6 Summary

The development of a three-dimensional numerical layer-by-layer model for modelling the laser melting of metal powders has been described. The model builds on the limitations highlighted in the literature review such as the addition of multiple powder layers, temperature dependent material properties, moving laser heat source, latent heat of fusion and non-linear mechanical behaviour.

The thermal analysis model was based around a transient finite element heat calculation with material properties which varied with state.

The development of the stress field model required the prediction of the temperature field and selection of a suitable material non-linear behaviour model. A thermal elasto-plastic formulation was adopted to model the strain hardening behaviour of the materials below their melting points. Two material strain hardening models were used: (i) linear isotropic strain hardening model using the von Mises yield criterion and an associative flow rule, (ii) kinematic (i.e. multilinear) strain hardening model.

In order to validate the methods employed for developing the numerical model, pilot simulations have been carried out. These included prediction of the maximum temperatures achieved during laser heating of a titanium powder bed and a steel plate for the thermal model, and a structural mismatch analysis involving the expansion and contraction of a constrained three-bar steel system. The analysis results were compared with published experimental results and analytical solutions. The predicted maximum temperatures agreed with those from publications for regions enclosed by the laser beam. However, discrepancies are observed for regions outside the laser beam area and the temperature path towards melting. The implications of the predictions of the thermal model on the evolution of thermal and residual stresses in laser melting of metal powders were discussed. The numerical model predicted a maximum temperature that was within 10% of those measured experimentally. The structural numerical model that utilised the kinematic hardening model was more accurate for the time variation of the thermal and residual stresses.

The development of the numerical layer-by-layer model was discussed. It incorporates a collection of process, material and geometry variables mimicking the step-by-step layer-by-layer operation of the laser melting process. In order to build further confidence on the numerical model for use in the parametric investigations to study their effects on the magnitude and distribution of residual stresses, a validation exercise is required to study its applicability.

5 Experimental Validation

5.1 Introduction

The layer-by-layer numerical model introduced in Chapter 4 has the potential to model the laser melting process and therefore, provide a unique understanding of the effects of process variables on the magnitude and distribution of residual stresses and part deformation during laser melting of metal powders. This chapter describes the experiments used to validate the proposed numerical model. Surface topography analyses using laser scanning confocal microscopy used to measure the surface displacements for designated paths across the platform surface are described. The measured profiles were used to validate and refine the developed numerical layer-by-layer numerical model for use in the parametric studies. Two sets of experiments were carried out to establish their relative effects. The first considered the direct laser heating of a steel base plate while the second considered laser melting of two layers of Ti64 powder onto a steel base plate.

5.2 Measurement Technique and Quantities

As discussed earlier in Chapter 2, the steep uneven temperature gradients during laser melting generate transient thermal stresses in the vicinity of the material that has been scanned. These result in non-uniform plastic deformation in the scanned region and elastic deformation for the surrouding regions, implying that the final deformation state is governed by the residual stresses in the material.

A number of techniques that measure strains and residual stresses in metal components currently exist. Stress relaxation methods using strain gauges, X-ray and neutron diffraction, stress-sensitive coatings, digital image correlation, Moiré interferometry, ultrasonic methods, electromagnetic and cracking techniques have been developed and applied in industry (Evans *et al*, 2009). These measurement methods monitor the strains produced and relate them to stress levels.

Each of these techniques approximate the strain present and with the development of improved residual stress measurement techniques, more comprehensive and reliable

experimental data could become available. These would allow for a more subjective assessment of residual stress simulations including the adequacy of simplified analytical models. The selection of the appropriate measurement technique is important as well as knowledge of its limitations – ease of use, cost and time effectiveness, damage to the material and quality of measurement need to be considered.

Some researchers have used stress relaxation and cracking techniques in previous works involving laser processing of materials. Karalekas and Rapti (2002) employed strain gauges in determining the residual stresses in SLS of an epoxy-based photopolymer. Li *et al* (2004) used crack profiles, directions, occurrence and depth to estimate the level of residual stresses in SLS of an alumina-based ceramic. Osakada and Shiomi (2006) used the material layer removal method to estimate the residual stresses in laser sintered parts by measuring the strain changes produced in the base plate while removing top layers of the part built on the base plate. The residual stress levels were then calculated using a linear stress-strain relationship assuming constant material properties.

The relative part sizes and other physical attributes associated with the scanned region, as will be seen in Section 5.5 and Section 5.6, make it extremely difficult to apply direct methods of measurement. Therefore, this work will focus on the surface deformation caused by the laser melting process. This indirect method monitors physical attributes which are representative of the strains and residual stresses (Masubuchi, 1980). The principle of indirect techniques is based on strain or displacement measurement relating to the rebalancing of internal stresses which are released when material is removed or allowed to deform (Ekmekci *et al*, 2004).

The proposed method involves capturing the topography of the upper surface and deriving the platform's surface displacement by mapping the surface positions before and after the laser melting process. This is similar to the method employed by Klingbeil *et al* (2002), where residual stress-induced warping displacements of a steel substrate on which laser powder deposition had taken place were measured. Gan *et al* (2004) and Branner *et al* (2008) also used a similar method of surface distortion measurement in the investigation of the residual stresses in the plasma laser deposition and metal laser sintering of titanium alloy powder respectively. In a recent study, Zaeh and Branner (2010) were able to measure the residual stress state in a T-shaped beam platform using neutron diffractometry in the laser melting of tool steel powder.

5.3 Sample Preparation and Measurement Method

5.3.1 Geometry of Laser-Melted Parts and Test Platform

A test platform machined out of hot-rolled mild steel was used. Steel was used in this work because in many cases it is the platform material for building LM parts. The test platforms are shown in Fig. 5.1. A free-hanging platform (i.e. cantilevered) design was chosen so as to allow measurable deformation of the platform to occur and hence facilitate comparison. Following machining, the test platforms were stress-relieved in a Heraeus oven at 200°C for 5 hours to eliminate machining-induced stresses. Fig. 5.2 shows a bespoke sample holder made for securing the test platforms. The sample holder was built from maraging steel powder on a 125 mm × 125 mm plate using the laser melting process.

Building the test sample holder using the same LM process served two very important purposes. Firstly, the exact location of the test block within the laser melting machine was known from the job file. Secondly, the location of the region to be scanned for the LM can always be referenced to the sample holder thereby ensuring repeatable placement of the sample holder and build platforms in the build chamber.

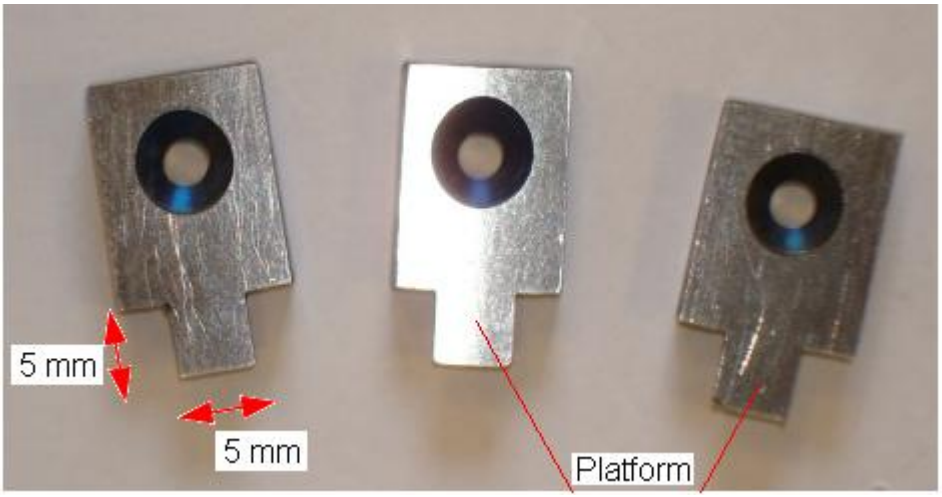

Fig. 5.1: Machined test base platforms

The test platform 5 mm × 5 mm × 1 mm was relatively sized to allow measurable deformation caused by the laser heating process. Its size was more than twice the size of the scanned region and was also stiff enough to withstand any excessive deformation induced by machining or handling. A set of 3 mm diameter countersunk screws were

used to secure the test samples on the sample holder. The countersunk holes were located 12 mm from the cantilever area – a distance far enough away from the overhang to prevent pre-stressing effects that could alter the stress distribution produced by the LM process in the cantilever platform. The experimental set up was similar to that used by Branner *et al* (2008) in studying the residual stresses and platform distortions during the laser melting of steel powders on thin steel substrates. The laser melting region had dimensions of 1 mm × 2 mm and was located centrally on the test platform. A maximum of two 30 µm layers of Ti64 alloy was considered for this work.

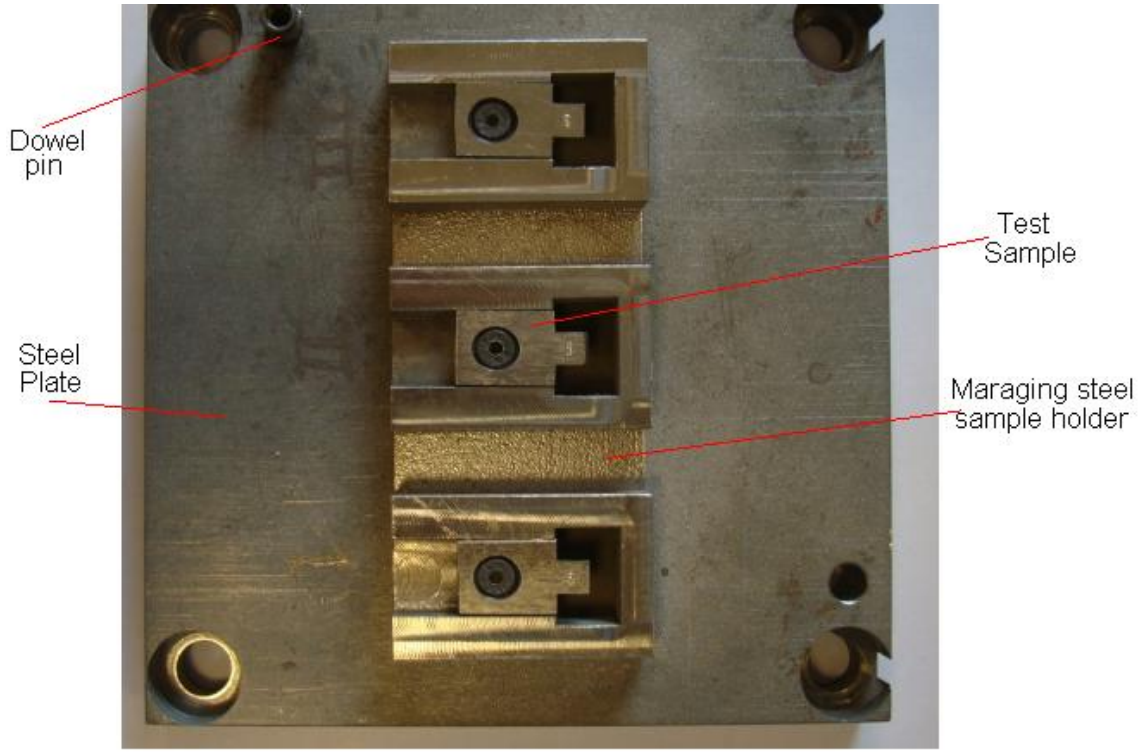

Fig. 5.2: Test sample holder and samples

Prior to the laser heating stage of the experiment, slight inclinations were observed in the cantilever area of the test platforms, which may have been caused by the released internal stresses during the stress-relieving process. The test procedure, however, determines the surface topography before and after laser melting. Considering that the test platforms began at zero internal stress levels prior to laser heating, any change in surface topography was therefore attributed to the laser melting process.

5.3.2 Laser Processing Parameters and Conditions

The laser heating experiments were carried out using standard defined scanning parameters the same as those published by the equipment manufacturer for building of Ti64 parts (Electrical Optical Systems, 2005). In accounting for losses through the system, the laser power quoted was that measured at the surface of the powder bed. The laser power was measured as 195 W, scanning speed set was to 1200 mm/s with 0.1 mm stepover (equivalent to the beam diameter) between the scanned tracks. The recoating time speed was set to give a deposition time lapse of 8 s. A raster scanning strategy was used and additional options like pre-profiling and post-profiling were deactivated for the tests. The air in the chamber was evacuated and replaced by argon until it reached the set point for the process (i.e. 0.1% oxygen). Thereafter the process operated in oxygen levels of 0.01% and 0.13%. The chamber temperature was raised to and maintained at 40°C for the duration of the scanning.

5.3.3 Procedure for Measuring Platform Deformation

The platform deformation was determined experimentally by comparing the top surface topography before and after the laser scanning of the test samples. The measurements were performed using an Olympus LEXT optical laser scanning confocal microscope (OLS3000) (Olympus, 2008). The OLS3000 uses a point illumination and spatial pinhole to eliminate out-of-focus light in sample regions outside the focal plane. With this process, all parts of the specimen in the optical path are fluoresced and return signals detected by a photo-detector as background signals. A three-dimensional image or topography is then built by capturing a series of images in layers within a specified scan depth. These images can then be individually analysed or combined to create a whole surface topography.

Fig. 5.3 gives an illustration of the top and bottom reference planes which bound the surface profile to be measured out of the laser light focus in either direction. This height difference between these planes is known as the z-range. The bottom reference plane was placed below the surface while the top reference plane was placed above it. The z-range was set to a value greater than a characteristic height to be measured (these were 40 µm and 100 µm for the two sets of experiments). Surface scans were then taken in 0.05 µm steps across the z-range.

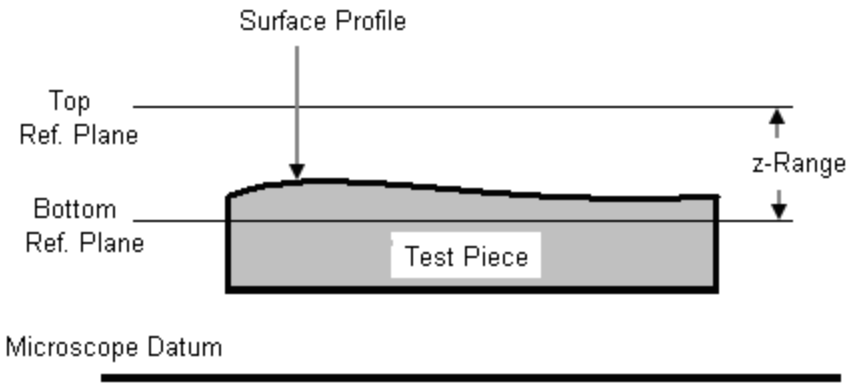

Fig. 5.3: OLS3000 surface profile measurement

An L-bracket machined out of 5 mm thick aluminium plate was used to secure the test sample holder onto the microscope table to ensure repeatability in positioning the test sample holder relative to the OLS3000 lens' origin.

Three-dimensional colour surface scanning option was used to scan windows (or cells) of the platform using a field size of 640 µm × 480 µm at a magnification of ×20. The magnification was selected to maximise the OLS3000 image processing memory and matrix size limitations for the platform dimensions used in this work. The scanned cells were then joined together using an image tiling tool to produce a 1024 pixel × 768 pixel image corresponding to 5120 µm × 4800 µm topographic plot of the platform surface. The default noise filtering strategies (i.e. smoothing, spike removal and profile shape correction) were used to remove noise signals to obtain a relatively smooth surface plot. Fig. 5.4 shows the designated paths for which the vertical surface displacements (i.e. *z* displacements) were obtained using the OLS3000 surface roughness analysis tool. The path lengths in the *x* and *y* directions are the same as those of the scanned geometry (i.e. 2 mm and 1 mm respectively). The entire process was performed before and after laser scanning of the surface of the platform for three test samples for each experiment.

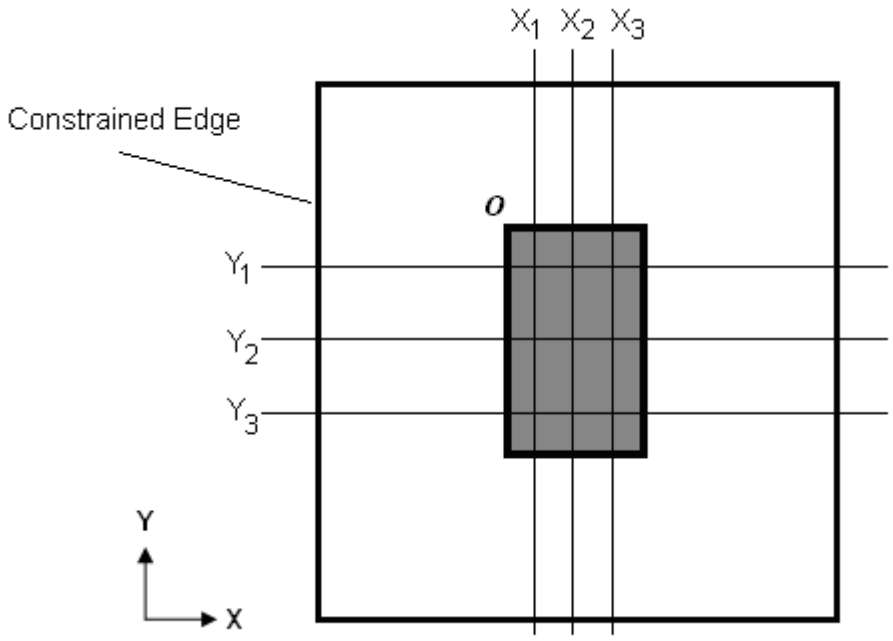

Fig. 5.4: Path designations – identifiers 1, 2, 3 refer to locations corresponding to 25%, 50% and 75% of built part dimensions

The platform surfaces were carefully ground with a fine aluminium oxide wheel giving an average surface roughness of 4.5 μm Ra for the initial surface measurements using the OLS3000 microscope. The surface roughness value obtained is significantly less than the size of the powder particles and would not have a direct effect on the layer height of the powder or cause significant changes to the laser beam diameter when focused on the top surface. In addition, slight roughness of the platform surface is an advantage as it enhances the spreading and bonding of the melted powder on the platform surface.

5.4 Experimental Equipment and Procedure

5.4.1 Laser Melting Machine

An EOSINT M270 laser melting machine with a 200 W continuous wave Nd:YAG laser having a variable focus diameter of 100-500 μm and capable of achieving scanning speeds of up to 7.0 m/s was used to carry out the laser melting tests (Electrical Optical Systems, 2005).

The test sample holder was mounted onto the machine bed in its as-built position. Dowel pins shown in Fig. 5.2 located along the diagonal of the sample holder were used to ensure repeatable placement of the test holder. The proximity of the recoating blade to the surface of the test sample was checked using a feeler gauge set. A 50 μm feeler gauge was swiped across the space between the recoater blade and the top of the platform while raising the machine bed simultaneously up to a point when it was no longer possible to do so. The platform was then raised by 50 μm thereby ensuring that the laser focal distance was near enough to the surface of the test platform and also during spreading a layer of powder: (i) the recoater blade did not collide with the test platform, which could cause damage to both the platform and the blade, and (ii) the desired powder layer height was obtained. The final step in the setting up process involved covering the test sample and holder in powder as well as filling the gaps underneath. This was then followed by a single recoater pass to give a uniform spread around the sample up to the platform surface level. This last step was not performed for the control experiment as it did not involve laser melting of Ti64 powder.

The part file containing the sliced geometry of the two-layer part to be built was loaded into the machine memory together with the job file containing information about the laser power, scanning speed, layer height and scanning information. The machine was inerted and the first powder layer was spread over the surface of the platform. Once scanning was complete, the process was stopped and the chamber door was opened allowing the sample to cool down to room temperature. The test sample holder was then removed to allow the part cool down to room temperature. Any loose powder particles were blown out before microscopy analysis was performed.

5.4.2 Olympus Optical Laser Scanning Confocal Microscope (OLS3000)

Fig. 5.5 shows the OLS3000 microscope set up. The anti-vibration mount underneath the motorised observation stage eliminated external disturbances. An important experimental issue was the calibration of the OLS3000 microscope. The accuracy of the test results depends on the accuracy of the measuring instrument. A calibration test was performed on standard gauge blocks of known thicknesses. The tests were performed at the same magnification (i.e. × 20) as that used in the surface topography measurements.

Standard gauge blocks of 1 μm, 2 μm and 5 μm thickness were measured. The percent errors in the measurements were found to be 9%, 2.5% and 2.4% for 1 μm, 2 μm and 5 μm steps respectively. The results of the calibration test are given in Appendix 4.

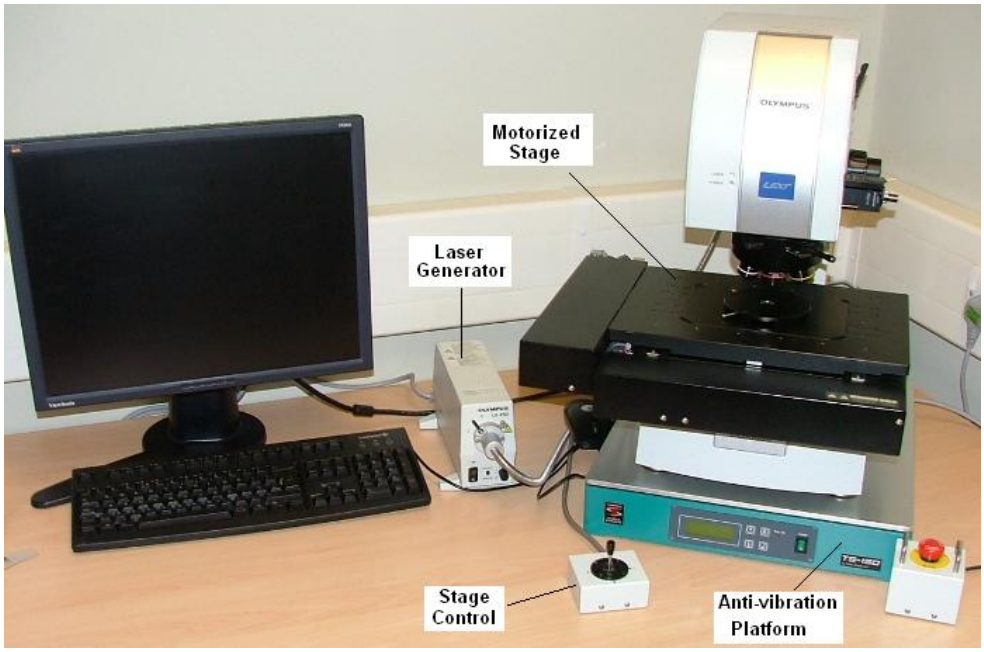

Fig. 5.5: OLS3000 Olympus laser scanning microscope

5.4.3 Co-ordinate Measurement Machine

The slots on the test block holder were built to be slightly smaller than the test pieces. The slots were then machined to the required sizes using a milling machine. This process removed the visually evident roughness on the maraging steel test block produced by the laser melting process to ensure that the test pieces were placed on smooth flat surfaces. A CNC Co-ordinate Measurement Machine (CMM) with a Renishaw PH10M measuring head with a touch trigger probe assembly was used. The co-ordinates of the slot walls and placement surface were measured to determine the depth of material to be removed.

5.5 Experiment I: Laser Heating of Base Plate (Control Experiment)

One consequence of the laser melting process is the direct laser heating of the base plate. With powders, this is possible because of the existence of pores in the powder

packing structure. As described by Kruth *et al* (2003), the laser can penetrate the powder pore structure and can directly heat up the build platform for the first layer or heat up the underlying material for subsequent layers. In order to distinguish the effect of melting metal powders onto a base platform, a control experiment was necessary. The experiment aimed to determine the extent of the deformation produced as a result of the direct laser melting of the surface of the platform.

For this experiment, the layer exposure was scanned on the surface of the platform without any powder material. The surface topography was subsequently measured.

5.5.1 Experiment Results

Fig. 5.6 shows the surface plot of the platform surface produced from the OLS3000 microscope before laser heating. A few surface imperfections from the machining process can be seen on the surface. The textured surface plot shows a continuous flowing surface and does not show pronounced discontinuities from the OLS3000 image knitting process. After sample preparation and machine set up, the laser heating process lasted for less than a second.

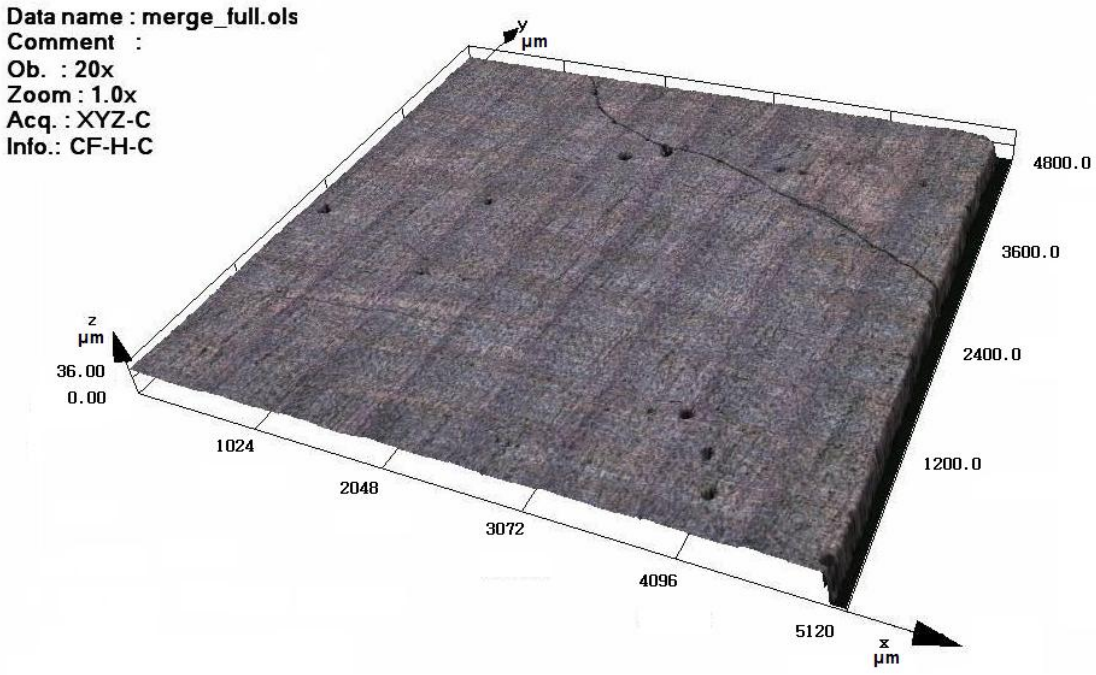

Fig. 5.6: Textured surface plot before laser scanning

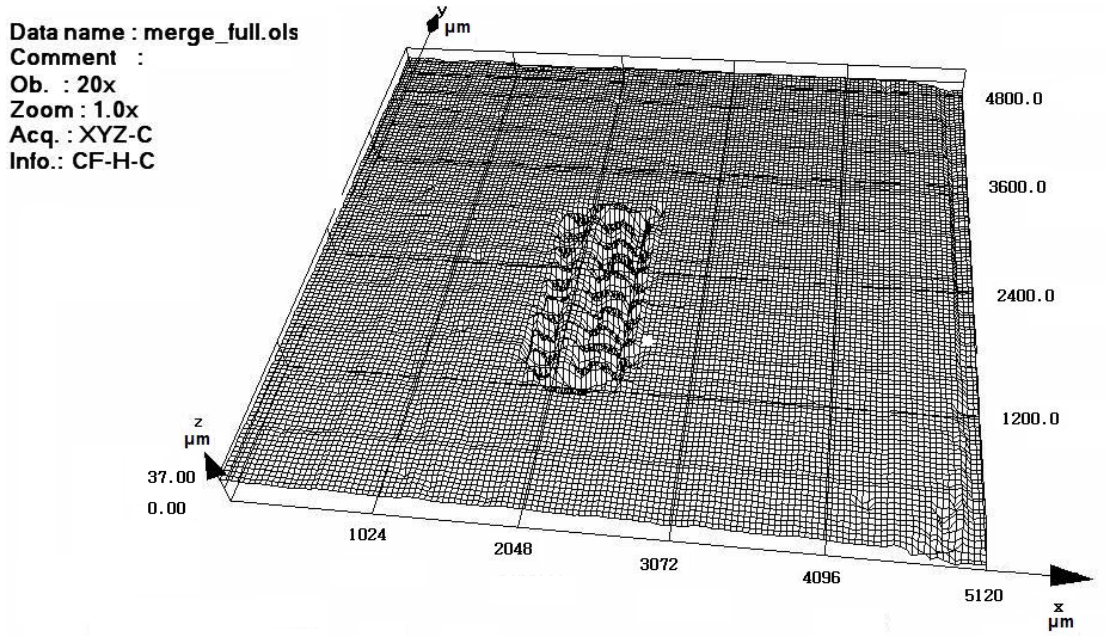

Fig. 5.7: Surface mesh plot after laser scanning

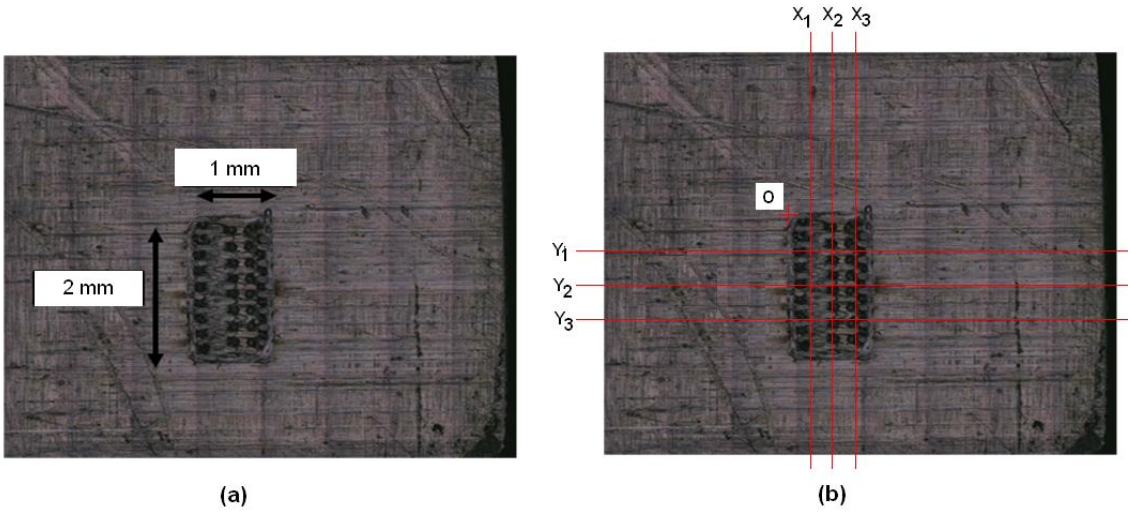

Fig. 5.8: (a) 2-D textured surface image, (b) Path designations

Fig. 5.7 and Fig. 5.8 show the scanned region resulting from the laser melting process. The path designations in Fig. 5.8(b) are the same as those given in Fig. 5.4. A number of observations were made during the laser melting process. The dimpled surface texture of the melted region are believed to be similar to those observed by Blackburn *et al* (2010) using high-speed cameras in studying the characteristics of Nd:YAG laser welded titanium alloy plates (Ti-2.5Cu). Visible splattering of molten material in front of the laser due to instability of the molten pool was observed. Creased tracks formed behind the laser beam as the molten material solidified, increasing the roughness in the scanned region and the heat affected zone around it. The random surface undulations

make it difficult to measure the residual stress distributions and displacements in the scanned region. The surface would require extensive surface preparation before any measurements could be made. Therefore, the surface displacement results of the unaffected platform regions were considered for the measurements.

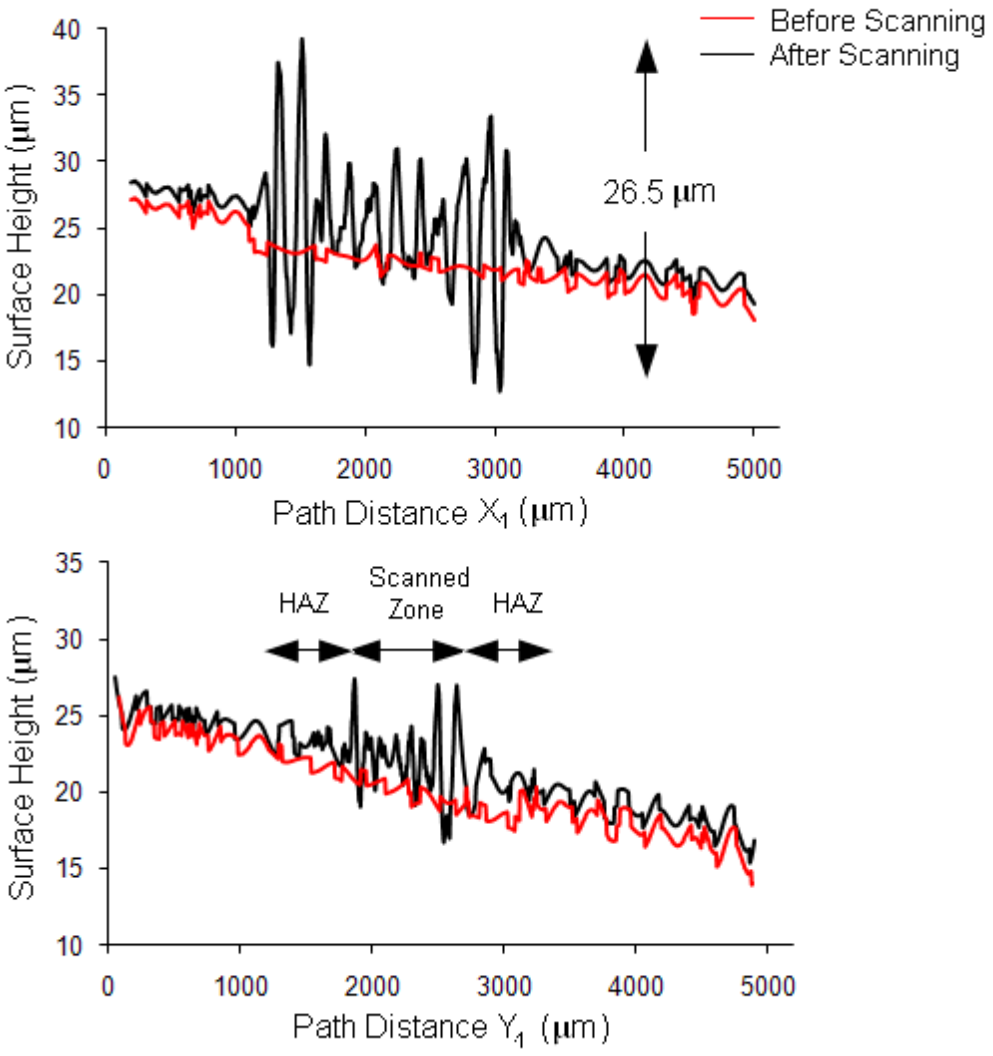

Fig. 5.9: Displacement profiles for X_1 and Y_1

Fig. 5.9 shows the primary height variation across the path X_1 and Y_1 for the initial measurement before laser scanning and the final measurement after laser scanning. The initial inclination of the platform after the stress-relieving process is clearly evident. It should be noted that the profiles have been plotted with an intentional 2 µm vertical offset for the purpose of clarity. The maximum disturbance on the surface is 26.5 µm which is less than the characteristic z-range of 40 µm chosen for this experiment. The

surface displacement profile plots in Fig. 5.9 for the selected paths showed consistent trends for the three samples used in this experiment.

For each test sample, a total of 6 path measurements were taken giving a combined total of 18 measurements for the validation process.

Branner *et al* (2008) in their platform deformation study were limited to monitoring the displacements at point locations on the surface of the substrate using a microscope with a glass scale. Using the laser optical scanning method, however, it can be seen that the displacement profiles across defined paths on the surface can be obtained.

5.5.2 Comparison with Simulation Results

Fig. 5.10 shows the vertical platform deformation distribution plot from the numerical model. As expected, the maximum deflection is recorded at the farthest edge from the cantilever support.

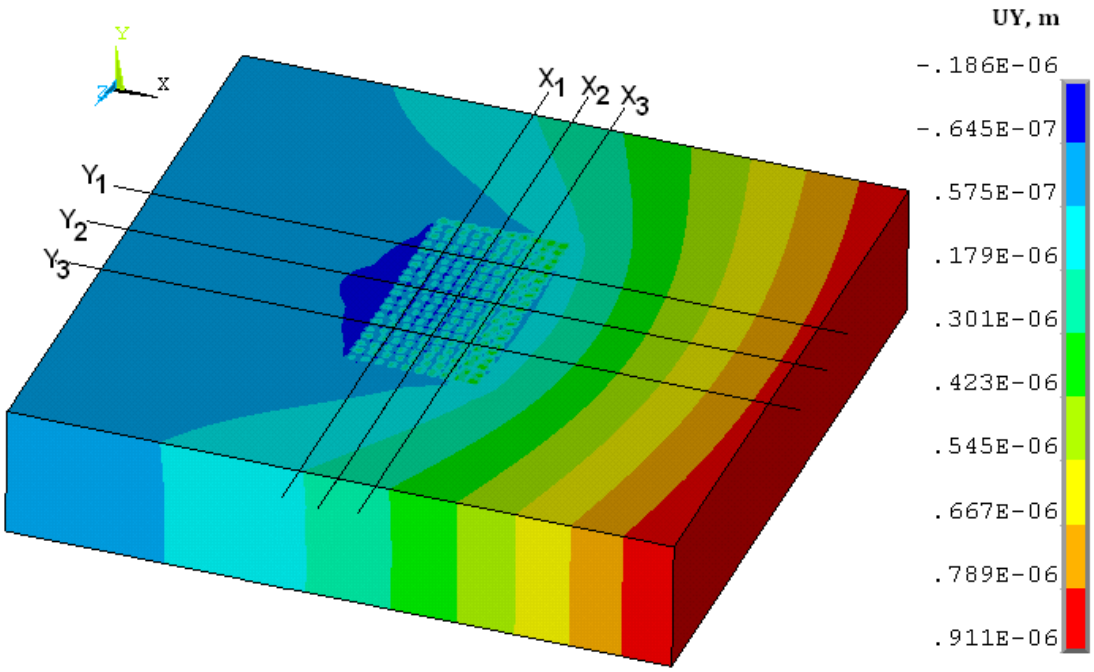

Fig. 5.10: Platform deformation plot

Fig. 5.11 and Fig. 5.12 compare the X-path displacement profiles of the platform surface (i.e. variation of vertical displacement with path distance) for the experiments and simulation for locations either side of the scanned region. The vertical axis quantity

(Δh) is the difference between the final and initial vertical surface displacements. The coordinate system, platform orientation and direction of laser travel from the simulation model were translated to match those of the experimental set-up to aid comparison.

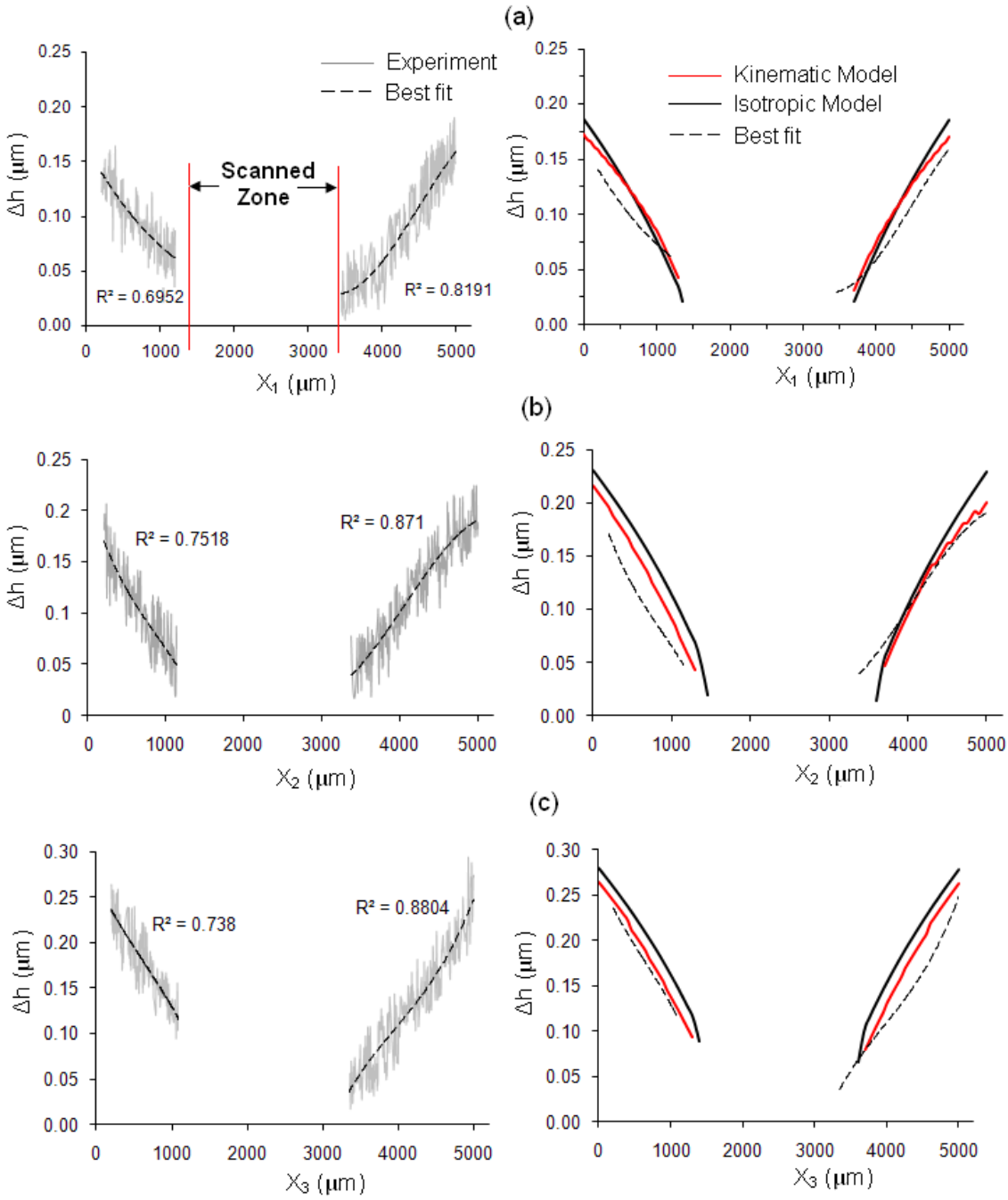

Fig. 5.11: Comparison of X-path displacements

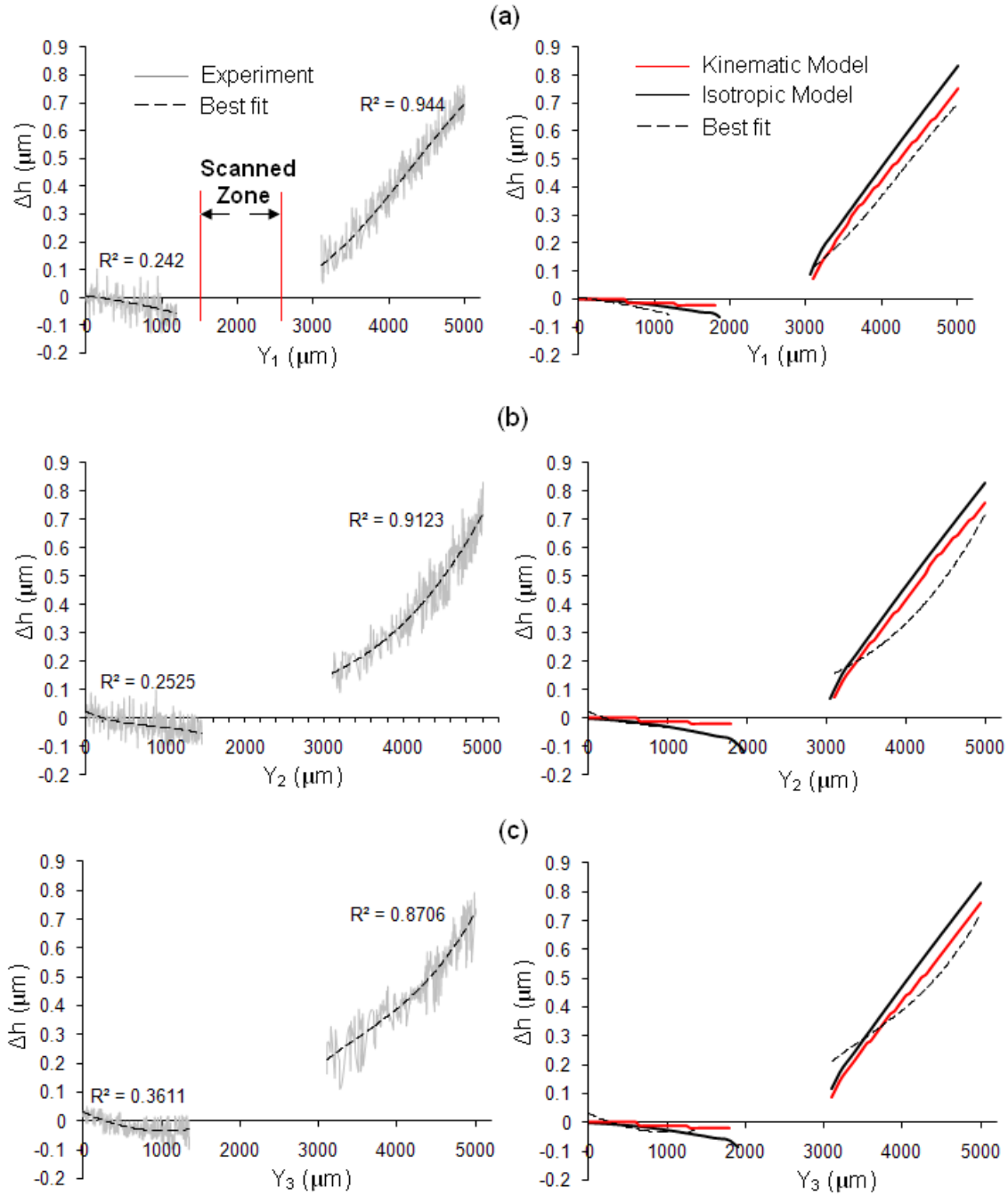

Fig. 5.12: Comparison of Y-path displacements

The path results for the surface profiles showed similar trends between the experiment and simulation models. Inspection of the experimental data for platform displacement with path distance shows that a relationship exists. The goodness of fit of the selected regression model can be deduced from its coefficient of determination (R^2). The formula for calculating R^2 is given in Montgomery (2001) as:

$$R^2 = \frac{SS_{\text{reg. model}}}{SS_{\text{total}}} = \frac{\sum_{i=1}^{n}(f(i)-\bar{y})^2}{\sum_{i=1}^{n}(y(i)-\bar{y})^2} \qquad \text{Eq. 5.1}$$

where y represents the platform displacement (Δh), $y(i)$ is the instantaneous value of Δh and $f(i)$ is predicted value of Δh predicted by the regression model. The calulation is facilitated by using the predefined functions in Microsoft Excel (2010).

The values of the coefficients of determination suggest good correlations ($R^2 > 0.8$) between the surface displacements and the path distance in all cases for the X-paths and Y-paths, the only exception to this is the displacement in the Y-path profiles leading into the scanned zone. The maximum measured displacements from the experiments were 0.25 μm and 0.70 μm for the X and Y paths respectively. Waviness observed in the experimental results can be attributed to uncontrollable factors arising from offsets in the repeated placement of the sample holder on the platforms of the EOS M270 machine as well as on the OLS3000 microscope observation platform. The image quality due to the resolution of the OLS3000 microscope at the specified magnification level could also have been a factor. Despite these error sources, the trends showed consistency for the test samples considered in the experiment.

The displacement trends by visual inspection alone do not give a definitive conclusion to the applicability of the numerical model. In order to test the uncertainty or reliability associated with the sampling estimate for points along the designated paths, a 95% confidence interval approach was adopted. The 95% confidence interval expresses the likelihood that the population mean is contained within a calculated interval.

Fig. 5.13 shows the extraction method from the experiment plot for use in further analysis. It shows the resultant displacement (i.e. ordinate) corresponding to the path distance (500 μm along path X_2) on the line of best fit. Respective displacements including those for other samples were obtained in the same manner.

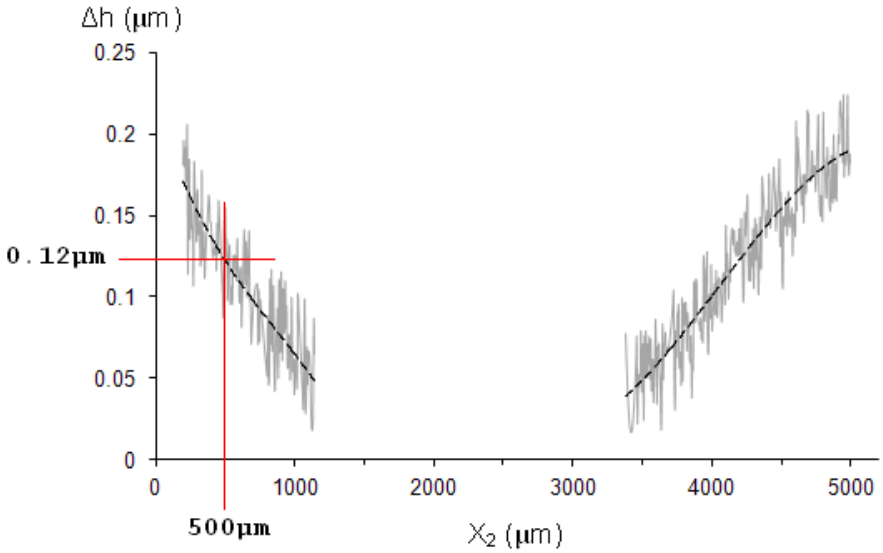

Fig. 5.13: Data extraction method

The 95% confidence interval is defined in Montgomery (2001) as:

$$95\%C.I. = \bar{x} - 1.96\left(\frac{s}{\sqrt{n}}\right), \bar{x} + 1.96\left(\frac{s}{\sqrt{n}}\right) \qquad \text{Eq. 5.2}$$

where $\bar{x}$ is the sample mean, *s* is the standard deviation and *n* is the sample size. The results of the calculation give the lower bound (LB) and upper bound (UB) values of the 95% confidence interval. This calulation is also facilitated by using the predefined functions in Microsoft Excel (2010).

Table 5.1 and Table 5.2 show the 95% confidence intervals for the mean platform displacements at various path locations for the three samples for the centreline paths X_2 and Y_2. The results show that the numerically predicted displacements using the kinematic model for similar points are in very close proximity to or enclosed by the 95% confidence intervals.

Table 5.1: Path X_2 95% Confidence Interval

Path X2	Sample Displacement (μm)			Mean	Standard Deviation	95% Confidence Interval		Predicted Displacement (μm)
Location (μm)	1	2	3	$\overline{x}$ (μm)	*s* (μm)	LB (μm)	UB (μm)	
500	0.12	0.15	0.13	0.133	0.015	0.12	0.15	0.16
1000	0.06	0.08	0.06	0.067	0.012	0.05	0.08	0.09
4000	0.10	0.12	0.14	0.120	0.020	0.10	0.14	0.10
4500	0.14	0.15	0.17	0.153	0.015	0.14	0.17	0.14
5000	0.18	0.2	0.21	0.197	0.015	0.18	0.21	0.20

Table 5.2: Path Y_2 95% Confidence Interval

Path Y2	Sample Displacement (μm)			Mean	Standard Deviation	95% Confidence Interval		Predicted Displacement (μm)
Location (μm)	1	2	3	$\overline{x}$ (μm)	*s* (μm)	LB (μm)	UB (μm)	
500	-0.02	0.00	0.00	-0.007	0.012	-0.02	0.01	0.00
1000	-0.04	-0.02	-0.02	-0.027	0.012	-0.04	-0.01	-0.01
1500	-0.05	-0.04	-0.08	-0.057	0.021	-0.08	-0.03	-0.02
3500	0.22	0.20	0.26	0.227	0.031	0.19	0.26	0.24
4000	0.34	0.35	0.38	0.357	0.021	0.33	0.38	0.41
4500	0.50	0.56	0.60	0.553	0.050	0.50	0.61	0.60
5000	0.72	0.75	0.75	0.740	0.017	0.72	0.76	0.76

Table 5.3 gives a comparison of the maximum measured displacements with those predicted by the simulation model. The experimental results showed an expected

increase in the X and Y path maximum displacements with increasing distance from the scanning start point.

Table 5.3: Comparison of maximum platform displacements – Experiment I

Path	Experiment (μm)				Isotropic Hardening Model (μm)	Kinematic Hardening Model (μm)
	Samples			Average		
	1	2	3			
X_1	0.16	0.15	0.16	0.157	0.19	0.17
X_2	0.18	0.20	0.21	0.197	0.23	0.20
X_3	0.25	0.26	0.24	0.250	0.28	0.24
Y_1	0.70	0.72	0.70	0.706	0.83	0.75
Y_2	0.72	0.73	0.72	0.723	0.84	0.76
Y_3	0.72	0.75	0.75	0.740	0.83	0.78

From Table 5.3, it can be seen that the numerical models mostly predicted higher maximum platform displacements than those obtained from the experiments. The displacement trends predicted by the numerical model varied in a similar manner to those measured in the experiments. On average, the displacements predicted by the isotropic hardening model were 13.4% and 16.8% higher than the measured values for the X and Y paths respectively while the kinematic model on average predicted values that were 4.8% and 7.0% higher than those measured. This shows that the isotropic hardening model which used a single high tangent modulus for the plastic behaviour gave higher platform displacements. Although the solution times for the isotropic hardening model were shorter than those of the kinematic model, it was less accurate than the kinematic model.

As expected, because the laser scans the surface in a raster fashion and the part sizes were relatively small, the bending of the platform was not as severe as it would have been had the laser scanned the surface back-and-forth repeatedly along a single defined track as demonstrated in the laser bending study of Shi *et al* (2007). The surface

displacement profiles showed that on either side of the scanned region, there was an upward slope leading away from the scanned region for the X-paths. An initial dip was observed leading up to the scanned region for the Y-paths in the first instance before sloping upwards away from the scanned region as a result of the cantilever arrangement. The combination of these surface trends indicates the formation of a concave depression or 'saddle' in the scanned region and is supported by the Temperature Gradient Mechanism (TGM) explanation given in Chapter 2. This is illustrated in Fig. 5.14 where a bow is formed across the sides (i.e. X-paths) and lifting occurs at the free cantilevered end (i.e. Y-paths). The numerical model also predicted the formation of a saddle in the scanned region, albeit an approximate linear variation leading up to and away from the scanned region for all X and Y paths.

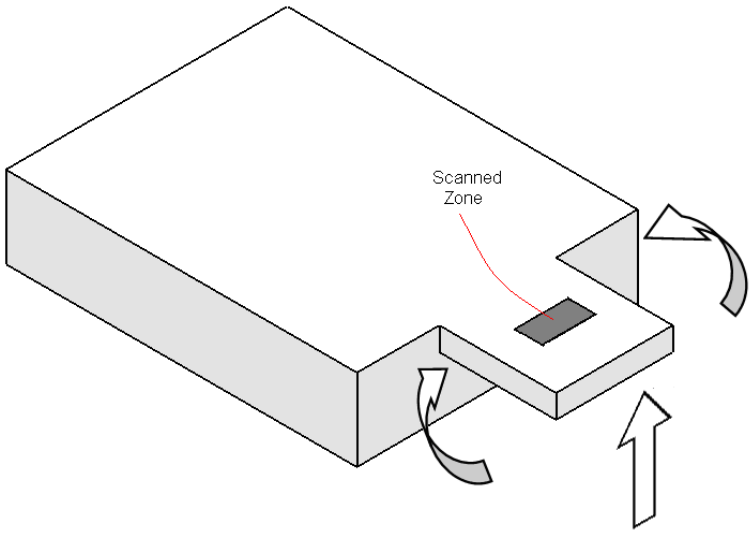

Fig. 5.14: Saddle formation

5.5.3 Mesh Sensitivity Study

The accuracy of the finite element simulation model generally depends on the mesh distribution and solution control settings. Refining the mesh by increasing the number of elements in areas that experience steep thermal gradients would normally lead to model predictions approaching the exact results. As stated in the Chapter 4, the element sizes were chosen to give whole number divisions of the laser beam diameter.

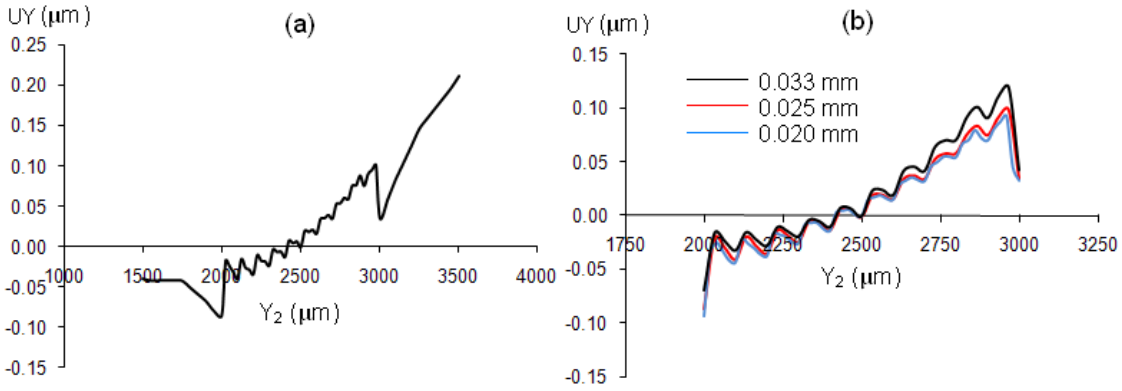

Fig. 5.15: Mesh refinement study: (a) Y_2-path displacement in scanned region, (b) profile in scanned region for different mesh sizes

Fig. 5.15 shows the effect of reducing the element sizes in the scanned region on the surface displacement for the Y_2-path. It was observed that the surface displacement profiles outside the scanned region were not affected by changes to the mesh density because they were not within the field of influence of the temperature gradients. However, the displacement variation within the scanned region showed significant variation. The surface displacement results for 0.033 mm element size gave the greatest displacements in the scanned region. Reducing the element sizes to 0.025 mm produced a similar displacement profile with noticeably lower displacement values but required longer solution times. The results were between 8% and 20% lower than that shown for the 0.033 mm element size case (from left to right in Fig. 5.15(b)). By reducing the element sizes further to 0.020 mm, the results were found to be between 4% and 8% lower than the 0.025 mm case; showing an improvement on the 0.033 mm case and an approach towards a numerical solution.

The cost of increasing the solution sub-steps and element divisions can be prohibitive (in terms of amount of computational time) and can also be out of proportion with the accuracy of the results. The 0.025 mm element size was, therefore, chosen considering the time and memory limitations as well as ease of post-processing.

5.5.4 Summary of Experiment I

The surface displacement trends from the simulation model which utilised the kinematic hardening model compared well with those obtained from the experiment. The results from this surface deformation analysis suggest that the assumptions made in the

modelling of the thermal and structural fields are valid. This supports the applicability of the simulation model for predicting the structural field associated with the laser heating of metal surfaces.

5.6 Experiment II: Laser Melting of Ti64 Powder

Unlike the SLS of plastics where a base platform is not required, laser melting of metal powders requires a base platform to effect deposition and fusion of the powder layers. The molten powder material undergoes expansion and contraction on top of the base platform. The difference in coefficient of thermal expansion and stiffness for the dissimilar metals is known to generate residual stresses. This experiment aimed to determine the surface deformation produced by laser melting two 30 μm layers of Ti64 powder on a steel base platform.

5.6.1 Experiment Results

Fig. 5.16 shows the surface plot with two layers of Ti64 laser melted onto the surface of the platform. There was visible splattering of powder and molten material during the process which can be seen in the surface plot. This was more severe than in the control experiment. It appeared to be more severe around the perimeter of the scanned region. A similar observation was made by Zaeh *et al* (2008) in electron beam scanning of tool steel powder (H11) where without transmitting any thermal energy into the material, the electron beam caused uncontrolled acceleration of the powder particles in the near surrounding of the point of impact They found that preheating the powder prior to scanning reduced the scattering effect.

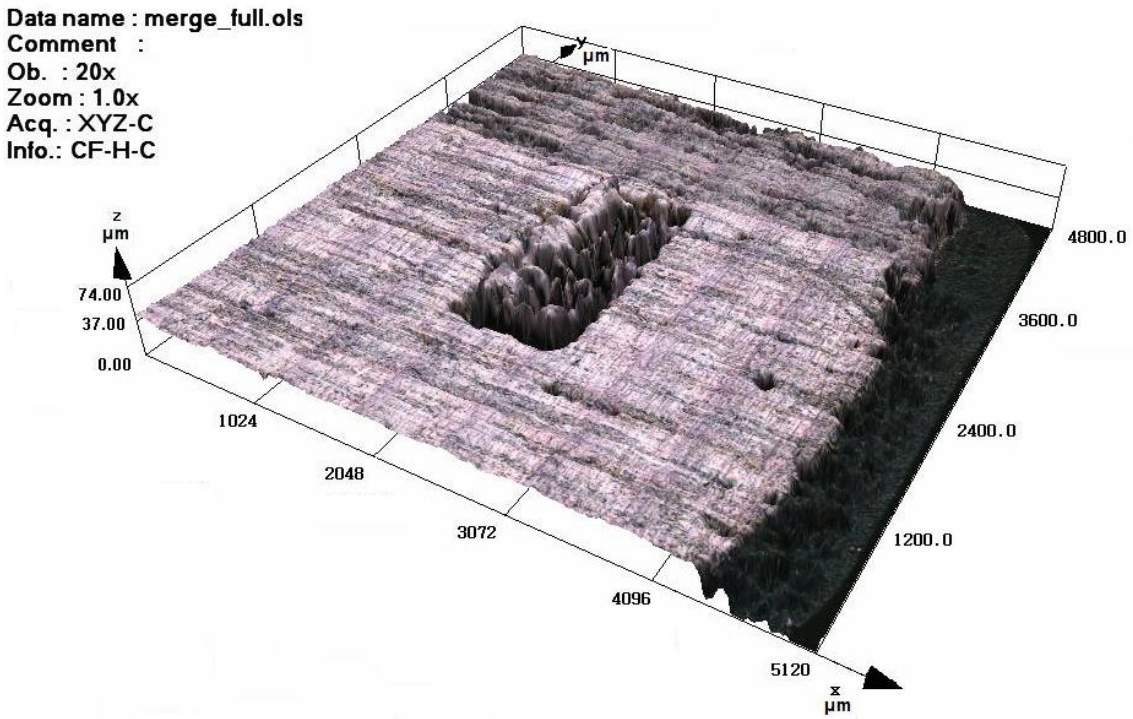

Fig. 5.16: 3-D Textured surface plot

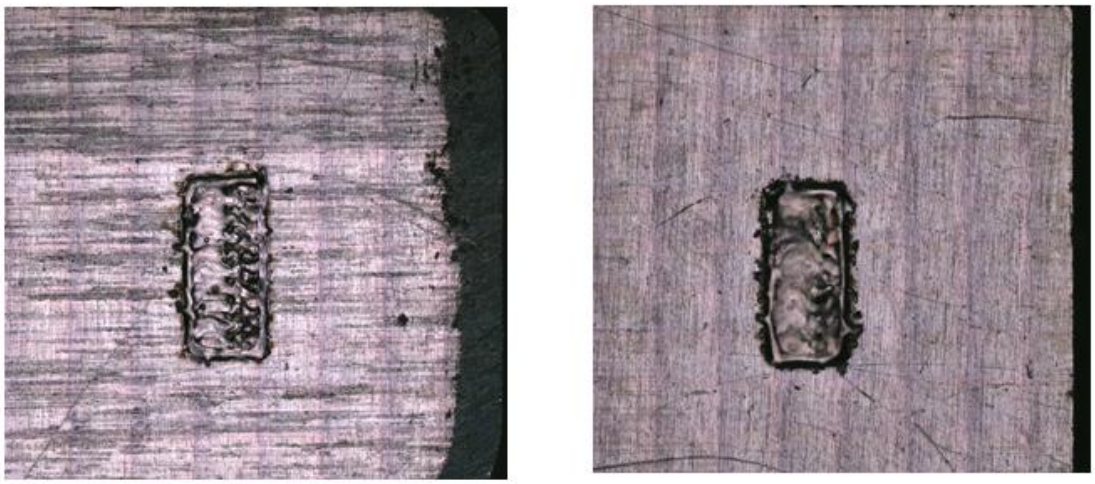

Fig. 5.17: Textured 2-D surface for two samples

Lack of cohesion of molten material was evident in some areas within the scanned region as seen in Fig. 5.16 and Fig. 5.17, highlighting the difficulty that would be present if stress measurement techniques were to be applied.

The surface characteristics of the scanned region observed here were also highlighted in the study by Kruth *et al* (2007) on the consolidification mechanism in full melting of metal powders where lack of control of flow of the molten material meant that upon

solidification the upper layer surface was not flat enough to ensure a good spread for the next powder layer.

Fig. 5.18 shows the surface displacements before and after laser scanning. The random nature of the scanned region can be clearly seen with some regions falling below their original positions even after the addition of two layers. A small vertical offset (2 μm) has been added to distinguish between both displacement profiles. The maximum disturbance on the surface was about 57 μm which is less than the characteristic 100 μm z-range chosen for this experiment.

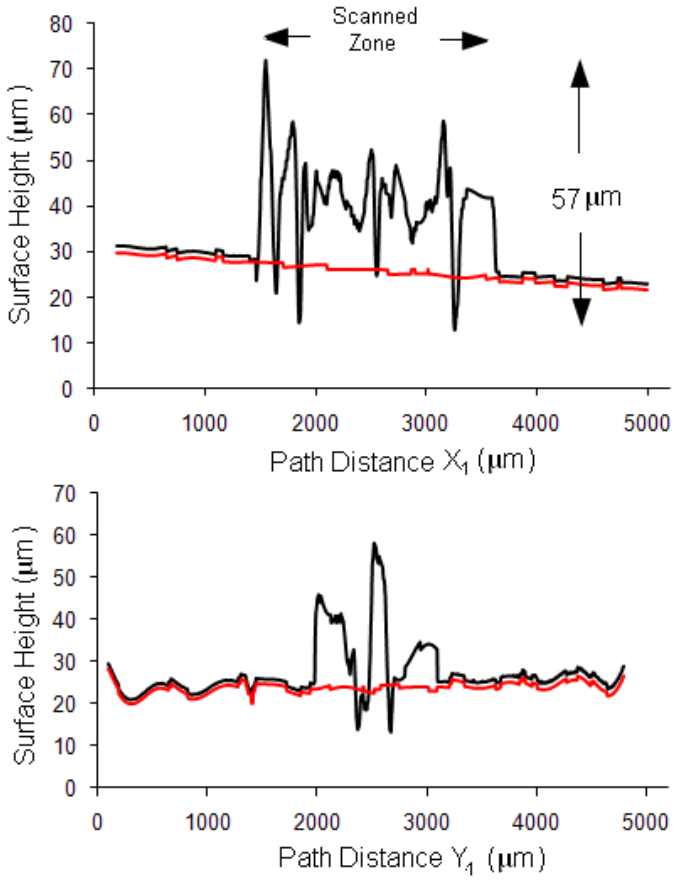

Fig. 5.18: Displacement profiles for X_1 and Y_1 paths

5.6.2 Comparison with Simulation Results

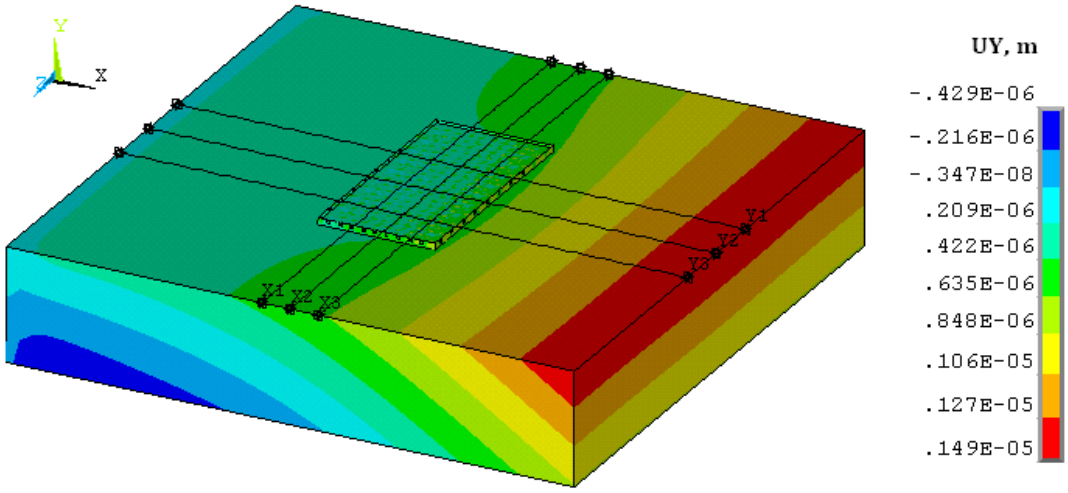

Fig. 5.19: Simulation displacement plot

Fig. 5.19 shows the simulation prediction of the platform deformation plot with two layers of Ti64 powder. The maximum displacement as expected is greatest at the free cantilevered edge. The displacement profiles through the designated paths on the surface of the platform for the X and Y profiles were compared with the experimentally measured ones in Fig. 5.20 and Fig. 5.21.

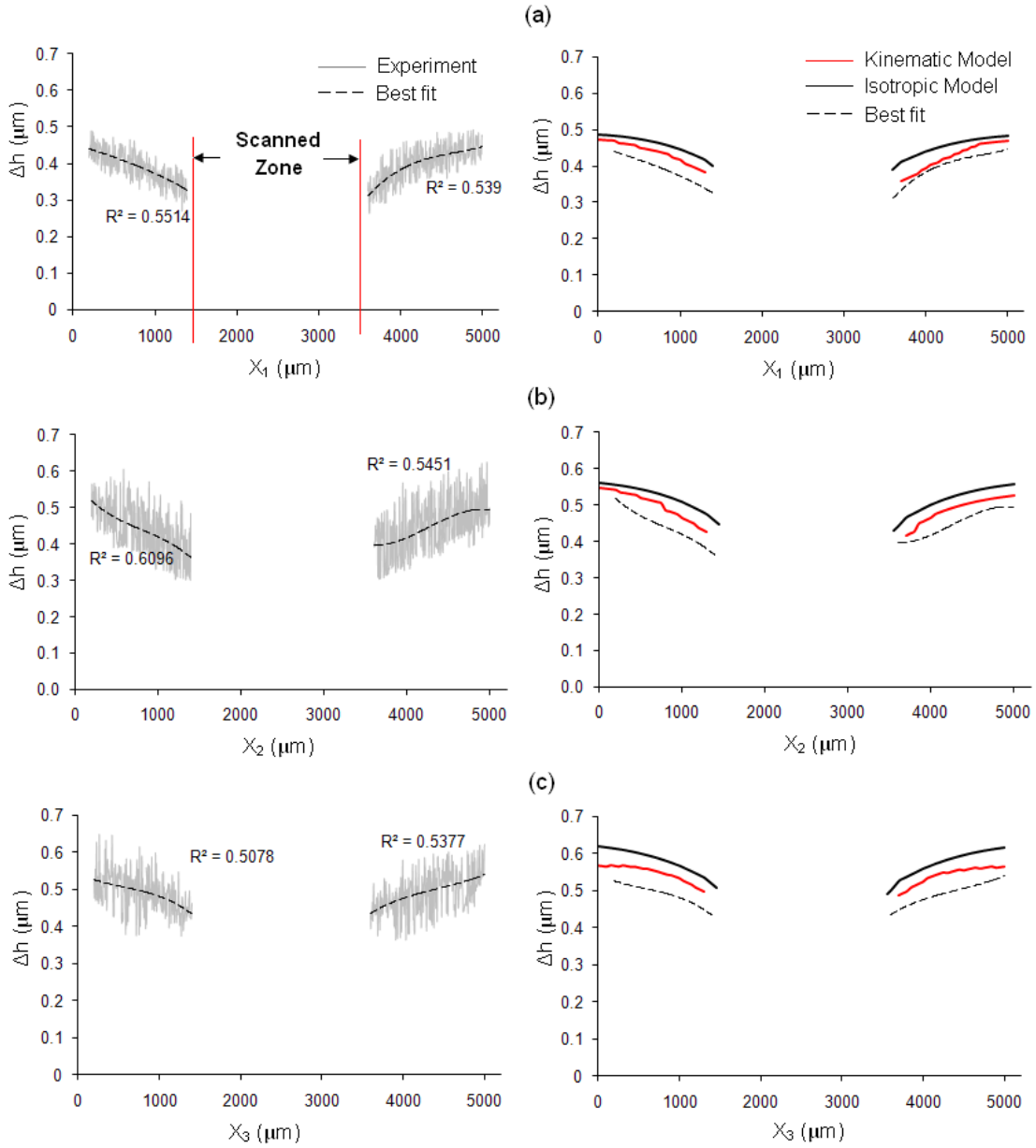

Fig. 5.20: Experiment X-path displacements

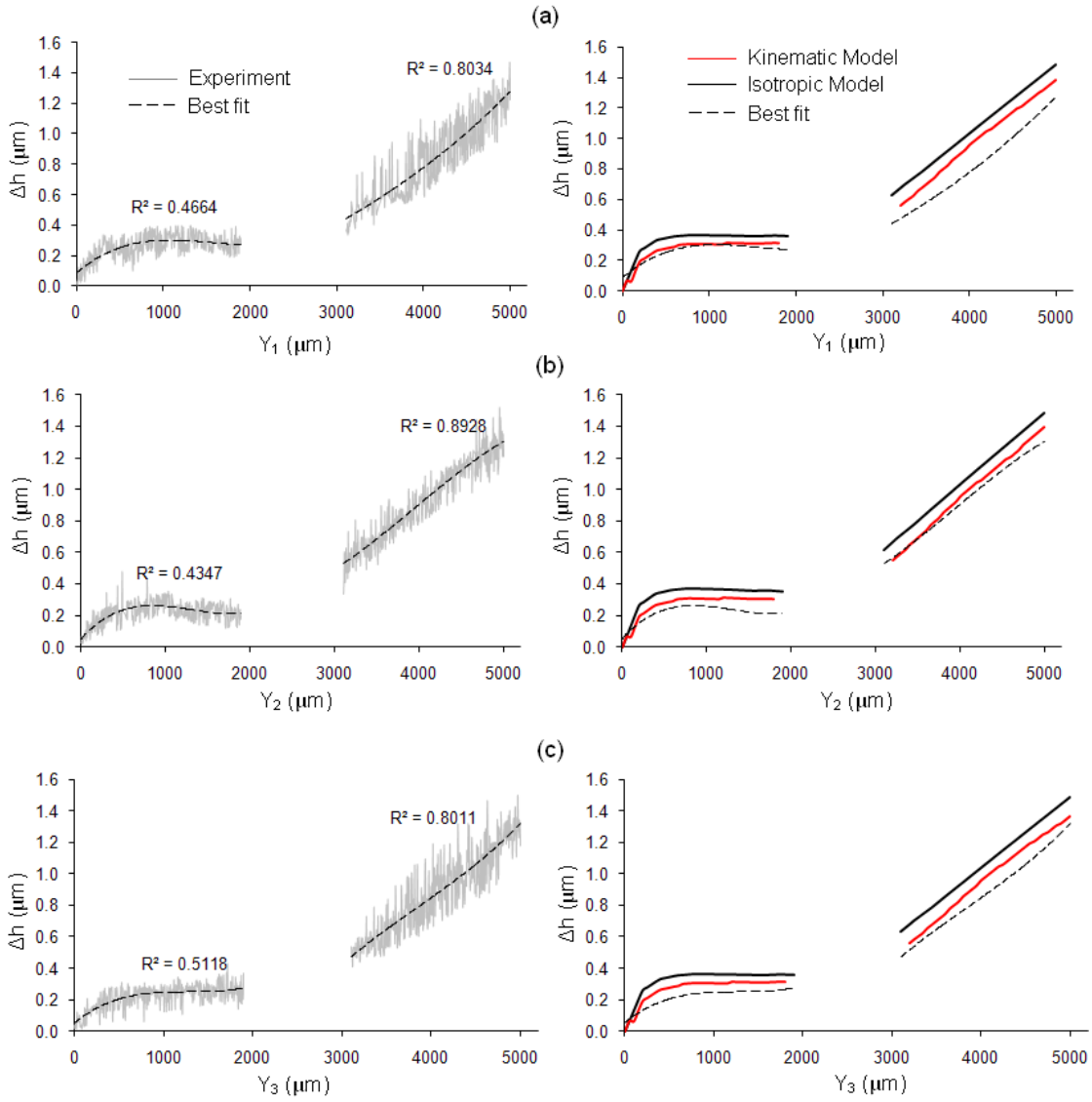

Fig. 5.21: Comparison of Y-path displacements

The results corroborate the finding of the control experiment by the formation of a saddle in the scanned region. A previous numerical simulation study by Dai and Shaw (2002) involving the laser melting of nickel powder also observed the 'saddle' effect. In their study, they also found that the scanning strategy adopted affected the depth and physical attributes of the saddle formed.

The experiment results in Fig. 5.20 and Fig. 5.21 show a significant increase in the X and Y path displacements from those obtained in the control experiment. The measured maximum displacements for the X_1 and Y_1 paths were 0.42 μm and 1.28 μm respectively. These correspond to increases of 0.26 μm and 0.58 μm for the X_1 and Y_1

displacements respectively. The displacement increase was the direct result of the scanning of the two added layers of Ti64 powder material on top of the platform.

In order to test the uncertainty associated with the sampling estimate for displacements along the profile paths, a 95% confidence interval approach is adopted. Table 5.4 and Table 5.5 show the 95% confidence intervals for the mean platform displacements at various path distances for the three samples for the centreline paths X_2 and Y_2. The results show that the numerically predicted displacements using the kinematic model for similar path points are in very close proximity to or enclosed by the 95% confidence intervals.

Table 5.4: Path X_2 95% Confidence Interval

Path X_2	Sample Displacement (μm)			Mean	Standard Deviation	95% Confidence Interval		Predicted Displacement (μm)
Location (μm)	1	2	3	$\overline{x}$ (μm)	s (μm)	LB (μm)	UB (μm)	
500	0.42	0.48	0.44	0.447	0.031	0.41	0.48	0.45
1000	0.37	0.40	0.38	0.383	0.015	0.37	0.40	0.42
4000	0.38	0.42	0.42	0.407	0.023	0.38	0.43	0.40
4500	0.42	0.40	0.42	0.413	0.012	0.40	0.43	0.44
5000	0.50	0.48	0.50	0.493	0.012	0.48	0.51	0.47

Table 5.5: Path Y_2 95% Confidence Interval

Path Y2	Sample Displacement (μm)			Mean	Standard Deviation	95% Confidence Interval		Predicted Displacement (μm)
Location (μm)	1	2	3	$\overline{x}$ (μm)	s (μm)	LB (μm)	UB (μm)	
500	0.24	0.30	0.32	0.287	0.042	0.24	0.33	0.28
1000	0.26	0.28	0.30	0.280	0.020	0.26	0.30	0.30
1500	0.22	0.30	0.28	0.267	0.042	0.22	0.31	0.30
3500	0.72	0.74	0.78	0.747	0.031	0.71	0.78	0.72
4000	0.90	0.86	0.94	0.900	0.040	0.85	0.95	0.96
4500	1.12	1.16	1.16	1.147	0.023	1.12	1.17	1.16
5000	1.30	1.35	1.32	1.323	0.025	1.29	1.35	1.40

Table 5.6: Comparison of maximum platform displacements – Experiment II

Path	Experiment (μm)				Isotropic Hardening Model (μm)	Kinematic Hardening Model (μm)
	Samples			Average		
	1	2	3			
X_1	0.42	0.40	0.44	0.420	0.50	0.46
X_2	0.50	0.48	0.50	0.493	0.56	0.53
X_3	0.54	0.55	0.52	0.534	0.62	0.56
Y_1	1.28	1.25	1.30	1.276	1.48	1.37
Y_2	1.30	1.32	1.34	1.320	1.51	1.41
Y_3	1.30	1.35	1.32	1.323	1.48	1.37

The results show a steady increase in the edge displacement from the constrained edge for the X paths similar to those obtained in the control experiment. The results from the

numerical model using isotropic strain hardening was found to overestimate the surface displacement values by 15.2% and 15.5% for the X and Y profiles respectively, while the kinematic model predicted displacements that were 6.4% and 6.9% for the X and Y paths respectively. The trend from the displacement profiles from simulation models tally with those measured in the experiments.

Comparison of the displacement results shows a better accuracy between the kinematic hardening model and the experiment results. The isotropic model suggests a trade-off between computational time and accuracy.

5.7 Discussion on Numerical Modelling

It has been established that the temperature cycles govern the development of thermal stresses and strains in the laser melting of metal powders. The analysis provided here shows good correlation between the measured and predicted displacements for the Ti64 layers built on a steel platform. This is despite the temperature model strongly predicting the maximum temperatures reached for regions enclosed by the laser beam, whilst showing discrepancies in the temperature rise path and the temperature gradients for regions outside the beam area. It should be recalled that thermal stresses do not exist in the loose powder bed. Thermal stresses become active only when solidification and bonding to the base material begins after melting has taken place as highlighted in Section 2.7. This implies that the rapid temperature rise path leading up to melting is not a vital component of the laser melting simulation for metal powders. The cooling path, however, is affected by heat transfer via conduction from the molten material into the surrounding material. This alters the manner in which the thermal strains evolve with time both in the solidifying material and its surroundings and ultimately the residual stresses. The suggestion here is that a numerical model which activates the powder material as molten state elements at a temperature above its melting point (measured or validated experimentally for a given set of laser melting parameters) could reduce thermal modelling assumptions as well as demand on computing resources.

5.8 Summary of Experimental Validation

Experiments using laser microscopy have been conducted to validate and refine the layer-by-layer numerical model. Surface topography analyses conducted distinguished

between the relative effects of directly heating the platform surface and melting two layers of Ti64 powder on the platform surface.

Concave depressions (i.e. saddle effect) were observed in the scanned region which agree with the temperature gradient mechanism described in the literature by Mercelis and Kruth (2006). The results showed a significant increase in the displacement of the platform as a result of the laser melting of Ti64 powder on the steel platform. The kinematic hardening model provided results that compared closely with those obtained from the surface topography analyses than the isotropic hardening model.

These studies justify the assumptions made in the modelling of the thermal and structural fields and show that the numerical model using the kinematic strain hardening gives a good approximation of the displacements and by implication, the stress fields associated with the LM of metal powders. Therefore, the layer-by-layer finite element model with thermal elasto-plastic material considerations is suitable and can be applied to the stress field analysis.

6 Numerical Model Analysis

6.1 Introduction

This chapter explores the characteristics of the temperature and stress fields predicted by the layer-by-layer numerical model described in Chapter 4 and validated in Chapter 5. The temperature field for multiple layers of Ti64 powder and the designation of the stress fields for the laser melting of the steel surface and Ti64 powder are discussed. The outputs are displayed in three-dimensional views, sectional views and graphically.

6.2 Multiple Layer Temperature Field

Predicting the three-dimensional temperature field in the laser melting of powders involving multiple layers has been a challenge to researchers in the subject area. As with multi-pass welding, the temperature history is a vital element for determining the transient stresses and final residual stress states (Jiang, 2006). The addition of layers of powder and subsequent scanning is known to influence the heat transfer and thermal stress development in the underlying material.

The three-dimensional temperature field simulation for five 30 μm layers of Ti64 powder is considered here. The dimensions of the scanned region are 1 mm × 1 mm and the dimensions of the base platform are 3 mm × 3 mm × 1 mm. The scanning pattern and the finite element model are shown in Fig. 6.1. The spacing between adjacent tracks is taken as that of the laser beam diameter. Table 6.1 lists the process parameters used as input for the layer-by-layer numerical model. A 1 second recoating time was used for this study.

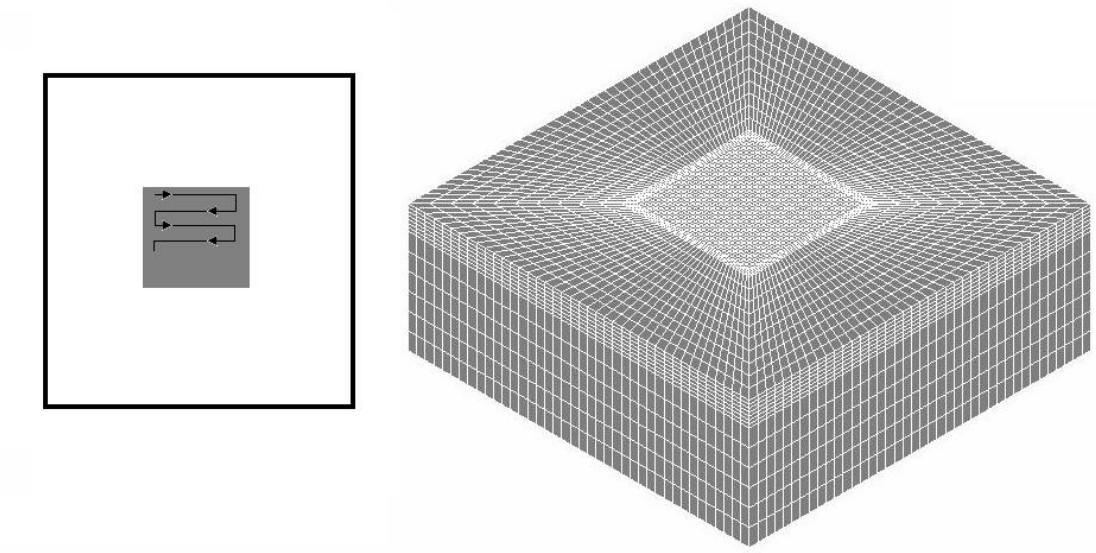

Fig. 6.1: Scanning pattern and finite element model

Table 6.1: Multiple layer temperature field analysis process parameters

Power (W)	Scan Speed (mm/s)	Beam Diameter (μm)	Layer Height (μm)	Raster Length (mm)	Chamber Temperature (°C)
195	1200	100	30	1	40

6.2.1 First Layer Temperature Field Results

Fig. 6.2 shows the temperature distribution plots for the first Ti64 layer at different times as the laser scans across the surface. The contour plots show similar temperature distributions around the irradiated regions. A 'tail out' condition of the high temperatures behind the heat source along the scanning direction is observed as a result of the rapid cooling that accompanies solidification of the material behind the laser. This 'tail' formation was also observed by Shen *et al* (2005) in a temperature field simulation study of tracks produced during the DMLS of steel powder.

The nature of the raster scanning pattern implies that there is a time lapse between successive scanned tracks. The preceding track enters its cooling phase as the adjacent track is being scanned. The heating and cooling corresponds to thermal expansion and contraction of the tracks (i.e. expansion in the current track and contraction in the preceding track).

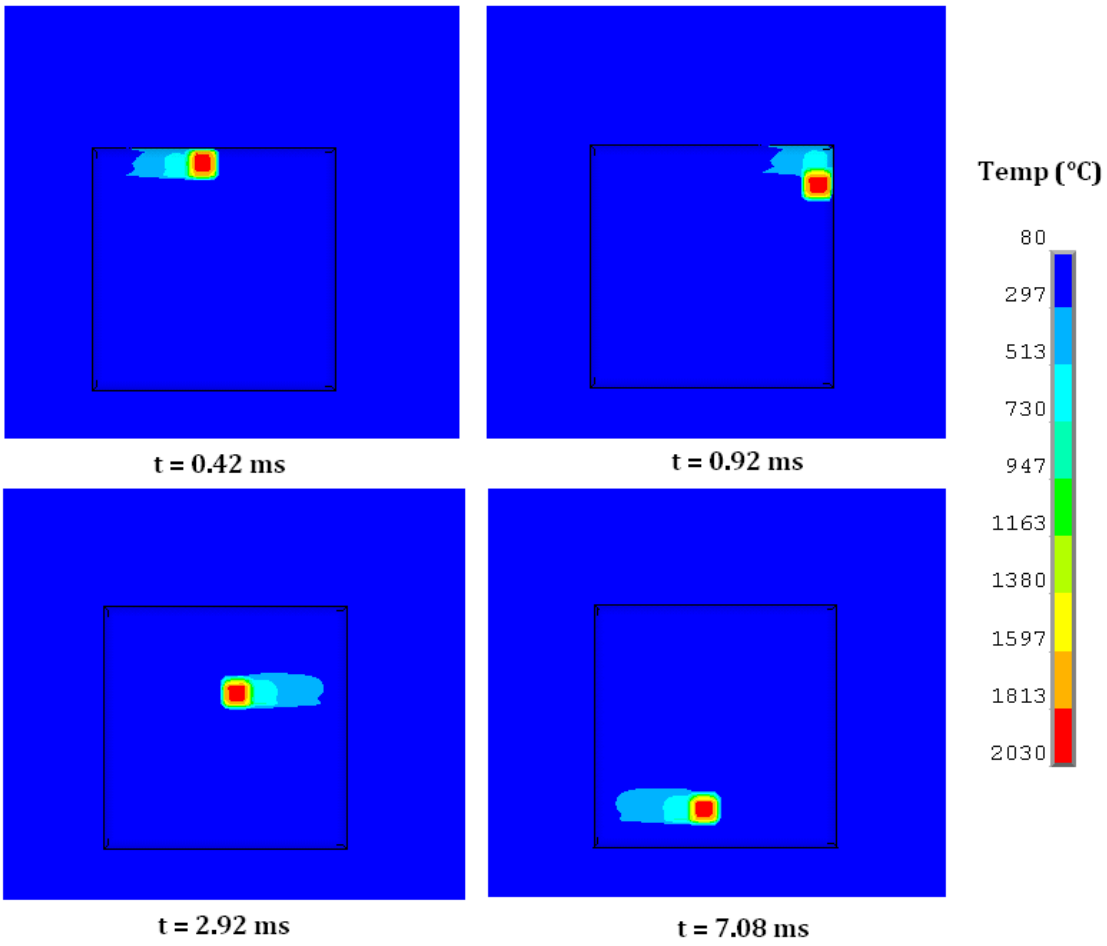

Fig. 6.2: Temperature distribution for first layer at different instances

Fig. 6.3 gives the temperature profile along the scan path *A-A*. The 'shrunk-in' region indicates the extent of shrinkage that occurred as a result of the solidification of the melted powder. The temperature distribution is skewed towards the rear of the laser and the previously scanned track due to the higher conductive molten or solid material, which effectively functions as a heat sink; conducting the heat from the current irradiated spot. The maximum surface temperature predicted by the numerical model is about 2030°C for the first layer.

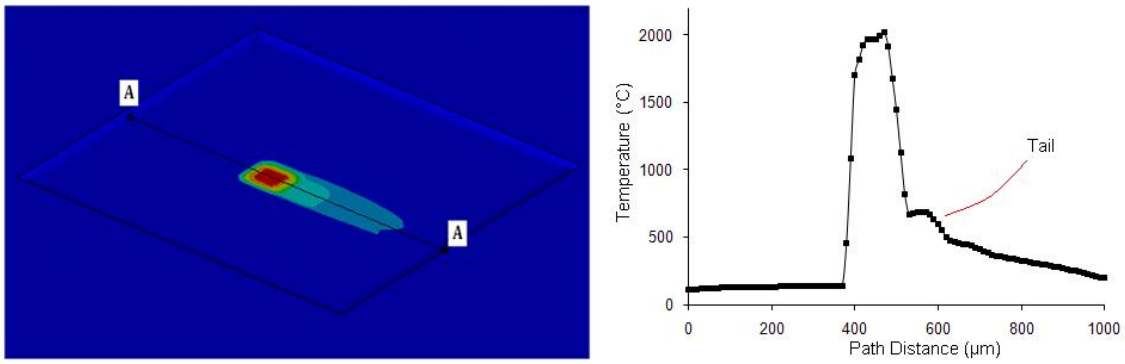

Fig. 6.3: Path temperature profile

Fig. 6.4 shows the transient temperatures for the first five irradiated spots. The average heating and cooling rates were 2.45×10^7 K/s and 3.38×10^6 K/s respectively. The calculated cooling rate lies in the range of typical cooling rates reported in Steen (2003) – between 10^3 K/s and 10^{11} K/s for laser processing technique. The temperature history shows strong similarities in the transient temperatures indicating that the various irradiated regions in a layer experience similar thermal cycles. A similar transient temperature characteristic was observed by Antonov and Iordanova (2007) using finite element models to analyse the temperature field produced by laser melting the surface of a mild steel sheet.

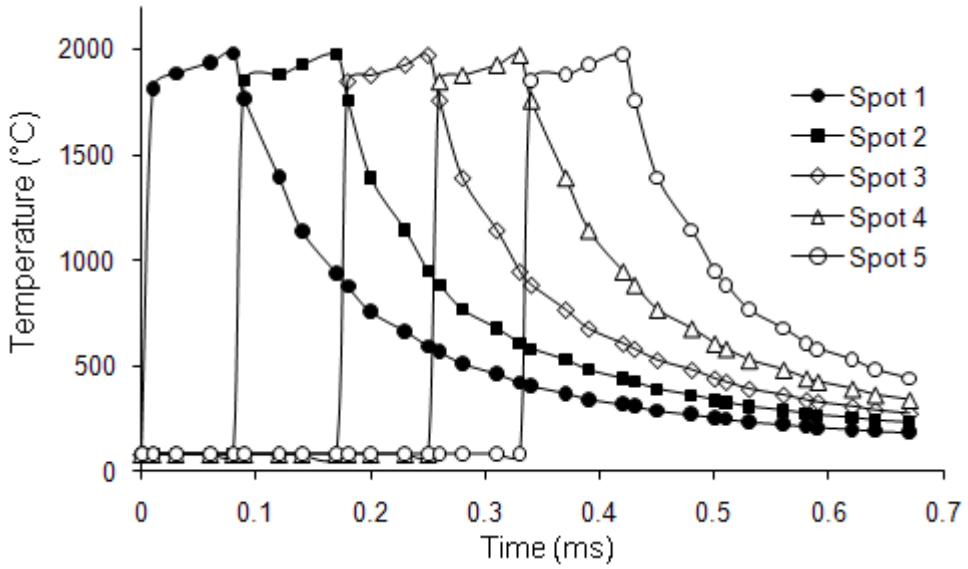

Fig. 6.4: Transient temperatures for the first 5 spots on first layer

The heating and cooling cycles occur in a few milliseconds – 0.083 ms and 0.6 ms respectively. The significance of this is that the rate of solidification is high enough to prevent convective redistribution of heat in the molten material.

6.2.2 Multiple Layer Temperature Results

The temperature histories at the surface centres of the first four layers following deposition and subsequent laser melting are shown in Fig. 6.5(a)-(d). The temperature history for each layer can be seen to be affected by the addition and scanning of new layers of powder. Secondary temperature peaks lower than the initial peak temperatures are observed in the underlying layers. These are due to the downward conduction of heat as the laser scans identical regions in the succeeding layers. The secondary peaks are similar to those observed in multi-pass welding studies by Jiang (2006) and are also concurrent with the findings of Gan *et al* (2004) in the temperature field studies of the plasma laser deposition for ten layers of metal powder. The secondary peak temperatures can be seen to decay with layer addition as seen in Fig. 6.5(a) for the first layer. They eventually disappear with increasing number of layers. It is therefore evident that the addition of layers of powder and subsequent scanning, affects the thermal history of the previous layers and underlying material.

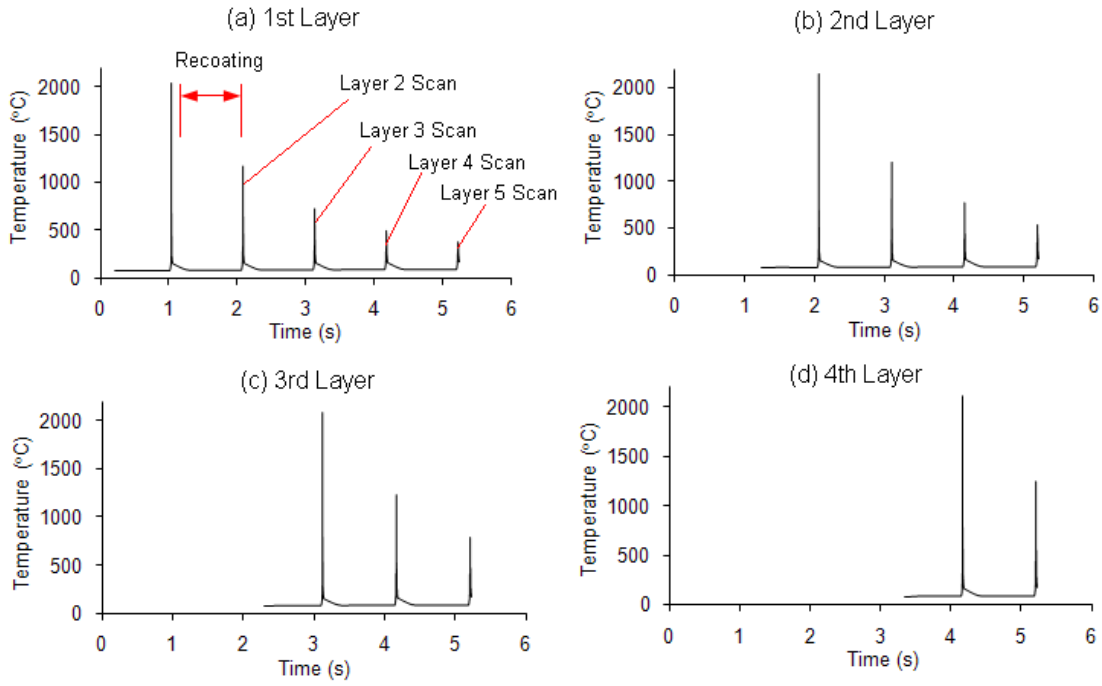

Fig. 6.5: Temperature variation with layer addition

The maximum predicted temperatures for each layer are summarised in Table 6.2. The results show a significant rise in the maximum achieved temperature of around 120°C between the first layer and the second layer. This hike in temperature is not observed for higher successive layers. In fact the maximum achieved temperatures are approximately

equal. The thermal conductivities of the dissimilar materials explains this finding. The first consolidated Ti64 layer has a lower thermal conductivity than the base steel material, whereas the subsequently melted layers are shielded from the steel base. The first layer with lower conductivity reduces the rate at which the heat from the laser is conducted downward into the solidified material thereby retaining a higher amount of heat in the scanned layer. This finding supports a practical application, where the first layer is normally scanned twice to ensure suitable bonding is obtained between the platform and the melted powder since the heat is more likely to be conducted away from the molten material.

Table 6.2: Maximum layer temperatures

Layer Number	Maximum Temperature (°C)
1	2030
2	2150
3	2149
4	2147
5	2150

6.2.3 Variation of Temperature with Depth

The temperature profile with depth gives further information as to the capability of the numerical model in understanding the temperature field in the LM process. The temperature variation with depth for the third layer is shown in Fig. 6.6.

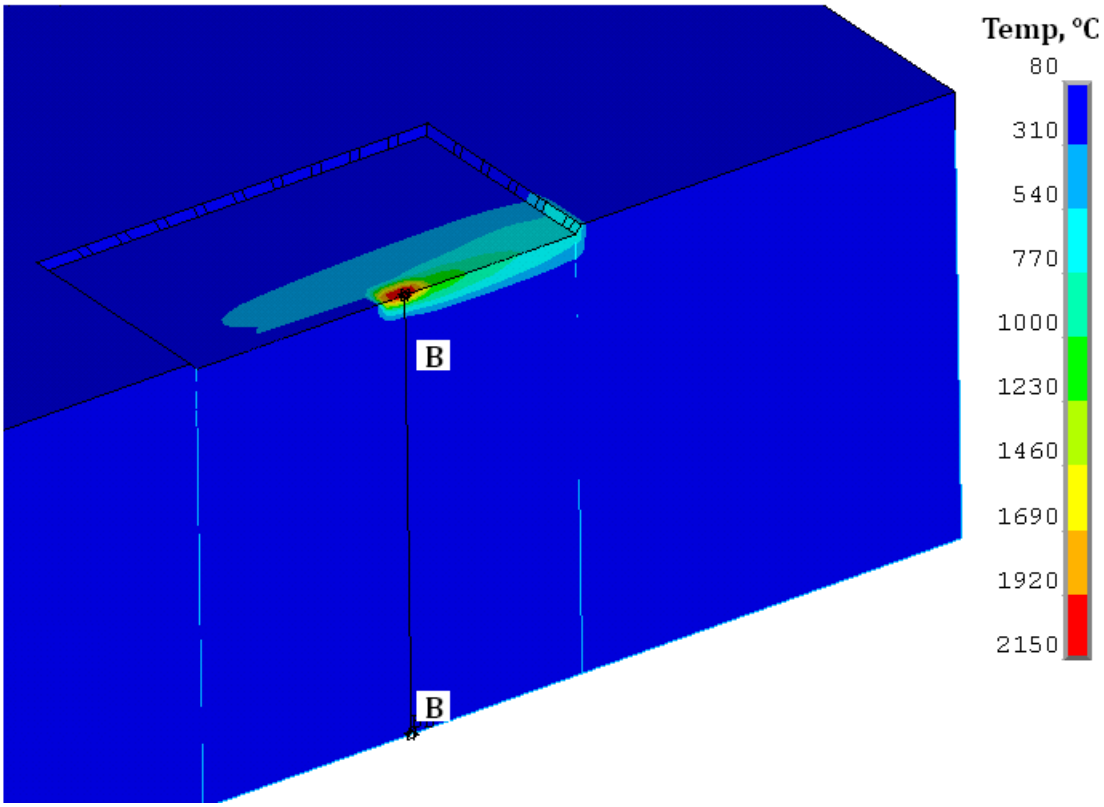

Fig. 6.6: Temperature-depth profile (sectional view though third layer)

It shows the highly localised temperatures at the surface layer. The localised temperature quickly decays to the temperature of the base material (i.e. chamber temperature) with depth. The temperature-depth profiles through the centre of the model along the path *B-B* for the first three layers are shown in Fig. 6.7.

The temperature-depth profiles show steep temperature gradients through the layer thickness. The 'interface line' indicates the boundary with the surface of the platform. It can be seen that for the first layer the boundary (i.e. at 30 μm depth) temperature is about 1690°C, above the melting point range of the Ti64 and steel material. This is desired as complete or partial melting of the platform surface is known to facilitate the fusion between the molten powder and the substrate during solidification (Schneider, 1998). The platform surface is shielded in the second and third layer cases.

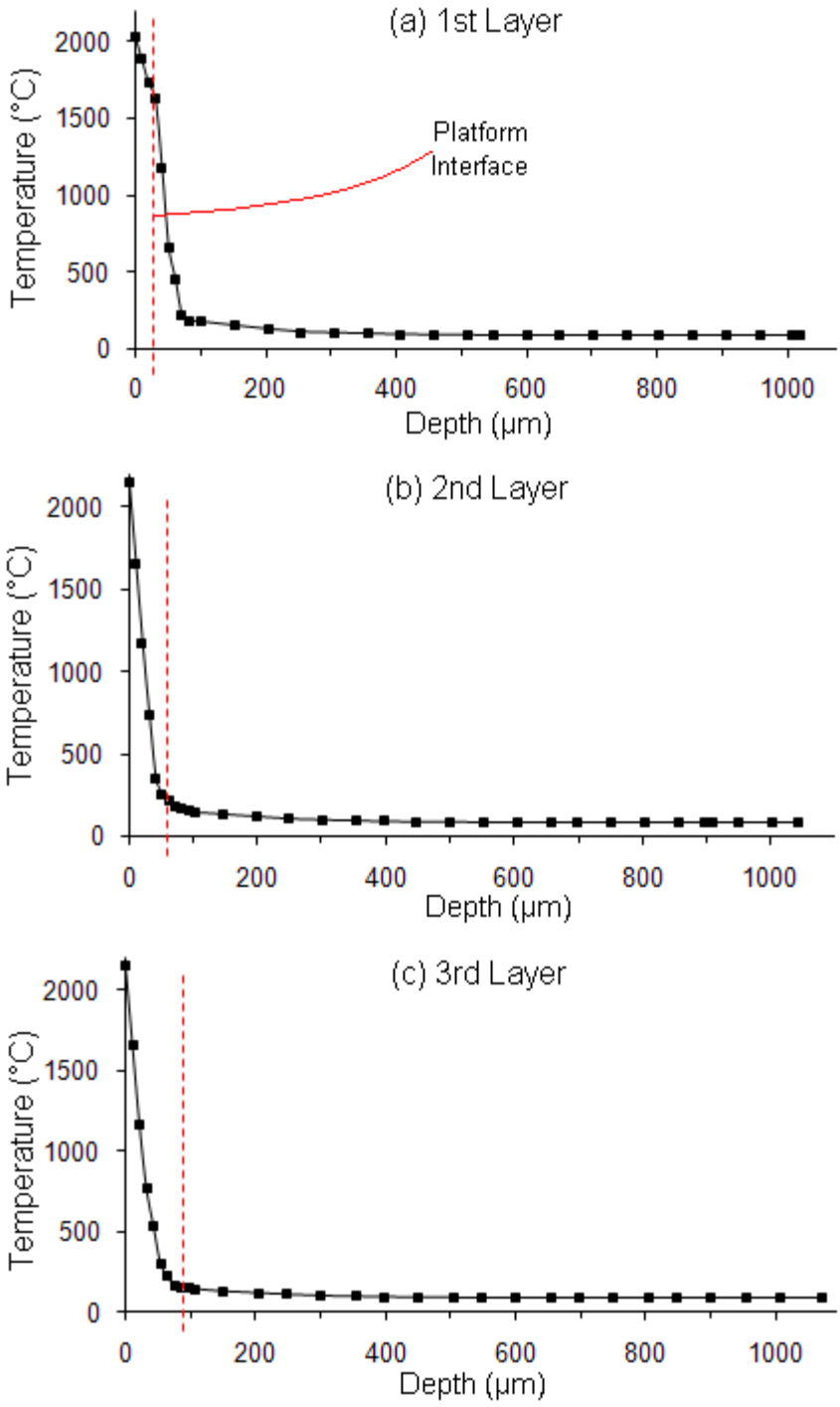

Fig. 6.7: Temperature-depth variation

6.2.4 Temperature Build-up in System

The dissipation of heat and heat build up in the system is considered in this section. The recoating period (i.e. time lapse during layer spreading) provides ample time to allow the system to cool down to a steady state temperature. The steady state temperature

during recoating is illustrated as the near horizontal temperature sections between peaks in the temperature profiles shown in Fig. 6.5. During recoating, heat is dissipated downwards into the underlying material and upwards to the newly added unscanned powder layer. It is expected that the temperature of the system would increase as a result. The steady state temperatures of three nodal points (P1, P2 and P3) located as shown in Fig. 6.8(a) are considered here.

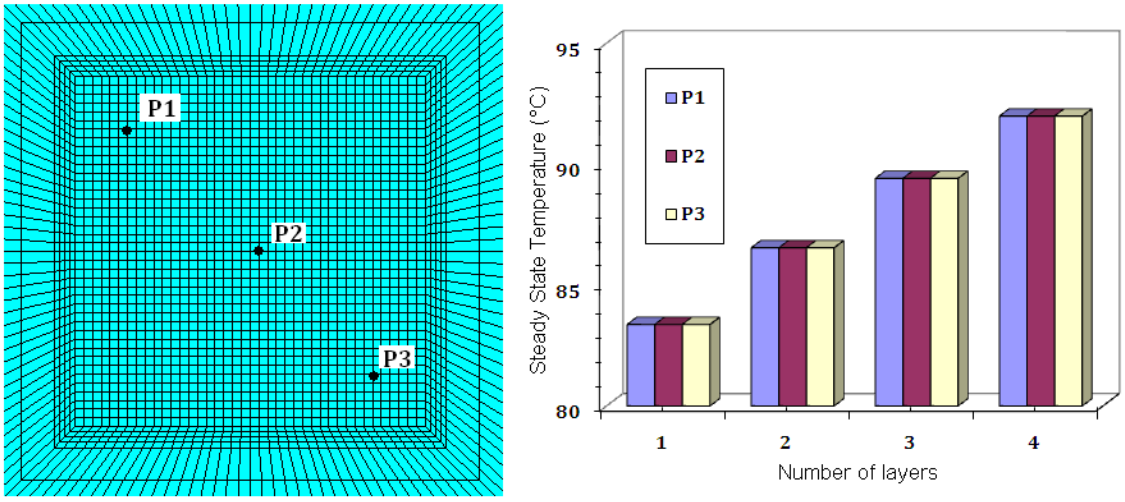

Fig. 6.8: Variation of platform steady state temperature with layer addition

The results for the nodal positions suggest a small but consistent temperature rise in the steady state temperature of 3°C after recoating as the number of layers increases. The steady and uniform rise in temperature in the system will be more significant for larger parts where the amount of laser heat input is extremely high.

6.2.5 Effect of Convective Heat Transfer Coefficient

It was highlighted in Chapter 2 that the convective heat transfer coefficient governs the convection heat losses at the surface during laser melting. It is therefore important to understand the effect of the convective coefficient on the temperature distribution on the surface layer. Two convective coefficients are used here: (i) h = 5 W/m^{2}K, and (ii) h = 20 W/m^{2}K, which correspond to the limits given by Pope (1997) at room temperature. An intentional horizontal spacing of 50 µm has been added to enable distinction.

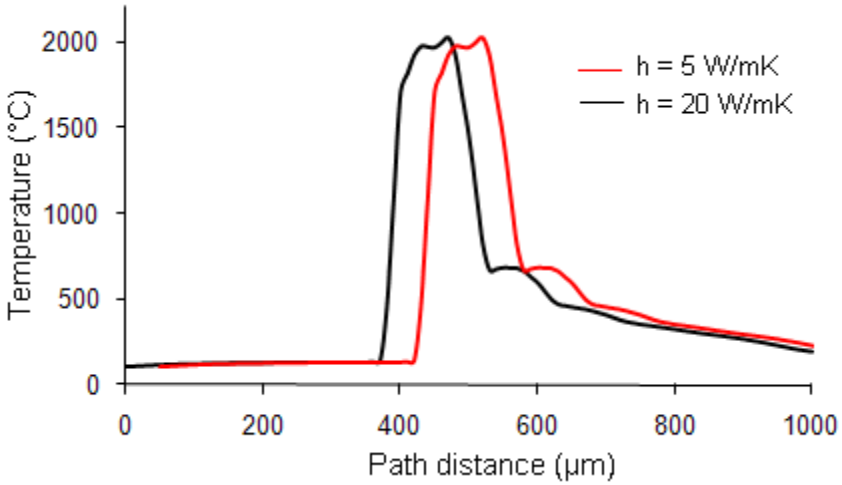

Fig. 6.9: Path temperature profiles (at t = 4.58 ms)

It can be seen that the temperature-path variations for both convective coefficient cases are similar, suggesting that the observed high cooling rates are predominantly due to the heat exchange between the irradiated region and the surrounding solid material than the exchange that occurs with the inert environment. This concurs with the statement by Badrossamay and Childs (2007) that the major source of heat loss through the powder bed is by conduction and contributions by convection and radiation are so small they can be neglected without any loss of accuracy in the numerical model.

6.3 Stress Analysis in Laser Heating of the Base Platform

In some industrial applications like laser polishing and laser surface hardening; metal surfaces are heated to alter their surface characteristics (Lamikiz *et al*, 2007 and Bailey *et al*, 2009), whereas in others like laser bending, thin sheets of metal are formed to shape by repeatedly scanning defined tracks on the surface (Shi *et al*, 2007 and Zhang *et al*, 2007). In the laser bending process of metal sheets, for example, the thermally induced stresses on the surface determine the sheet curvature produced. This section studies the stress field produced by the raster scanning of the surface of the steel platform used in the control experiment.

6.3.1 Designation of Stress Field Quantities

The various measurement techniques highlighted in Chapter 5 relate the strains to the stresses which in turn can be designated in different ways. The strain gauge method,

regarded as a non-full field technique, determines the stress values at a given location on a component. The principal strain and its direction are determined by the configuration and set up of the gauges. The use of this method in deep-hole drilling can also give the cylindrical components (i.e. radial and tangential components) of the residual stresses at the point of interest. Full field methods, which give the strain distribution over a wider area of the observation, such as Moiré interferometry and use of stress-sensitive coatings give a measure of the principal strains and directions from which the principal stresses are derived. The digital image correlation technique or speckle pattern interferometry measures the strains in three Cartesian coordinate directions (Evans *et al*, 2009).

The directional or spatial stress components at a location combine to give the resultant stress distribution at that location. Previous studies relating to the residual stresses in SLS and LM of metal powders have dealt with the directional stress components. Gan *et al* (2004) and Jiang (2006) in their works designated stress components based on the Cylindrical coordinate system (i.e. axial, radial and tangential components) while Klingbeil *et al* (2002), Dai and Shaw (2001) and Dai and Shaw (2006) based theirs on a Cartesian coordinate system (i.e. *x*, *y*, and *z* components).

The stress field quantities used for this work use the Cartesian coordinate system and are illustrated in Fig. 6.10. They are:

- Longitudinal stress, σ_L : This is the component of the residual stress acting parallel to the direction of the laser scanning path. It is given by the *x*-direction stress component (SX).

- Transverse stress, σ_T : This is the component of the residual stress acting perpendicular to the direction of the laser scanning path. It is given by the *z*-direction stress component (SZ).

- Normal stress, σ_N : This component of the residual stress acts normal to the surface plane (pointing out of the page). It is given by the *y*-direction stress component (SY).

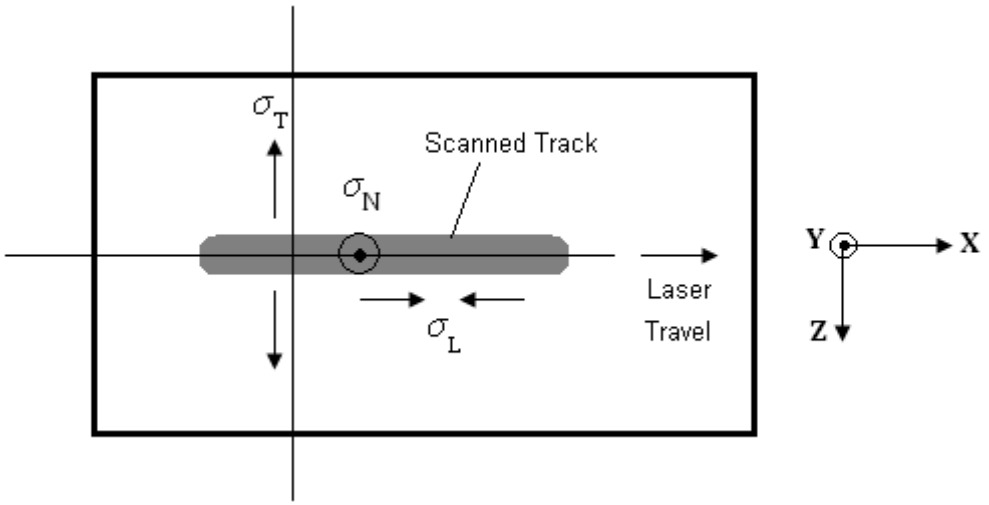

Fig. 6.10: Directional stress components

6.3.2 Stress Distribution Results

Fig. 6.11 shows the evolution of longitudinal stresses on the surface of the platform at various times during scanning. It can be seen that peak compressive thermal stresses appear at the moment of laser heating and rapidly change to tensile stresses the instant the heat source moves away from the irradiated region. The rapid thermal stress change is then accompanied by a slow gradual increase to a steady state residual stress value. The occurrence of high tensile thermal stresses behind the laser and high compressive stresses in front of the laser concurs with the analysis of welding stress fields by Masubuchi (1980).

In Fig. 6.11 it can also be seen that at different instances, the boundaries shared by successive scanned tracks show reduced longitudinal stresses as a result of the reheating of the previously scanned track. Ignoring the edges, it can be seen that the longitudinal stresses are similar for the scanned tracks. This is expected because the scanned tracks have been found to undergo similar thermal cycles.

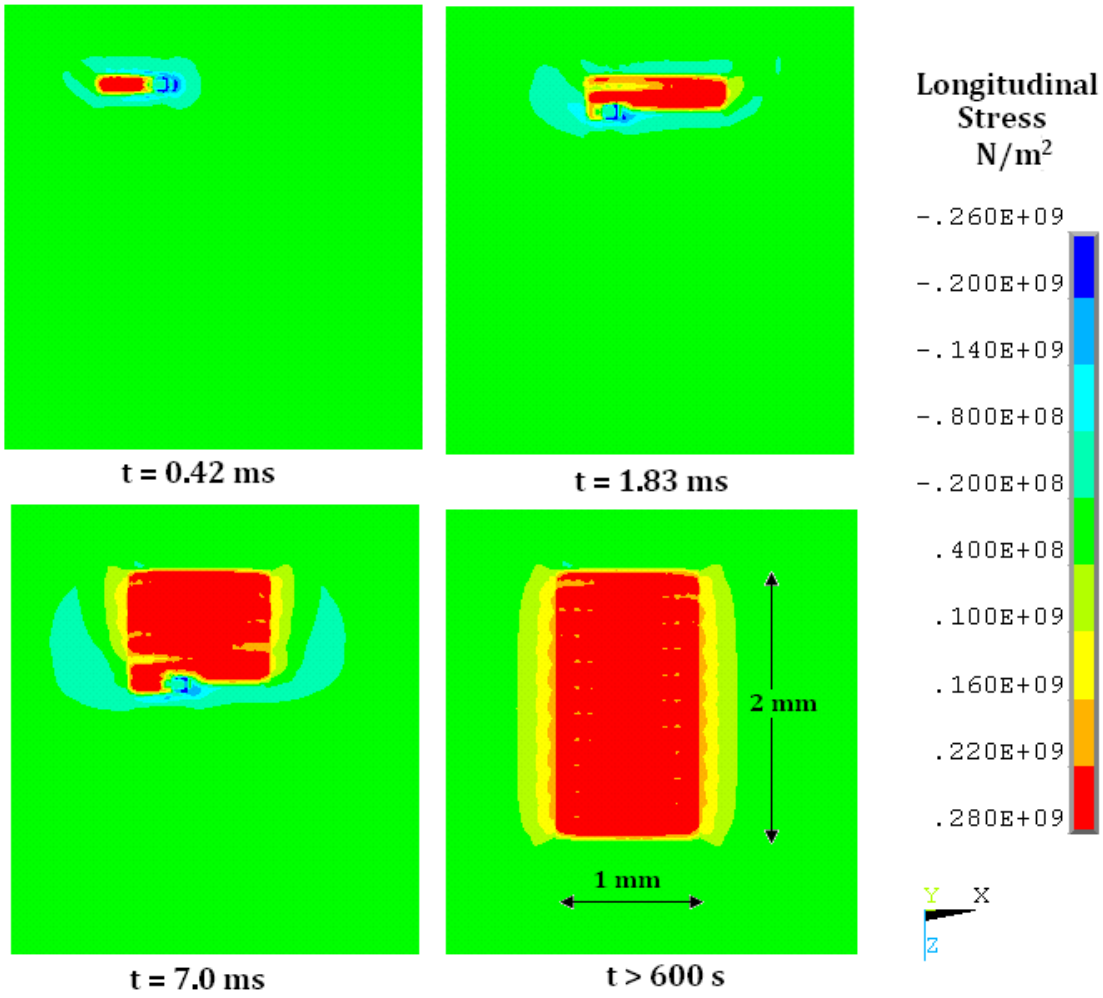

Fig. 6.11: Longitudinal stresses history

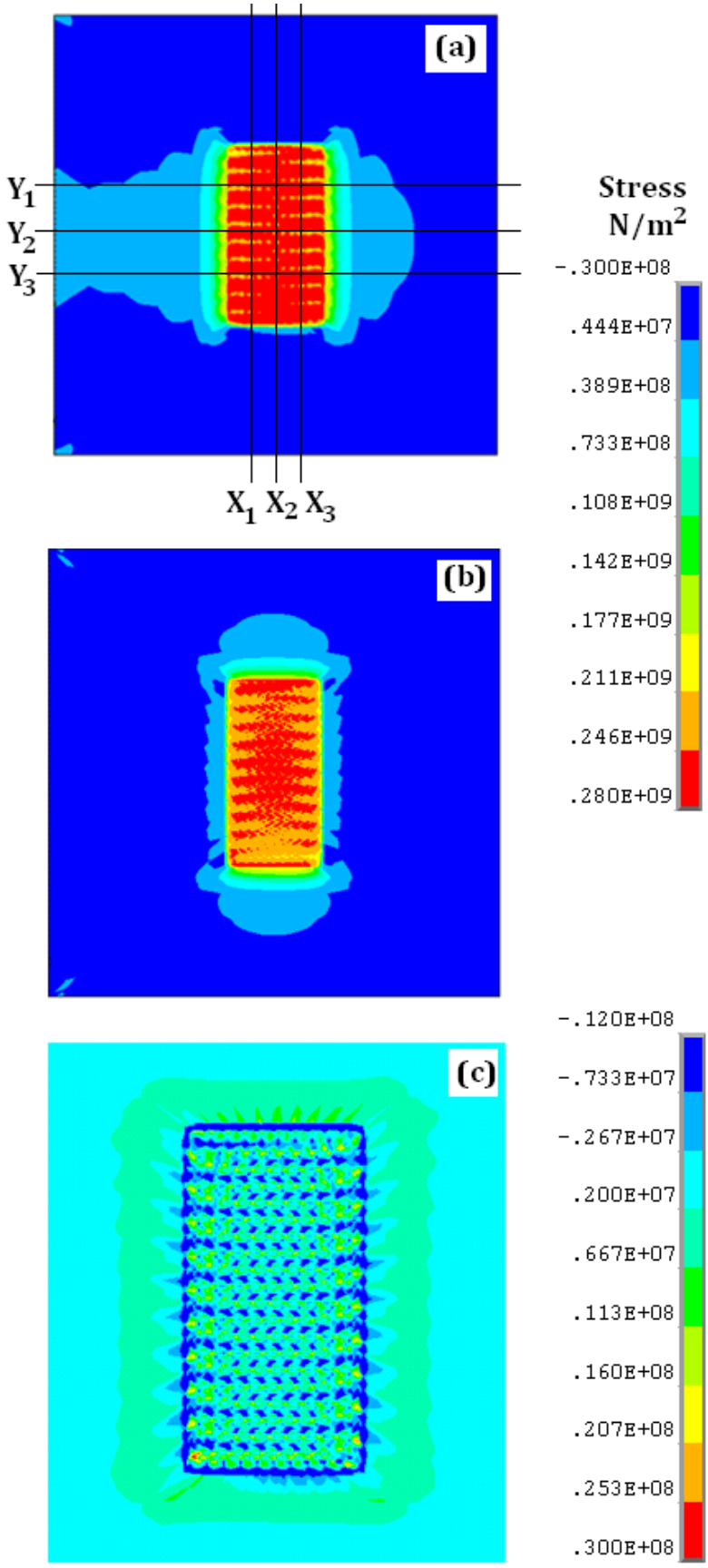

Fig. 6.12: Surface residual stress distribution – (a) longitudinal, (b) transverse, (c) normal

Fig. 6.12 gives the surface stress distribution for the residual stress components. It is evident that the normal stress component is small compared to the longitudinal and transverse stress components. The maximum predicted normal stress is less than 30 MPa as shown in Fig. 6.12(c) compared to 276 MPa and 248 MPa obtained for the peak longitudinal and transverse components respectively. The stress field results show that the longitudinal stresses are greater than the transverse stresses for both strain-hardening model cases. This agrees with the findings of Dong *et al* (2005). In studying the residual stresses in weld repairs, they found that the transverse stresses were always less than the longitudinal stresses.

Fig. 6.13 shows the longitudinal and transverse stress profiles predicted by the kinematic and isotropic hardening models for the centreline paths (Y_2 and X_2). The isotropic model can be seen to predict higher surface stresses than its kinematic hardening counterpart.

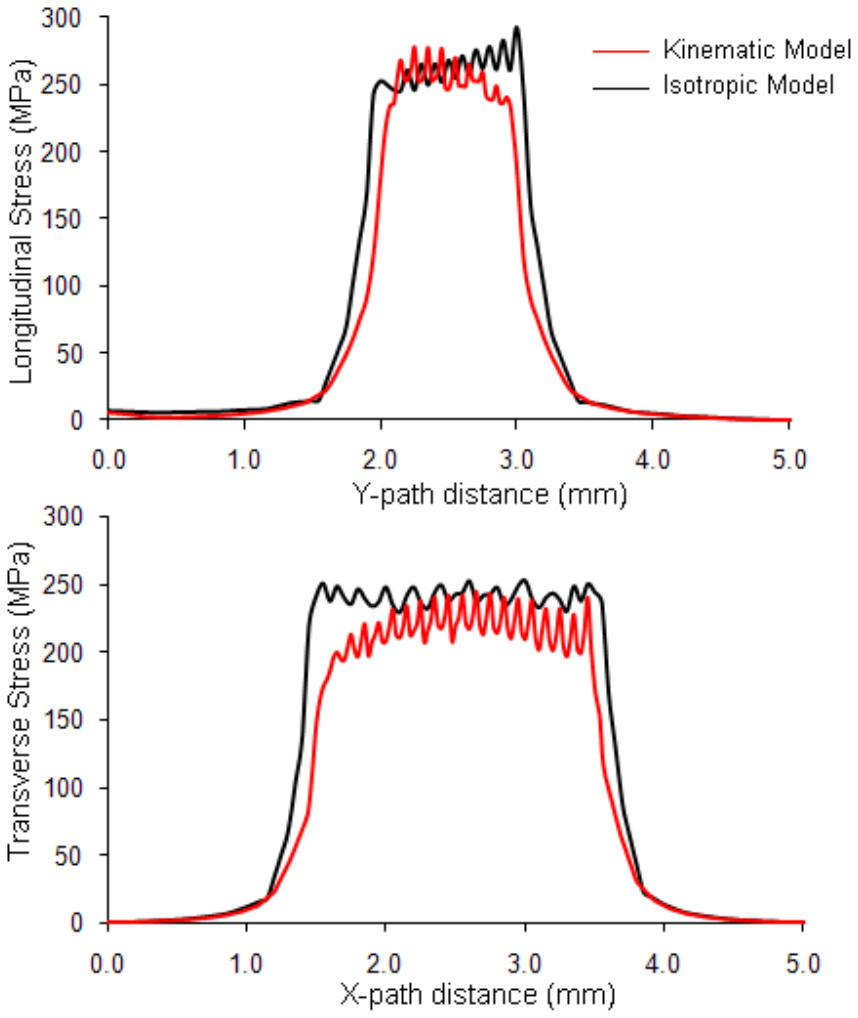

Fig. 6.13: Comparison of stress components predicted by hardening models

The stress profiles across the X and Y paths on the surface of the platform are shown in Fig. 6.14 – the average stresses are calculated from the path nodal stresses bounded by spot region. The kinematic hardening model predicts longitudinal and transverse stresses that hump towards the centre of the paths but taper off at the edges. The isotropic hardening model can be seen to predict longitudinal stresses that increase with path distance whereas the predicted transverse stresses remain fairly constant across the paths.

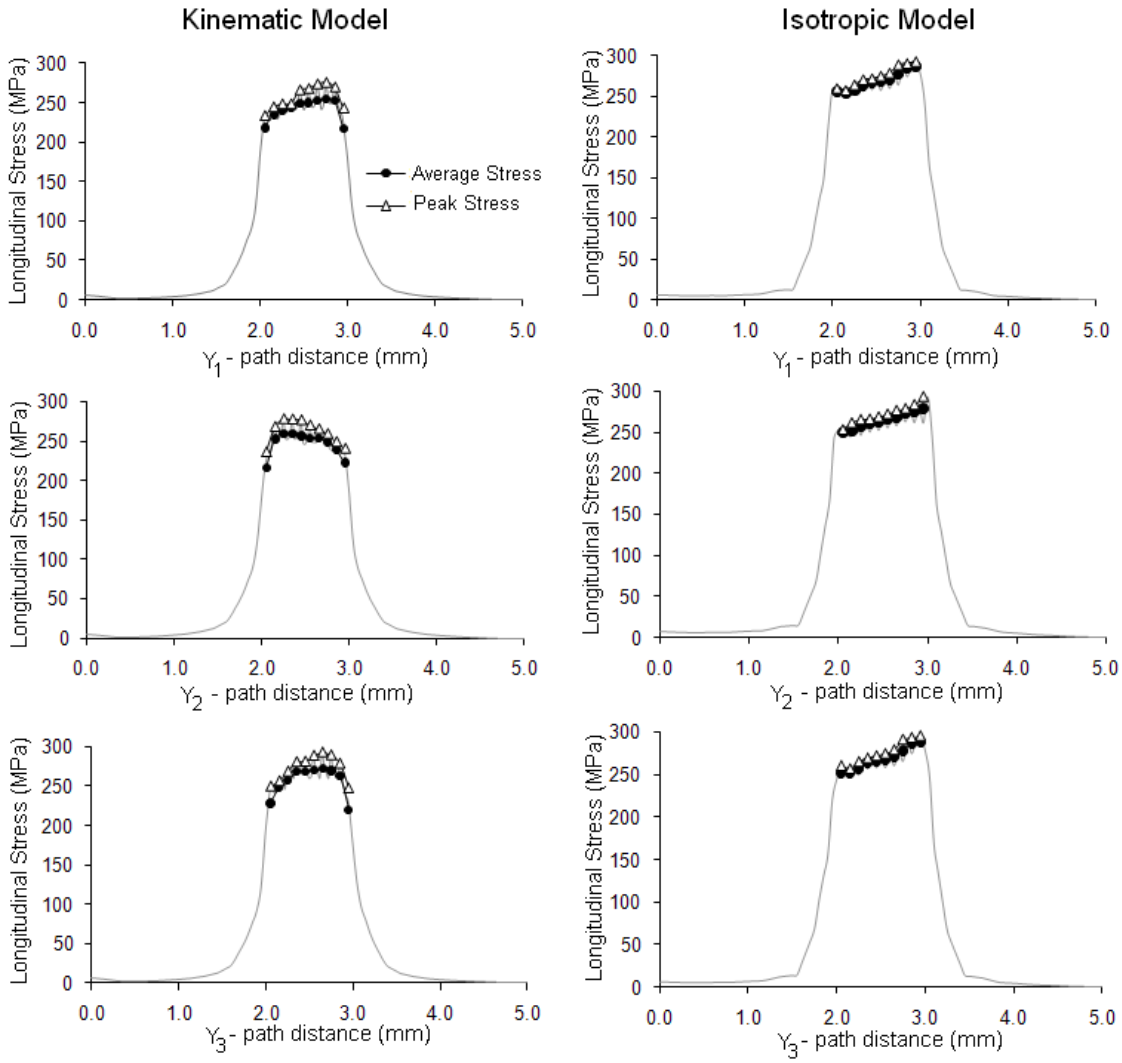

Fig. 6.14: Longitudinal residual stress profiles

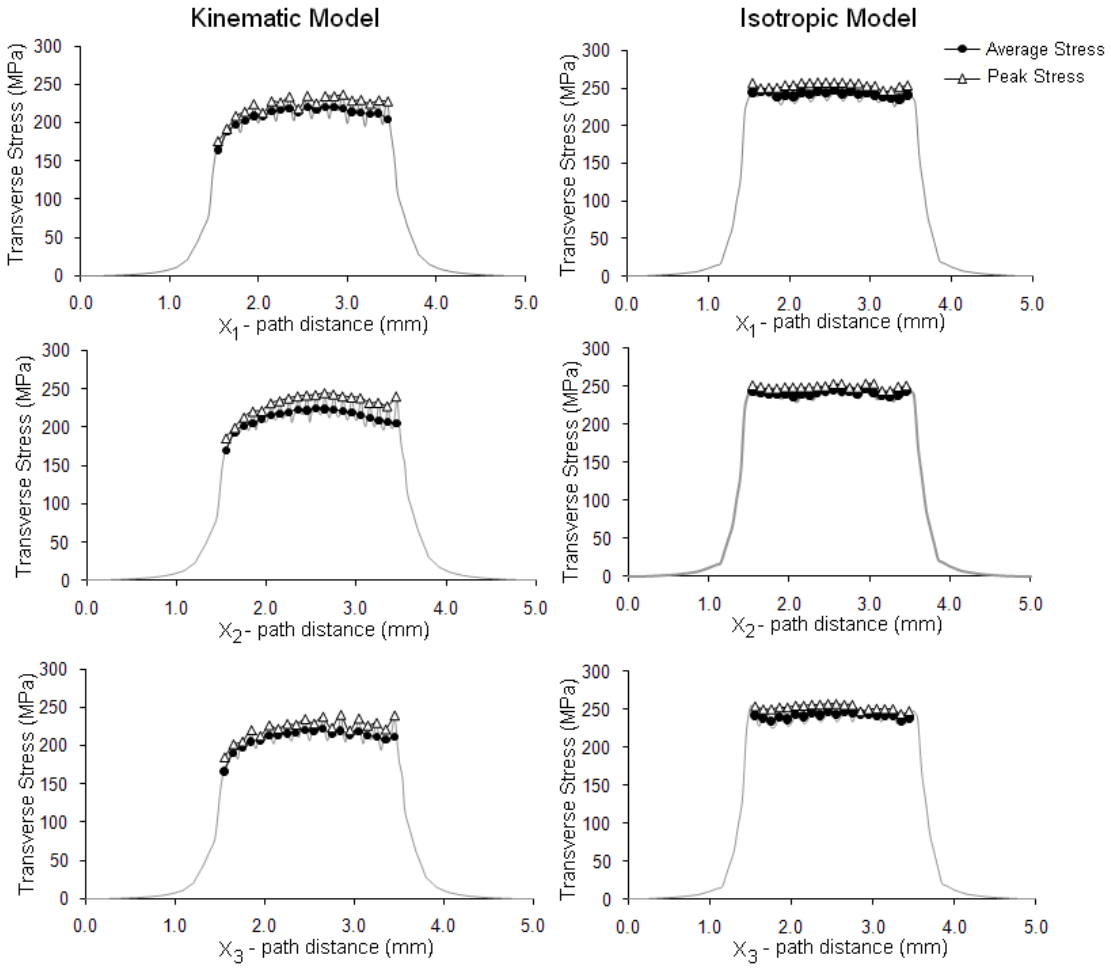

Fig. 6.15: Transverse residual stress profiles

The stress profiles across the surface of the platform are similar for the three paths for each strain hardening model case. A steep stress gradient across the heat affected zone around the scanned region can be observed for both stress components in all cases. For both the longitudinal and transverse cases, the stress fields disappear a short distance (0.5 mm) away from the scanned region suggesting that the selected part dimensions do not induce near field effects. Ignoring the edges in the scanned region, it can be seen that the tracks experience very similar residual stress distributions. Table 6.3 gives a summary of the average stresses and standard deviations across the paths. The standard deviations are less than 10% of the mean value, suggesting a reasonable precision about the mean stress. The average longitudinal stress ($0.97\sigma_y$) and transverse stresses across the paths predicted by the kinematic hardening model are below the yield strength of the steel material while the average longitudinal stress ($1.05\sigma_y$) predicted by the isotropic hardening model is higher than the yield strength. The average longitudinal stress for

the platform surface predicted by the isotropic model is 11% higher than that predicted by the kinematic model.

Table 6.3: Average surface stresses – base platform

Path Designation	Kinematic Hardening Model				Isotropic Hardening model			
	Longitudinal Stress (MPa)		Transverse Stress (MPa)		Longitudinal Stress (MPa)		Transverse Stress (MPa)	
	$\overline{x}$	σ	$\overline{x}$	σ	$\overline{x}$	σ	$\overline{x}$	σ
1	241.7	13.8	209.3	13.4	268.4	11.5	243.3	3.3
2	246.3	15.4	213.0	13.1	264.4	9.8	251.9	9.5
3	256.6	18.6	209.9	12.9	268.5	13.1	248.6	6.9

6.3.3 Stress-Depth Variation

The stress-depth distribution reveals some important features associated with the laser heating of platform material. Fig. 6.16(a) shows a sectional view through the middle of the platform of the longitudinal stresses with depth of the platform. It can be seen that the residual tensile stresses which exist at the surface transform to compressive stresses with depth of platform. The tensile stresses are found to be limited by the yield and flow stresses of the steel material at room temperature (Region 1). As the depth increases, the observed tensile stresses decrease in magnitude until they become compressive after a certain depth (Region 2) as seen in Fig. 6.16(b). The stress behaviour with depth shows similar variation for both material hardening models. The compressive stresses are reaction stresses which are generated to resist the tensile stresses generated by the contracting material at the surface vicinity. Due to the method of constraint used in this work, the platform is free to deform about the fixed edge. As a result, secondary tensile stresses are seen to emerge beyond the compressive stress region towards the bottom of the plate purely due to the bending of the platform (Region 3).

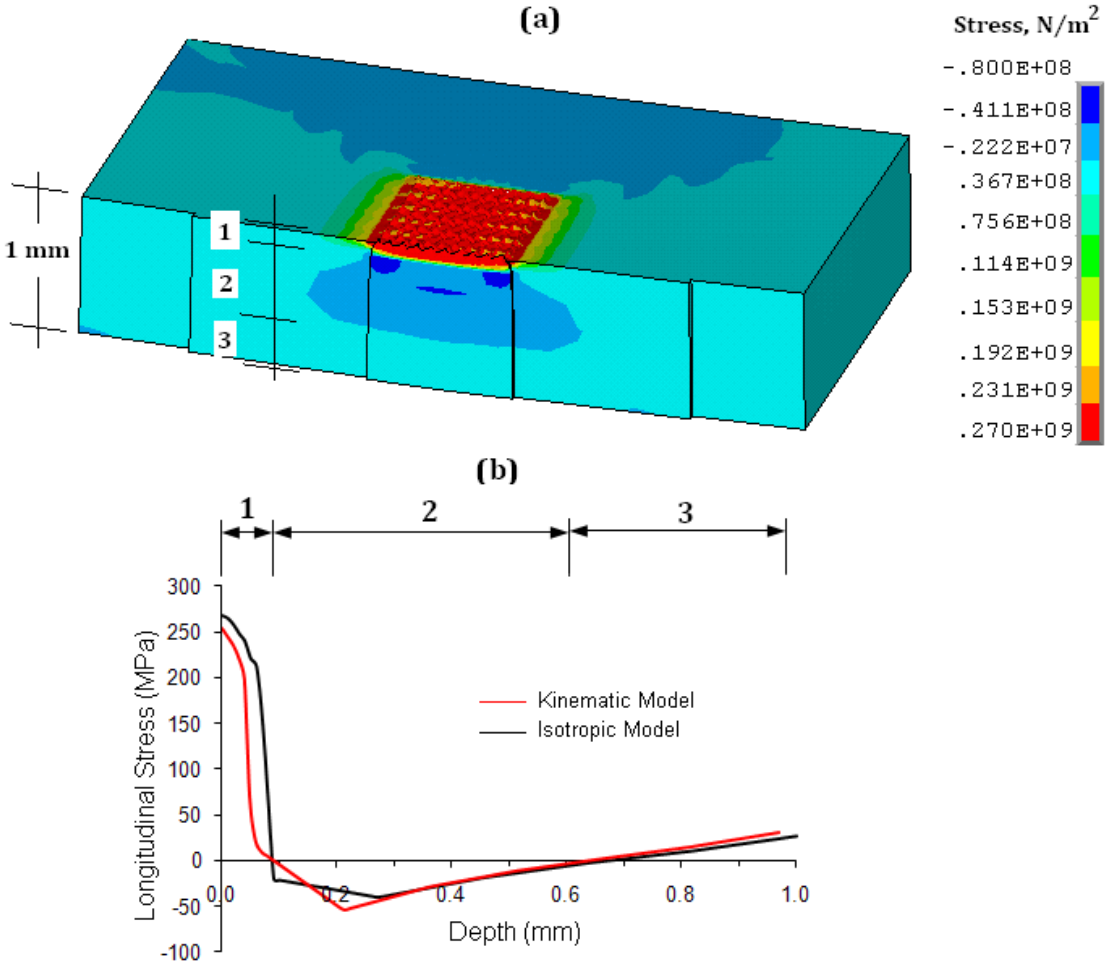

Fig. 6.16: (a) Longitudinal stress distribution, (b) Stress-depth profile

6.3.4 Laser Bending of Platform

The material at the surface of the platform thermally expands during heating, and the expansion at the top surface is greater than that of the underlying material. Therefore, during cooling, the top surface material contracts pulling surrounding material causing the platform to bend towards the laser scanned region (Shi *et al*, 2007). The applicability of the numerical model as a laser bending prediction tool is considered here. The model platform and scanned region considered here have dimensions 3 mm × 3 mm and 1 mm × 1 mm respectively.

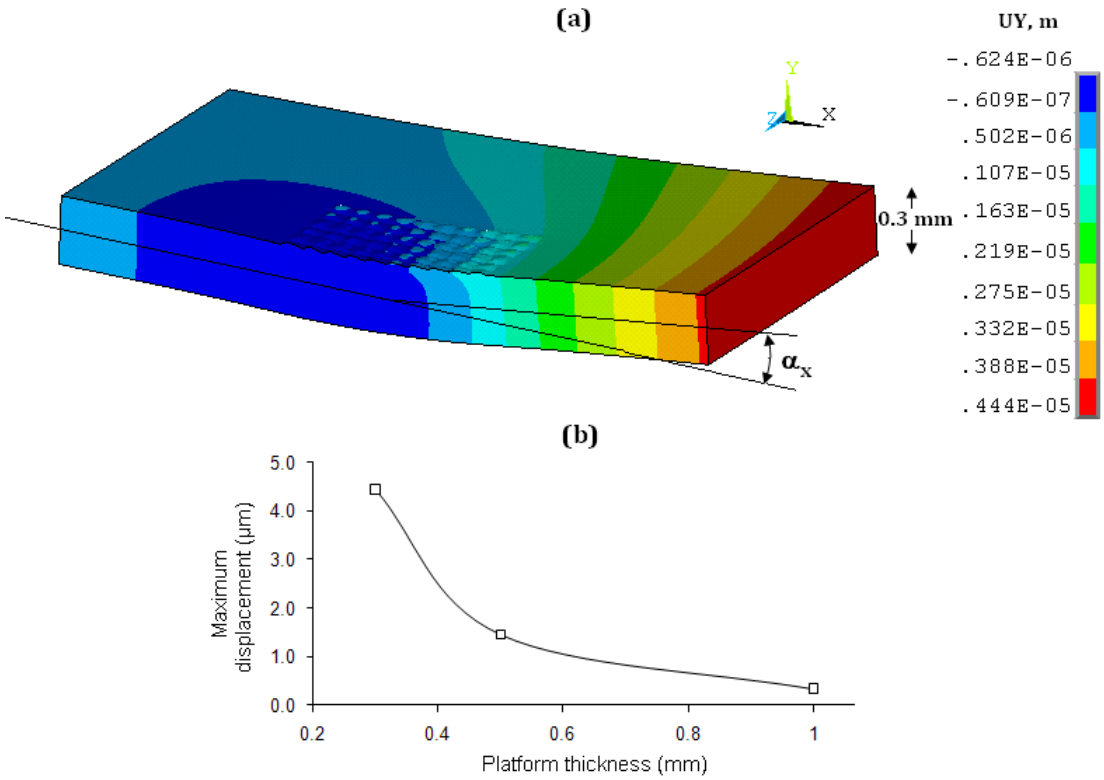

Fig. 6.17: (a) Platform deformation (sectional view), (b) Maximum displacement for various platform thicknesses

The method of constraint causes a bow as shown in Fig. 6.17(a). The bend angle and bend radius can be estimated from the plate dimensions and maximum predicted displacement. A variable study of the influence of the platform thickness on the displacement characteristics of the platform shown in Fig. 6.17(b) indicates the variation of the maximum predicted displacement with thickness. It can be seen that for the given set of laser processing parameters, the platform displacement is dependent on the thickness.

Although the raster method is not the preferred scanning pattern in laser bending applications, this study demonstrates the capability of the numerical model for use in laser bending simulations.

6.4 Stress Analysis in the Laser Melting of Ti64 Powder

It has been found from the laser microscopy experiments that the addition and subsequent scanning of the Ti64 powder layers caused an increase in the deformation of

the platform. The stress field associated with the spreading and scanning of two layers of Ti64 powder is analysed in this section.

6.4.1 Transient Stress Distribution

The longitudinal stress distributions at various times of the laser melted powder material are shown in Fig. 6.18. In order to enhance clarity and prevent contamination of the results, only the elements representing regions that have been scanned at the process times in consideration (i.e. active elements) are shown. It should be recalled that the layer elements were deactivated at the start of the structural simulation and activated at the times they were scanned.

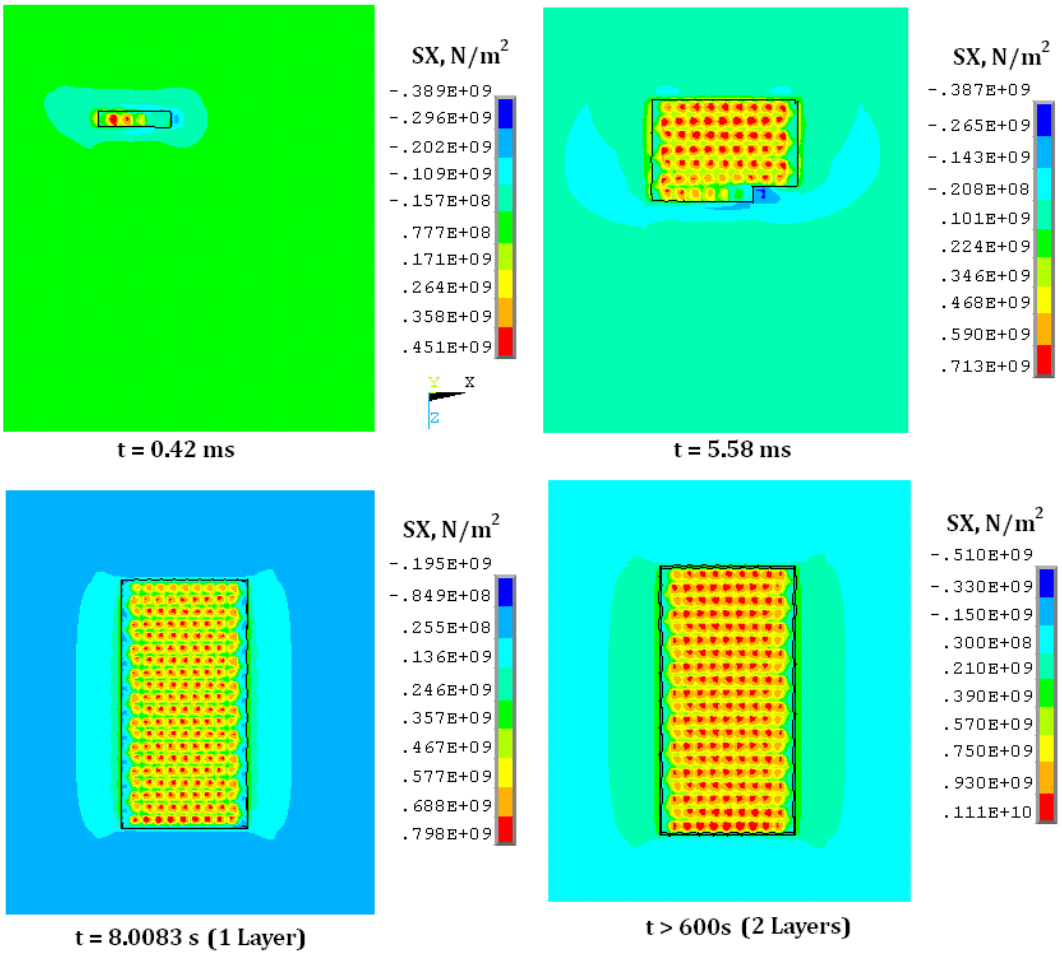

Fig. 6.18: Longitudinal stress distribution at various times

Laser melting of the first added Ti64 powder layer onto the base platform can be seen to induce compressive stresses on the surface of the platform. It is reasonable to assume

that the addition of the second layer would introduce compressive stresses on the first Ti64 layer underneath, but because the surface of the first layer is in tension after recoating, the net effect is a reduction of the stresses at the top of the first layer. Alteration of the stress state of the first layer subsequently changes the stress distribution in the platform. This shows that the sequential addition and scanning of the powder layers affect the stress distributions of the underlying materials.

Numerical simulation studies by Dai and Shaw (2001) and Dai and Shaw (2002) on the thermal and residual stress in the DMLS of nickel powder ignored the contribution of the base platform. The base platform acting as a heat sink contributes to the transient thermal and residual stress fields and its importance is evidenced by this study.

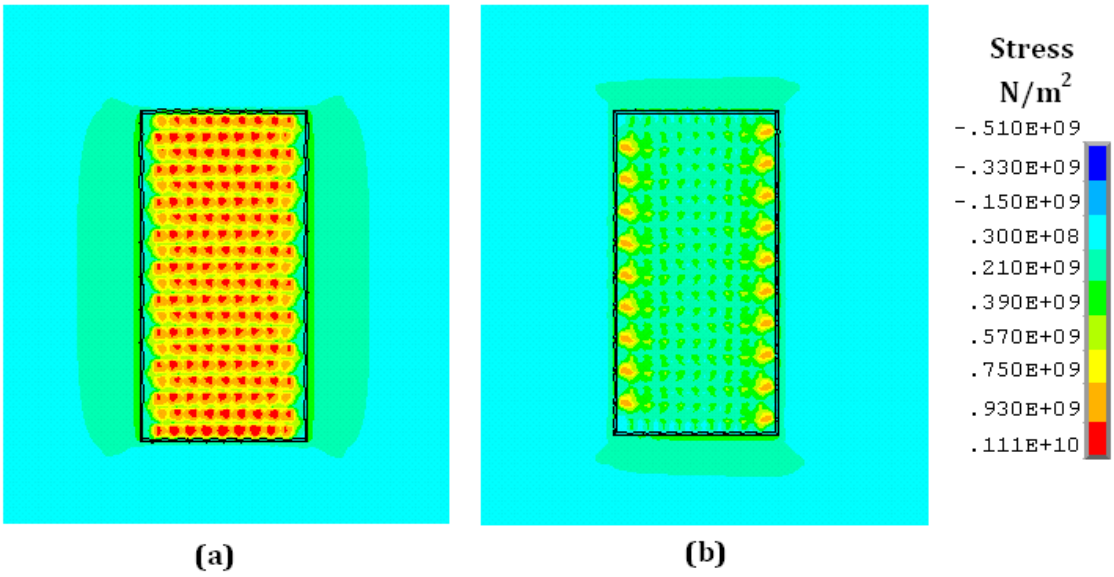

Fig. 6.19: Residual Stress components – (a) longitudinal, (b) transverse

The step-wise movement of the laser heat source results in the formation of bell-shaped mounds in the scanned region as opposed to a smooth track of solidified material. This in itself introduces waviness in the nodal stress distribution as seen in Fig. 6.19, the contour plots show peak stresses at the centre of the spot region which taper-off towards the edge. These should not be confused with the pitting on the surface or the creased tracks observed in the experiments, which were attributed to fluid phenomena.

The temperature histories for the irradiated regions, apart from edge locations, were found to be similar as observed in Section 6.2.1. Due to heat lost through conduction to the surrounding powder, predicted temperatures in regions close to the surrounding

powders were less than those within the scanned region of the layer. This difference in the thermal history of points around the edges and the absence of edge restraints apart from consolidation with the underlying material accounts for the observed reduced longitudinal stresses. The longitudinal stresses are reduced on either side of the scanned region while the opposite is observed for the transverse distribution. The transverse stresses can be seen to be greatest at the ends of the raster, as a result of the directional change in movement of the laser heat source. The change in direction can be likened to a very short track where the stresses parallel to the scan direction (i.e. longitudinal stresses) are greater than the stresses in the perpendicular direction. However, ignoring edge effects, the longitudinal and transverse stress distributions are similar for the scanned tracks supporting once again that the different tracks in the layer experience very similar thermal and stress cycles..

Fig. 6.20 shows the longitudinal evolution at the centre point of the first scanned layer. The effects of scanning an adjacent track the same point but on a successive layer are evident as secondary dips in the transient stress plots.

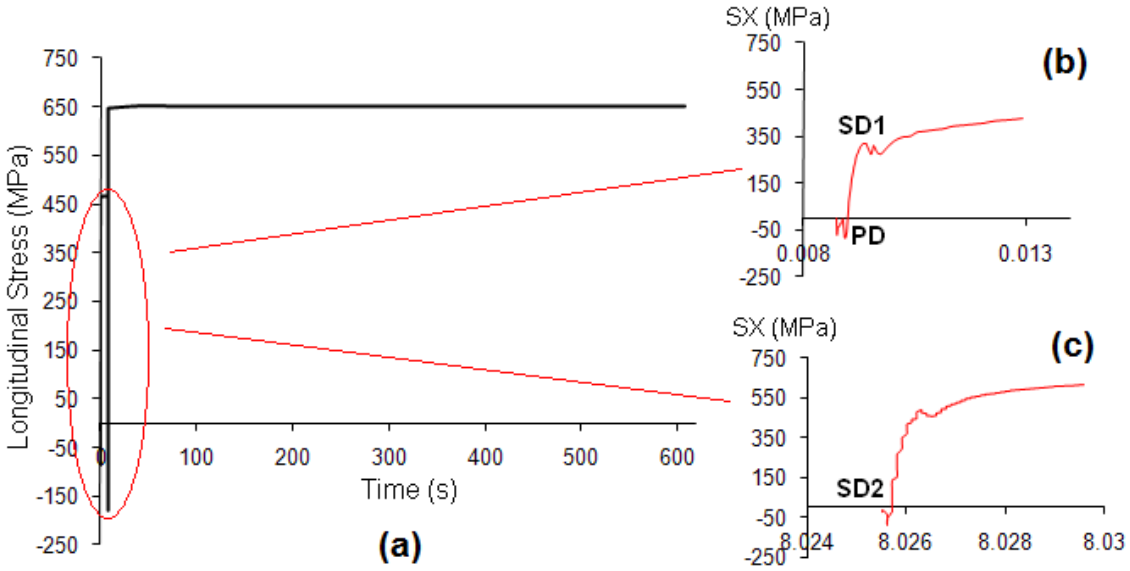

Fig. 6.20: (a) Longitudinal stress history, (b) first secondary dip, (c) Second secondary dip

The results show that the transient stresses transform to residual stresses within a few milliseconds following laser melting. The initial primary dip (PD) seen in Fig. 6.20(b) corresponds to the compressive stresses induced during heat application of the actual spot location, while the secondary dips (SD1 and SD2) represent stress reductions as a

result of reheating when the laser scans the adjacent track and reaches the same location on the next layer.

Fig. 6.20(b) and (c) also show a rapid attainment of a steady state stress value, which suggests that the relatively long recoating time does not play a significant role in the stress evolution. The speed of recoating can therefore be increased to speed up the process. However, other factors such as effective spread and packing of the powder material would need to be considered.

6.4.2 Residual Stress Distribution

Fig. 6.21 and Fig. 6.22 show the longitudinal and transverse stress profiles for the surface of the platform, first layer and second layer.

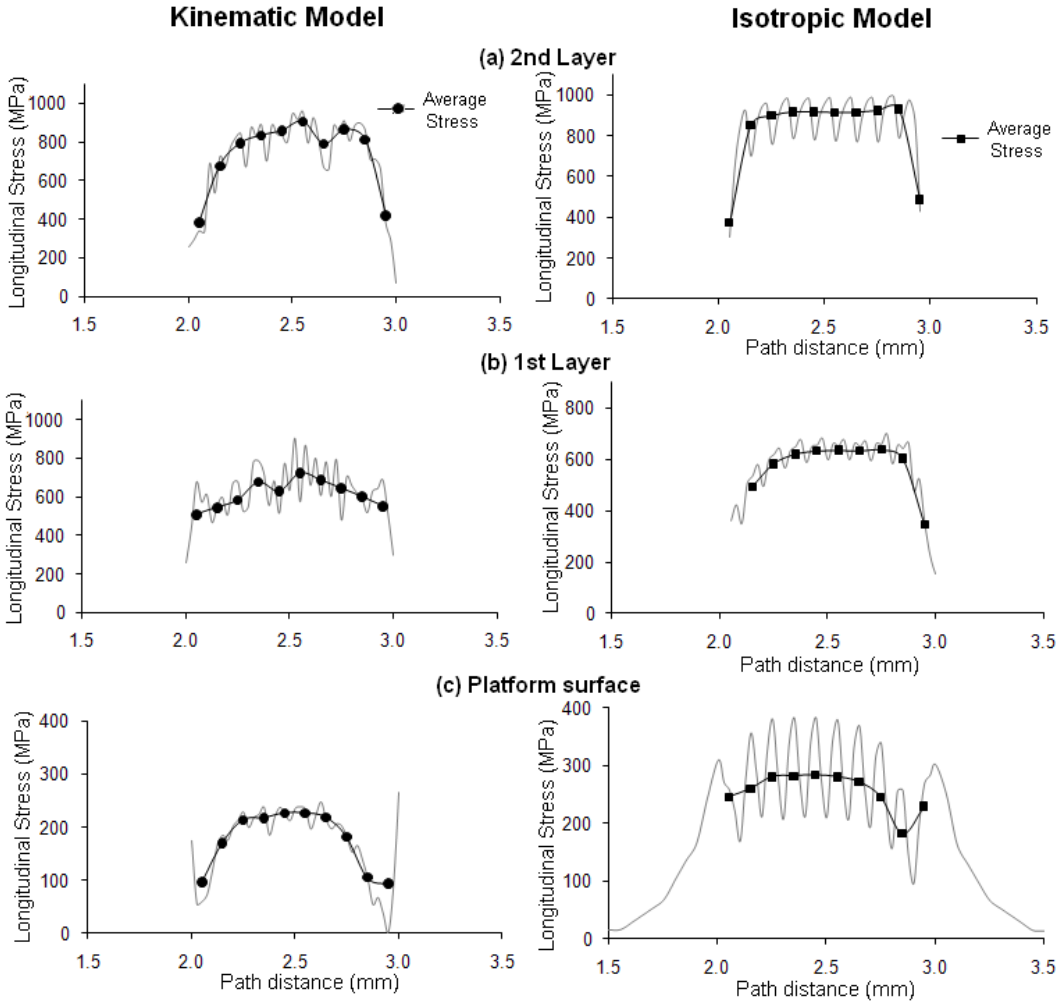

Fig. 6.21: Longitudinal stresses along paths

It can be seen in Fig. 6.21 that the longitudinal stresses on either end of each path for the added layers (corresponding to the free edges) are much lower than in the middle. This is expected because the edges of the layers are free of any form of mechanical constraint since they are surrounded by loose powder. The tapering off in tensile stresses on either path end is also observed in the transverse direction as shown in Fig. 6.22.

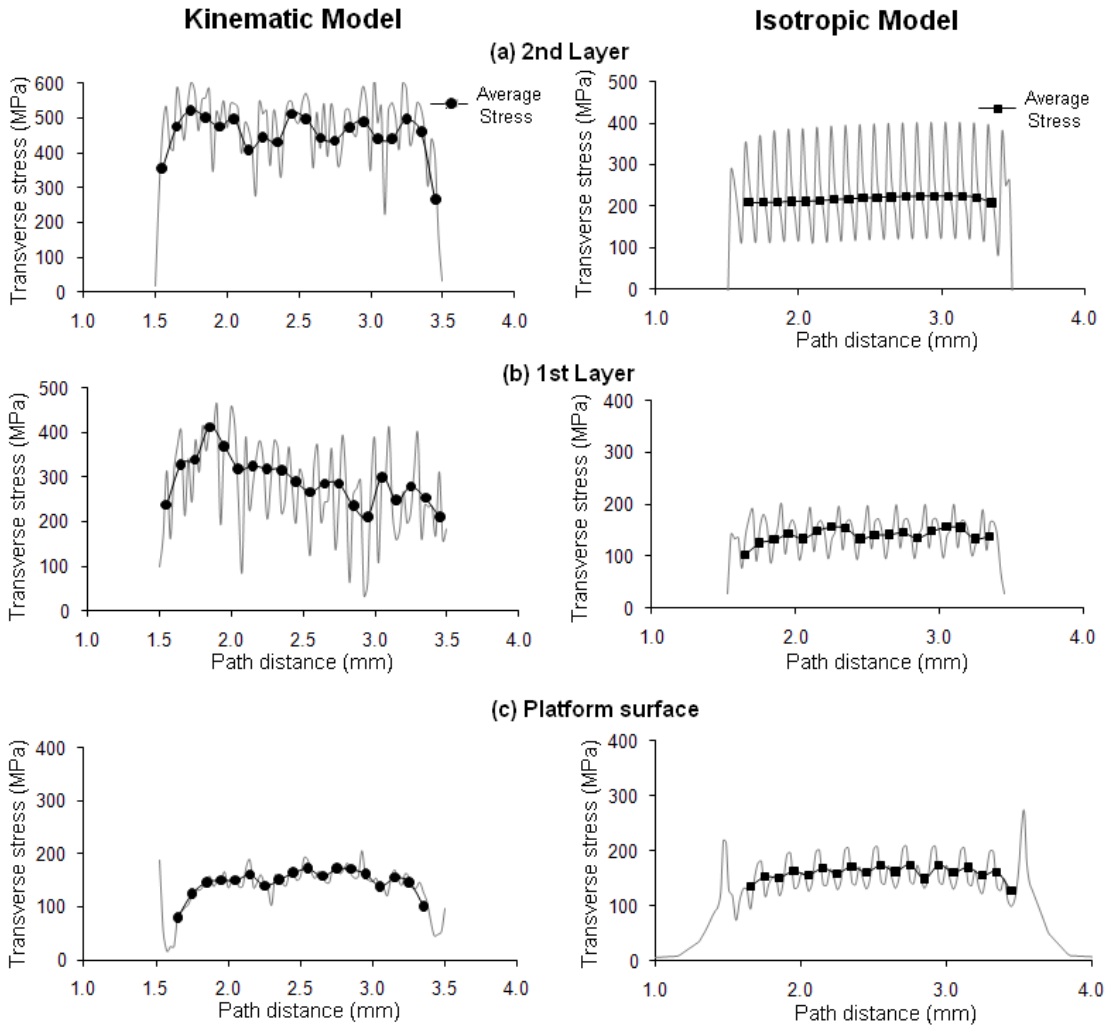

Fig. 6.22: Transverse stresses along paths

The waviness observed in the stress field profiles are representative of the bell-shaped tracks described in the development of the numerical model in Chapter 4. The peak stresses can be seen to occur at the centre of each spot region. Also, similar to the direct surface heating case, the longitudinal stresses are greater than the transverse stresses. The average residual stress components are summarised in Table 6.4. The results here show that the stresses on the surface of the platform are limited by the yield and flow

stresses of the steel platform. Through the first layer, the stress gradient increases in the Ti64 solid material, but is limited by the mismatch in structural properties (i.e. stiffness and yield strength) between the Ti64 and steel material. For the second layer, there is an even greater increase in the average longitudinal stress, tending towards the yield strength of Ti64 (i.e. 1090 MPa). This is because the second layer is shielded from the steel base material by the first Ti64 layer resulting in a less severe mismatch than that observed in the first layer.

Table 6.4: Average surface stresses – multiple Ti64 layers

Layer Number	Kinematic Hardening Model				Isotropic Hardening model			
	Longitudinal Stress (MPa)		Transverse Stress (MPa)		Longitudinal Stress (MPa)		Transverse Stress (MPa)	
	$\overline{x}$	σ	$\overline{x}$	σ	$\overline{x}$	σ	$\overline{x}$	σ
2	783.7	69.0	453.4	59.7	908.2	24.9	217.1	16.3
1	614.3	59.6	291.6	51.6	620.8	49.5	140.8	16.3
0	175.0	41.5	140.4	32.2	256.0	34.3	159.1	16.0

It can be seen from Table 6.4 that both material strain hardening models predicted a increase in the residual stress components with increasing layer numbers. The isotropic hardening model predicted a higher average longitudinal stresses for the Ti64 layers than the kinematic model while the reverse can be observed with the transverse stresses. The average longitudinal stress for the second layer predicted by the isotropic model is 15.8% higher than that predicted by the kinematic model. Comparison with the 11% difference obtained in the direct laser heating of the platform elucidates the cumulative effect of the material strain hardening consideration on the complexity of the problem.

6.4.3 Stress Distribution with Depth

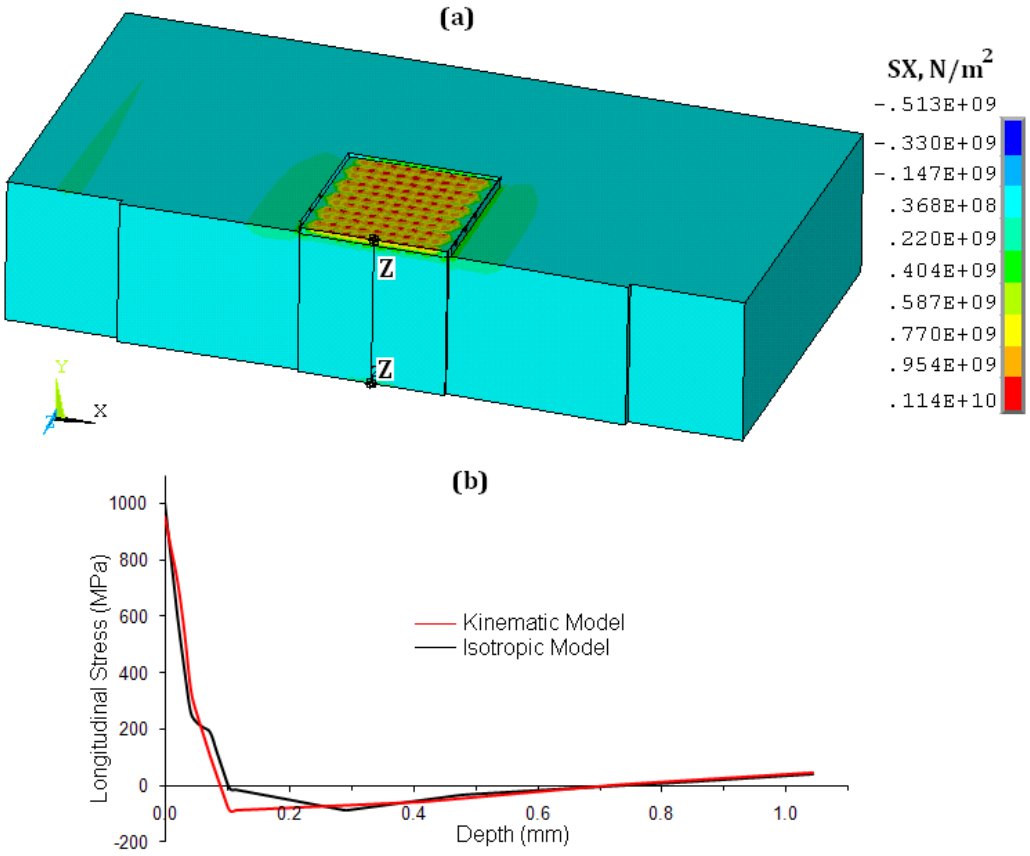

Fig. 6.23: (a) Stress variation, (b) Stress-depth variation

Fig. 6.23(a) shows the longitudinal stress distribution through a section of the platform. Similar to the direct laser heating of the platform case, it can be seen that the residual stresses at the surface are tensile in nature. The stress-depth profile for a path *Z*-*Z* through the middle of the part is given in Fig. 6.23(b). The tensile stresses decrease with depth before transforming to compressive stresses in the base platform. The induced compressive stresses then resist the contraction in the Ti64 layers, before finally ending up as tensile stresses further deep into the platform.

The existence of tensile stress regions beneath the compressive stress zone was also been observed by Dai and Shaw (2004) in their study of the laser melting of nickel and dental porcelain. The temperature gradient dictates the high compressive stresses near the high temperature interface which has a higher tendency to expand than the rest of the undisturbed material (i.e. bending). As a result, corresponding tensile stresses were generated away from the interface.

6.4.4 Platform Deformation

Fig. 6.24 shows the displacement contour plot for the solidified layers and the base platform. The maximum displacement as expected occurs at the free end of the platform. Initial analysis has shown the existence of a concave depression in the scanned region.

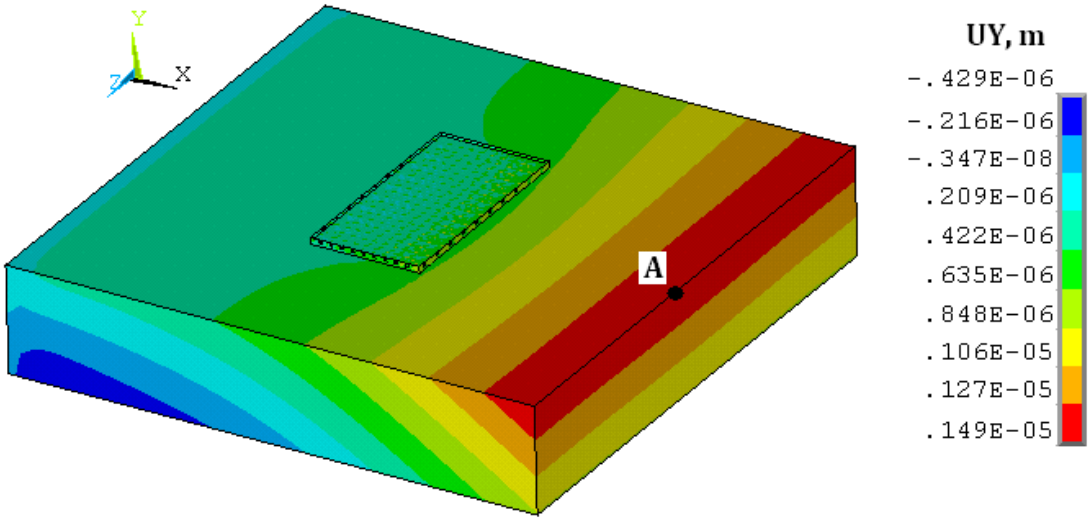

Fig. 6.24: Platform displacement plot

The displacement history of the point *A* following laser melting and cooling of the Ti64 layers is shown in Fig. 6.25. Close observation of transient platform displacement in Fig. 6.25(a) reveals two dips in the displacement at point *A* corresponding to the addition and laser scanning of the two layers similar to that observed in the stress history in Fig. 6.20. The initial negative displacement at *A* in Fig. 6.25(b) is due to the dead weights of the platform as well as the contribution of the initial convex curvature caused by the greater expansion of the platform surface than the bottom surface during laser heating. Once the heat source is removed, the surface expansion rapidly changes to contraction and the reverse effect occurs – increasing the edge vertical displacement of the platform.

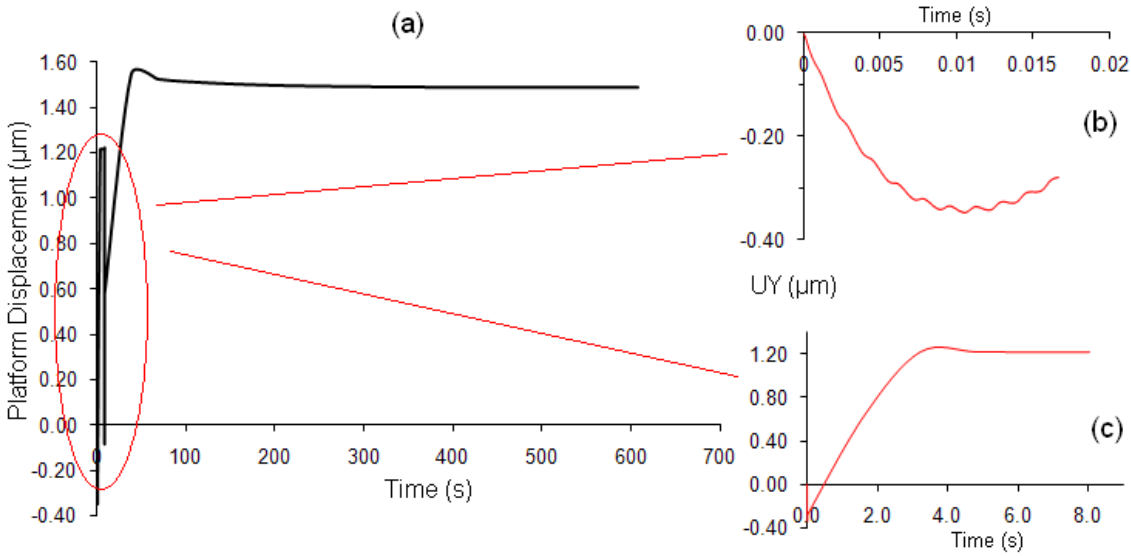

Fig. 6.25: (a) Displacement of point *A* with time, (b) Heating of first layer, (c) Cooling during recoating

The rapid rise in the displacement at *A* during the recoating phase is shown in Fig. 6.25(c). A similar trend is also observed for the second layer addition. The steep rise in the displacement with time stabilises soon after the laser heat source is removed, following which further cooling results in no additional deformation. In Fig. 6.25, the difference between the peak displacement and the steady state displacement is 1.6%, suggesting that the deformation of the plate is highly dependent on the changes in the elastic modulus during the cooling of the heated layer. This agrees with the findings of Dai and Shaw (2002) in their study of the layer displacements in the numerical simulation of the laser solid free-forming of nickel for different scanning strategies. They concluded that residual stresses have very small effects on the distortion of the part compared to the transient thermal stresses.

The predicted maximum displacements for the addition of the first and second layers are 1.22 µm and 1.49 µm respectively, indicating that the displacement of the platform increased with addition of Ti64 layers.

6.5 Summary of Numerical Model Analysis

In this chapter, analysis of the temperature and stress fields during the laser melting of Ti64 powder using the numerical model have been presented. Limitations and

difficulties experienced in previous numerical models and a number of key material and process features were considered.

The numerical model has been used to predict the temperature field for the laser melting of multiple Ti64 layers on a steel platform. The analysis showed that three-dimensional temperature field predictions are an improvement over the idealisations of two-dimensional models.

Although in the laser melting process, fluid effects are known to exist and were not accounted for, the model has proved to be useful for both temperature and stress field predictions agreeing with findings made by other researchers in the subject area.

The applicability of the numerical model for use in the stress field prediction of laser melting of metal powders has been demonstrated as well as its potential use in studying laser heating characteristics of metal surfaces for applications like laser bending.

The results of the model analyses positively add to the understanding of the thermal gradients, thermal stresses and residual stresses that are developed during the laser melting of metal powders.

The main findings from the analyses can be summarised as follows:

- The scanned tracks experienced similar temperature cycles, thermal stresses and residual stress distributions with the exception of the edge locations.
- The addition and subsequent scanning of a Ti64 powder layer altered the temperature and stress distribution in the scanned layer and the underlying material.
- The surrounding powder insulated the scanned region, while the surrounding material act as a heat sink, conducting a greater fraction of heat from the irradiated region than that lost to the inert atmosphere via convection.
- A small but steady increase in the temperature of the system occurred after each layer recoating period.
- The normal stress component of the residual stress was small compared to the longitudinal and transverse components.

- In all cases, the residual stresses are limited by the yield strengths and flow stresses of Ti64 and steel material.

- Edge effects are prominent at the areas where the scanning direction changed. Longitudinal stresses diminished at these locations while the transverse stresses were observed to increase.

- The residual stresses were greatest at the surface of the part. Variation with depth showed that the residual stresses decreased with increasing depth, giving rise to counter-balancing compressive stresses beneath the surface of the platform.

Since the longitudinal and transverse stresses are the higher stress components, the average longitudinal and transverse stresses across the tracks are used as the basis of comparison for the parametric studies in Chapter 7.

7 Parametric Studies in Laser Melting of Metal Powders

7.1 Introduction

Process variables like laser power and scan speed can be adjusted to alter the resulting material properties (density, strength and elasticity) of LM parts. The process and the material variables are also known to influence the magnitude and distribution of residual stresses in the built parts. Previous works that investigated the effects of some of the process variables on the residual stress distribution and their limitations were discussed in Chapter 2. In order to optimise process variables for the minimisation of residual stresses in laser melting, it is important to understand their influence on the residual stress field characteristics. A complete parametric study involving a combination of all the variables would be required to study this, but this would be impractical, therefore, a number of piecemeal parametric studies using the developed three-dimensional numerical model using the kinematic strain hardening formulation are conducted for selected process variables. The response variables for which the effects are investigated include the number of layers, thickness of the base platform, platform material type, raster length, chamber temperature, scan speed and layer thickness.

In each case, the response variable of interest is varied independently while other variables are kept constant at known operating conditions. To maintain consistency in the analysis and discussion of results, the field characteristics of interest that will be used for comparison are:

- Residual stress distribution along centreline paths
- Deformation of the platform
- Stress-depth variation

The studies undertaken in this work were based on a 1 mm × 1 mm Ti64 part built onto a steel platform 3 mm × 3 mm similar to the finite element model in Fig. 6.1. The centreline paths have lengths similar to the dimension of the scanned region (i.e. 1 mm).

7.2 Effect of Addition of Layers

Addition and subsequent scanning of powder layers in laser melting is similar to the weld passes in multi-pass welding, where the number of passes and size of the deposited molten material was found to alter the residual stress state in the weld and base material (Jiang, 2006). Experiments carried out by Shiomi *et al* (2004) were able to measure the strain changes in a build platform when built SLS steel layers were successively milled off. They found that the residual stresses deduced from the measured strains decreased (i.e. stress relief) as more layers were removed from the built part. In an analytical model used by Mercelis and Kruth (2006), they proved that by increasing the number of layers, the residual stresses in the part and the base platform increased in an approximate linear fashion.

This section uses the numerical model to investigate the effect of increasing the number of layers on the stress distribution in the layers and the base platform. The process variables are given in Table 7.1.

Table 7.1: Addition of layers study process parameters

P (W)	v (mm/s)	d (μm)	h_p (μm)	r_L (mm)	t (mm)	T(°C)
195	1200	100	30	1.0	0.3	40

where *P* is the laser power, *v* is the scan speed, *d* is the laser beam diameter, *hp* is the layer thickness, r_L is the raster length, *t* is the platform thickness and *T* is the chamber temperature.

7.2.1 Deformation Results

Fig. 7.1 shows the deformation plot for the one-layer and two-layer parts. The predicted displacement contour plots were similar for both cases with the free end of the platform

experiencing the most deflection. The maximum predicted displacements are given in Table 7.2.

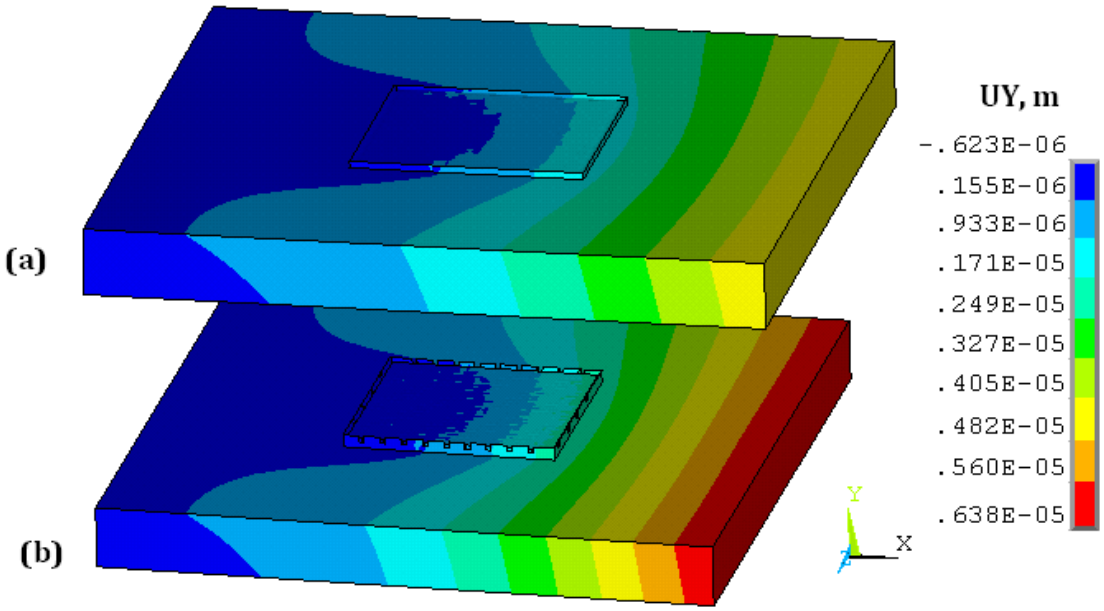

Fig. 7.1: Deformation plot for single layer (a) 1 layer, (b) 2 layers

It can be seen that the edge displacement increased with layer addition. An increase of 35% in the maximum displacement was obtained by the addition of the second Ti64 layer. This suggests that the structural mismatch between the two materials (i.e. solidified Ti64 and steel) accounts for the severity in the displacement for the one-layer part. In the two-layer part case, the mismatch introduced by adding the second layer is less severe, hence the fractional increase in the maximum platform displacement.

7.2.2 Stress Results

Fig. 7.2 shows the longitudinal stress distribution for the one-layer and two-layer parts. In both cases, the distribution patterns were similar and the end effects on the longitudinal stresses are evident. The stress contour plots show an increase in the surface longitudinal stresses with the addition of the second Ti64 layer.

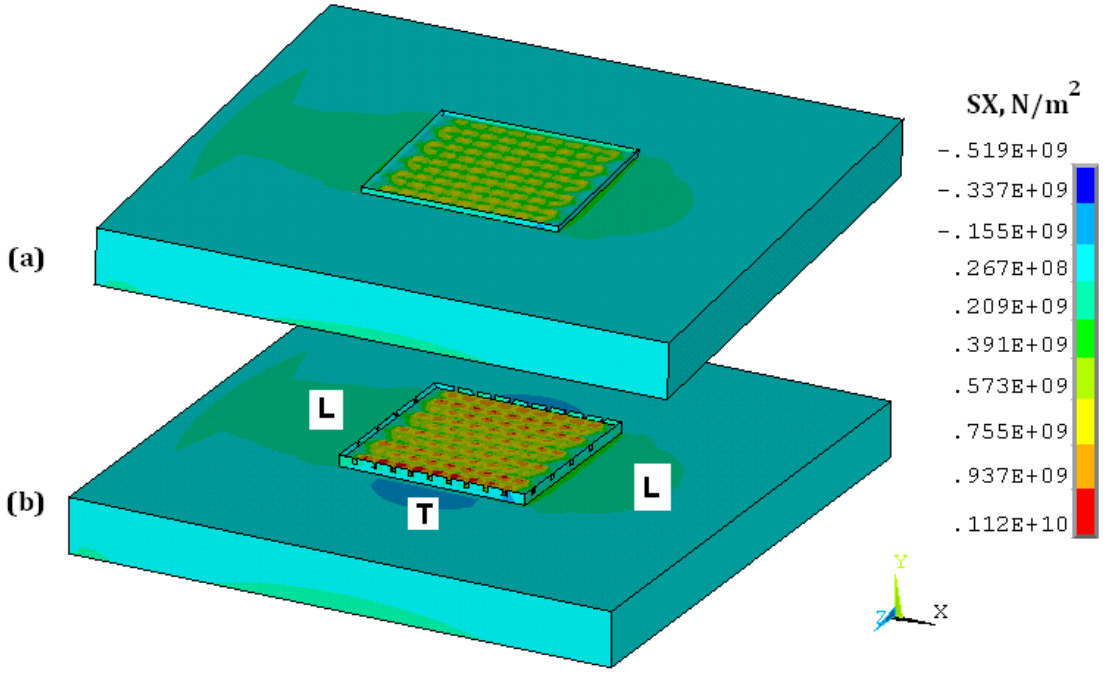

Fig. 7.2: Residual stress distribution (a) 1 layer, (b) 2 layers.

The stress distribution in the HAZ around the scanned region was more pronounced in the case of the two-layer part. Tensile stresses can be seen on either side of the layers in the longitudinal direction (L-L) while compressive stresses were produced at the transverse end (T). The stress gradient in the one-layer part is limited by the yield and flow stresses of both the steel base material and the Ti64 material, hence the lower stress values, whereas because the first Ti64 layer effectively shields the second Ti64 layer from the steel base, the second Ti64 layer stresses are limited only by the yield strength and flow stresses of the Ti64 material, hence the increase in stress values. Similar to the displacement trend, Table 7.2 shows that the average residual stresses increased with the addition of layers. It can be seen that the average longitudinal and transverse stresses for the first Ti64 layer are 52.4% and 7% of the yield strength respectively. The second layer attained 68% and 11% for the average longitudinal and transverse stresses resepectively.

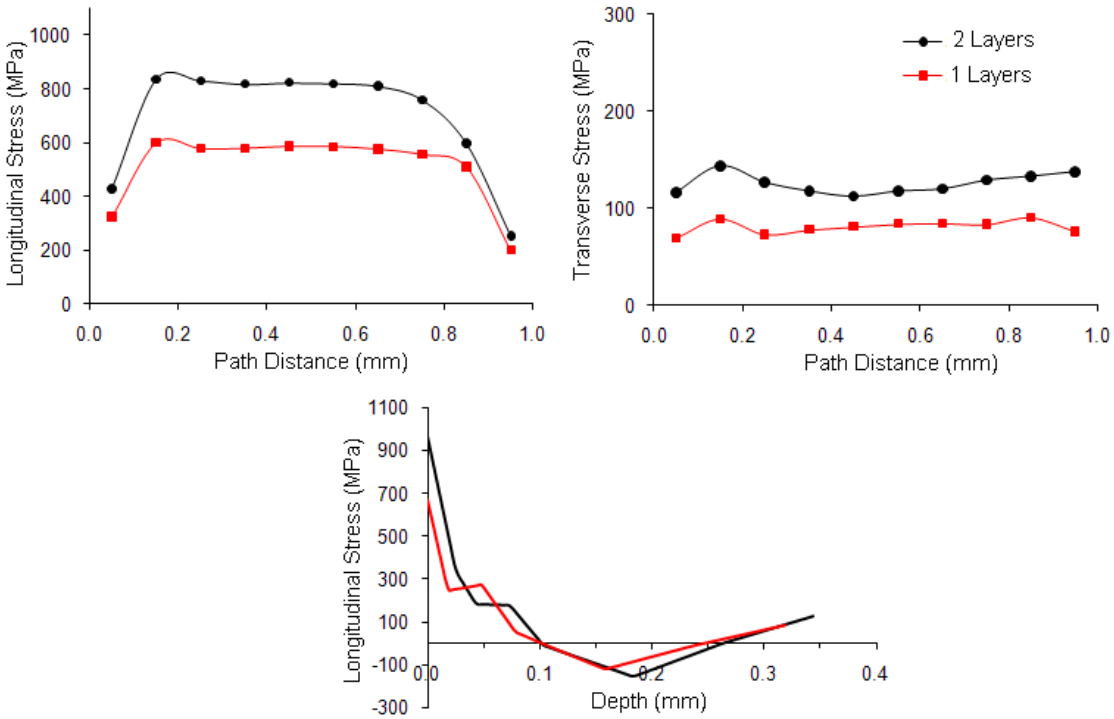

Fig. 7.3: Residual stress variation with number of layers

Fig. 7.3 show the variation of the average longitudinal and transverse stresses across the surface of the top layers. The tapering off of the longitudinal stresses at the end locations can be seen. There is a noticeable increase in the average stresses for both residual stress components as the layer number increases.

In the stress-depth profile shown in Fig. 7.3, it is observed that apart from the higher surface stress value, there is an increase in the depth of the compressive stress zone in the platform as a result of the addition of the second layer. The steady decrease in the stress with depth is discontinued at the surface of the platform due to the difference in mechanical properties of the Ti64 and steel material. The decay in the tensile stresses through the layers then continues until the stresses disappear in the platform and become compressive in nature.

The surface tensile stresses would not increase indefinitely with Ti64 layer addition, rather would be limited by the yield and flow stresses of Ti64. Similarly, the maximum compressive stress in the steel platform is limited by the yield stress of steel (i.e. 255 MPa). Although the tensile and compressive stresses of steel and Ti64 are not necessarily equal in magnitude, the numerical model allowed for the input of only one

strength quantity (i.e. tensile yield strength). Using the higher tensile strength alone represents a more conservative stress limit condition.

Table 7.2: Addition of Ti64 layers study results

Number of Layers	Average Longitudinal Stress (MPa)	Average Transverse Stress (MPa)	Max. Platform Deformation (μm)
1	571.8 ($0.52\sigma_y$)	81.1 ($0.07\sigma_y$)	4.74
2	737.8 ($0.68\sigma_y$)	125.4 ($0.12\sigma_y$)	6.38

7.2.3 Discussion

This study has shown the capability of the layer-by-layer numerical model for predicting the variation of the stresses with addition of Ti64 layers. The variation of stresses found in this study concur with the findings of other researchers. It has been shown that increasing the number of layers increases both the tensile stresses in the built layers and the compressive stresses in the underlying platform material.

Storage and file size limitations mean that only two layers have been considered here. Nevertheless, strong similarities do exist in the stress distribution of the scanned tracks even though the raster scanning method removes any model symmetry. Therefore, there is a potential for condensing the model using ‘substructuring’ simulation techniques for addressing this problem.

7.3 Effect of Platform Thickness

Laser melting of metal powders is normally done on a substrate or base platform. The first layer of melted powder material diffuses into the substrate forming a strong bond when it solidifies, provided the conditions are right. In certain cases, a facilitating agent is required to improve bonding like the addition of titanium powder to a ferro-boron (Fe-FeB) powder mix (Kruth *et al*, 2007). An implication of this is a contribution of the platform to the residual stress development in the built-up layers as well as the overall system’s residual stress distribution.

Depending on the application, steel plates may be used as the platform material for laser melting of metal powders because they are economical, have stable microstructures and can easily be machined with the built-on parts (referred to as onserts) to desired shapes to produce finished parts. In other cases, a series of thin-walled ribbed support structures are initially built on the platform around the geometry of the part to be built to aid separation during post-processing (EOS-GmbH, 2005). The difference in the material properties between the base platform and the added material, especially conduction, thermal expansion and stiffness introduces a structural mismatch condition which has an influence on the stress field characteristics.

The contribution of the build platform or substrate material has been overlooked in previous studies as highlighted in Chapter 6, but experimental studies in Chapter 5 have shown that it has an important role in the build up and distribution of residual stresses in the LM of metal powders. Mercelis and Kruth (2006) used an analytical model, using the two-dimensional general beam bending theory, to show the influence of the base plate height on the residual stress profile. They showed that the magnitude of the stresses is dependent on the height of the base plate. The relaxation stress component following layer removal was shown to increase with base plate height.

The effect of thickness of the platform on the residual stresses and deformation is investigated in this section using the numerical model. The process parameters are summarised in Table 7.3. Base platform thickness values of 1 mm, 0.5mm and 0.3mm were used as input in the model for a two-layer part.

Table 7.3: Platform thickness study process parameters

P (W)	v (mm/s)	d (μm)	h_p (μm)	r_L (mm)	t (mm)	T(°C)
195	1200	100	30	1	Response Variable	40

7.3.1 Deformation Results

Fig. 7.4 shows the displacement of the platform after cooling for two platform thicknesses. It clearly shows permanent deformation of the platform caused by the residual stresses induced by the addition and laser melting of Ti64 powder layers. It has

been found from studies in Chapter 6 that the transient stresses are the main driving forces of the deformation of the platform and that the steady state displacement is a less than the peak transient displacement.

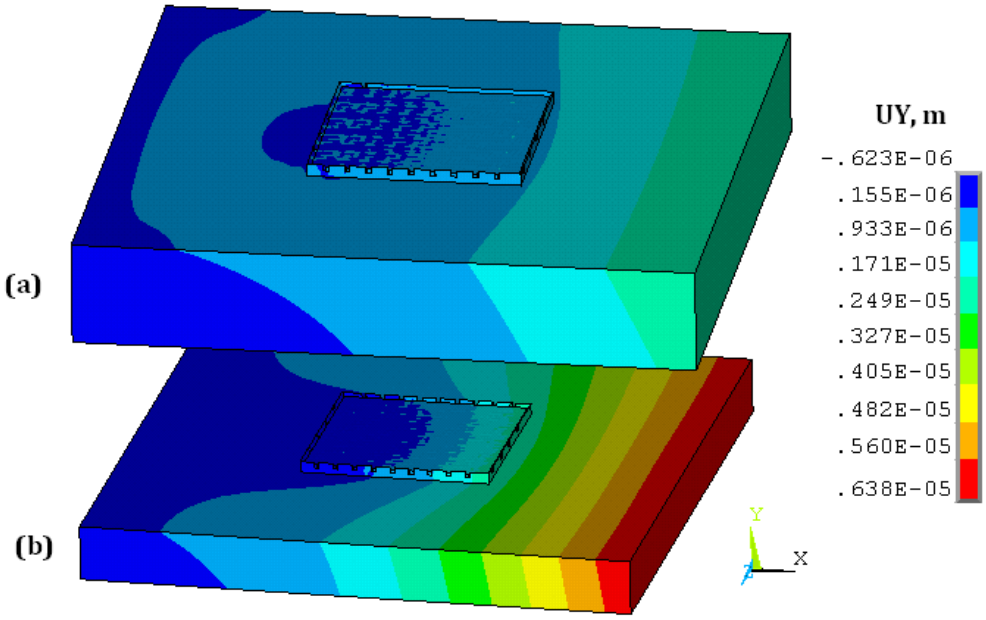

Fig. 7.4: Platform displacements (a) t = 0.5mm, (b) t = 0.3 mm

The platform displacement results are summarised in Table 7.4. A consistent increase in the deformation is observed with decreasing platform thickness. The trend is not a linear one but most likely a higher order polynomial in line with that observed in the direct laser heating of the base platform in the Section 6.3.4. The result shows a reduction of 85.7% in the maximum edge displacement as the thickness increased from 0.3 mm to 1 mm.

For the current study, the maximum platform displacement is considerably less than the powder layer thickness. In practice, when considerably more layers are built on thin substrates, the distortion greatly increases and leads to significant loss of accuracy in the built part as observed in DMLS experiments carried out by Branner *et al* (2008).

7.3.2 Stress Results

Fig. 7.5 shows the average residual stress components on the surface across the centreline paths. The residual stress trends for the different platform thicknesses indicate

a slight steady decrease in longitudinal component with thickness but a more noticeable decrease with thickness for the transverse component. Table 7.4 lists the average residual stress values across the surface paths. Ignoring end locations, the predicted average stresses are 802 MPa and 185 MPa for the longitudinal and transverse components respectively for a 1.0 mm thick platform. The results show that they decrease by 8.0% and 32.2% respectively when the thickness was reduced to 0.3 mm. Relaxation of the stresses evidenced by increased platform deformation accounts for this observation. The reduction in flexural stiffness (related to the second moment of area) of the thinner platform allows the stresses in the part to be released through platform deformation.

In the stress-depth plot shown in Fig. 7.5, there is a steep stress gradient through the top layer and into the platform. The variation with thickness shows quite marked differences. The maximum compressive stress in the base material is seen to increase as the platform thickness decreases, while the depth of the compressive stress zone increases as the platform thickness decreases. The maximum predicted compressive stress in the steel platform decreased by 54.5% when the thickness increased from 0.3 mm to 1.0 mm.

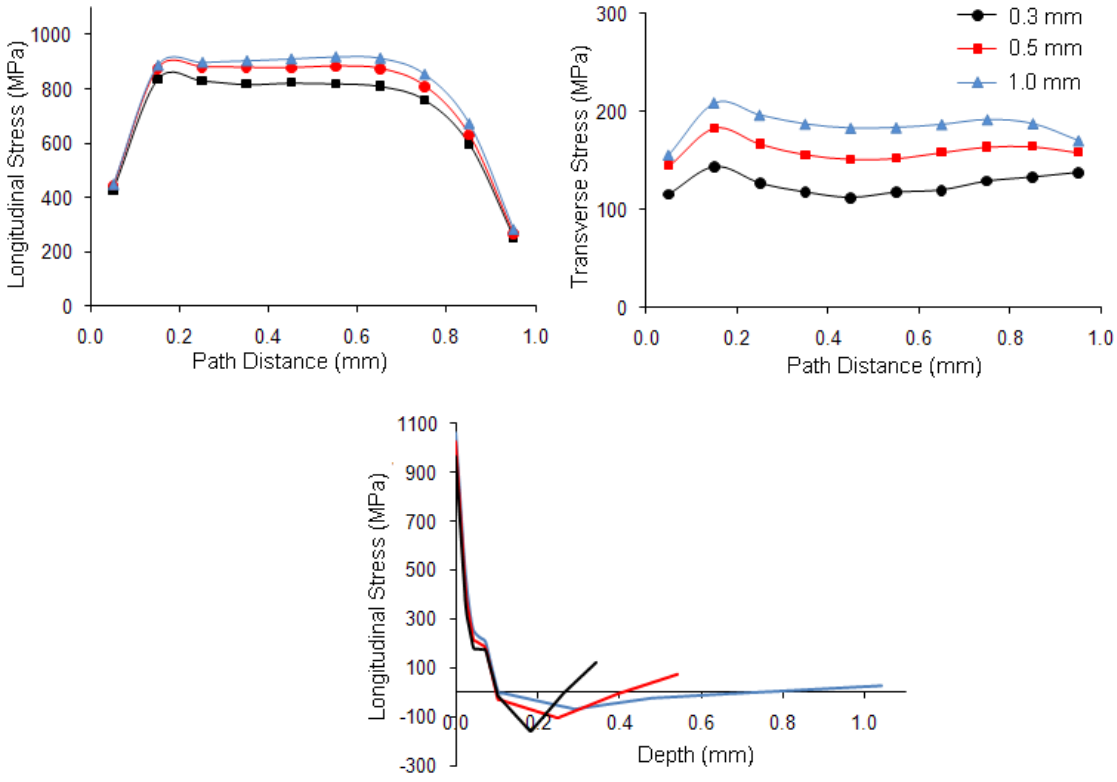

Fig. 7.5: Residual stress variation with platform thickness

It can also be seen from Fig. 7.5 that the secondary tensile stresses at the bottom of the platform also increased as the thickness decreased. Again, the compressive and secondary stresses in the platform are limited by the yield strength of the steel platform material. The stress-depth trend shows that if the platform thickness increases further, the bottom of the plate will experience no deformation and by implication no stress activity.

Table 7.4: Platform thickness study results

Platform Thickness (mm)	Average Longitudinal Stress (MPa)	Average Transverse Stress (MPa)	Max. Platform Deformation (μm)
0.3	737.8 ($0.68\sigma_y$)	125.4 ($0.12\sigma_y$)	6.38
0.5	778.5 ($0.71\sigma_y$)	160.1 ($0.15\sigma_y$)	2.30
1.0	802.1 ($0.74\sigma_y$)	185.0 ($0.17\sigma_y$)	0.92

7.3.3 Discussion

It is apparent from this study that the residual stresses and platform deformation are somewhat inversely related. By increasing the platform thickness, the residual stresses components were found to increase while the platform deformation decreased. As the base platform becomes thicker, it is able to support the induced stresses without significant distortion.

LM parts are normally built on thick platforms, typically greater than 12.5 mm, which are bolted on slotted holes to the machine bed. This form of restraint allows the platform to expand in a planar direction and prevents it from buckling (Electrical Optical Systems, 2005). Certain applications of laser melting of metal powders in electronics like that investigated by Im *et al* (2007) in production of prototype multi-layer printed circuit boards require the laser melting of metal tracks on thin substrates. In such cases, considerations will have to be made on how the platforms need to be restrained to prevent loss of accuracy.

7.4 Effect of Platform Material

Laser melting of Ti64 powder is mostly done on Ti64 plates. However, this study has up to this point considered the building of parts on a steel platform. It is important to understand the influence these two materials have on the residual stress states in the built layers. The process parameters are given in Table 7.5

Table 7.5: Platform material study process parameters

P (W)	v (mm/s)	d (μm)	h_p (μm)	r_L (mm)	t (mm)	T(°C)
195	1200	100	30	1	0.3	40

7.4.1 Deformation Results

Fig. 7.6 shows the displacement distribution using a Ti64 platform. It shows an increase in the edge displacement over the steel platform case. On one hand, the lower elastic modulus of Ti64 implies less resistance to the contraction that occurs in the scanned region. On the other hand, the relatively lower thermal expansion coefficient of both the scanned Ti64 and the Ti64 platform counteracts the effect of the relatively lower stiffness. The combination of the effects of the two quantities results in an overall increase in the displacement of the platform.

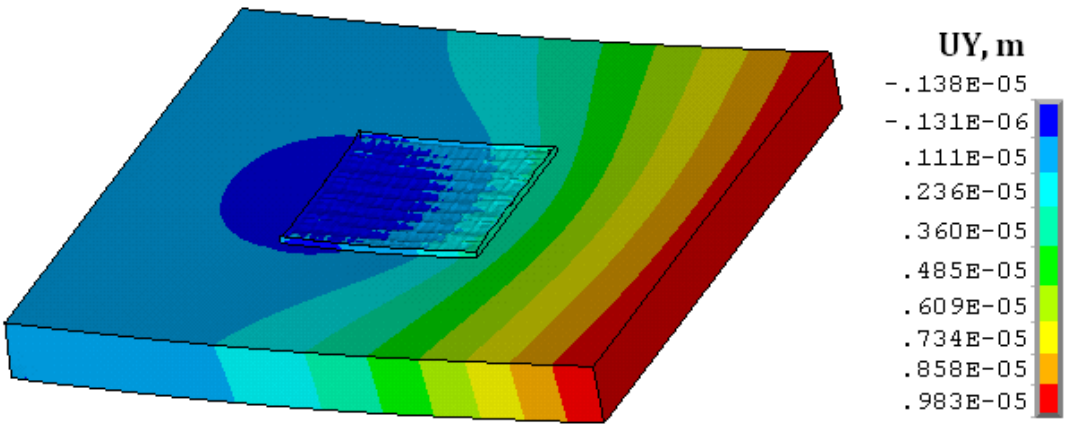

Fig. 7.6: Platform displacement with Ti64 platform

Table 7.6 gives a comparison of the maximum predicted displacements between using a steel platform and a Ti64 platform. The results indicate a 54% increase in displacement with a Ti64 platform over a steel platform.

7.4.2 Stress Results

Fig. 7.7 and Fig. 7.8 give the residual stress distribution and stress profiles respectively for a Ti64 platform. The longitudinal stress contour distribution is similar to that obtained with the steel platform. The results show a small reduction in the average longitudinal stresses but a noticeable increase in the average transverse stresses across the surface paths.

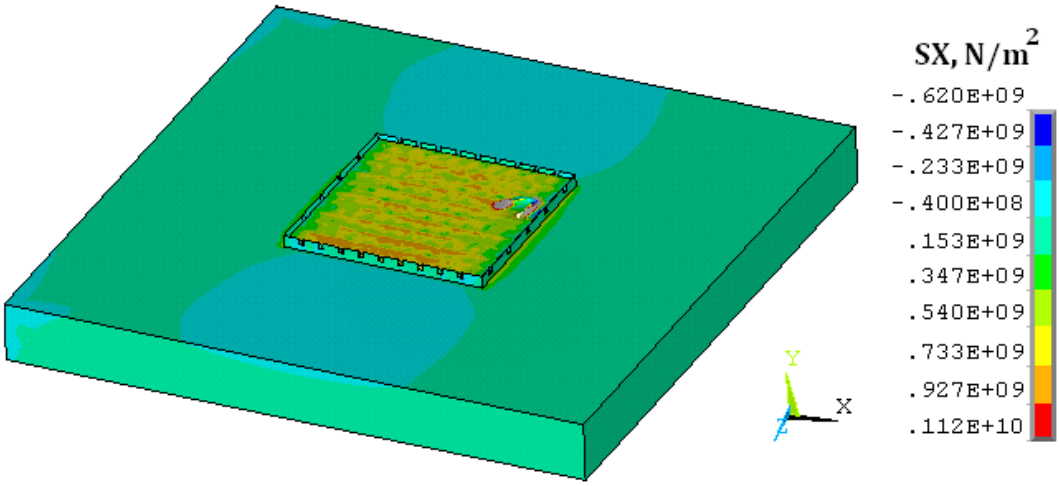

Fig. 7.7: Longitudinal stress distribution with Ti64 platform

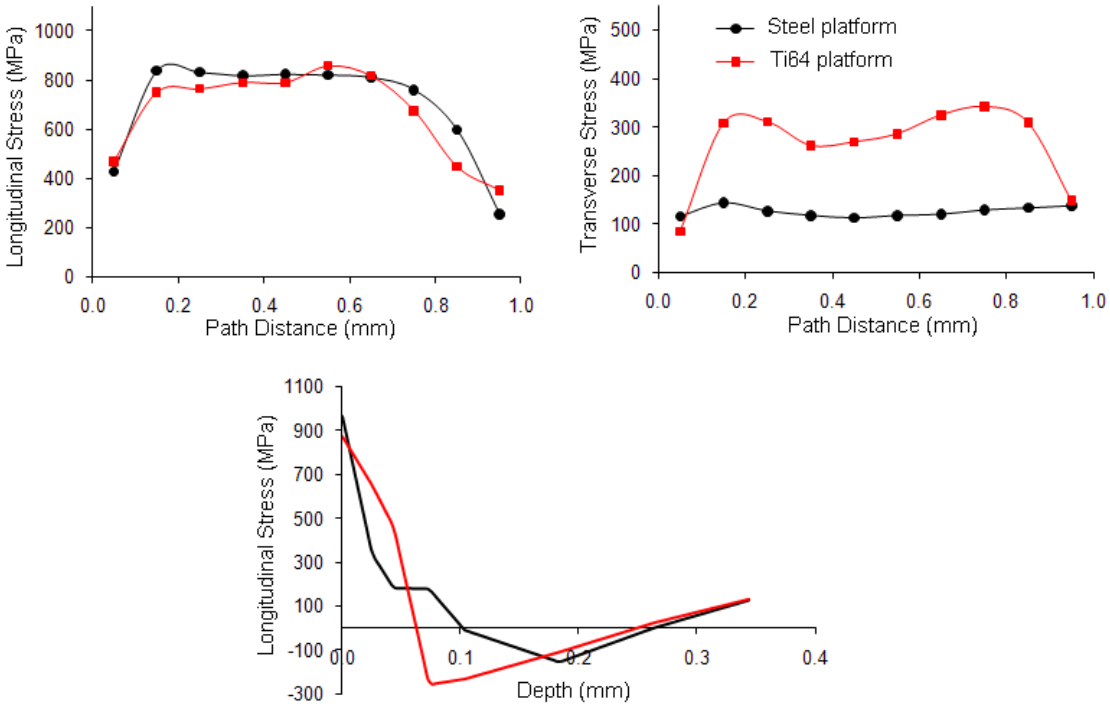

Fig. 7.8: Residual stress variation with platform material

Table 7.6 gives a summary of the platform material study results. By changing the base platform material from Ti64 to steel, the average longitudinal stress in the top layer is seen to decrease by 21.7 MPa while the transverse stress is increased by 139 MPa.

The stress-depth distribution in Fig. 7.8 shows marked differences between the Ti64 and steel platform cases. With the Ti64 platform, a smooth transition into the platfom can be seen, due to less mismatch in structural properties, wheareas a pronounced step is observed in the case of a steel platform. Also, the maximum compressive stress in the Ti64 platform (268 MPa) is much greater than that in the steel platform (156 MPa). This is primarily because the residual stresses are limited by the yield and flow stresses of the material. Therefore, the compressive stresses are greater in the higher yield strength Ti64 than in the lower strength steel platform.

Table 7.6: Platform material study results

Platform Material	Average Longitudinal Stress (MPa)	Average Transverse Stress (MPa)	Max. Platform Deformation (μm)
Steel	737.8 ($0.68\sigma_y$)	125.4 ($0.12\sigma_y$)	6.38
Ti64	716.1 ($0.66\sigma_y$)	264.4 ($0.24\sigma_y$)	9.83

7.5 Effect of Raster Length

The raster length, used interchangeably with the scan length or vector length, describes the distance the laser beam travels across the surface of the powder before changing direction in accordance with the defined scanning pattern. Matsumoto *et al* (2002) suggested that dividing the powder layer into small segments and scanning each with short tracks helped to reduce the residual stresses between scan tracks. Morgan *et al* (2001), in studying the DMLS of stainless steel 316L powders using a CW Nd:YAG laser, found that for small scan lengths (1-2 mm) the scanned tracks remained intact and of good quality. However, for high scan lengths (greater than 15 mm), the scanned tracks were highly deformed (tearing and curling were evident). This section investigates the effect of the raster length on the residual stresses in the laser melting of Ti64 powder. The process parameters for this study are given in Table 7.7.

Table 7.7: Raster length study process parameters

P (W)	v (mm/s)	d (μm)	h_p (μm)	r_L (mm)	t (mm)	T(°C)
195	1200	100	30	Response Variable	0.3	40

For ease of modelling, the raster lengths used in this study are 1 mm and 0.5 mm. The 0.5 mm raster length study case was performed by splitting the 1 mm × 1 mm scanned region of a layer (shown earlier in Fig. 6.1) into two 0.5 mm × 1 mm scan regions positioned side-by-side and sharing common nodes at the interface. In the numerical model, the scan regions on a layer were built sequentially, with the left hand side scan region treated first.

7.5.1 Deformation Results

The displacement plots for a one-layer and a two-layer part with 0.5 mm raster lengths are shown in Fig. 7.9. The contour plots show an increase in the displacement with the addition of the second powder layer but also show a 7.6% decrease in the edge vertical displacement from the 1.0 mm raster length case shown in Fig. 7.1. The displacement results are summarised in Table 7.8. Although there is a small reduction in the platform deformation, the 'saddle' effect at the scanned region was not eliminated by halving the raster length.

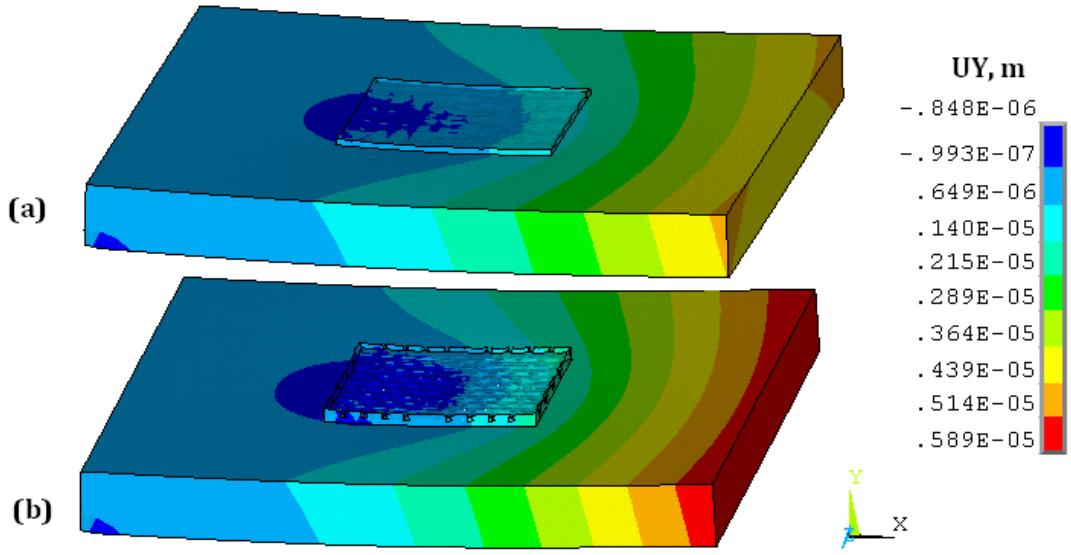

Fig. 7.9: Deformation plot for 0.5 mm raster (a) 1 layer, (b) 2 layers

This decrease in the displacement agrees with the findings of Morgan *et al* (2001). In their work, they stated that as the scan track length increases, the time taken to complete a single scan track also increases. The time lapse between scan tracks alters the temperature gradients in the material surrounding the scanned region during solidification of the molten material which, in turn, govern the extent of bending.

7.5.2 Stress Results

Fig. 7.10 shows the longitudinal stress component of the two-layer part with 0.5 mm raster length. It shows the boundary of the scanned regions where the longitudinal stresses appear to have been markedly reduced. It can be seen that the stress distribution in the HAZ around the scanned region is also noticeably different from the 1.0 mm

raster case seen in Fig. 7.2(b). The compressive stresses on the transverse ends (T-T) of the scanned region appear to have been replaced by tensile stresses.

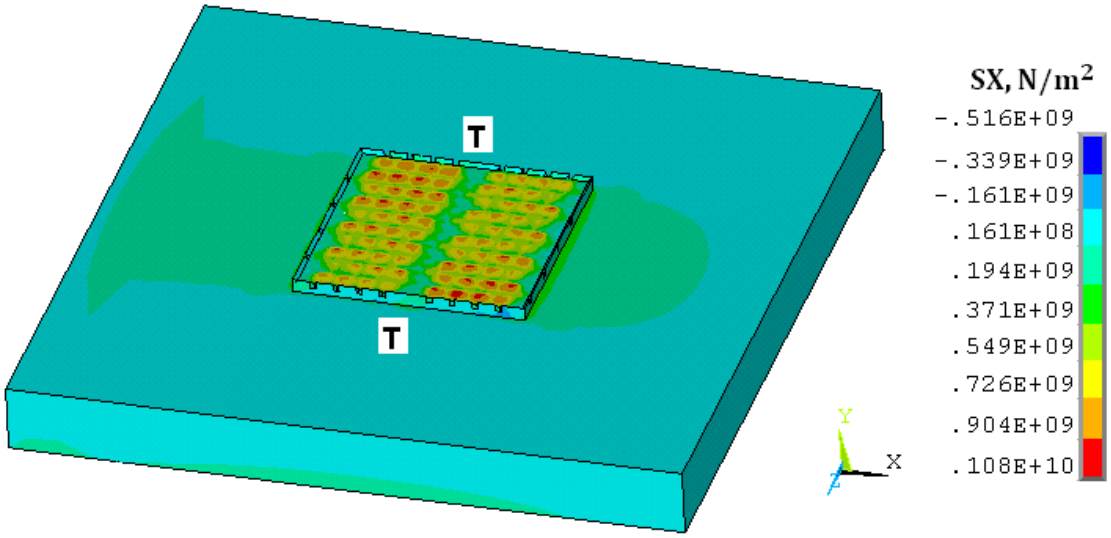

Fig. 7.10: Longitudinal stress distribution for 0.5 mm raster length

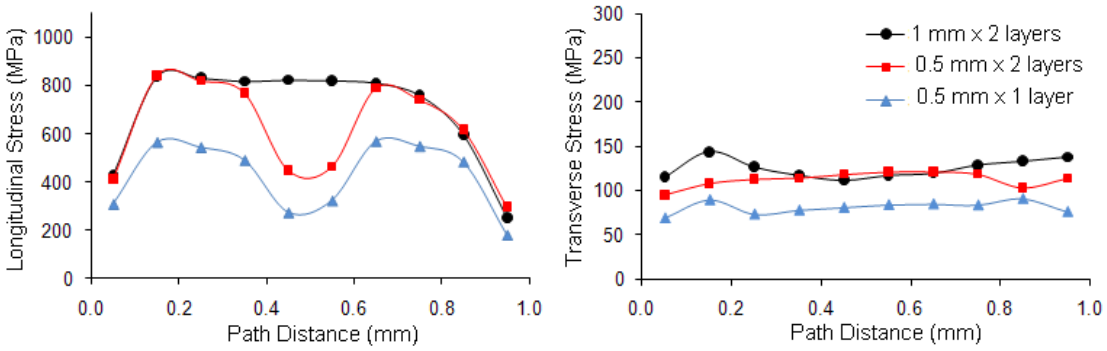

Fig. 7.11: Residual stress variation with raster length

The stress distribution plots in Fig. 7.11 show a corresponding dip (approximately 50% reduction) in the longitudinal stress profile at the interface of the two 0.5 mm raster regions. However, towards the middle of each raster track, the longitudinal stresses vary in a similar manner for both the 0.5 mm and 1.0 mm raster length cases. The reheating of the previously solidified track accounts for the observed stress reduction around the interface area. The transverse stress profile for the 0.5 mm raster length case across the middle of the scanned regions differs slightly from that obtained for the 1 mm raster length case. Table 7.8 is a summary of the average residual stresses across the designated paths on the surface of the part. The average longitudinal and transverse stresses are seen to decrease by 50.8 MPa and 5.9 MPa respectively when the raster length was reduced from 1.0 mm to 0.5 mm.

The lower transverse and longitudinal stresses for the one-layer part are consistent with findings of the earlier study in Section 7.1 in which the residual stresses were seen to increase with the number of layers.

Table 7.8: Raster length study results

Raster length (mm)	Number of layers	Average Longitudinal Stress (MPa)	Average Transverse Stress (MPa)	Max. Platform Deformation (μm)
0.5	1	473.4 ($0.43\sigma_y$)	81.1 ($0.07\sigma_y$)	4.68
0.5	2	687.0 ($0.63\sigma_y$)	119.5 ($0.11\sigma_y$)	5.89
1.0	2	737.8 ($0.68\sigma_y$)	125.4 ($0.12\sigma_y$)	6.38

7.5.3 Discussion

This study has shown that the average longitudinal stresses in the Ti64 layer reduced by shortening the raster length. The re-melting of previously solidified tracks has been found to alleviate the longitudinal stresses at the boundary of the raster regions. This finding concurs with the findings of Kahnert *et al* (2007). In their experiments, they reduced the scan tracks of H13 steel powder as well as alternated the scanning orientation in 90° turns using an electron beam (i.e. EBM). They found that the bonding and deformation characteristics via visual inspection of the parts produced were improved by this action.

7.6 Effect of Chamber (Preheat) Temperature

In the laser melting of metal powders, the heating stage of the powder material is closely followed by two (2) distinct stages of cooling. These have been identified as:

- Localised rapid cooling rate of the molten powder after laser heating, and
- Moderate cooling rate of the layers and the base platform from the chamber temperature to room temperature following build completion.

These stages were referred to as the ‘early’ and ‘later’ stages of cooling by Dai and Shaw (2004). According to Dai and Shaw (2004), preheating performs dual functions

by: (i) controlling the rate of cooling in both stages, and (ii) facilitating the bonding of the molten material(s). The cooling rate is a primary factor that determines the final metallurgical structure of laser melted materials. According to Fischer *et al* (2004), the high cooling rates during the SLS of titanium powder increases the microhardness of the scannned tracks. Also, findings from SLS and multi-pass welding studies have shown that increasing the working temperature reduces the resulting residual stress (Shiomi *et al*, 2004 and Jiang, 2006).

This section investigates the effect of increasing the preheat temperature on the residual stresses in laser melting of metal powders using the developed finite element model. Temperatures used here are 40°C, 150°C and 300°C for a two-layered Ti64 part. The process variables are listed in Table 7.9.

Table 7.9: Preheat temperature study process parameters

P (W)	v (mm/s)	d (μm)	h_p (μm)	r_L (mm)	t (mm)	T(°C)
195	1200	100	30	1.0	0.3	Response Variable

To simulate the interaction with the preheated chamber, the surface heat losses via convection needed to be considered. Measurements by Mardolcar *et al* (1986) and calculations by Lemmon and Jacobsen (2004) have shown that the thermal conductivities of argon and air increase with temperature as discussed in Chapter 2. According to Rohsenow *et al* (1998), under natural convection conditions, the value of the convective heat transfer coefficient of air increases with temperature and varies as a fractional power of the temperature difference (ΔT) – typically as $\Delta T^{1/4}$ or $\Delta T^{1/3}$. Due to lack of data for the convective heat transfer coefficient of argon at high temperatures, the values for air were used in this study. With a reference value of h = 20 W/m^{2}K at 25°C, the values calculated for the convection coefficient assuming a $\Delta T^{1/3}$ relationship were 49 W/m^{2}K, 100 W/m^{2}K, and 130 W/m^{2}K at 40°C, 150°C and 300°C respectively.

7.6.1 Deformation Results

From the displacement plots shown in Fig. 7.12(a) and (b), it can be seen that the contour bands are quite dissimilar at 40°C and 300°C. Table 7.10 gives a summary of

the maximum platform displacements for the various chamber temperatures. The results show a small steady decrease in the maximum displacements as the chamber temperature increases.

The edge displacement-time history plot in Fig. 7.12(c) shows clear distinctions between the two stages of cooling for different chamber temperatures. The lower cooling rate at 300°C during the second stage (i.e. the later stage) of cooling clearly causes a noticeable reduction in the transient displacement. The difference in the peak transient displacement and the steady state displacement also increases with increase in the chamber temperature. The results show drops of 2.1% and 4.2% for the 40°C and 300°C chamber temperature cases respectively.

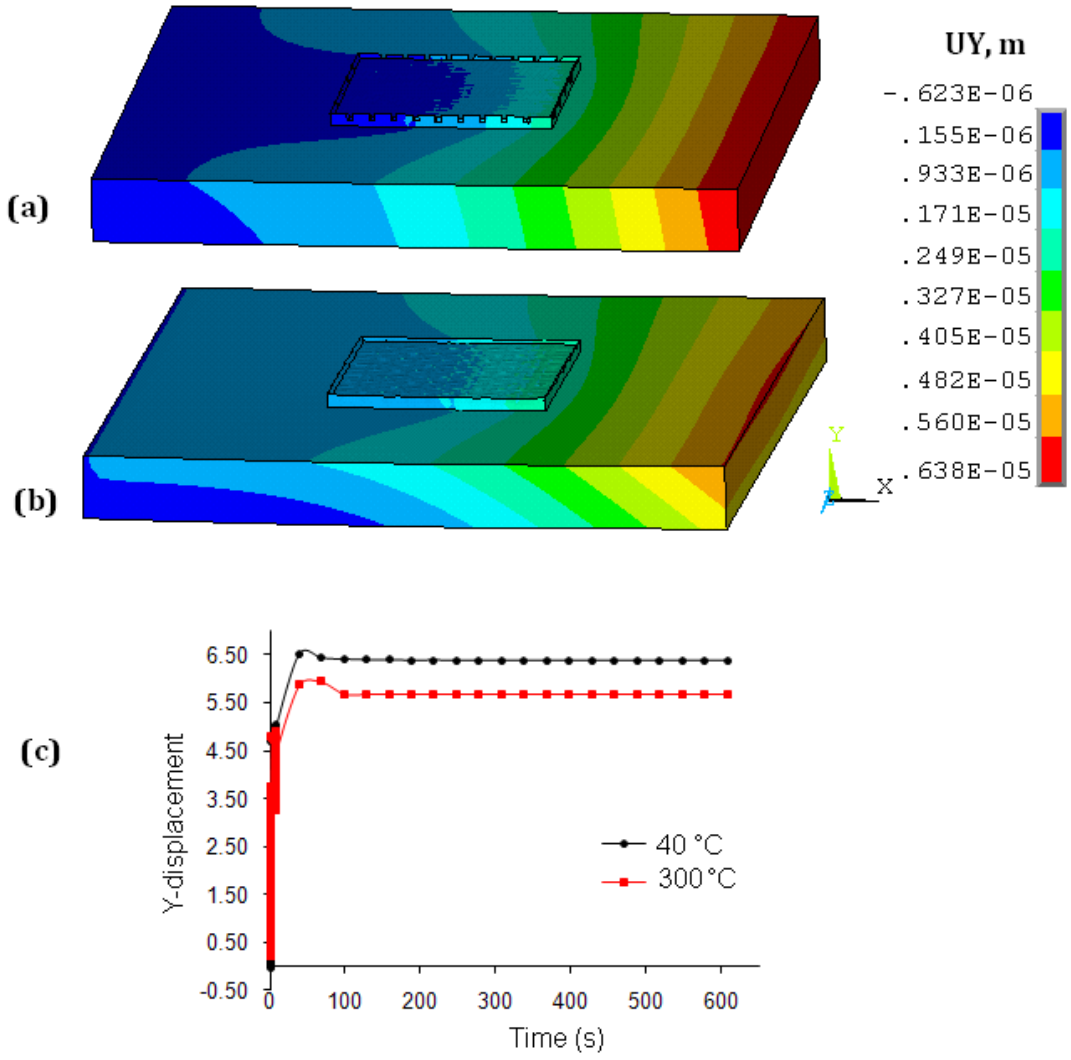

Fig. 7.12: Displacement plots for chamber temperatures (a) 40°C, (b) 300°C, (c) edge displacement with time

7.6.2 Stress Results

Fig. 7.13(a)-(c) shows the longitudinal residual stress distribution for the three chamber temperatures considered. A consistent reduction in the longitudinal stress contour distribution on the surface layer with increasing chamber temperature can be seen.

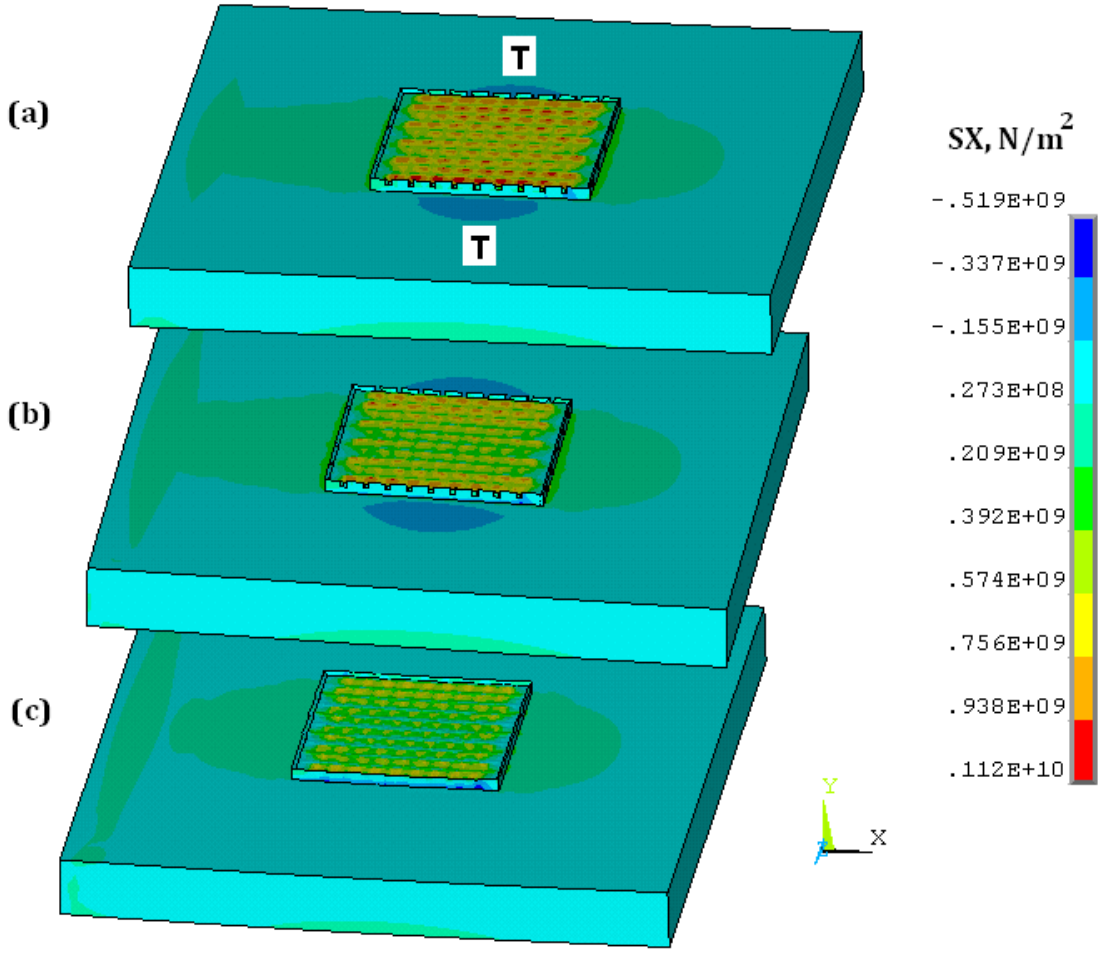

Fig. 7.13: Residual stress distribution for different preheat temperatures (a) 40°C, (b) 150°C, (c) 300°C

The distribution of the residual stresses around the scanned region on the surface of the platform can be seen to be affected by the increase in chamber temperature. The compressive stress areas at the transverse ends (T-T) in the HAZ around the scanned region appear to reduce as the temperature increased and at 300°C are completely replaced by tensile stresses.

Fig. 7.14 shows the variation of residual stresses across the surface of the top layer. It can be seen that preheating had a positive effect by reducing the tensile residual stresses in the Ti64 layers when the temperature was increased from 40°C to 150°C.

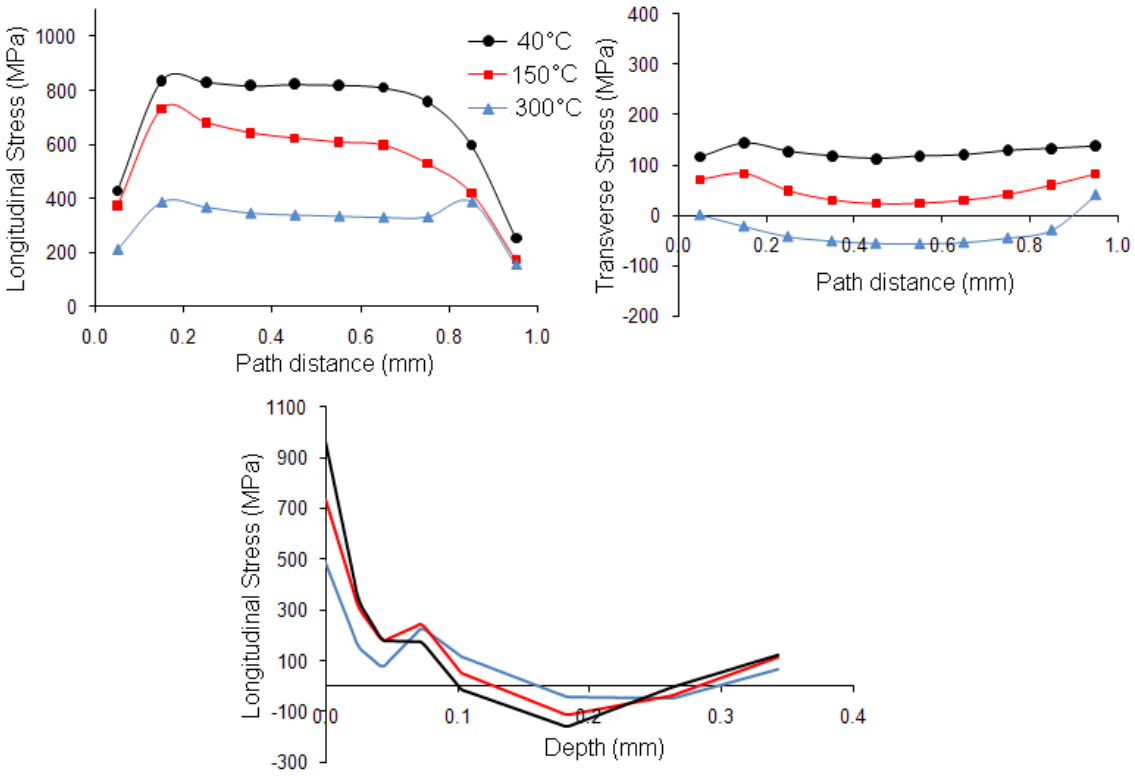

Fig. 7.14: Residual stress variation with preheat temperature

It can be seen that at 300°C, there is an even greater reduction in both the longitudinal and transverse residual stresses. Table 7.10 gives a summary of the stress results for the preheat temperature study. The predicted average longitudinal stress can be seen to have reduced by more than 50% as a direct result of increasing the temperature from 40°C to 300°C. This observed stress reduction in the surface layer is more pronounced with the transverse component where the average stress generated at the surface at 40°C markably changes from tensile to compressive at 300°C.

Fig. 7.14 also shows the stress-depth variation at the different chamber temperatures. At 150°C, it can be seen that the longitudinal stress decreases with depth up to the point it reaches the platform, where a momentary increase in the tensile stress in the platform material is evident. At 300°C, the increase in the tensile stress at the platform interface can also be seen to tend to the yield strength of the steel material. The tensile stress in the base platform then appears to decrease with depth transforming into compressive

stress in the platform. This is in contrast with the variation at 40°C where the tensile stress at the platform interface shows a slight initially decrease before rapidly transforming to compressive stresses as the depth into the platform increases.

As a direct consequence, the compressive stress in the platform decreases with increasing chamber temperature. It is quite apparent that by reducing the tensile stresses in the Ti64 layers, the stresses are partly transferred elsewhere – the base platform in this case.

Table 7.10: Preheat temperature study summary

Preheat Temperature (°C)	Average Longitudinal Stress (MPa)	Average Transverse Stress (MPa)	Max. Platform Deformation (μm)
40	737.8 ($0.68\sigma_y$)	125.4 ($0.12\sigma_y$)	6.38
150	604.1 ($0.55\sigma_y$)	42.7 ($0.04\sigma_y$)	6.11
300	355.9 ($0.33\sigma_y$)	-31.3 ($-0.03\sigma_y$)	5.75

7.6.3 Analysis of Cooling Rates

The rate of cooling which controls the stress gradients in the first cooling phase can be observed by monitoring the temperature reduction profiles across a path *A-A* shown in Fig. 7.15. It can be seen that the maximum spot temperature reached at 300°C is slightly higher than that at 40°C in both preheat temperature cases. The rate of cooling at the early stages show only slight differences for both chamber temperature cases. The calculated cooling rates at 40°C and 300°C are 1.26×10^7 K/s and 1.22×10^7 K/s respectively after 0.083 ms (representative of the laser located at the next spot on the track), and 2.05×10^6 K/s and 1.82×10^6 K/s respectively after 0.42 ms (representative of the laser located five spot further down the track). The close proximity of the cooling rates at the first cooling stage suggests that the observed differences in residual stresses as a result of the increase in the chamber can be attributed to the second phase of cooling – i.e. cooling down from the chamber temperature to room temperature. The principle of operation of Electron Beam Manufacturing (EBM) supports this finding (ARCAM, 2010). In EBM, full melting of the metal powders is carried out in a vacuum

chamber maintained at temperatures near the melting point followed by slow cooling to room temperature. The result is a significant reduction in the residual stresses in the built parts. The study by Dai and Shaw (2006) also supports this finding. In the laser densification of nickel and porcelain powders, they found that the reduction in both the longitudinal and transverse residual stresses was due to the reduced temperature gradient induced by the chamber preheat temperature, which results in more uniform heating during laser scanning and more uniform cooling after laser densification.

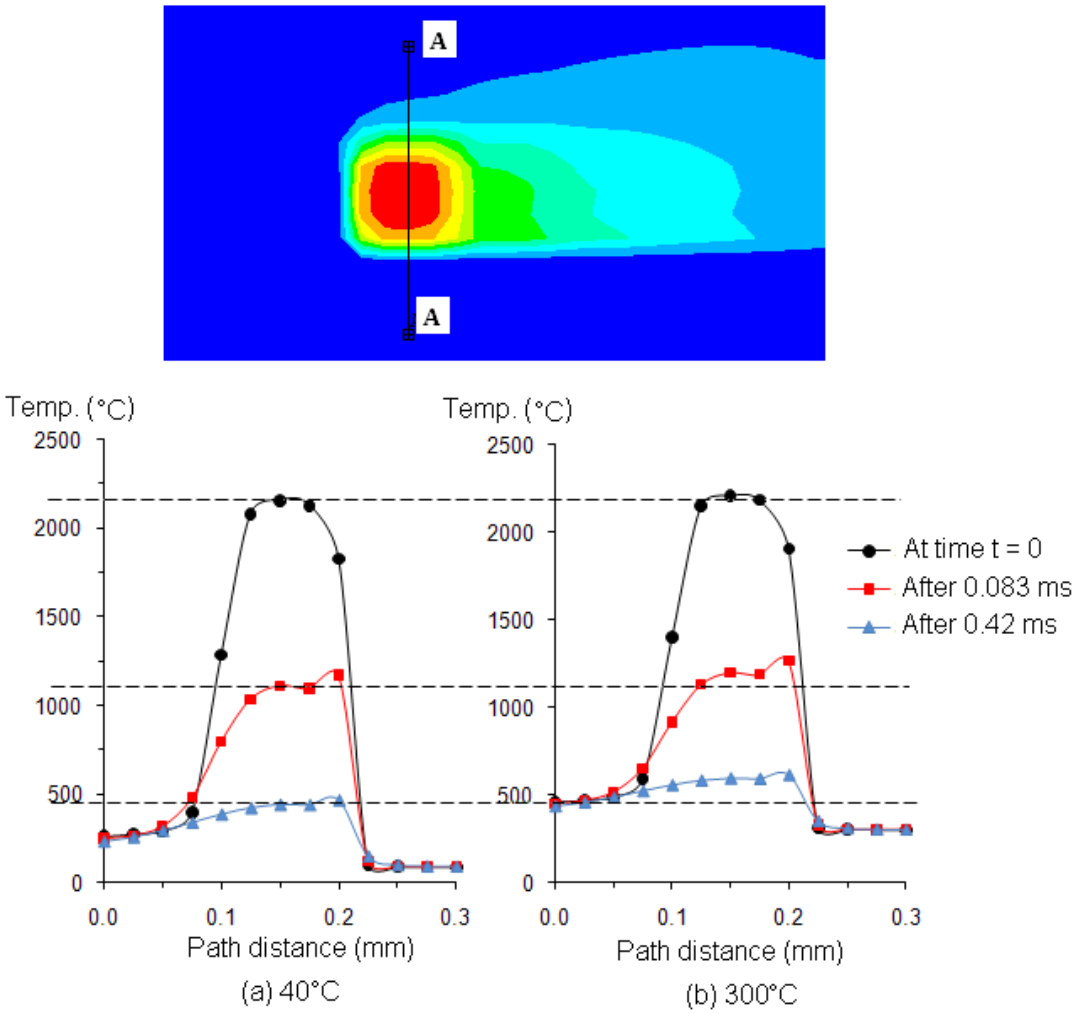

Fig. 7.15: Temperature reduction rate at different chamber temperatures

7.6.4 Discussion

This study shows that changing the preheat temperature of the chamber is an effective means of altering the stress states in the LM process. The maximum displacement of the platform and the magnitude of the residual stresses decreased as the chamber temperature increased. From a residual stress reduction standpoint, the ideal scenario

would be to maintain the chamber near the material's melting point so that the powder can be melted and solidified followed by slow uniform cooling to room temperature without large temperature gradients. Otherwise, stresses due to the volume changes and temperature gradients associated with the solidification process are inevitable.

Higher chamber temperatures can be applied, but may be too expensive and detrimental to the performance of some system components at elevated temperatures.

7.7 Effect of Scan Speed

The success of laser melting of metal powders depends on the heat input to the powder and appropriate control of the rate of solidification. The laser power and scan speed control most notably the amount of energy delivered into the powder and hence, the amount of melting and consolidation that takes place (Morgan *et al*, 2001). Good bonding between the added layer and the substrate can only occur when there is considerable liquid diffusion at the interface between the scanned layers. The scan speed is also linked with the balling effect described in Chapter 2 as observed by Shiomi *et al* (1999) in the DMLS of copper powder. They found that with a higher scan speed, the solidified parts of the powder were unconnected with each other as the laser traversed the surface of the powder bed.

The laser scan speed governs the dwell time of the laser on the irradiated region. If constant material properties are assumed and heat losses to the surroundings are neglected, the amount of laser energy required to melt a single spot area of 30 μm Ti64 powder under the current operating conditions is 1.52 mJ using data from the enthalpy tables in Mills (2002). This translates to about 31.3% of the energy supplied by the laser at $\alpha = 0.3$, which is the initial fraction of the laser energy that goes into raising the temperature to the melting point and overcoming the latent energy of the powder. The remainder of the laser energy goes into stabilising the molten pool as well as heating the surrounding material to facilitate bonding with the base layer or previously scanned track.

In a laser cladding study by Schneider (1998), it was stated that the power-to-scan speed ratio or specific energy explained the quality of the tracks as well as quality of the bonds formed. At low scan speeds, the specific energy is high and excessive diffusion at the

interface can occur which makes the building process uneconomical, whereas at high scan speeds, the specific energy is low and material fusion may not occur. Olakanmi *et al* (2011), in sudying the laser densification of Al-12Si powder found that the average density of the sintered tracks was inversely proportional to the scan speed, therefore, directly proportional to the specific energy. In laser polishing for example, experiments conducted by Lamikiz *et al* (2007) showed that slow scan speeds were required to achieve smooth surface finish effects. From the foregoing, it is clear that achieving the right qualitative balance as well as reducing the residual stress field characteristics is important for a successful laser melting outcome.

This section investigates the effect of decreasing the scan speed on the residual stress fields using the developed numerical element model. Decreasing the scan speed would ensure that the Ti64 powder is fully melted for the operating conditions as more heat energy would be delivered. Scan speeds investigated here are 1200 mm/s, 1000 mm/s and 800 mm/s. The process variables for the study are listed in Table 7.11.

Table 7.11: Scan speed study process parameters

P (W)	v (mm/s)	d (μm)	h_p (μm)	r_L (mm)	t (mm)	T(°C)
195	Response Variable	100	30	1.0	0.3	40

7.7.1 Deformation Results

Fig. 7.16 shows the final platform displacement plot at 1000 mm/s scan speed. It shows an increase in the maximum displacement from the 1200 mm/s case shown in Fig. 7.1. Table 7.12 lists the maximum displacement results for the different scan speeds considered. An increase in the maximum edge displacement of 1.11 μm is observed as the scan speed is reduced from 1200 mm/s to 800 mm/s. This can be attributed to the increased amount of heat added to the system. A basic explanation for this would be that as the interaction time increases, the heat input increases; hence, the amount of bending in agreement with Morgan *et al* (2001). Although Dai and Shaw (2006) found that increasing the laser scanning rate slightly increased the out-of-plane distortion in a laser densified nickel and porcelain layer, this was attributed to the combined effect of the thermal gradients, material properties and processing variables.

Two thermal gradients can be distinguished here. Firstly, as the laser scans the Ti64 layer in a raster fashion, the preceding tracks are reheated when the laser scans the adjacent track. Therefore, the temperature gradient across the scanned tracks decreases with increasing scan speed. Secondly, the temperature gradient through the layer thickness increases with increasing scan speed because the temperature difference between the top and bottom surfaces of the Ti64 layer increases due to the shorter dwell time. The first temperature gradient tends to reduce the out-of-plane distortion while the second temperature gradient increases the distortion. The combined effect of these directional temperature gradients determines the outcome of the stress field. Therefore, the increase in platform displacement observed here indicates that the temperature gradient through the layer thickness and the base platform are more dominant.

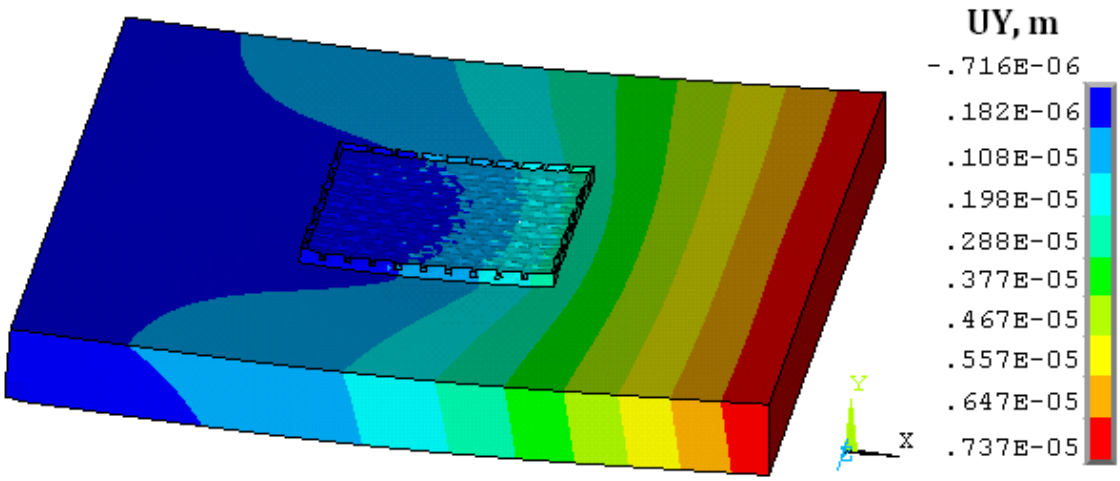

Fig. 7.16: Platform displacement plot for v = 1000 mm/s

7.7.2 Stress Results

Fig. 7.17 shows the residual stress distribution for the 1000 mm/s scan speed case. The stress contour plots are similar for the scan speed cases considered. However, it shows a small steady increase in the longitudinal stresses as the speed reduces. This is because the increase in the dwell time as a result of decreasing speed influences only the first cooling stage as discussed earlier. The second cooling stage rate depends on the difference between the maximum attained temperature and the chamber temperature.

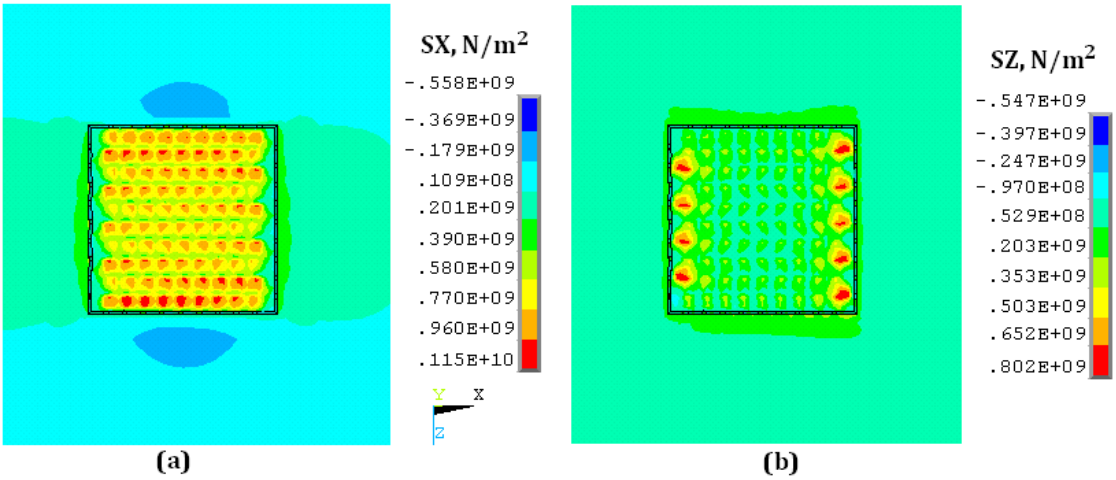

Fig. 7.17: Residual stress distributions for v = 1000 mm/s (a) Longitudinal, (b) Transverse

The variation of the residual stress components across the selected paths is shown in Fig. 7.18. A slight steady increase in the longitudinal stresses with decreasing scan speed can be clearly seen. Reducing the scan speed from 1200 mm/s to 800 mm/s caused the longitudinal stress to increase by 57 MPa. The transverse stresses however show a more pronounced response to the scan speed. Reduction in the scanning speed from 1200 mm/s to 800 mm/s reduces the transverse stresses by 46 MPa. Table 7.12 lists the average stresses across the paths. It shows that the longitudinal and transverse stress components respond in opposing ways with respect to the scan speed.

Fig. 7.18 gives the stress-depth profile variation with scan speed. It shows similar variations for the scan speed cases considered. The predicted maximum tensile and compressive stresses in the added layers and the base platform are not greatly affected by the decrease in the scan speed.

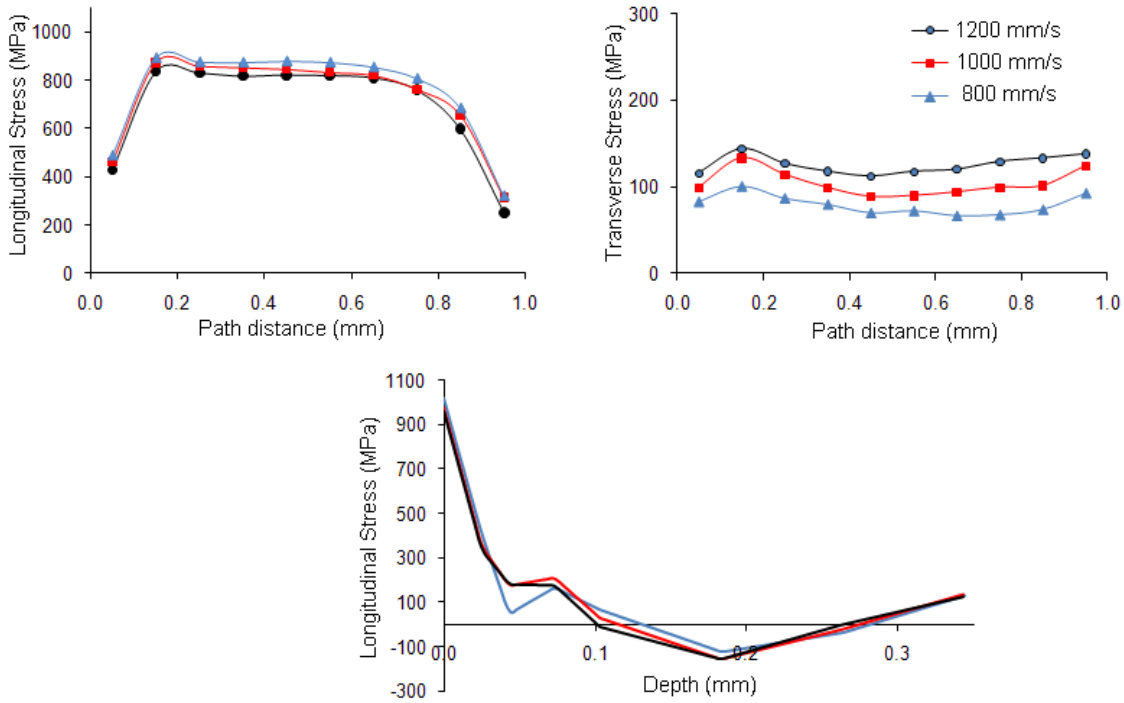

Fig. 7.18: Residual stress variation with scan speed

Table 7.12: Scan speed study results summary

Scan Speed (mm/s)	Average Longitudinal Stress (MPa)	Average Transverse Stress (MPa)	Max. Platform Deformation (μm)
1200	737.8 ($0.68\sigma_y$)	125.4 ($0.12\sigma_y$)	6.38
1000	754.9 ($0.69\sigma_y$)	102.2 ($0.09\sigma_y$)	7.37
800	794.5 ($0.73\sigma_y$)	79.4 ($0.07\sigma_y$)	7.49

7.7.3 Discussion

The study shows that the scan speed is an influential factor on the residual stresses and platform deformation in the laser melting process. The numerical model predicts that decreasing the scan speed steadily increases the longitudinal component and simultaneously decreases the transverse component of the residual stress.

In order to reduce process times, the scanning speed would have to increase. It is known that the scanning speed cannot be increased indefinitely as pointed out in studies by Tolochko *et al* (2004) and Morgan *et al* (2001) in the DMLS of metal powders where

fusion was not achieved at high speeds. This study did not consider the diffusion of molten material; therefore, the highest achievable scanning speed that would result in acceptable cohesion between the layers and the underlying material may still have to be determined experimentally. The suggestion from the scan speed study is that the scan speed has no significant effect on the equivalent stress level and its selection is mainly qualitative – to ensure acceptable adhesion between the layers.

7.8 Effect of Powder Layer Height

The layer height strongly dictates the number of layers required to complete a building operation, which subsequently determines the process run time. In the manufacture of Functionally Graded Materials (FGM) using laser deposition of metal powders, the layer height is one variable that determines the compositional gradients required to achieve the desired part characteristics (Yakovlev *et al*, 2005). In such operations, varying the layer height with part depth or scanning alternate layers produces the desired part characteristics. Furthermore, the amount of powder material melted and its pool depth depend on the layer thickness (Oliveira *et al*, 2005). Olakanmi *et al* (2011) showed that the density of laser sintered Al-12Si tracks decreased as the layer thickness increased. It follows that the degree of densification, shrinkage and consolidation of the molten material has a direct impact on the temperature gradients which consequently determines the thermal and residual stress fields in layers.

In this section, the numerical model is used to investigate the effect of the layer height on residual stresses. The process parameters are given in

Table 7.13. Two part height cases are considered here:

- a 30 μm thick part built by two 15 μm Ti64 powder layers and another by a single 30 μm layer, and
- a 60 μm thick part built by two 30 μm layers and another by a single 60 μm layer of powder.

Table 7.13: Powder thickness study process parameters

P (W)	v (mm/s)	d (μm)	h_p (μm)	r_L (mm)	t (mm)	T(°C)
195	1200	100	Response Variable	1.0	0.3	40

7.8.1 Deformation Results

Fig. 7.19 shows the platform displacement plot for a one-layer 60 μm part. The displacement contours are similar to those of the two-layer 30 μm height case shown in Fig. 7.1. The plot shows a lower maximum platform displacement than the two-layer 30 μm part, suggesting that for the same part thickness the platform displacement increases as the layer height decreases. Halving the layer height doubles the amount of heat added to the system; hence, a greater degree of bending. Dai and Shaw (2006) made a similar observation in their laser densification study of nickel and porcelain powder. The displacement results for the layer height study are summarised in Table 7.14. The results show a 34% increase by halving the layer height in the 60 μm part height case and a 5% increase in the 30 μm part height case. This marked reduction in the effect of the layer height, implies that the thermal gradient in the thickness direction and through the depth of the base platform becomes more influential in limiting the displacement of the part as the layer height is further reduced.

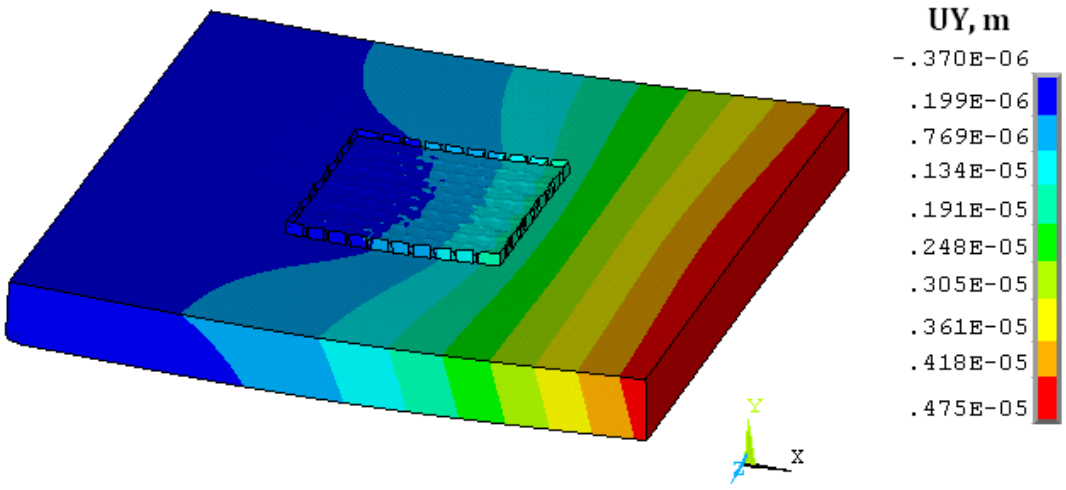

Fig. 7.19: Deformation plot for single 60 μm layer

7.8.2 Stress Results

Fig. 7.20 shows the longitudinal and transverse components of the residual stresses for the one-layer 60 µm part height case. The stress contour plots are similar to the two-layer 30 µm height case shown in Fig. 7.2. A reduction in the longitudinal stress on the Ti64 layer surface as well as differences in the distribution in the HAZ around the scanned region can be seen.

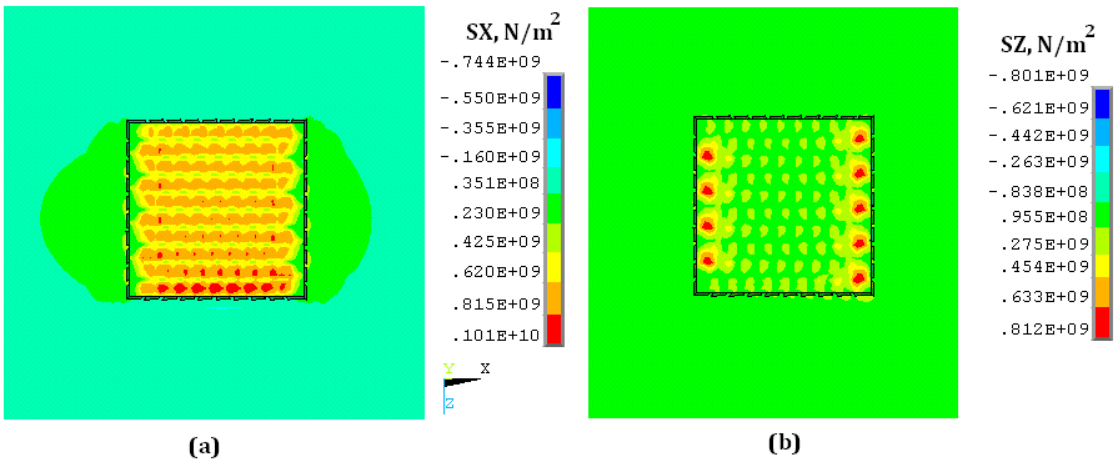

Fig. 7.20: Residual stress distribution for single 60 µm layer (a) Longitudinal, (b) Transverse

Fig. 7.21 shows the average residual stress variations across the centreline paths. It can be seen that for the 60 µm part height case, halving the layer thickness increases the longitudinal stresses by 36 MPa and simultaneously decreases the transverse stress by 13.8 MPa. With the 30 µm part height case, pronounced differences in the residual stress profiles can be seen. By halving the layer thickness to 15 µm, there is a 46 MPa rise in the longitudinal stress component, while the transverse stress component shows a 107 MPa increase. This seems to suggest that the transverse stresses are more responsive to changes in layer height. The layer height study results are summarised in Table 7.14.

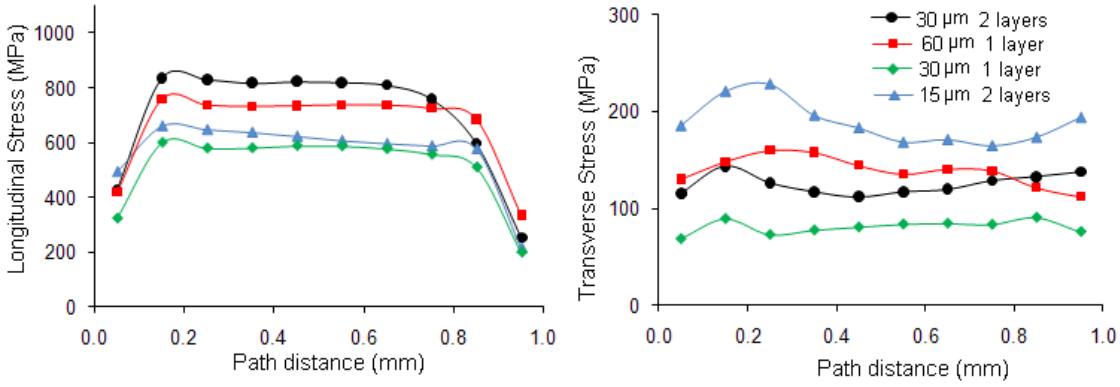

Fig. 7.21: Residual stress variation with layer thickness

Table 7.14: Powder layer height result summary

Layer Height (µm)	Number of Layers	Average Longitudinal Stress (MPa)	Average Transverse Stress (MPa)	Max. Platform Deformation (µm)
15	2	617.9 ($0.57\sigma_y$)	188.3 ($0.17\sigma_y$)	4.98
30	1	571.8 ($0.52\sigma_y$)	81.1 ($0.07\sigma_y$)	4.74
30	2	737.8 ($0.68\sigma_y$)	125.4 ($0.12\sigma_y$)	6.38
60	1	701.7 ($0.64\sigma_y$)	139.2 ($0.13\sigma_y$)	4.76

7.8.3 Discussion

The results from this study show that the residual stresses are sensitive to the layer height. With regard to the displacement of the platform, the effect of reducing the layer height became less significant because the thermal gradients through the thickness and the base platform became more dominant. The decrease in longitudinal stresses with powder layer height found out in this study concurs with an investigative study by Dai and Shaw (2006) in their DMLS study involving nickel powder. In their work, they also found that increasing the layer height reduced the temperature gradient by increasing the heat sink effect into the base platform.

For the same amount of heat energy supplied to the powder surface, the layer heights are directly proportional to the thermal gradients generated. In practice, during the DMLS of metal powders, some building strategies allow the scanning of every other

added layer. This study has shown that this may be advantageous as it reduces the resultant residual stresses.

7.9 Summary of Parametric Investigation of Process Variables

In this chapter, the effects of a number of LM process variables on the residual stresses and platform deformation have been studied using the developed three-dimensional numerical model. Parametric studies involving the number of powder layers, chamber temperature, layer thickness, platform material, scan length, scan speed and platform thickness have been carried out. These studies were carried out by independently altering one variable at a time to investigate their relative effects on the magnitude and distribution of the residual stresses.

The results and trends from the analyses were shown to be concurrent with qualitative and quantitative findings from similar laser-based ALM studies by previous research work in the subject area.

The main findings from the parametric studies can be summarised as follows:

- The residual stress components and platform deformation increased as the number of layers increased. The structural mismatch of material properties was found to be greatest between the first layer and the base platform. For the first Ti64 layer, the longitudinal stress was 52.4% of the yield strength, which increased to 81.4% of the yield strength when the second Ti64 layer was added.

- The surface residual stresses decreased steadily with decreasing platform thickness, but the platform displacement increased significantly as a result of lower stiffness. The findings on the platform thickness analysis supports why thin plates are not suitable for use in the building of large LM parts. In instances where their use is inevitable, adequate restraint considerations would have to be made to prevent excessive distortions. The findings from the platform study also support practical observations. This is analogous to scaling the two layer model considered in this work to actual part sizes in practice (i.e. thousands of layers built on thick platforms). It is observed that platforms become excessively deformed affecting the accuracy of the part and making the process uncontrollable.

- Using a similar platform material as the metal powder reduces the structural mismatch effect. The longitudinal and transverse stresses were reduced by 2.9% and 18.5% respectively when a Ti64 platform was used instead of a steel platform.

- Dividing the layer raster length was found to reduce the average longitudinal stresses in the layer by reducing the stresses at the boundary. Reheating of the interface area during the scanning of the adjacent raster region reduced the longitudinal stresses at the interface by approximately 50%. The side-by-side configuration of the scan regions in this study slightly reduced the platform deformation by 7.7%, but did not eliminate the 'saddle effect'.

- The preheat temperature was found to have the most significant effect on the magnitude and distribution of the residual stresses. Increasing the chamber temperature considerably reduced the residual stress components as a direct result of the reduced cooling rate and reduced thermal gradients. Increasing the temperature from 40°C to 300°C reduced the average longitudinal stresses by more than 50%. At 300°C, pockets of compressive stresses were seen to appear on the surface layer in the longitudinal direction between the scan tracks, while the transverse stresses were found to be completely compressive.

- Reducing the scan speed increases the platform deformation and longitudinal stresses but reduces the transverse stresses on the surface layer. Decreasing the scan speed from 1200 mm/s to 800 mm/s increased the longitudinal stresses by 57 MPa but reduced the transverse stresses by 46 MPa. The increased amount of heat added at reduced scan speeds resulted in greater bending of the platform. In relation to the residual stresses, the scan speed has no significant effect and its selection is mainly based on qualitative characteristics of the built part.

- Halving the layer height decreases the platform deformation but increases the longitudinal stresses. The transverse stresses were found to be sensitive to changes in the layer height, with the temperature gradient through the thickness and the base platform dominating the stress field characteristics if further reduction in the layer height occurs.

Normally, the parts built by the LM process comprise thousands of layers which make it impractical for this study to emulate due to the storage and file size limitations. Nevertheless, the similarities in the stress distributions of the scanned tracks that have been found to exist in this study provide a good case for compressing the simulation process in future research using 'substructuring' or similar simulation techniques.

7.10 Contribution to Knowledge

In addition to the main findings from this work, a few key factors that could serve as pointers for prospective numerical models as well as serve as practical applications of the LM process are presented here.

7.10.1 Numerical Modelling

The review on the development of the residual stresses showed that the thermal stresses become active during consolidation of the molten powder material. In light of this, the temperature field simulation prior to melting may not be critical to the numerical model. This implies that the thermal model could be made more efficient by activating molten elements at temperatures which could be measured experimentally or obtained from a validated calculation model for a given set of process parameters. This would save time and computing resources that could then be applied to the more valuable structural field analysis. The cooling phase of the thermal model has been identified to be dominant stage and can be solved normally as adopted in this work.

The choice of material strain-hardening model clearly had an effect on the accuracy of the structural field analysis and was found to be a key factor in the model. The isotropic hardening model although quicker to solve produced less accurate displacement results than the kinematic hardening model. It was seen in the modelling of three-bar system for the mild steel bars that the choice of strain-hardening model did not significantly affect the final residual stress values. However, the thermal strains and stresses evolved along different paths with time. This kind of interaction with surrounding material is important for obtaining an overall understanding of residual stresses in laser melting.

The findings from this work support the fact that the residual stress fields possess three-dimensional characteristics. The scanned tracks showed similarities in the stress field patterns for the scanned tracks. This might suggest the possibility of further idealisation

like using plate or shell elements. This could result in significant time and storage savings. However, modelling the shrinkage from powder to molten material and modelling one layer on top another may be challenging using this assumption. Using the method of activating the molten material above its melting point as described earlier is a way of circumventing the shrinkage problem, while coupling the nodes may address the multiple-layer problem. These methods provide further challenges and it is the opinion of the author that an effective solution is a three-dimensional one.

The stepwise movement of the laser beam in accordance to the raster scanning method is another important feature of the laser melting process. It is important that the essence of the laser melting process is not compromised by activating whole scan tracks or layers at a single instance.

7.10.2 Practical Application of Findings

Practical applications of the findings of this work that could enhance the experience of users of the laser melting technology include:

- Operating at high chamber temperatures
- Using the shortest possible raster length setting during laser scanning
- Using the highest possible powder recoating speed
- Using the highest possible scan speed that yields acceptable qualitative characteristics (i.e. visual appearance of built parts)
- Setting the layer thickness to give acceptable qualitative characteristics for the selected scan speed and laser power settings.

7.11 Future Work

It is important to note that attempting to account for all the physical aspects in modelling the laser melting problem is extremely difficult and unrealistic. However, the following recommendations could be considered for future work:

- The parametric studies conducted in this work provide a basis for selecting process parameters having seen their relative effects on the residual stresses produced. A further step would be to conduct 2^n design of experiments or factorial experiment. This is the experimental strategy in which factors are varied together, instead of one at a time (Montgomery, 2001). The procedure can be applied to simulation studies to understand the interaction between the process variables and their resultant effects on the distribution of residual stresses.

- The discrete step-wise movement of the laser heat source between spot regions adopted in this work has been found to produce bell-shaped mound tracks and not smooth tracks of solidified material. A potentially accurate method would be to consider step movements according to single element divisions within the irradiation regions.

- It has been seen from the studies that the thermal and residual stress fields experienced by the tracks are very similar; therefore, a future study could embark on compressing the analysis using substructuring techniques for solidified layers.

- The stress variations show characteristic trends, hence data normalisation could be done to obtain a direct mathematical relationship between the parameters and the residual stresses.

- The current model did not take into account fluid behaviour of the molten pool and assumed that the melted tracks fused with the substrate or the previous layer. In the future, contact elements could be used to analyse the delamination effect of added layers as well as the contribution of the fluid behaviour to the thermal stress evolution.

8 Summary

8.1 Project Summary

The aim of this work was to investigate the effect of process and material parameters on the residual stress distribution in the laser melting of metal powders. The main material considered was Ti-6Al-4V powder. A review to establish the relevance of this work was carried out, highlighting the successes and limitations of analytical and numerical models used by previous researchers. This led to the objective of developing a three-dimensional layer-by-layer model for predicting the temperature and the stress field distributions during the LM process.

The model considered key process features like a moving laser heat source, temperature dependent material properties, material state changes and inclusion of multiple powder layers. An innovative simulation technique known as 'element birth and death' was used to simulate the addition of powder layers with time.

The mechanisms governing the development of residual stresses were identified as:

- Steep localised temperature gradients during the cooling of the laser melted powder material, and
- Shrinkage and consolidation of the molten material with the platform or previous layers.

Residual stresses may be detrimental to the functionality or downstream properties of the built parts. Minimising residual stresses would reduce undesired part failure during building and post-processing. Since the laser melting of metal powders is a multivariate process, the process and material variables affect the magnitude and distribution of the residual stresses generated in the scanned powder layers as well as the solid metal platform on which the layers are built. Before considering ways to optimise the process variables, it is pertinent to understand how each variable affects the residual stresses.

In developing the numerical model, a sequentially coupled thermal-structural field analysis was used as described in Chapter 2 and Chapter 4. The temperature history

from the thermal analysis was then used as the load input in the dependent structural analysis to obtain the stress field distributions. The interaction between the Nd:YAG laser beam and the material required some special attention. The attenuation of the laser beam energy as a result of changes in the absorptance due to scattering and change of state of the laser melted material meant that the assumption of constant absorptance value was unrealistic. Therefore, phase dependent absorptance was required to account for changes in laser absorption with material state.

Pilot numerical simulation studies were carried out to validate the adopted analysis method as well as justify the modelling assumptions. The temperature field model was validated against published experimental results. The simulation model predicted maximum temperatures that were within 10% of those published. The structural field was validated against an analytical three-bar structural mismatch model. The accuracy of the structural model was found to depend greatly on the material strain hardening formulation. The kinematic strain hardening model was found to provide better accuracy than the linear isotropic hardening model in predicting the transient and residual stresses in the three-bar structural analysis.

Surface topography experiments using an optical laser confocal scanning microscope were used to validate the displacement fields obtained from the numerical model. The layer-by-layer numerical model using all brick elements and kinematic hardening model was then used to carry out parametric studies to obtain correlations between laser melting process parameters and residual stresses. The parameters investigated were the number of layers, platform thickness, preheat or chamber temperature, platform material, raster length, scan speed and the powder layer height.

8.2 Main Findings

The developed numerical model provides a greater depth of analysis of the thermal and stress fields generated during the LM process. The thermal analysis revealed that:

- The temperature field was characterised by rapid temperature cycles as well as steep and localised temperature gradients in the irradiated regions.
- The irradiated regions experienced very similar temperature histories, except for edge locations.

- The addition and melting of powder layers affected the temperature history of the underlying material (i.e. previously scanned layer(s) and base platform). The temperature-time characteristics as a result of scanning subsequent layers showed strong similarities with those obtained by the multi-pass welding process.

- There was a 120°C difference between the maximum temperature achieved for the first layer and the second layer. The subsequently added layers showed no maximum temperature hikes.

- The recoating process provided ample time for the scanned material to cool back down to a steady temperature close to the chamber temperature. A small but steady increase in temperature above the chamber temperature was observed with each added layer scanned.

The structural analysis revealed that:

- Compressive stresses appear in the irradiated region at the moment of laser scanning, but transform rapidly to tensile stresses as the laser heat source traverses the surface to another location.

- The stress gradients were highly localised around the surface of the layers and the base platform.

- The residual stresses were tensile in the Ti64 layers, compressive in the base platform and were limited by the yield strengths and flow stress characteristics of the Ti64 and steel material.

- The normal component of the residual stresses was very small compared to the longitudinal and transverse stress components.

- The longitudinal stress component was generally greater than the transverse stress component.

- The scanned tracks showed strong similarities for both the longitudinal and transverse stress distributions, except for edge locations.

In terms of the parametric studies, the following conclusions can be drawn:

- Increasing the number of powder layers increased the average residual stress components. The structural mismatch was found to be greater between the first layer and the platform than for the subsequently added second layer.

- Decreasing the platform thickness from 1 mm to 0.3 mm reduced the surface residual stresses. The stress relaxation was found to be greater in the less stiff platform which was a direct increase in the deformation of the platform. This could lead to loss of accuracy in built parts if thin substrates are used.

- Reducing the raster length reduced the stresses at the boundary of the raster regions as a result of the reheating of the interface area. Due to the side-by-side arrangement of the 0.5 mm scan regions, only a 0.49 μm reduction in the platform deformation was obtained and the 'saddle' effect was not eliminated.

- The chamber temperature had the most significant effect on the residual stress distribution. The second cooling stage which involved cooling from the chamber temperature to room temperature was found to be the more dominant stage in the reduction of the residual stresses. Reducing the cooling rate by increasing the chamber temperature was found to significantly reduce the residual stresses in the layers. By increasing the temperature from 40°C to 300°C, the average longitudinal stress in the surface layer was reduced by more than 50% and the 'saddle' effect in the scanned region appeared to be greatly diminished. At 300°C, pockets of compressive stresses in the longitudinal direction were evident on the surface layer, while in the transverse direction they were completely compressive. The longitudinal stresses at the surface of the platform were also found to have reversed from compressive to tensile at 300°C.

- Decreasing the scan speed from 1200 mm/s to 800 mm/s increased the longitudinal stresses by 57 MPa but reduced the transverse stresses by 46 MPa.

- Reducing the layer height resulted in a consistent decrease in the platform displacement and but increased the longitudinal stress in the surface layer. The transverse stresses were found to be sensitive to changes in the layer height, with

the temperature gradient through the thickness and the base platform dominating the stress field characteristics following further reduction in the layer height.

The findings from the parametric study on the effect of process variables agree with qualitative findings of the works undertaken by other researchers relating to the characteristics and distribution of residual stresses in laser-based ALM processes.

In conlcusion, the work presented in this thesis illustrates the potential of numerically modelling the laser melting process. It positively influences the understanding of the development and distribution of residual stresses in the laser melting of metal powders. Through parametric studies, it would not only improve process parameter selection, but also eliminate costly problems and downstream post-processing difficulties. The use of simulation techniques also provides a wide range of information critical for proposing recommendations to optimise the laser melting process.

References

Abe, F., Osakada, K., Shiomi, M., Uematsu, K. and Matsumoto, M. (2001). "The manufacturing of hard tools from metallic powders by selective laser melting". *Journal of Materials Processing Technology* **111**(1-3). pp. 210-213

Adams, V. and Askenazi, A. (1999). "*Building better products with finite element analysis*". Santa Fe, USA, OnWord Press. 156690160X

Altan, T. and Vazquez, V. (1997). "Status of process simulation using 2D and 3D finite element method 'What is practical today? What can we expect in the future?'". *Journal of Materials Processing Technology* **71**(1). pp. 49-63

ANSYS10 (2007). ANSYS Release 10.0 Documentation. ANSYS, Inc.

Antonov, V. and Iordanova, I. (2007). "Development and Application of a Numerical Model for Characterization of Thermal Fields during Surface Laser Treatment of Solid Materials". *Bulgaria Journal of Physics* **34**. pp. 295-306

ARCAM (2010). "*Electron Beam Manufacturing Process*." Last accessed Sep. 2010 from *arcam.com/technology/ebm-process.aspx*.

ASM (1990). "*Metals Handbook: Vol.1 Properties and Selection: Irons, Steels, and High-performance alloys*". Ohio, ASM International.

Badrossamay, M. and Childs, T. H. C. (2007). "Further studies in selective laser melting of stainless and tool steel powders". *International Journal of Machine Tools and Manufacture* **47**(5). pp. 779-784

Bai, P.-K., Cheng, J., Liu, B. and Wang, W.-F. (2006). "Numerical simulation of temperature field during selective laser sintering of polymer-coated molybdenum powder". *Transactions of Nonferrous Metals Society of China* **16**(2). pp. 603-607

Bailey, N. S., Tan, W. and Shin, Y. C. (2009). "Predictive modeling and experimental results for residual stresses in laser hardening of AISI 4140 steel by a high power diode laser". *Surface and Coatings Technology* **203**(14). pp. 2003-2012

Behrendt, U. and Shellabear, M. (1995). "The EOS rapid prototyping concept". *Computers in Industry* **28**(1). pp. 57-61

References

Bejan, A. and Kraus, A. D. (2003). "*Heat Transfer Handbook*", John Wiley & Sons. 978-0-471-39015-2

Bergstrom, D., Powell, J. and Kaplan, A. F. H. (2007). "The Absorptance of Steels to Nd:YLF and Nd:YAG Laser Light at Room Temperature". *Applied Surface Science* **253**(11). pp. 5017-5028

Bertolotti, M. (1983). "*Physical Processes in Laser-Materials Interactions*". New York, Plenum Press. 0-306-41107-5

Beuth, J. L. and Klingbeil, N. W. (1996). "Residual stress-driven delamination in deposited multi-layers". *International Journal of Solids and Structures* **33**(1). pp. 65-78

Blackburn, J. E., Allen, C. M., Hilton, P. A. and Li, L. (2010). "Dual focus Nd:YAG laser welding of titanium alloys". *Proceedings of the 36th International MATADOR Conference*, Manchester, Springer. pp. 279-283.

Boivie, K. (2003). "A Generic System for Homogenous SLS Steel Materials". *Proceedings of the Solid Freeform Fabrication Symposium 2003*, University of Texas, Austin, Texas, USA. 632-642.

Branner, G., Zaeh, M. F. and Groth, C. (2008). "Coupled-Field Simulation in Additive Layer Manufacturing". *Proceedings of the 3rd International Conference on Polymers and Moulds Innovations*, Tokyo, Japan. pp. 184-193.

BSI (2004). "*BS EN ISO 11551:2003:Optics and optical instruments - Lasers and laser-related equipment - Test method for absorptance of optical laser components*". British Standards Institute. pp. 1-26

BSI (2005). "*BS EN ISO 11146-1:2005:Lasers and laser-related equipment - Test methods for laser beam widths, divergence angles and beam propagation ratios - Part 1: Stigmatic and simple astigmatic beams*". British Standards Institute. pp. 1-28

Burakowski, T. and Wierzchon, T. (1998). "*Surface Engineering of Metals: Principles, Equipment and Technologies*", CRC Press. 0849382254

CES (2005). CES Selector Software. Cambridge, Granta Design Limited.

Chakrabarty, J. (2010). "*Applied Plasticity*", Springer: New York. 9780387776736

References

Chen, W.-L., Yang, Y.-C. and Lee, H.-L. (2007). "Estimating the absorptivity in laser processing by inverse methodology". *Applied Mathematics and Computation* **190**. pp. 712-721

Childs, T. H. C., Hauser, C. and Badrossamay, M. (2005). "Selective laser sintering (melting) of stainless and tool steel powders: experiments and modelling". *Proceedings from the Institute of Mechanical Engineers*. pp. 339-357.

Corus. (2010). "*Steelwork Fire Resistance*." Last accessed April 2009 from *corusconstruction.com/en/design_guidance/structural_design/fire/steelwork_fire_resistance*.

Costa, L., Vilar, R., Reti, T. and Deus, A. M. (2005). "Rapid tooling by laser powder deposition: Process simulation using finite element analysis". *Acta Materialia* **53**. pp. 3987-3999

Crafer, R. C. and Oakley, P. J. (1993). "*Laser processing in manufacturing*". London, Chapman & Hall. 0412415208

Dai, K., Crocker, J. E., Shaw, L. and Marcus, H. L. (2003). "Thermal modeling of selective area laser deposition (SALD) and SALD vapor infiltration of silicon carbide ". *Rapid Prototyping Journal* **9**(4). pp. 231-239

Dai, K., Li, X.-X. and Shaw, L. (2004). "Comparisons between thermal modeling and experiments: effects of substrate preheating ". *Rapid Prototyping Journal* **10**(1). pp. 24-34

Dai, K. and Shaw, L. (2001). "Thermal and stress modeling of multi-material laser processing ". *Acta Materialia* **49**(20). pp. 4171-4181

Dai, K. and Shaw, L. (2002). "Distortion minimization of laser-processed components through control of laser scanning patterns ". *Rapid Prototyping Journal* **8**(5). pp. 270-276

Dai, K. and Shaw, L. (2004). "Thermal and mechanical finite element modeling of laser forming from metal and ceramic powders". *Acta Materialia* **52**(1). pp. 69-80

Dai, K. and Shaw, L. (2005). "Finite element analysis of the effect of volume shrinkage during laser densification ". *Acta Materialia* **53**(18). pp. 4743-4754

Dai, K. and Shaw, L. (2006). "Parametric studies of multi-material laser densification". *Materials Science and Engineering: A* **430**(1-2). pp. 221-229

Das, P. (1991). "*Lasers and Optical Engineering*". New York, USA, Springer-Verlag. 0387971084

Donachie, M. (1989). "*Titanium: A Technical Guide*". Ohio, ASM International.

Dong, P., Hong, J. K. and Bouchard, P. J. (2005). "Analysis of residual stresses at weld repairs". *international Journal of Pressure Vessels and Piping* **82**(4). pp. 258-269

Dong, Z. B. and Wei, Y. H. (2006). "Three dimensional modeling weld solidification cracks in multipass welding". *Theoretical and Applied Fracture Mechanics* **46**(2). pp. 156-165

Ekmekci, B., Ekmekci, N., Tekkaya, A. E. and Erden, A. (2004). "Residual stress measurement with layer removal method". *Proceedings of the First Cappadocia International Mechanical Engineering Symposium*, Cappadocia, Turkey.

El-Ghany, S. E.-S. A. (2006). "On the evaporation of a semi-infinite target induced by a pulsed laser". *Optics & Laser Technology* **38**(2). pp. 77-86

Electrical Optical Systems (2005). EOSINT M250Xtended, M270 Basic Operation Manual.

EOS-GmbH (2005). EOSINT M250Xtended, M270 Basic Operation Manual.

EOS-GmbH (2007). "EOS Titanium Ti64 for EOSINT M270 Systems: Material data sheet (provisional data)".

Evans, J. E., Dulieu-Barton, J. M. and Burguete, R. L. (2009). "*Modern stress and strain analysis: A state of the art guide to measurement techniques*". Eureka, U.K. pp. 1-41

FEMA (2010). "*Overview of Fire Protection in Buildings*." Last accessed March 2010 from *fema.gov*.

Fischer, P., Locher, M., Romano, V., Weber, H. P., Kolossov, S. and Glardon, R. (2004). "Temperature measurements during selective laser sintering of titanium powder". *International Journal of Machine Tools and Manufacture* **44**(12-13). pp. 1293-1296

Fischer, P., Romano, V., Weber, H. P., Karapatis, N. P., Boillat, E. and Glardon, R. (2003). "Sintering of commercially pure titanium powder with a Nd:YAG laser source". *Acta Materialia* **51**(6). pp. 1651-1662

Fischer, P., Romano, V., Weber, H. P. and Kolossov, S. (2004). "Pulsed laser sintering of metallic powders". *Thin Solid Films* **453-454**. pp. 139-144

Frewin, M. R. and Scott, D. A. (1999). "Finite Element Model of Pulsed Laser Welding". *Welding Research Supplement*. pp. 15-22

Fu, Y. C., Loredo, A., Martin, B. and Vannes, A. B. (2002). "A theoretical model for laser and powder particles interaction during laser cladding". *Journal of Materials Processing Technology* **128**. pp. 106-112

Gan, Z., Ng, H. W. and Devasenapathi, A. (2004). "Deposition-induced residual stresses in plasma-sprayed coatings". *Surface and Coatings Technology* **187**(2-3). pp. 307-319

Gur, C. H. and Pan, J. (2008). "*Handbook of Thermal Process Modeling of Steels*", CRC Press. 0849350190

Gusarov, A. V., Laoui, T., Froyen, L. and Titov, V. I. (2003). "Contact thermal conductivity of a powder bed in selective laser sintering". *International Journal of Heat and Mass Transfer* **46**(6). pp. 1103-1109

Gusarov, A. V., Yadroitsev, I., Bertrand, P. and Smurov, I. (2007). "Heat transfer modelling and stability analysis of selective laser melting". *Applied Surface Science*. doi:10.1016/j.apsusc.2007.08.074

Im, Y. G., Cho, B. H., Seo, S. H., Son, J. H., Chung, S. I. and Jeong, H. D. (2007). "Functional prototype development of multi-layer board (MLB) using rapid prototyping technology". *Journal of Materials Processing Technology* **187-188**. pp. 619-622

Jaafar, M. S., Bayagoob, K. H., Noorzaei, J. and Thanoon, W. A. M. (2007). "Development of finite element computer code for thermal analysis of roller compacted concrete dams". *Advances in Engineering Software* **38**(11-12). pp. 886-895

Jamal, N. M. (2001). Finite Element Analysis of Curl Development in the Selective Laser Sintering Process. Department of Mechanical Engineering, University of Leeds, Leeds, Ph.D Thesis.

Jiang, W. (2006). 3D FE simulation of the welding process to optimise residual stress profiles in complex geometries. School of Engineering and the Built Environment, University of Wolverhampton, Wolverhampton, Ph.D.

Jiang, W. and Yahiaoui, K. (2007). "Finite element modelling of multi-pass fusion welding with application to complex geometries". *Journals of Materials Design and Applications* **221**(4). pp. 225-234

JunChang, L., Langlade, C. and Vannes, A. B. (1999). "Evaluation of the thermal field developed during pulsed laser treatments: semi analytical calculation ". *Surface and Coatings Technology* **115**(1). pp. 87-93

Kahnert, M., Branner, G. and Zaeh, M. F. (2007). "Adaptive Scanning Strategies for Metal Processing in Additive Layer Manufacturing Methods". *5th International Conference on Laser Assisted Net Shape Engineering (LANE 2007)*, Erlangen, Germany. pp. 25-28.

Karalekas, D. and Rapti, D. (2002). "Investigation of the processing dependence of SL solidification residual stresses ". *Rapid Prototyping Journal* **8**(4). pp. 243-247

Klingbeil, N. W., Beuth, J. L., Chin, R. K. and Amon, C. H. (2002). "Residual stress-induced warping in direct metal solid freeform fabrication". *International Journal of Mechanical Sciences* **44**. pp. 57-77

Klocke, F., Wagner, C. and Klocke, F. (2003). "Coalescence Behaviour of Two Metallic Particles as Base Mechanism of Selective Laser Sintering". *CIRP Annals - Manufacturing Technology* **52**(1). pp. 177-180

Kolossov, S., Boillat, E., Glardon, R., Fischer, P. and Locher, M. (2004). "3D FE simulation for temperature evolution in the selective laser sintering process". *International Journal of Machine Tools and Manufacture* **44**(2-3). pp. 117-123

Koric, S. and Thomas, B. G. (2008). "Thermo-mechanical models of steel solidification based on two elastic visco-plastic constitutive laws ". *Journal of Materials Processing Technology* **197**(1-3). pp. 408-418

Kruth, J.-P., Levy, G., Klocke, F. and Childs, T. H. C. (2007). "Consolidation phenomena in laser and powder-bed based layered manufacturing". *CIRP Annals - Manufacturing Technology* **56**(2). pp. 730-759

Kruth, J. P., Froyen, L., Vaerenbergh, J. V., Mercelis, P., Rombouts, M. and Lauwers, B. (2004). "Selective laser melting of iron-based powder". *Journal of Materials Processing Technology* **149**(1-3). pp. 616-622

Kruth, J. P., Wang, X., Laoui, T. and Froyen, L. (2003). "Lasers and materials in selective laser sintering ". *Assembly Automation* **23**(4). pp. 357-371

Lamikiz, A., Sánchez, J. A., Lacalle, L. N. L. D. and Arana, J. L. (2007). "Laser polishing of parts built up by selective laser sintering". *International Journal of Machine Tools and Manufacture* **47**(12-13). pp. 2040-2050

Lemmon, E. W. and Jacobsen, R. T. (2004). "Viscosity and Thermal Conductivity Equations for Nitrogen, Oxygen, Argon and Air". *International Journal of Thermophysics* **25**(1). pp. 21-69

Li, J. F., Li, L. and Stott, F. H. (2004). "Thermal stresses and their implication on cracking during laser melting of ceramic materials ". *Acta Materialia* **52**(14). pp. 4385-4398

Li, J. Z., Johnson, W. L. and Rhim, W.-K. (2006). "Thermal expansion of liquid $TiAl_6V_4$ measured by electrostatic levitation". *Applied Physics Letters* **89**. doi:10.1063/1.2349840

Li, X. C., Stampfl, J. and Prinz, F. B. (2000). "Mechanical and thermal expansion behavior of laser deposited metal matrix composites of Invar and TiC". *Materials Science and Engineering A* **282**(1-2). pp. 86-90

Majumdar, P. and Xia, H. (2007). "A Green's function model for the analysis of laser heating of materials ". *Applied Mathematical Modelling* **31**(6). pp. 1186-1200

Mardolcar, U. V., Castro, C. A. N. D. and Wakeham, W. A. (1986). "Thermal conductivity of liquid argon in the temperature range 107K to 423K". *International Journal of Thermophysics* **7**(2). pp. 259-272

Masubuchi, K. (1980). "*Analysis of Welded Structures*". Massachusetts: Pergamon Press. 0-08-022714-7

Matsumoto, M., Shiomi, M., Osakada, K. and Abe, F. (2002). "Finite element analysis of single layer forming on metallic powder bed in rapid prototyping by selective laser processing". *International Journal of Machine Tools and Manufacture* **42**(1). pp. 61-67

Mercelis, P. and Kruth, J.-P. (2006). "Residual stresses in selective laser sintering and selective laser melting". *Rapid Prototyping Journal* **12**(5). pp. 254-265

Microsoft Excel (2010), Microsoft Excel Function Reference. Microsoft Corporation, USA.

Mills, K. C. (2002). "*Recommended Values of Thermophysical Properties for Selected Commercial Alloys*", Cambridge: Woodhead Publishing. 1855735695

Montgomery, D. C. (2001). "*Design and Analysis of Experiments*". New York: Wiley. 0471316490

Morgan, R., Sutcliffe, C. J. and O'Neill, W. (2001). "Experimental investigation of nanosecond pulsed Nd:YAG laser re-melted pre-placed powder beds". *Rapid Prototyping Journal* **7**(3). pp. 159-172

Morris-Technologies (2007) "Direct Metal Laser-Sintering (DMLS) Technology for Rapid Tooling and Parts." pp. 1-62

Nisar, A., Schmidt, M. J. J., Sheikh, M. A. and Li, L. (2003). "Three-dimensional transient finite element analysis of the laser enamelling process and moving heat source and phase change considerations". *Proceedings of the Institution of Mechanical Engineers -- Part B -- Engineering Manufacture* **217**(6). pp. 753-764

Niu, H. J. and Chang, I. T. H. (2000). "Selective Laser Sintering of Gas Atomised M2 High Speed Steel Powder". *Journal of Materials Science 2000* **35**(1). pp. 31-38

Noorani, R. I. (2006). "*Rapid Prototyping: Principles and Applications*". New Jersey, USA, John Wiley & Sons Inc. 0471730017

Noorzaei, J., Bayagoob, K. H., Thanoon, W. A. and Jaafar, M. S. (2006). "Thermal and stress analysis of Kinta RCC dam". *Engineering Structures* **28**(13). pp. 1795-1802

Olakanmi, E. O., Cochrane, R. F. and Dalgarno, K. W. (2011). "Densification mechanism and microstructural evolution in selective laser sintering of Al-12Si powders". *Journal of Materials Processing Technology* **211**. pp. 113-121

Oliveira, U. D., Ocelík, V. and Hosson, J. T. M. D. (2005). "Analysis of coaxial laser cladding processing conditions". *Surface and Coatings Technology* **197**(2-3). pp. 127-136

Olympus (2008). "Confocal Laser Scanning Microscope - LEXT OLS3000/3100 User's Manual.

Osakada, K. and Shiomi, M. (2006). "Flexible manufacturing of metallic products by selective laser melting of powder". *International Journal of Machine Tools and Manufacture* **46**(11). pp. 1188-1193

Patil, R. B. and Yadava, V. (2007). "Finite element analysis of temperature distribution in single metallic powder layer during metal laser sintering". *International Journal of Machine Tools and Manufacture* **47**(7-8). pp. 1069-1080

Pinkerton, A. J. and Li, L. (2004). "The significance of deposition point standoff variations in multiple-layer coaxial laser cladding (coaxial cladding standoff effects)". *International Journal of Machine Tools and Manufacture* **44**(6). pp. 573-584

Pope, E. J. (1997). "*Rules of Thumb for Mechanical Engineers*". Houston, Texas, Gulf Publishing Company. 978-0-088415-790-8

Raghunath, N. and Pandey, P. M. (2007). "Improving accuracy through shrinkage modelling by using Taguchi method in selective laser sintering". *International Journal of Machine Tools and Manufacture* **47**(6). pp. 985-995

Ramberg, W. and Osgood, W. (1943)."Description of stress-strain curves by three parameters." NASA Scientific and Technical Information Facility. pp. 1-48

Ready, J. F. (1971). "*Effects of high-power laser radiation* ". New York ; London Academic Press. 0125839502

Rohsenow, W. M., Hartnett, J. P. and Cho, Y. I. (1998). "*Handbook of Heat Transfer*". New York, McGraw-Hill. ISBN 0-07-053555-8

Rombouts, M., Froyen, L., Gusarov, A. V., Bentefour, E. H. and Glorieux, C. (2005). "Light extinction in metallic powder beds: Correlation with powder structure". *Journal of Applied Physics* **98**(1). pp. 013533 – 013533-9. doi: 10.1063/1.1948509

Rombouts, M., Kruth, J. P., Froyen, L. and Mercelis, P. (2006). "Fundamentals of Selective Laser Melting of Alloyed Steel Powders". *CIRP Annals - Manufacturing Technology* **55**(1). pp. 187-192

Samarskii, A. A. and Vabishchevich, P. N. (1995). "*Computational heat transfer, Mathematical modelling.* ". Chichester John Wiley & Sons. 0471956597

Santos, E. C., Shiomi, M., Osakada, K. and Laoui, T. (2006). "Rapid manufacturing of metal components by laser forming". *International Journal of Machine Tools and Manufacture* **46**(12-13). pp. 1459-1468

Schneider, M. (1998). Laser Cladding with Powder: Effect of some machining parameters on clad properties. University of Twente, Enschede, Ph.D

Shen, X.-F., Wang, Y., Yao, J. and Yang, J.-L. (2005). "Finite element simulation of thermal distribution in direct metal laser multi-track sintering". *Journal of Sichuan University (Engineering Science Edition)* **37**(1). pp. 47-51

Shen, Z. H., Zhang, S. Y., Lu, J. and Ni, X. W. (2001). "Mathematical modeling of laser induced heating and melting in solids". *Optics & Laser Technology* **33**. pp. 533-537

Shi, Y., Shen, H., Yao, Z. and Hu, J. (2007). "Temperature gradient mechanism in laser forming of thin plates". *Optics & Laser Technology* **39**. pp. 858-863

Shiomi, M., Osakada, K., Nakamura, K., Yamashita, T. and Abe, F. (2004). "Residual stress within metallic model made by selective laser melting process". *International Journal of Machine Tools and Manufacture* **46**(11). pp. 1188-1193

Shiomi, M., Yoshidome, A., Abe, F. and Osakada, K. (1999). "Finite element analysis of melting and solidifying processes in laser rapid prototyping of metallic powders". *International Journal of Machine Tools and Manufacture* **39**(2). pp. 237-252

Sih, S. S. and Barlow, J. W. (2004). "The prediction of the emissivity and thermal conductivity of powder beds". *Particulate Science and Technology* **22**. pp. 427-440

Simchi, A. (2006). "Direct laser sintering of metal powders: Mechanism, kinetics and microstructural features". *Materials Science and Engineering A* **428**(1-2). pp. 148-158

Sowdari, D. and Majumdar, P. (2010). "Finite element analysis of laser irradiated metal heating and melting processes". *Optics & Laser Technology* **42**. pp. 855-865

Steen, W. M. (2003). "*Laser Material Processing*". Berlin, Springer-Verlag. 1852336986

Stewart, T. D., Dalgarno, K. W. and Childs, T. H. C. (1999). "Strength of the DTM RapidSteel 1.0 Material". *Materials and Design* **20**. pp. 133-138

Tang, Y., Loh, H. T., Wong, Y. S., Fuh, J. Y. H., Lu, L. and Wang, X. (2003). "Direct laser sintering of a copper-based alloy for creating three-dimensional metal parts". *Journal of Materials Processing Technology* **140**(1-3). pp. 368-372

Taylor, C. M. (2004). Direct Laser Sintering of Stainless Steel: Thermal Experiments and Numerical Modelling. School of Mechanical Engineering, University of Leeds, Leeds, Ph.D

Thummler, F. and Oberacker, R. (1993). "*An Introduction to Powder Metallurgy*". London, The University Press, Cambridge. 090171626X

Tolochko, N., Laoui, T., Khlopkov, Y. V., Titov, V. I. and Ignatiev, M. B. (2000). "Absorptance of powder materials suitable for laser sintering". *Rapid Prototyping Journal* **6**(3). pp. 155-160

Tolochko, N. K., Arshinov, M. K., Gusarov, A. V., Titov, V. I., Laoui, T. and Froyen, L. (2003). "Mechanisms of selective laser sintering and heat transfer in Ti powder". *Rapid Prototyping Journal* **9**(5). pp. 314-326

Tolochko, N. K., Mozzharov, S. E., Yadroitsev, I. A., Laoui, T., Froyen, L., Titov, V. I. and Ignatiev, M. B. (2004). "Balling processes during selective laser treatment of powders ". *Rapid Prototyping Journal* **10**(2). pp. 78-87

Touloukian, Y. S. (1977). "*Thermal Expansion: Metallic Elements and Alloys*", IFI/Plenum. 0306670321

TRUMPF (2007). "Laser Processing - CO_2 Laser: Technical Documentation"**.** pp. 1-156.

USDD (1998). "*Military Handbook - MIL-HDBK-5H: Metallic Materials and Elements for Aerospace Vehicle Structures*", U.S. Department of Defence. 978-1-59124-543-8

Wang, X. (1999). "Calibration of Shrinkage and Beam Offset in SLS Process". *Rapid Prototyping Journal* **5**(3). pp. 129-133

Wang, X. C., Laoui, T., Bonse, J. E., Kruth, J. P., Lauwers, B. and Froyen, L. (2002). "Direct Selective Laser Sintering of Hard Metal Powders: Experimental Study and Simulation". *International Journal of Advanced Manufacturing Technology* **19**. pp. 351-357

Wohlers, T. (2006). "Rapid Prototyping and Manufacturing: State of the Industry: Executive Summary, Wohlers Report 2006". Colorado, USA. pp. 1-8.

Wrekin-Steels (2009). BS970 070M20 material properties data sheet, Wrekin Steels Limited.

Yadroitsev, I., Bertrand, P. and Smurov, I. (2007). "Parametric analysis of the selective laser melting process". *Applied Surface Science* **299**(1-2). pp. 138-145

Yakovlev, A., Trunova, E., Grevey, D., Pilloz, M. and Smurov, I. (2005). "Laser-assisted direct manufacturing of functionally graded 3D objects". *Surface and Coatings Technology* **190**(1). pp. 15-24

Yang, H.-J., Hwang, P.-J. and Lee, S.-H. (2002). "A study on shrinkage compensation of the SLS process by using the Taguchi method". *International Journal of Machine Tools and Manufacture* **42**(11). pp. 1203-1212

Yilbas, B. S., Sami, M. and Shuja, S. Z. (1998). "Laser-induced thermal stresses on steel surface". *Optics and Lasers in Engineering* **30**(1). pp. 25-37

Young, M. (1977). "*Optics and lasers : an engineering physics approach*". Berlin; New York, Springer-Verlag. 3540081267

Zaeh, M. F. and Branner, G. (2010). "Investigations on residual stresses and deformations in selective laser melting". *Production Engineering Research and Development* **4**. pp. 35-45

Zaeh, M. F., Lutzmann, S., Branner, G. and Strasser, G. (2008). "Solutions for Modelling the Energy Input in Electron Beam Material Processing". *Proceedings of the 9th Biennial ASME Conference on Engineering Systems Design and Analysis*, Haifa, Israel.

Zhang, P., Guo, B., Shan, D.-B. and Ji, Z. (2007). "FE simulation of laser curve bending of sheet metals". *Journal of Materials Processing Technology* **184**(1-3). pp. 157-162

Appendices

Appendix 1: TITANIUM POWDER TEMPERATURE FIELD SIMULATION

```
!TITANIUM SPOT TEMPERATURE ANALYSIS
!VALIDATION REF. (Kolossov 2004)
! TEMP-DEPENDENT MAT. PROP.
!PURE Ti POWDER.

D=100E-6                !BEAM DIAMETER (m)
PH=30E-6                !LAYER HEIGHT (m)
V=1E-3                  !SCAN SPEED (m/s)
T=D/V                   !SPOT IRRADIATION TIME (s)
NL=15                   !NUMBER OF LAYERS
HD=PH*NL                !DEPTH OF POWDER BED, depth = 0.45mm
B=1.5E-3                !POWDER BED LENGTH
A=3.142*(D/2)**2        !SPOT AREA
NU=0.865                !AVG CONSTANT FROM GAUSS DIST.
ABS=0.3                 !ABSORPTANCE POWDER
AB=0.1                  !ABSOPTANCE MELT
RT=25                   !ROOM TEMP

TOL=1E-6                !NUMERICAL TOLERANCE
BTOL,TOL
H=20                    !CONVECTION COEFF. (W/m2K)
PWR=3                   !LASER POWER (W)

/CONFIG,NPROC,3
/FILNAME, SPOT_TEMP
/PREP 7
/VIEW,1,-0.5,-0.75,0.5

ET,1,77                 !2D THERMAL ELEMENT
ET,2,70                 !3D THERMAL ELEMENT

!DEFINE MATERIAL PROPERTIES
MPT=1670                                                    !MELTING PT.
MPTEMP,,25,400,800,1660,1670,2800                           !TEMPERATURE DEPENDENT MAT. PROP
MPDATA,KXX,1,,20.5,20.8,31,31,31,31
!MPDATA,ENTH,1,,0,217E3,483E3,1190E3,1485E3,2575E3          !ENTHALPY  J/kg
MPDATA,ENTH,1,,1,973.2e6,2137.3e6,5105.1e6,6148e6,9991e6    !ENTHALPY  J/m3
DENS_RATIO = 0.6                                            !MEASURED BULK DENSITY RATIO
MP,KXX,2,0.25                                               !POWDER CONDUCTIVITY
MPDATA,ENTH, 2,,0,583.9e6,1282.4e6,3063e6,6148E6,9991E6     !POWDER ENTHALPY

!BUILD MODEL
CYL4,,,D/2,,,90,                                            !CREATE SPOT AND SURR. REGIONS.
CYL4,,,D/2+D/3,,,90
BLC4,,,B/2,B/2,
AOVLAP,ALL
LSEL,S,LINE,,1,4,3
LESIZE,ALL,,,10
LSEL,S,LENGTH,,D/3-TOL,D/3+TOL
LESIZE,ALL,,,5
ASEL,S,AREA,,1
LSLA,S,
LESIZE,ALL,,,8
LSEL,S,LENGTH,,B/2-D/2-D/3,B
LESIZE,ALL,,,20
ND=3                                                        !LAYER DIVISION CONSTANT
ASEL,S,LOC,Z,0                                              !TOP SURFACE
CM,ATOP,AREA
AATT,2,,1
ALLSEL,ALL
TYPE,1                                                      !MESH 2D OPT.
MSHAPE,0,2D
T1=T/200
MSHKEY,0
```

```
AMESH,ALL
TYPE,2                                          !EXTRUDE TO 3D MESH
EXTOPT,ESIZE,ND*2
EXTOPT,ATTR,1
EXTOPT,ON
!EXTOPT,ACLEAR,1
VEXT,ATOP,,,,,-ND*PH

ASEL,S,LOC,Z,-ND*PH
CM,ABOT,AREA
EXTOPT,ESIZE,5
EXTOPT,ACLEAR,1
VEXT,ABOT,,,,,-HD

NORG=NODE(0,0,0)
NX=NODE(b,0,0)
NPL=NODE(0,b,0)
CS,11,1,NORG,nx,npl                             !CYL COORD SYS

CSYS,11                                         !DEFINE SURFACE NODE COMPS.
NSEL,S,LOC,Z,0
NSEL,S,LOC,X,D/2
CM,NSPOT,NODE
NSEL,S,LOC,Z,0
NSEL,U,LOC,X, D/2
CM,NSURF,NODE
ALLSEL,ALL
CSYS,0
CDWRITE,DB,SPOT_TEMP,CDB                        !ARCHIVE NODES AND ELEMENTS
FINISH
/FILNAME,SPOT_TEMP
/CLEAR
/PREP7
CDREAD,DB,SPOT_TEMP,CDB
SHPP,OFF

/SOLU
ANTYPE,4                                        !TRANSIENT ANALYSIS
TRNOPT,FULL                                     !FULL TRANSIENT OPTION
NROPT,FULL                                      !FULL NEWTON-RAPHSON OPTION
LUMPM,0                                         !NON-LINEAR SOLUTION SETTINGS
LNSRCH,ON
SOLCONTROL,ON
EQSLV,ITER,1                                    !USE ITERATIVE SOLVER
NEQIT,50
TUNIF,RT                                        !START TEMP.
CNVTOL,HEAT,,0.02,,1e-6
OUTRES,ALL,ALL
AUTOTS,OFF
KBC,0
NSUBST,3

!APPLY BOUNDARY CONDITIONS
SF,NSURF,CONV,H,RT                              ! CONV. TO SURFACE
R=NU*ABS*PWR/A                                  !RESULTANT HEAT FLUX
SF,NSPOT,HFLUX,R
TIME,T1
ALLSEL,ALL
SOLVE                                           !SOLVE FIRST TIME STEP
OUTRES,ERASE
TSRES,ERASE
NSEL,S,TEMP,,MPT                                !CHECK ELEMENT STATE
CM,NMELT,NODE
ESLN,S,0
CM,EMELT,ELEM
MPCHG,1,ALL                                     !CONVERT ELEMENTS T > MPT.
ALLSEL
ESEL,U,ELEM,,EMELT
CM,EPWD,ELEM                                    !UNCONVERTED ELEMS.
NSLE,S,ALL
```

```
CM,NPWD,NODE
ALLSEL,ALL
NSEL,S,NODE,,NMELT
NSEL,U,NODE,,NPWD
CM,NMOVE1,NODE
ALLSEL,ALL
SFDELE,NSPOT,HFLUX                                  !REMOVE B.C.S AFTER STEP
SFEDELE,ALL,ALL,HFLUX

/PREP7                                              !ENFORCE SHRINKAGE
NMODIF,NMOVE,1,,, 0.2*PH
/SOLU
ANTYPE,,REST

!MANUALLY APPLY PRG. EXT FOR EACH LOOP AT THIS POINT
NP=2                                                !REPEAT FOR INTERMEDIATE
DIVISIONS
NSUBST,1
OUTRES,BASIC,LAST
*DO,NTM,1,1,1
R=NU*AB*PWR/A                                       !ADJUSTED ABSORPTANCE FOR MELT
SF,NSPOT,HFLUX,R
TIME,T1+NTM*(T-T1)/NP
ALLSEL,ALL
SOLVE
NSEL,S,TEMP,,MPT
CM,NMELT,NODE
ESLN,S,1
CM,EMELT,ELEM
MPCHG,1,ALL
ALLSEL,ALL
SFDELE,ALL,HFLUX
SFEDELE,ALL,ALL,HFLUX
*ENDDO

!/POST1                                             !PLOT NODAL TEMP. DISTRIBUTION
!PLNSOL,TEMP

/POST26
NSOL,2,NORG,TEMP,,T_CTR                             !PLOT NODAL TEMP HISTORY
PLVAR,2,
```

Appendix 2: PARAMETRIC SIMULATION MODEL

```
!PARAMETRIC STUDY PROGRAM
!1MM BY 1MM LAYERS ON 3MM BY 3MM PLATFORM
!----------------------------------------
H=30E-6                 !LAYER THICKNESS
P=100000                !LAYER CONSTANT
L=1E-3                  !RASTER LENGTH
D=100E-6                !SPOT SIZE (DIA)
TX=1.0001E-3            !SURROUNDING REGION ALLOWANCE
TZ=1.0001E-3
BY=0.3001E-3            !BLOCK HEIGHT
BH=BY                   !BLOCK Y-COORDINATE
SD=0.0601E-3            !BORDER OFFSET
!-----------------------------------------------------
N=2                     !NO. OF LAYERS
NS=10                   !NUMBER OF STRIPES
NX=L/D                  !NO. OF SCAN DIVISIONS ON RASTER
NT=1                    !NUMBER OF RASTERS
TR=8                    !RECOATING TIME IN SEC
NHV=NS*NX               !NO. OF HATCHES IN ONE RASTER
!-----------------------------------------------------------
!-----------------------------------------------------
MU=0.865                !AVG. CONSTANT FROM GAUSS DIST.
ABS=0.3                 !ABSORPTANCE
AB=0.1                  !absorptance post-melting pt.
A=3.142*(D/2)**2        !SPOT AREA
!-----------------------------------------------------
!-----------------------------------------------
PWR=195                 !POWER
LSPD=1200E-3            !LASER SPEED
TM=D/LSPD               !SPOT IRRADIATION TIME
!-----------------------------------------------
!-----------------------------------------------
HF=20                   !CONV. COEFF.
TC=40                   !CHAMBER TEMPERATURE
!-----------------------------------------------
TOL=1E-8                !TOLERANCE
OVL=1E-6
!----------------------------------------
/CONFIG,NRES,30000              !SUBSTEP LIMIT
/CONFIG,NPROC,4
!----------------------------------------
!---------------
/FILNAME,laser
/PREP7
/VIEW,1,1,1,1
!-----------------
!CREATE BASE KEYPTS
!-------------------
J=1
K,(J-1)*P+21,-TX,-2*H,-TZ                                       !BASE BLOCK KPS
K,(J-1)*P+22,,-2*H,,
K,(J-1)*P+23,,-2*H,NS*D-OVL
K,(J-1)*P+24,-TX,-2*H,NS*D+TZ
K,(J-1)*P+25,L*NT+TX,-2*H,-TZ
K,(J-1)*P+26,L*NT,-2*H,,
K,(J-1)*P+27,L*NT,-2*H,NS*D-OVL
K,(J-1)*P+28,L*NT+TX,-2*H,NS*D+TZ
K,(J-1)*P+31,-SD,-2*H,-SD
K,(J-1)*P+32,L*NT+SD,-2*H,-SD
K,(J-1)*P+33,-SD,-2*H,NS*D+SD
K,(J-1)*P+34,L*NT+SD,-2*H,NS*D+SD
K,(J-1)*P+35,-TX,-BH,-TZ                                        !2nd division
K,(J-1)*P+36,,-BH,,
K,(J-1)*P+37,,-BH,NS*D-OVL
K,(J-1)*P+38,-TX,-BH,NS*D+TZ
K,(J-1)*P+41,L*NT+TX,-BH,-TZ
K,(J-1)*P+42,L*NT,-BH,,
K,(J-1)*P+43,L*NT,-BH,NS*D-OVL
```

```
K,(J-1)*P+44,L*NT+TX,-BH,NS*D+TZ
K,(J-1)*P+45,-SD,-BH,-SD
K,(J-1)*P+46,L*NT+SD,-BH,-SD
K,(J-1)*P+47,-SD,-BH,NS*D+SD
K,(J-1)*P+48,L*NT+SD,-BH,NS*D+SD
!----------------------
!CREATE MODEL LAYERS
!----------------------
*DO,J,1,N,1
!J----LAYER NO.
!G---X-ROW MULTIPLIER
!G1----Z-ROW MULTIPLIER
K,(J-1)*P+1,-TX,(J-1)*H,-TZ                                    !LOWER TIER KPS
K,(J-1)*P+2,,(J-1)*H,,
K,(J-1)*P+3,,(J-1)*H,NS*D-OVL
K,(J-1)*P+4,-TX,(J-1)*H,NS*D+TZ
K,(J-1)*P+5,L*NT+TX,(J-1)*H,-TZ
K,(J-1)*P+6,L*NT,(J-1)*H,,
K,(J-1)*P+7,L*NT,(J-1)*H,NS*D-OVL
K,(J-1)*P+8,L*NT+TX,(J-1)*H,NS*D+TZ
K,(J-1)*P+9,L*NT+SD,(J-1)*H,-SD
K,(J-1)*P+10,-SD,(J-1)*H,-SD
K,(J-1)*P+11,-SD,(J-1)*H,NS*D+SD
K,(J-1)*P+12,L*NT+SD,(J-1)*H,NS*D+SD
K,J*P+1,-TX,J*H,-TZ                                                !UPPER TIER KPS
K,J*P+2,,J*H,,
K,J*P+3,,J*H,NS*D-OVL
K,J*P+4,-TX,J*H,NS*D+TZ
K,J*P+5,L*NT+TX,J*H,-TZ
K,J*P+6,L*NT,J*H,,
K,J*P+7,L*NT,J*H,NS*D-OVL
K,J*P+8,L*NT+TX,J*H,NS*D+TZ
K,J*P+9,L*NT+SD,J*H,-SD
K,J*P+10,-SD,J*H,-SD
K,J*P+11,-SD,J*H,NS*D+SD
K,J*P+12,L*NT+SD,J*H,NS*D+SD
!!CREATE SURROUNDING POWDER VOLUME
V,(J-1)*P+1,(J-1)*P+10,(J-1)*P+11,(J-1)*P+4,J*P+1,J*P+10,J*P+11,J*P+4
V,(J-1)*P+10,(J-1)*P+2,(J-1)*P+3,(J-1)*P+11,J*P+10,J*P+2,J*P+3,J*P+11
V,(J-1)*P+1,(J-1)*P+5,(J-1)*P+9,(J-1)*P+10,J*P+1,J*P+5,J*P+9,J*P+10
V,(J-1)*P+10,(J-1)*P+9,(J-1)*P+6,(J-1)*P+2,J*P+10,J*P+9,J*P+6,J*P+2
V,(J-1)*P+5,(J-1)*P+8,(J-1)*P+12,(J-1)*P+9,J*P+5,J*P+8,J*P+12,J*P+9
V,(J-1)*P+9,(J-1)*P+12,(J-1)*P+7,(J-1)*P+6,J*P+9,J*P+12,J*P+7,J*P+6
V,(J-1)*P+8,(J-1)*P+4,(J-1)*P+11,(J-1)*P+12,J*P+8,J*P+4,J*P+11,J*P+12
V,(J-1)*P+12,(J-1)*P+11,(J-1)*P+3,(J-1)*P+7,J*P+12,J*P+11,J*P+3,J*P+7

NUMSTR,VOLU,J*P
        *DO,NR,1,NT,1                                          !CREATE RASTER VOLUMES
        *DO,G1,0,NS-1,2                                        !DUPLICATE X-ROW HATCHES IN Z-DIR
                *DO,G,(NR-1)*NX,NR*NX-1,1                      !CREATE X-DIR. ROW HATCHES SQUARE
STRIPING SEQUENCE
                *IF,G1,EQ,0,THEN
                BLOCK,G*D,(G+1)*D,(J-1)*H,J*H,G1*D,(G1+1)*D
                *ELSE
                BLOCK,G*D,(G+1)*D,(J-1)*H,J*H,G1*D-OVL,(G1+1)*D-OVL
                *ENDIF
                *ENDDO
        *IF,G1,EQ,NS-1,CYCLE
                *DO,G,NR*NX-1,(NR-1)*NX,-1
                *IF,G1,EQ,0,THEN
                BLOCK,(G+1)*D,G*D,(J-1)*H,J*H,(G1+1)*D,(G1+2)*D-OVL
                *ELSE
                BLOCK,(G+1)*D,G*D,(J-1)*H,J*H,(G1+1)*D-OVL,(G1+2)*D-OVL
                *ENDIF
                *ENDDO
        *ENDDO                                                 !END STRIPES
        *ENDDO
*ENDDO                                                         !END LAYERS
!----------------------
!BASE BLOCK VOLUME
```

```
!----------------------
J=1
V,(J-1)*P+1,(J-1)*P+10,(J-1)*P+11,(J-1)*P+4,(J-1)*P+21,(J-1)*P+31,(J-1)*P+33,(J-1)*P+24
V,(J-1)*P+10,(J-1)*P+2,(J-1)*P+3,(J-1)*P+11,(J-1)*P+31,(J-1)*P+22,(J-1)*P+23,(J-1)*P+33
V,(J-1)*P+1,(J-1)*P+5,(J-1)*P+9,(J-1)*P+10,(J-1)*P+21,(J-1)*P+25,(J-1)*P+32,(J-1)*P+31
V,(J-1)*P+10,(J-1)*P+9,(J-1)*P+6,(J-1)*P+2,(J-1)*P+31,(J-1)*P+32,(J-1)*P+26,(J-1)*P+22
V,(J-1)*P+5,(J-1)*P+8,(J-1)*P+12,(J-1)*P+9,(J-1)*P+25,(J-1)*P+28,(J-1)*P+34,(J-1)*P+32
V,(J-1)*P+9,(J-1)*P+12,(J-1)*P+7,(J-1)*P+6,(J-1)*P+32,(J-1)*P+34,(J-1)*P+27,(J-1)*P+26
V,(J-1)*P+8,(J-1)*P+4,(J-1)*P+11,(J-1)*P+12,(J-1)*P+28,(J-1)*P+24,(J-1)*P+33,(J-1)*P+34
V,(J-1)*P+12,(J-1)*P+11,(J-1)*P+3,(J-1)*P+7,(J-1)*P+34,(J-1)*P+33,(J-1)*P+23,(J-1)*P+27
V,(J-1)*P+2,(J-1)*P+6,(J-1)*P+7,(J-1)*P+3,(J-1)*P+22,(J-1)*P+26,(J-1)*P+27,(J-1)*P+23

V,(J-1)*P+21,(J-1)*P+31,(J-1)*P+33,(J-1)*P+24,(J-1)*P+35,(J-1)*P+45,(J-1)*P+47,(J-1)*P+38
V,(J-1)*P+31,(J-1)*P+22,(J-1)*P+23,(J-1)*P+33,(J-1)*P+45,(J-1)*P+36,(J-1)*P+37,(J-1)*P+47
V,(J-1)*P+21,(J-1)*P+25,(J-1)*P+32,(J-1)*P+31,(J-1)*P+35,(J-1)*P+41,(J-1)*P+46,(J-1)*P+45
V,(J-1)*P+31,(J-1)*P+22,(J-1)*P+23,(J-1)*P+33,(J-1)*P+45,(J-1)*P+36,(J-1)*P+37,(J-1)*P+47
V,(J-1)*P+31,(J-1)*P+32,(J-1)*P+26,(J-1)*P+22,(J-1)*P+45,(J-1)*P+46,(J-1)*P+42,(J-1)*P+36
V,(J-1)*P+25,(J-1)*P+28,(J-1)*P+34,(J-1)*P+32,(J-1)*P+41,(J-1)*P+44,(J-1)*P+48,(J-1)*P+46
V,(J-1)*P+32,(J-1)*P+34,(J-1)*P+27,(J-1)*P+26,(J-1)*P+46,(J-1)*P+48,(J-1)*P+43,(J-1)*P+42
V,(J-1)*P+28,(J-1)*P+24,(J-1)*P+33,(J-1)*P+34,(J-1)*P+44,(J-1)*P+38,(J-1)*P+47,(J-1)*P+48
V,(J-1)*P+34,(J-1)*P+33,(J-1)*P+23,(J-1)*P+27,(J-1)*P+48,(J-1)*P+47,(J-1)*P+37,(J-1)*P+43
V,(J-1)*P+22,(J-1)*P+26,(J-1)*P+27,(J-1)*P+23,(J-1)*P+36,(J-1)*P+42,(J-1)*P+43,(J-1)*P+37

!!ELEMENT TYPE
ET,1,70                                                    !SOLID70
!DEFINE TEMP DEPENDENT MATERIAL PROPS
MPT=1660
MPTEMP,,25,400,800,1640,1660,2800
!MPDATA,DENS,1,,4420,4365,4310,4190,3920,3140
MPDATA,KXX,1,,7,11.35,17.8,28.4,33.4,34.6                  !THERMAL CONDUCTIVITY
!MPDATA,ENTH,1,,0,220E3,490E3,1185E3,1465E3,2425E3         ! ENTHALPY J/kg
MPDATA,ENTH,1,,1,960.3e6,2111.9e6,4965.2e6,5707.5e6,7614.5e6   !VOLUMETRIC ENTHALPY  J/m3
!MPDATA,DENS,2,,7950,7785,7575,6720,6725,5630              !STEEL BASE

MPDATA,KXX,2,,51.9,49.9,29.3,30,30,30                      !THERMAL CONDUCTIVITY
! MPDATA,ENTH,2,,0,225e3,490e3,1340e3,1355e3,1710e3        ! ENTHALPY J/kg
MPDATA,ENTH,2,,1,1751.6E6,3711.8E6,9004.8E6,9112.4E6,9627.3E6   ! ENTHALPY J/m3
MP,KXX,3,0.3                                               !POWDER PROPS.
MPDATA,ENTH,3,,0,576.2e6,1267.1e6,2980e6,5707.5E6,7614.5E6
!---------------------------
!ASSIGN MATLS TO REGIONS
!---------------------------
VSEL,S,LOC,Y,-BH,TOL
VATT,3,,1
VSEL,S,LOC,Y,-TOL,N*H+TOL
VATT,3,,1
!MESH VOLUMES
NA=4                                                       !SPOT AREA DIVS
NH=1
VSEL,S,LOC,X,TOL,NT*L-TOL                                  !DIVIDE LAYERS
VSEL,R,LOC,Z,TOL,NS*D-TOL
VSEL,R,LOC,Y,TOL,N*H
CM,VREQ,VOLU                                               !VOLUME OF INTEREST
ASLV,S,ALL
LSLA,S,ALL
LSEL,S,LENGTH,,D-TOL,D+TOL
LSEL,A,LENGTH,,D-OVL-TOL,D-OVL+TOL
LESIZE,ALL,,,NA                                            !DIVIDE AREA LINES INTO 4 DIVISIONS
LSEL,S,LENGTH,,H-TOL,H+TOL
LESIZE,ALL,,,NH                                            !DIVIDE LAYER THICKNESS INTO N LEVELS
VMESH,ALL

ALLSEL,ALL                                                 !SURROUNDING POWDER VOLUME
VSEL,U,VOLU,,VREQ
VSEL,U,LOC,Y,-BH,0
CM,VPWD,VOLU
ALLSEL,ALL                                                 !DIVIDE SURROUNDING POWDER
LSEL,S,LENGTH,,L*NT-TOL,L*NT+TOL
LSEL,A,LENGTH,,L*NT+2*SD-TOL, L*NT+2*SD+TOL
LESIZE,ALL,,,NT*NX*NA
```

```
LSEL,S,LENGTH,,NS*D-OVL-TOL,NS*D-OVL+TOL
LSEL,A,LENGTH,,NS*D+2*SD-TOL,NS*D+2*SD+TOL
!LSEL,A,LENGTH,,NS*D+2*TX-TOL,NS*D+2*TX+TOL
!LSEL,A,LENGTH,,NS*D+2*TZ-TOL,NS*D+2*TZ+TOL
LESIZE,ALL,,,NS*NA
T1=TM/8
LSEL,S,LENGTH,,SQRT((TX-SD)**2+(TZ-SD)**2)-TOL,SQRT((TX-SD)**2+(TZ-SD)**2)+TOL
LESIZE,ALL,,,10
LSEL,S,LENGTH,,SQRT(2)*SD-TOL,SQRT(2)*SD+TOL
LSEL,a,LENGTH,,SQRT((SD+OVL)**2+sd**2)
LESIZE,ALL,,,4
LSEL,S,LENGTH,,H-TOL,H+TOL
LESIZE,ALL,,,NH
LSEL,S,LENGTH,,2*H-TOL,2*H+TOL
LESIZE,ALL,,,2
LSEL,S,LENGTH,,BH-2*H-TOL,BH-2*H+TOL                    !DIVIDE BASE BLOCK
LESIZE,ALL,,,4
VMESH,ALL
ALLSEL,ALL
NUMMRG,ALL,OVL+TOL

NSEL,S,LOC,Y,-BH,0                                      !SPECIFY MILD STEEL BASE
ESLN,S,1
MPCHG,2,ALL
ALLSEL,ALL

CMSEL,S,VPWD,VOLU                                       !GROUP ELEMENTS INTO LAYER
COMPS.
NSLV,S,1
CM,NPWD,NODE
NSEL,S,LOC,Y,-BH,H
ESLN,S,1
CM,LYR1,ELEM
NSEL,S,LOC,Y,-BH,2*H
ESLN,S,1
CM,LYR2,ELEM
NSEL,S,LOC,Y,-BH,3*H
ESLN,S,1
CM,LYR3,ELEM
NSEL,S,LOC,Y,-BH,4*H
ESLN,S,1
CM,LYR4,ELEM
ALLSEL,ALL
CDWRITE,DB,T03,CDB
FINISH
/FILNAME,T03
/CLEAR
/PREP7
CDREAD,DB,T03,CDB
SHPP,OFF

/SOLU
ANTYPE,4                                                !SOLUTION SETTINGS
TRNOPT,FULL
NROPT,FULL
LUMPM,0
TUNIF,TC                                                !STARTING TEMP TC
OUTRES,BASIC,LAST
SOLCONTROL,ON
CNVTOL,TEMP,,0.10,,1e-6
EQSLV,ITER,2                                            !ITERATIVE SOLVER
LNSRCH,ON
NEQIT,30
AUTOTS,OFF
KBC,0
ESTIF,1e-9                                              !ELEMENT BIRTH & DEATH MULTIPLIER


!--------------
!ELEMENT BIRTH/LAYER ADDITION
```

```
!--------------
YN1=0                                   !LAYER HEIGHT SHRINKAGE TERM

NSEL,S,LOC,Y,0,1                        !TOP-DOWN MODEL, KILL ALL LAYER ELEMENTS
ESLN,S,1
EKILL,ALL

ALLSEL,ALL
*DO,NB,1,N,1
YN0=YN1
YN=NB*H
YN1=(YN-YN0)*PD+YN0                     !SHRINKAGE DROP IN HEIGHT
NSEL,S,LOC,Y,-BH,NB*H                   !ACTIVATE CURRENT LAYER
ESLN,S,1
EALIVE,ALL
ALLSEL,ALL

ESEL,S,LIVE
NSLE,S
NSEL,R,EXT
CM,NEXT,NODE
ESLN,R,0
SF,NEXT,CONV,HF,TC
ALLSEL,ALL

!SOLVE RECOATING PHASE
LST=TM*NHV*NT
TBSL=NB*TR+(NB-1)*LST
TIME,TBSL
NSUBST,5
OUTRES,BASIC,ALL
SOLVE
TSRES,ERASE
OUTRES,ERASE

!-----------------------------------
!APPLY HEAT FLUX I.E. LASER IRRADIATION
!-----------------------------------

*DO,NR,1,NT,1
HV=0                                    !HATCH REGION COUNTER

*DO,ZN,0,NS-1,2                         !RASTER LOOP
        *DO,XN,(NR-1)*NX,NR*NX-1,1
        *IF,HV,EQ,NHV,CYCLE
        HV=HV+1
        *IF,NB,EQ,1,THEN
        NSUBST,3
        *ELSE
        NSUBST,1
        *ENDIF
        NSEL,S,LOC,X,XN*D,(XN+1)*D
        NSEL,R,LOC,Z,ZN*D,(ZN+1)*D
        NSEL,R,LOC,Y,YN0,YN
        CM,NSCAN,NODE
        ESLN,S,1
        CM,ESCAN,ELEM
        NSEL,R,LOC,Y,YN
        CM,NHT,NODE
        ESLN,S,0
        SFEDELE,ALL,ALL,CONV
        SFDELE,ALL,CONV

        R=MU*ABS*PWR/A
        CMSEL,S,ESCAN
        SF,NHT,HFLUX,R
        ALLSEL,ALL
        TIME,T1+(HV-1)*TM+TBSL+(NR-1)*NHV*TM
        SOLVE
        NSEL,S,NODE,,NPWD
```

```
NSEL,A,NODE,,NSCAN
ESLN,S,1
NSEL,R,TEMP,,MPT
ESLN,R,0
ESEL,R,LIVE
ESEL,R,MAT,,3
MPCHG,1,ALL
ALLSEL,ALL
TSRES,ERASE
OUTRES,ERASE
SFDELE,ALL,HFLUX
SFEDELE,ALL,ALL,HFLUX
/PREP7
NMODIF,NHT,,YN1
/SOLU
ANTYPE,,REST

*IF,NB,EQ,1,THEN
NSUBST,2
*ELSE
NSUBST,3
*ENDIF
ND=3
        !--LOOP2
        *DO,NTM,1,ND,1                                  !TIME ARITHM PRGSN CALC.
        CMSEL,S,NSCAN,NODE
        NSEL,R,LOC,Y,YN1
        CM,NHT,NODE
        R=MU*AB*PWR/A                                   !RESULTING HEAT FLUX
        CMSEL,S,ESCAN
        SF,NHT,HFLUX,R
        ALLSEL,ALL
        TIME,TBSL+T1+(HV-1)*TM+NTM*(TM-T1)/ND+(NR-1)*NHV*TM

        SOLVE
        NSEL,S,NODE,,NPWD
        NSEL,A,NODE,,NSCAN
        ESLN,S,1
        NSEL,R,TEMP,,MPT
        ESLN,R,0
        ESEL,R,LIVE
        ESEL,R,MAT,,3
        MPCHG,1,ALL
        ALLSEL,ALL
        SFDELE,ALL,HFLUX
        SFEDELE,ALL,ALL,HFLUX
        *ENDDO                                          !--END LOOP2
TSRES,ERASE
OUTRES,ERASE
CMSEL,S,ESCAN
SF,NHT,CONV,HF,TC
ALLSEL,ALL
*ENDDO

*IF,ZN,EQ,NS-1,CYCLE
*DO,XN,NR*NX-1,(NR-1)*NX,-1
*IF,HV,EQ,NHV,CYCLE
HV=HV+1
*IF,NB,EQ,1,THEN
NSUBST,3
*ELSE
NSUBST,1
*ENDIF
NSEL,S,LOC,X,XN*D,(XN+1)*D
NSEL,R,LOC,Z,(ZN+1)*D,(ZN+2)*D
NSEL,R,LOC,Y,YN0,YN
CM,NSCAN,NODE
ESLN,S,1
CM,ESCAN,ELEM
NSEL,R,LOC,Y,YN
```

```
CM,NHT,NODE
ESLN,S,0
SFEDELE,ALL,ALL,CONV
SFDELE,ALL,CONV

R=MU*ABS*PWR/A                                          !INITIALISE TREATMENT
CMSEL,S,ESCAN
SF,NHT,HFLUX,R
ALLSEL,ALL
TIME,T1+(HV-1)*TM+TBSL+(NR-1)*NHV*TM
SOLVE
NSEL,S,NODE,,NPWD
NSEL,A,NODE,,NSCAN
ESLN,S,1
NSEL,R,TEMP,,MPT
ESLN,R,0
ESEL,R,LIVE
ESEL,R,MAT,,3
MPCHG,1,ALL
ALLSEL,ALL
TSRES,ERASE
OUTRES,ERASE
SFDELE,ALL,HFLUX
SFEDELE,ALL,ALL,HFLUX
/PREP7
NMODIF,NHT,,YN1
/SOLU
ANTYPE,,REST

*IF,NB,EQ,1,THEN
NSUBST,2
*ELSE
NSUBST,3
*ENDIF
ND=3                                                    !NO. OF INTERMEDIATE TIME DIVS
        !--LOOP2
        *DO,NTM,1,ND,1                                  !TIME ARITHM PRGSN CALC.
        NSEL,S,LOC,X,XN*D,(XN+1)*D
        NSEL,R,LOC,Z,(ZN+1)*D,(ZN+2)*D
        NSEL,R,LOC,Y,YN1
        CM,NHT,NODE
        CMSEL,S,ESCAN
        R=MU*AB*PWR/A                                   !RESULTING HEAT FLUX
        SF,NHT,HFLUX,R
        ALLSEL,ALL
        TIME,TBSL+T1+(HV-1)*TM+NTM*(TM-T1)/ND+(NR-1)*NHV*TM

        SOLVE
        NSEL,S,NODE,,NPWD
        NSEL,A,NODE,,NSCAN
        ESLN,S,1
        NSEL,R,TEMP,,MPT
        ESLN,R,0
        ESEL,R,LIVE
        ESEL,R,MAT,,3
        MPCHG,1,ALL
        ALLSEL,ALL
        SFDELE,ALL,HFLUX
        SFEDELE,ALL,ALL,HFLUX
        *ENDDO                                          !--END LOOP2
TSRES,ERASE
OUTRES,ERASE
SF,NHT,CONV,HF,TC
*ENDDO                                                  !END REV. DIR.
*ENDDO
SFDELE,ALL,CONV
SFEDELE,ALL,ALL,CONV
*ENDDO                                                  !END RASTER+
*ENDDO                                                  END BIRTH
ALLSEL,ALL
```

```
!--------
!COOLING TIME
!--------
CT=600                                          !COOLING TIME
NSEL,R,EXT                                      !!DEFINE CONVECTION BC ON 4 SIDES
CM,NEXT,NODE
ESLN,R,0
SF,NEXT,CONV,HF,TC
ALLSEL,ALL
NSUBST,2
OUTRES,BASIC,ALL
TIME,N*(LST+TR)+2*TM
SOLVE
NSUBST,20
OUTRES,BASIC,ALL
TIME,N*(LST+TR)+2*tm+CT
SOLVE
SFDELE,ALL,CONV
SFEDELE,ALL,ALL,CONV
TSRES,ERASE
OUTRES,ERASE
FINISH
SAVE
SAVE,T03_TH,DB
!-------------------
!STRUCTURAL ANALYSIS
!-------------------
/PREP7
ETCHG,TTS

MPDELE,ENTH,1                                   !DELETE ALL THERMAL ANALYSIS MAT. PROP.
MPDELE,KXX,1
MPDELE,ENTH,2
MPDELE,KXX,2
MPDELE,ENTH,3
MPDELE,KXX,3

ESEL,S,MAT,3                                    !REMOVE UNCONVERTED POWDER ELEM
EDELE,ALL
ALLSEL,ALL

MPTEMP,,                                        !CLR MPTEMP TABLE
MPTEMP,,25,200,315,540,800,2800

MPDATA,DENS,5,,4420,4365,4310,4190,3920,3140
MPDATA,EX,5,,114E9,100E9,93E9,57E9,1.001e9,1.001E9
MPDATA,PRXY,5,,0.342,0.342,0.342,0.38,0.42,0.45
MPDATA,ALPX,5,,8.9E-6,1.03E-5,1.08E-5,1.14E-5,1.16E-5,2.5E-5

MPDATA,DENS,2,,7950,7785,7575,7260,6880,5630
MPDATA,EX,2,,200E9,200E9,190E9,147E9,1.05E9,1.001E9
MPDATA,PRXY,2,,0.26,0.26,0.28,0.38,0.42,0.45
MPDATA,ALPX,2,,1.07E-5,1.37E-5,1.48E-5,1.62E-5,1.62E-5,2.5E-5

MPDELE,ALL,3

TB,BISO,5,6                                     !DEFINE ISOTROPIC HARDENING MATERIAL PROPERTIES
TBTEMP,25
TBDATA,,1062E6,12e9
TBTEMP,200
TBDATA,,743E6,13e9
TBTEMP,315
TBDATA,,670E6,16e9
TBTEMP,540
TBDATA,,478E6,19e9
TBTEMP,800
TBDATA,,1E6,1e9
TBTEMP,2800
TBDATA,,1E6,1e9
```

```
TB,BISO,2,6                          !DEFINE STEEL ISO HARDENING PROPERTIES
TBTEMP,25
TBDATA,,255E6,2e9
TBTEMP,200
TBDATA,,248E6,3e9
TBTEMP,315
TBDATA,,178E6,2e9
TBTEMP,540
TBDATA,,112E6,1e9
TBTEMP,800
TBDATA,,1E6,1e9
TBTEMP,2800
TBDATA,,1E6,1e9

LSCLEAR,ALL
NSEL,S,LOC,X,-TX                     !CONSTRAIN RHS PLATFORM
NSEL,R,LOC,Y,-BH,0
D,ALL,UX,0
D,ALL,UY,0
NSEL,R,LOC,Y,-BH
D,ALL,UZ,0
ALLSEL,ALL

ACEL,,9.81                           !-Y DIR. ACCEL.

/SOLU
ANTYPE,4
TRNOPT,FULL
NROPT,FULL
LNSRCH,ON
EQSLV,PCG
NEQIT,30
TREF,25                              !REFERENCE TEMP.
OUTRES,BASIC,LAST
cnvtol,u,,0.80,,1e-6
AUTOTS,OFF
KBC,0
NSUBST,1

!-------------
!*ELEM BIRTH
!-------------
NSEL,S,LOC,Y,0,N*H                          !DEACTIVATE ALL LAYER ELEMENTS
ESLN,S,1
ESEL,R,MAT,,1
MPCHG,5,ALL
EKILL,ALL
ALLSEL,ALL

YN1=0
*DO,NBS,1,N,1
YN0=YN1
YN=NBS*H
YN1=(YN-YN0)*PD+YN0

TBSLS=NBS*TR+(NBS-1)*LST

*DO,NRS,1,NT,1
HVS=0

*DO,ZN,0,NS-1,2
*DO,XN,(NRS-1)*NX,NRS*NX-1,1

        *IF,HVS,EQ,NHV,CYCLE
        HVS=HVS+1
        NSEL,S,LOC,X,XN*D,(XN+1)*D
        NSEL,R,LOC,Z,ZN*D,(ZN+1)*D
        NSEL,R,LOC,Y,YN0,YN1
        CM,NSCAN,NODE
        ESLN,S,1
```

```
CM,ESCAN,ELEM
CMSEL,S,NPWD
NSEL,R,LOC,Y,0,NBS*H
ESLN,S,1
CM,EPWD,ELEM
CMSEL,S,NSCAN
ESLN,R,0
CMSEL,A,ESCAN
EALIVE,ALL
ALLSEL,ALL
*DO,TP,T1+(HVS-1)*TM+TBSLS+(NRS-1)*NHV*TM,HVS*TM+TBSLS+(NRS-1)*NHV*TM,(TM-T1)/ND
TIME,TP
LDREAD,TEMP,,,TP,,T03SHR,RTH
OUTRES,BASIC,LAST
SOLVE
*ENDDO
*ENDDO
*IF,ZN,EQ,NS-1,CYCLE

*DO,XN,NRS*NX-1,(NRS-1)*NX,-1
*IF,HVS,EQ,NHV,CYCLE
HVS=HVS+1
NSEL,S,LOC,X,XN*D,(XN+1)*D
NSEL,R,LOC,Z,(ZN+1)*D,(ZN+2)*D
NSEL,R,LOC,Y,YN0,YN1
CM,NSCAN,NODE
ESLN,S,1
CM,ESCAN,ELEM
CMSEL,S,NPWD
NSEL,R,LOC,Y,0,NBS*H
ESLN,S,1
CM,EPWD,ELEM
CMSEL,S,NSCAN
ESLN,R,0
CMSEL,A,ESCAN
EALIVE,ALL
ALLSEL,ALL

*DO,TP,T1+(HVS-1)*TM+TBSLS+(NRS-1)*NHV*TM,HVS*TM+TBSLSs+(NRS-1)*NHV*TM,(TM-T1)/ND
TIME,TP
LDREAD,TEMP,,,TP,,T03,RTH
OUTRES,BASIC,LAST
SOLVE
*ENDDO
*ENDDO
*ENDDO                                          !END REVERSE DIRECTION

*ENDDO                                          !END RASTER LOOP

*IF,NBS,EQ,N,CYCLE

*DO,TP,TBSLS+LST+TR/5,TBSLS+LST+TR,TR/5         !RECOATING LOOP
TIME,TP
LDREAD,TEMP,,,TP,,T03,RTH
OUTRES,BASIC,LAST
SOLVE
OUTRES,ERASE
*ENDDO

*ENDDO                                          !END ELEM BIRTH LOOP

!-----
!RESIDUAL STRESSES
!-----
TREF,25

*DO,TTS,TP+TM,TP+2*TM, TM TIME,TTS
LDREAD,TEMP,,,TTS,,T03,RTH
TSRES,ERASE
OUTRES,BASIC,LAST
```

```
SOLVE
OUTRES,ERASE
*ENDDO

*DO,TTR,TTS+CT/20, TTS+CT,CT/20
TIME,TTR
LDREAD,TEMP,,,TTR,,T03,RTH
OUTRES,BASIC,LAST
SOLVE
OUTRES,ERASE
*ENDDO

FINISH
```

Appendix 3: OLS MICROSCOPE CALIBRATION

OLYMPUS

Report No. 40C55001

Calibration Report

Product name	:	Step Gauge
Manufacturer	:	Mitutoyo
Code No.	:	178-610
Serial No.	:	0700037
Control No.	:	OT3253-0700037

Name of Client : Olympus Life Science Europa GmbH
Address : Wendenstr. 14-18 D-20097 Hamburg Germany
Date of receive : 20th December, 2007 (Inspection number : 40C550)
Date of calibration : 28th December, 2007
Measurement Standard usede for calibration
: Gauge Block:22011008
Standard Measuring instrument:11011004
Calibration method : Procedures of Step Gauge(Number of Document : 24201001)
Calibration place : OLYMPUS Corporation Quality Assurnce
Ambient Condition of Calibration Room
: Temperature : 20° C ±0.2° C, Humidity : 50%±15%,

1. Resilt of Calibration

(μm)

NO.	1	2	3	4	5
Accumulative	0	-1	-3	-8	-18

Nominal step	1	2	5	10
Measured value	0.91	2.05	5.12	10.34
Result of calibration	0.09	-0.05	-0.12	-0.34

2. Note
1) Measurement Standerd used for calibration is tracable with Primary Mesarement Standerd
2) Measurement expanded uncertainty(k=2) : 0.60μm
k:coverage factor
3) The report shall not be reproduced without the prior written approval of the issuing laboratory

Date of Issue 11th January, 2008
Olympus Corporation
Calibration Laboratory
Corporate Quality Assurance Department
2951 Ishikawa-cho, Hachioji-shi Tokyo 192-8507 Japan

Chief Examiner — Examiner

S. Tanaka — I. tairaku

オリンパス株式会社 品質保証部 試験評価センター
東京都八王子市石川町 2951 番地

Publications

International Journal of Machine Tools & Manufacture 49 (2009) 916–923

Contents lists available at ScienceDirect

International Journal of Machine Tools & Manufacture

journal homepage: www.elsevier.com/locate/ijmactool

A three-dimensional finite element analysis of the temperature field during laser melting of metal powders in additive layer manufacturing

I.A. Roberts [a,*], C.J. Wang [a], R. Esterlein [b], M. Stanford [a], D.J. Mynors [a]

[a] Department of Engineering and Technology, University of Wolverhampton, Telford TF2 9NT, United Kingdom
[b] University of Dortmund, 44221 Dortmund, Germany

ARTICLE INFO

Article history:
Received 15 April 2009
Received in revised form
2 July 2009
Accepted 2 July 2009
Available online 15 July 2009

Keywords:
Multilayer
Additive layer manufacturing
Element birth and death
Laser melting

ABSTRACT

Simulating the transient temperature field in additive layer manufacturing (ALM) processes has presented a challenge to many researchers in the field. The transient temperature history is vital for determining the thermal stress distribution and residual stress states in ALM-processed parts that utilise a moving laser heat source. The modelling of the problem involving multiple layers is equally of great importance because the thermal interactions of successive layers affect the temperature gradients, which govern the heat transfer and thermal stress development mechanisms. This paper uses an innovative simulation technique known as element birth and death, in modelling the three-dimensional temperature field in multiple layers in a powder bed. The results indicate that the heated regions undergo rapid thermal cycles that could be associated with commensurate thermal stress cycles. Deposition of successive layers and subsequent laser scanning produces temperature spikes in previous layers. The resultant effect is a steady temperature build-up in the lower layers as the number of layers increases.

1. Introduction

Laser melting (LM) of metal powders is an additive layer manufacturing (ALM) technology that enables freeform fabrication of complex three-dimensional metal parts utilising numerical control to bond defined layer geometries in a powder bed by a moving laser beam. The LM process is similar to the direct metal laser sintering (DMLS) process; only in the former the metal powder is completely melted by a continuous wave Nd:YAG laser to produce parts of near full density. The process heat transfer mechanisms are complex and have been investigated in previous studies [1,2]. Mathematical models have been proposed to explore the heat transfer mechanisms in single laser scan tracks [3,4]. These have provided an insight into the flow of matter and energy in the laser sintering process. JunChang et al. [5] evaluated the thermal field created on a titanium sample during pulsed Nd:YAG laser treatment using an analytical model.

Finite element analyses (FEA) using commercial packages have been employed to perform temperature field analysis of various ALM processes. Nisar et al. [6] developed a model to study the temperature fields generated during laser enamelling using a high-power diode laser for a single track scan. Kolossov et al. [7] developed a finite element model to predict the temperature distribution on the top surface of a titanium powder bed during laser sintering of titanium powder. The FEM model considered sintering potential and specific heat capacity as functions of temperature. They also carried out temperature validation measurements on the top surface of the powder bed with an infra-red camera.

Although models have been proposed to investigate the temperature distribution in laser-based ALM processes, few have simulated the practical layer-wise building process and have been restricted by the complexity of the problem. In this paper, a computational model for determining the temperature history in a practical LM process involving the scanning of multiple layers is developed. This model builds on previously developed concepts by Cervera and Lombera [8] and Kolossov et al. [7], taking into account the process variables, multiple layers, as well as non-linearities produced by temperature-dependent material properties and phase changes. The advances of the present work are: (1) a three-dimensional model is employed in the study rather than making assumptions for two-dimensional idealisations, (2) a detailed understanding of the temperature history resulting from the addition of layers can be obtained using this technique.

1.1. Background to heat transfer analysis in laser melting

Fig. 1 shows a schematic diagram of laser melting the surface of a powder bed. The laser scans the powder surface according to a defined scanning pattern. During the process, the metal powder undergoes state and phase changes from powder to liquid and finally to solid.

* Corresponding author. Tel.: +441902323908; fax: +441902323843.
E-mail address: ibiye.roberts2@wlv.ac.uk (I. A. Roberts).

0890-6955/$ - see front matter © 2009 Elsevier Ltd. All rights reserved.
doi:10.1016/j.ijmachtools.2009.07.004

Nomenclature

Q	vector heat quantity (J)	r	radial distance (m)
I	laser irradiance (W/m^2)	H	enthalpy (J/m^3)
q	laser heat flux (W/m^2)	ρ	density (kg/m^3)
P	laser power (W)	k	thermal conductivity (W/m K)
α	absorptance	h	convection heat transfer coefficient (W/m^2 K)
		T	temperature (°C)
		φ	porosity

The general energy balance equation in the closed system in accordance with the first law of thermodynamics can be written as

$$\vec{Q}_L = \vec{Q}_{CD} + \vec{Q}_{CV} + \vec{Q}_R \quad (1)$$

where $\vec{Q}_L$, $\vec{Q}_{CD}$, $\vec{Q}_{CV}$ and $\vec{Q}_R$ are the vector heat quantities for the laser flux, conduction, convection losses and radiation losses, respectively.

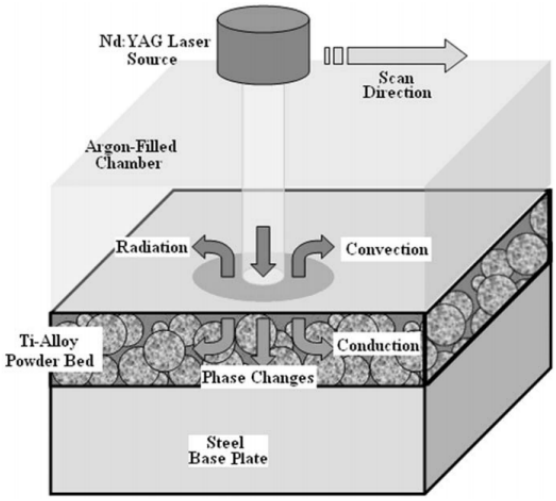

Fig. 1. Schematic representation of heat transfer.

1.2. Laser energy modelling

The Gaussian model, which is the most widely adopted model, utilises the symmetrical distribution of laser irradiance across the beam [9]. It assumes that the laser irradiance is symmetric about their propagation direction and in most cases the maximum irradiance (power per unit area) I_o is at the centre of the beam pattern, as shown in Fig. 2 [10].

The beam irradiance at any point for the fundamental mode (TEM_{oo}) is defined as

$$I(r) = I_o e^{-2d^2/d_1^2} \quad (2)$$

where d_1 is the beam diameter corresponding to the point where the irradiance diminishes to $1/e^2$ and d the diametrical distance of a point from the centre. Similarly, the thermal heat flux follows by definition [11] as

$$q(r) = \frac{2P}{\pi r_0^2} e^{-2r^2/r_0^2} \quad (3)$$

where P is the laser power, r_0 the spot radius and r the radial distance.

The laser energy absorptance of a material α is known to depend on a number of factors—nature of surface, level of oxidation, wavelength of laser, surface temperature, etc. [12–14]. The absorptance of metal powders is known to vary between the in-coupling absorptance as proposed by Kruth et al. [14] to a few percent when the metal melts [10]. This variation in absorptance is not yet certain; therefore, the absorptance of pure titanium powder at the Nd:YAG wavelength (1.06 μm), as reported by Fischer et al. [15], is taken as the representative absorptance value for the bulk material.

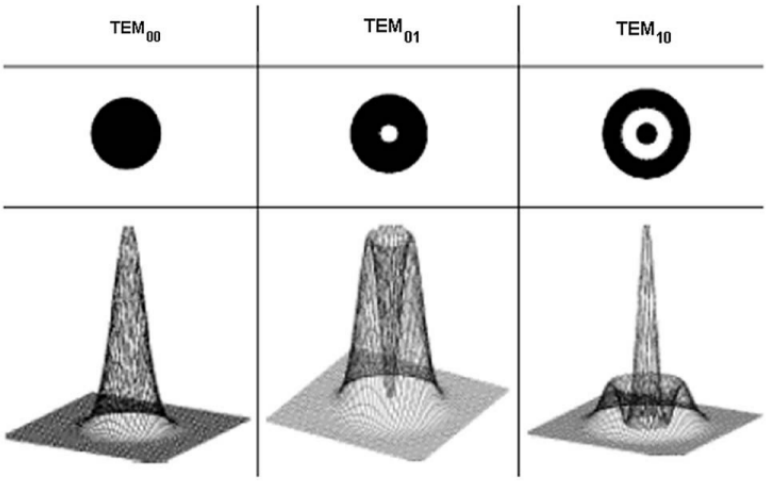

Fig. 2. Gaussian beam mode profiles [10].

The heat flux input is, therefore, expressed as

$$\overline{q} = \alpha \cdot q(r) \tag{4}$$

1.3. Governing equations

The thermal problem to be solved involves a progressive laser beam traversing the surface of the powder bed at a constant velocity. Bejan and Kraus [16] pointed out that the heat transfer equation for an isotropic material, taking the centre of the beam as the reference co-ordinate, can be written as

$$\rho\left(\frac{\partial H}{\partial t}\right) = \nabla(k\nabla T) \tag{5}$$

With Eq. (5), most thermal processes can be described mathematically. According to the specific problem, additional terms must be included to reflect the particular loads and boundary conditions [16] as follows:

$$\text{Preheat temperature} : T = T_0$$
$$\text{Input heat flux} : (-k\nabla T)\cdot \hat{n} = \overline{q}$$
$$\text{Surface convection} : (-k\nabla T)\cdot \hat{n} = h(T = T_0)$$

where ρ is the density, ΔH the change in enthalpy, k the thermal conductivity and h the film convection coefficient; $\hat{n}$ is the unit vector normal to the surface of the domain.

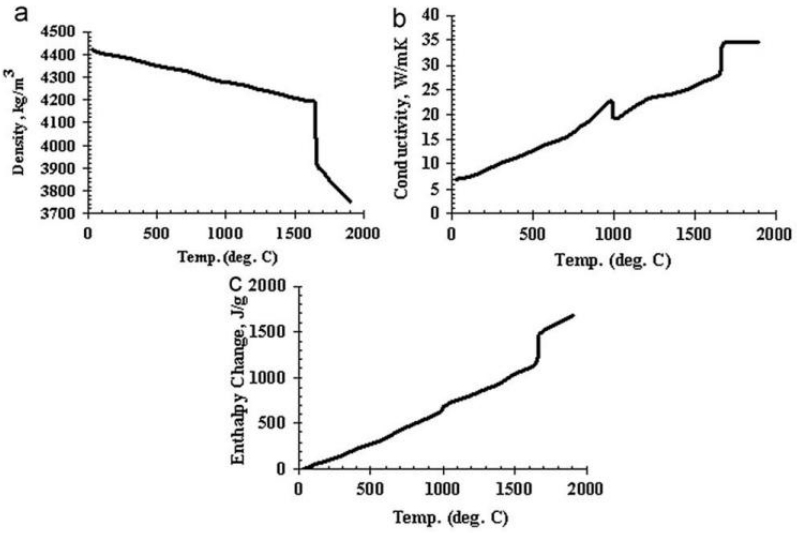

Fig. 3. Variation of thermophysical properties for Ti-alloy ($TiAl_6V_4$) with temperature [23].

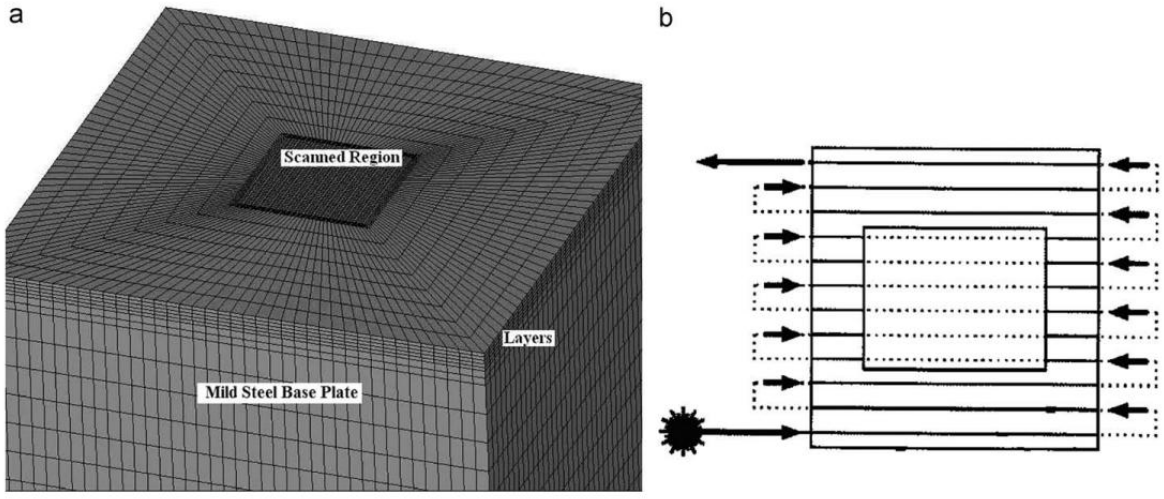

Fig. 4. (a) Finite element model and (b) scanning pattern.

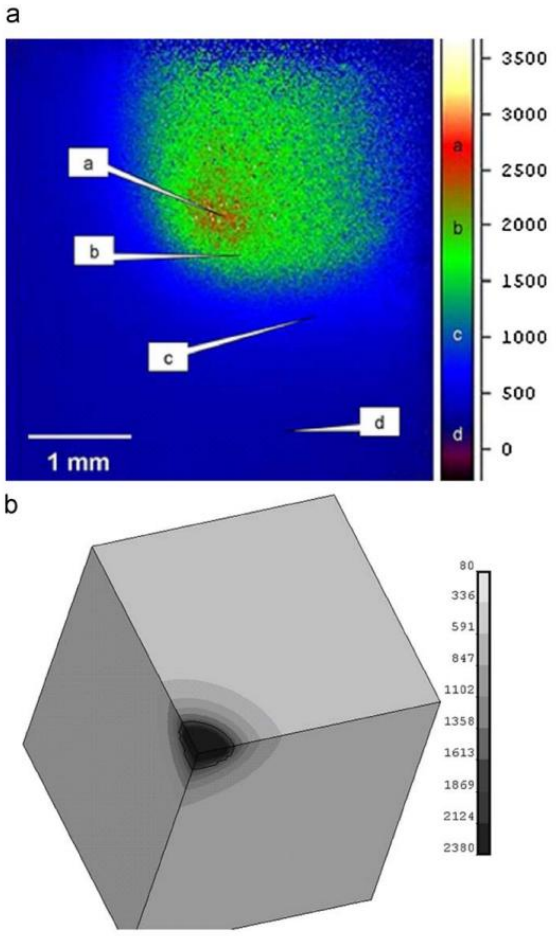

Fig. 5. (a) Infra-red temperature contour plot [26] (*T* in Kelvin) and (b) Simulation model (Quarter symmetrical model) temperature contour plot (°C).

2. Simulation technique for multilayer part

2.1. Element birth and death

The model in this study employs the method of element birth and death to simulate the addition of layers with time. The deposition of powder material and the laser scanning of geometry cross-sections on a powder bed to create solids is analogous with the activation of new elements at desired time points [17]. Before they are activated the elements are visually present (in a top-down model); however, they do not add to the overall stiffness of the matrix. This simulation technique has been employed by Gan et al. [18] in the residual stress analysis of deposited plasma-spray coatings on a metal substrate.

2.2. Temperature-dependent material properties

The thermophysical properties of materials can be classed as field and non-field properties [19]. The thermal conductivity, which is dependent on porosity, is a field property; however, the enthalpy and density, which are controlled by the mass of a given composition, are non-field properties. A number of models have been proposed for the relationship between the powder bed and solid thermal conductivities [8,20]. Thummler and Oberacker [19] proposed that the field properties depend, in a complicated manner, on porosity and pore geometries but can be represented by a simplified generic relationship

$$\lambda_p = \lambda(1-\varphi) \tag{6}$$

where λ_p, λ and φ are the powder bed, solid metal and the representative porosity terms, respectively.

The effective thermal conductivity of loose metallic powders is controlled by gas in the pores. Rombouts et al. [21], in their study of light extinction in powder beds, found that the effective thermal conductivity of a powder bed is essentially independent of material but depends on the size and morphology of the particles and the void fraction, as well as on the thermal conductivity of the gas. It was found that for 10–50-μm-size powders, the effective thermal conductivity is typically from 0.1 to 0.2 W/mK in air at room temperature. The thermal conductivity of a gas increases approximately as the square root of temperature, so that a value of about 0.3 W/mK is expected about the melting

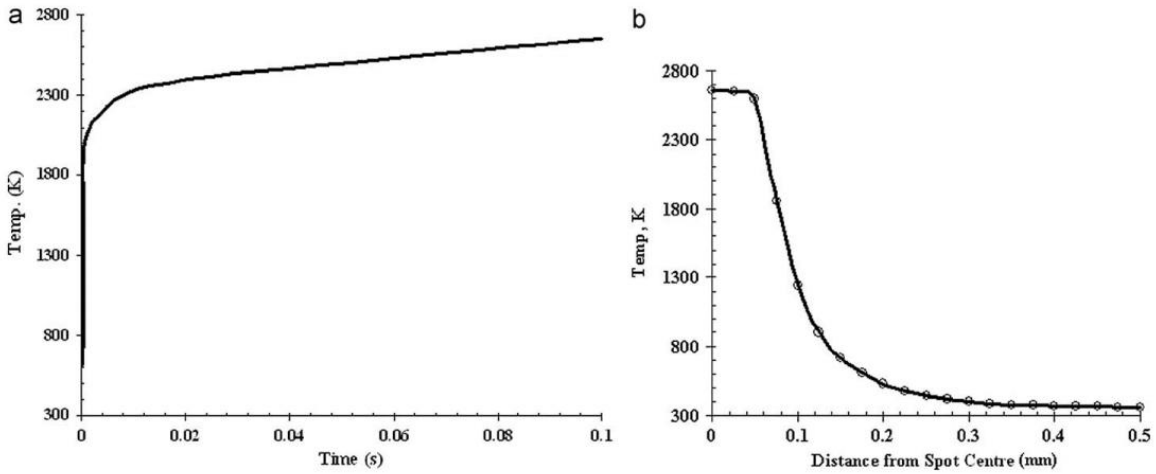

Fig. 6. (a) Spot temperature contour plot and (b) spot temperature variation.

point [22]. It follows, therefore, that the thermal conductivity of $TiAl_6V_4$ starts off from this low conductivity value for powder material but sharply rises at the material melting point.

Fig. 3 shows the variation of the solid thermophysical properties with temperature for $TiAl_6V_4$ [23].

2.3. Simulation model

A simulation model consisting of five 30 μm layers of $TiAl_6V_4$ is presented in this work. Numerical simulation is carried out using the ANSYS Multiphysics finite element package. A rectangular block of $1 \times 1 \times 0.15$ mm built on a $3 \times 3 \times 3$ mm mild steel base plate using 8-node brick elements is shown in Fig. 4. The simulation region is large enough and has been selected to allow the heat from the laser source to dissipate without interfering with the temperature distribution in the scanned region. The recoating time is the time taken to add new layers prior to laser scanning, and for the purpose of this simulation, a time delay of 1 s has been chosen. The chamber (preheat) temperature is maintained at 80 °C. The scanning pattern (striping format) is shown in Fig. 4(b). The finite element mesh for the scanned region is fine enough to accurately simulate the steep temperature gradients with element length divisions of 0.025 mm (i.e. one-fourth of the laser beam diameter). The mesh of the surrounding powder bed coarsens, the further away it is from the scanned region. A 10% convergence test was conducted to ascertain the suitability of the chosen mesh divisions.

For the simulation model, the energy from the laser is applied as heat flux on the powder bed surface at a spot location for a time interval defined by the scanning speed and spot size [24]. The nodal temperatures are monitored in sub-time steps to determine

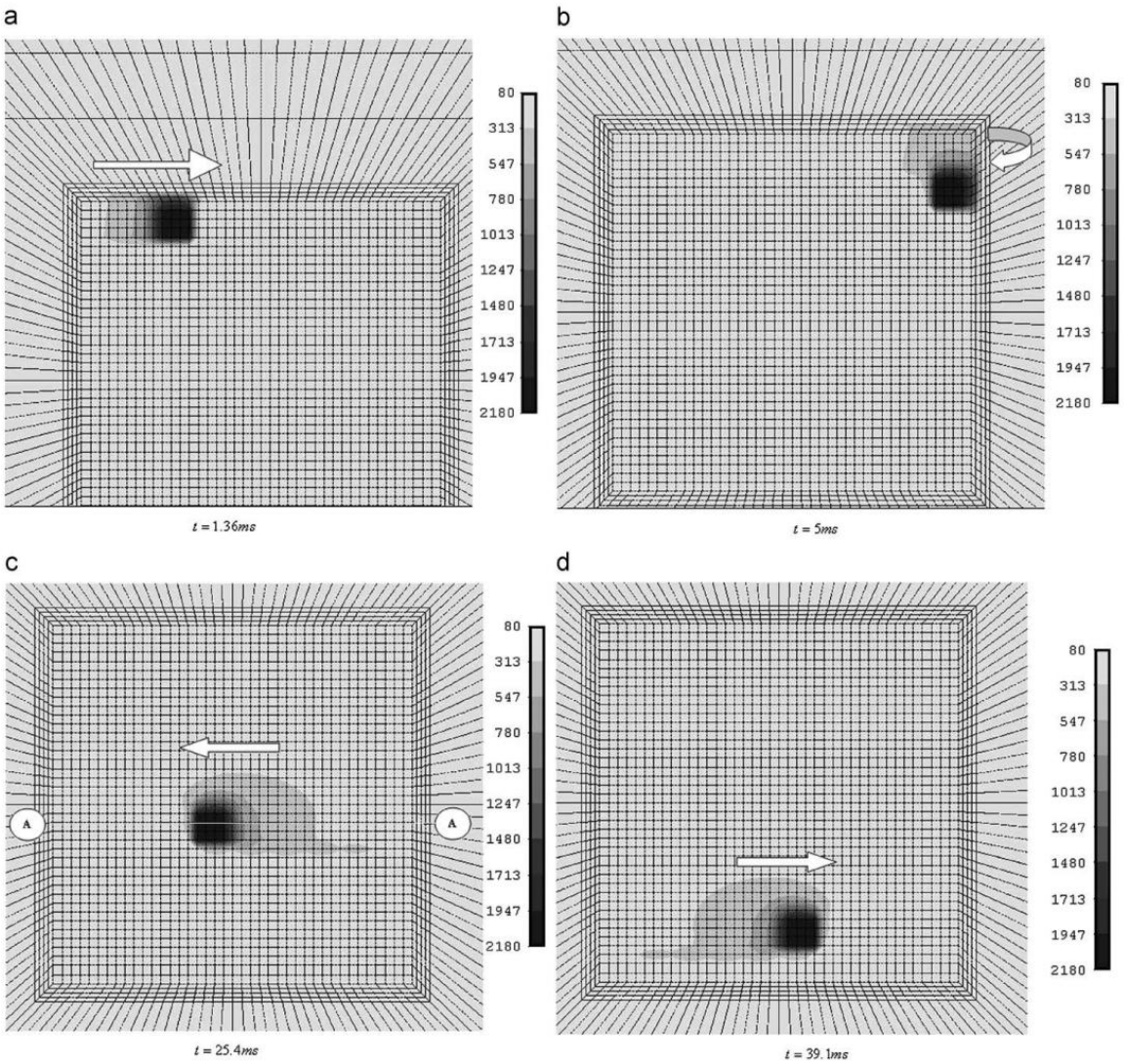

Fig. 7. Temperature distribution plots at various times from start of laser scanning (°C).

which elements have reached the melting point. The material properties are then updated for the appropriate elements (by interpolation where necessary), and the process is repeated until the irradiation time is reached. On completion, the heat flux moves to the next spot. This routine is continued until all the regions defining the geometry on a layer have been analysed. A new layer is then activated (via element birth) and the necessary boundary conditions and inputs applied. The entire process is again repeated until the last layer is complete.

The process parameters for the simulation model for the power, spot size, scan speed and powder size are 120 W, 100 μm, 220 mm/s and 30 μm, respectively. These values are typical process parameters for building $TiAl_6V_4$ parts as advised by the original equipment manufacturer [25].

The LM process involves rapid melting and solidification. Frewin and Scott [13] suggested that convective redistribution of heat within the small molten pool is not as significant as it is in processes where a liquid molten pool is permanent. Also radiation losses are not included in the simulation model; although such losses at the surface of the powder bed occur, the bulk of heat transfer is by conduction into the bed.

3. Results and discussion

3.1. Simulation validation

In order to determine the suitability of the simulation model, a comparative study with the experimental work was conducted. The simulation results were compared with published experimental findings by Fischer et al. [26] in measuring the peak skin temperature of laser irradiation spot on a pure titanium powder bed. The process variables for the experiment were 3 W, 100 μm, 1 mm/s and 30 μm for the average laser power, laser spot size, scan speed and powder size, respectively.

The temperature on the surface was measured with a Raytheon infra-red camera. Fig. 5 (a) shows the temperature contour plot on the surface [26].

Fig. 5(a) shows a maximum temperature range of $2500 < T_{max} < 3000$ K, and the reported measured value is 2400 ± 200 °C [7].

The temperature distribution for the simulation model using the process parameters from the experiment after 0.1 s for a quarter symmetry model is shown in Fig. 5(b). The temperature contour results show strong similarities with the published experimental measurements, giving a maximum predicted temperature of 2380 °C (2653 K).

Fig. 6(a) shows a rapid temperature rise leading up to the melting point 1665 °C (1938 K), above which, due to the emergence of the very conductive molten material, the temperature change rate drops significantly as the temperature rises to its peak value.

The temperature variation plot in Fig. 6(b) shows a region with radial distance, $x < 50$ μm, where the temperature exceeds the melting point, a region $50\,\mu m < x < 100\,\mu m$ with a very steep temperature gradient and a region $x > 200$ μm that appears to be relatively unaffected by the laser irradiation in agreement with the experimental measurements and observations.

3.2. Thermal analysis results for multilayer model

Fig. 7(a–d) show the temperature distribution plots at different times as the laser scans across the surface of the first layer. The arrows indicate the direction of travel of the heat flux.

The results indicate that the heating and subsequent cooling to the ambient (chamber) temperature occur within a few tenths of a millisecond of each other, thus suggesting that the irradiated spots are subjected to rapid thermal cycles. These rapid cycles are associated with commensurate thermal stress changes [27].

The temperature profile for path (A–A) through the centre of the spot in Fig. 7(c) shows a pronounced skewed temperature distribution towards the rear of the laser as shown in Fig. 8(a). This can be attributed to the fact that the rapidly cooling molten material has greater conductive properties than the untreated powder in front of the laser. This trend can be observed in Fig. 5(a) and also from temperature field simulations by Shen et al. [28].

The temperature profiles for consecutive spots in the multilayer model are shown in Fig. 8(b). The spots exhibit very similar thermal cycles, indicating that every point on a layer experiences very similar temperature histories.

The temperature profiles at the centre of the multiplayer model for the first four layers generated by continuous wave Nd:YAG laser are shown in Fig. 9(a–d).

Fig. 9(a) indicates a number of lower secondary peaks corresponding to the laser, scanning the same position on successive upper layers. This is also exhibited for the upper layers and suggests that the addition of layers and subsequent scanning are of significance to the temperature field in the model.

The results show significantly higher maximum temperatures for the upper layers. This is due to the fact that the first consolidated layer has a lower conductivity than the steel base plate. The upper layers retain the heat from the laser for long

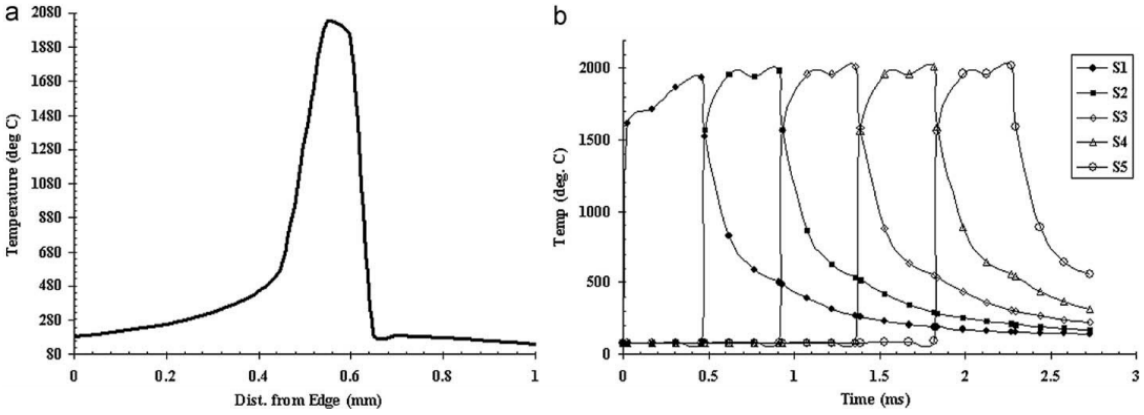

Fig. 8. (a) Temperature distribution for profile path A–A and (b) spots temperature profiles.

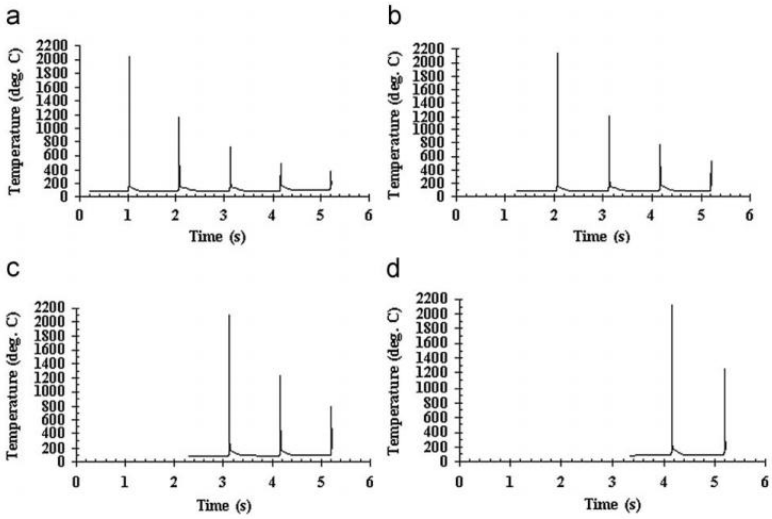

Fig. 9. Variation of temperature at the centre of the model with number of layers: (a) first layer, T_{max} = 2028°C, (b) second layer, T_{max} = 2176°C, (c) third layer, T_{max} = 2155°C and (d) fourth layer, T_{max} = 2150°C.

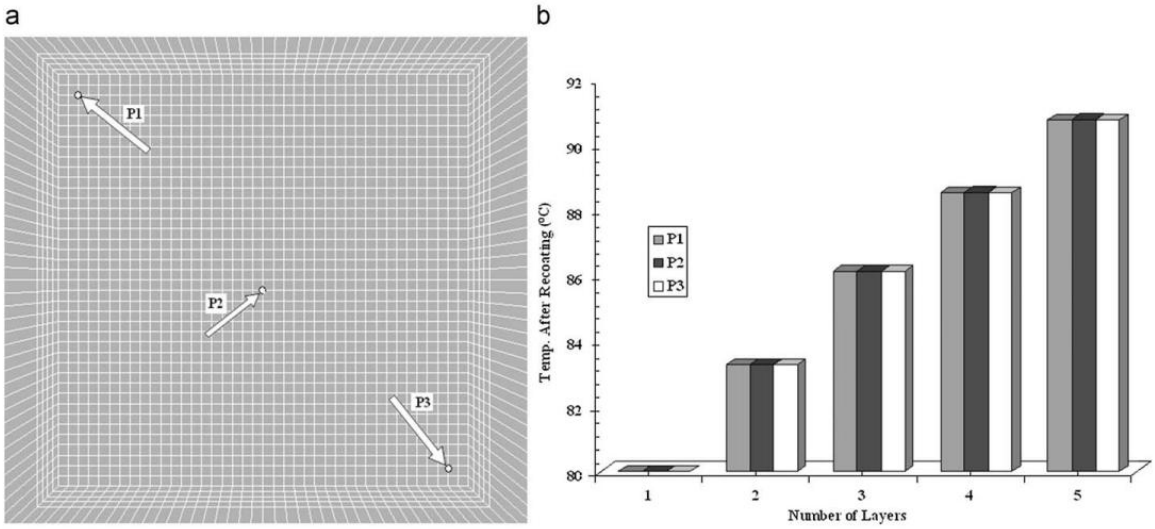

Fig. 10. Steady-state temperature variation with number of layers added.

because they are shielded, to a great extent, from the steel base plate. The recoating time is significantly greater than the spot irradiation time; therefore, dissipation of heat to the newly added layer by the previous one provides ample time to reach the steady state (i.e. near ambient temperature) as shown by the horizontal sections in Fig. 9(a–d).

The results also indicate a slight and consistent rise in first layer steady-state temperature as the number of added layers increases as shown in Fig. 10(b) for data points P1–P3 in Fig. 10(a). This rise in final temperature in the lower layer could result in the development of residual stresses during cooling on completion of the process.

4. Conclusion

A three-dimensional finite element model for predicting the transient temperature field for multiple layers of parts produced by the LM process has been developed. The model has taken into account the laser energy absorption including the non-linearities produced by temperature-dependent material properties and phase changes. An innovative simulation technique known as element birth and death has been employed in capturing the complexities presented by the addition of multiple layers. A study validating the simulation method was conducted and the results were in agreement with published experimental measurements.

From the simulation results we can conclude that

- the laser-scanned regions within a layer undergo rapid temperature cycles that are similar, discounting edge locations
- the upper layers reach higher stable temperatures than the first layer in contact with the base plate
- the addition of more layers and subsequent laser scanning alter the temperature distribution in the preceding layers, resulting in secondary peaks in their temperature histories
- although the recoating phase provides ample time for cooling, there is a small but incremental temperature build-up in the part and base plate.

The simulation results provide a better understanding of the LM heat transfer process. Further research will focus on the use of this method in the study of the development of thermal and residual stresses in multi-layer LM parts.

References

[1] N.K. Tolochko, et al., Mechanisms of selective laser sintering and heat transfer in Ti powder, Rapid Prototyping Journal 9 (5) (2003) 314–326.
[2] A. Simchi, Direct laser sintering of metal powders: mechanism, kinetics and microstructural features, Materials Science and Engineering A 428 (1–2) (2006) 148–158.
[3] B. Xiao, Y. Zhang, Laser sintering of metal powders on top of sintered layers under multiple-line laser scanning, Journal of Physics D: Applied Physics 40 (21) (2007) 6725–6734.
[4] T. Chen, Y. Zhang, Three-dimensional modeling of laser sintering of a two-component metal powder layer on top of sintered layers, Journal of Manufacturing Science and Engineering 129 (2007) 575–582.
[5] L. JunChang, C. Langlade, A.B. Vannes, Evaluation of the thermal field developed during pulsed laser treatments: semi analytical calculation, Surface and Coatings Technology 115 (1) (1999) 87–93.
[6] A. Nisar, et al., Three-dimensional transient finite element analysis of the laser enamelling process and moving heat source and phase change considerations, in: Proceedings of the Institution of Mechanical Engineers—Part B—Engineering Manufacture, vol. 217(6), 2003, pp. 753–764.
[7] S. Kolossov, et al., 3D FE simulation for temperature evolution in the selective laser sintering process, International Journal of Machine Tools and Manufacture 44 (2–3) (2004) 117–123.
[8] G.B.M. Cervera, G. Lombera, Numerical prediction of temperature and density distributions in selective laser sintering processes, Rapid Prototyping Journal 5 (1) (1999) 21–26.
[9] R.C. Crafer, P.J. Oakley, Laser Processing in Manufacturing, Chapman & Hall, London, 1993.
[10] J.F. Ready, Effects of High-Power Laser Radiation, Academic Press, New York, London, 1971, p. 433.
[11] K. Dai, L. Shaw, Finite element analysis of the effect of volume shrinkage during laser densification, Acta Materialia 53 (18) (2005) 4743–4754.
[12] W.-L. Chen, Y.-C. Yang, H.-L. Lee, Estimating the absorptivity in laser processing by inverse methodology, Applied Mathematics and Computation 190 (2007) 712–721.
[13] M.R. Frewin, D.A. Scott, Finite element model of pulsed laser welding, Welding Research Supplement (1999) 15–22.
[14] J.P. Kruth, et al., Lasers and materials in selective laser sintering, Assembly Automation 23 (4) (2003) 357–371.
[15] P. Fischer, et al., Sintering of commercially pure titanium powder with a Nd:YAG laser source, Acta Materialia 51 (6) (2003) 1651–1662.
[16] A. Bejan, A.D. Kraus, Heat Transfer Handbook, Wiley, New York, 2003, p. 1480.
[17] ANSYS10.0, ANSYS Release 10.0 Documentation, 2007.
[18] Z. Gan, H.W. Ng, A. Devasenapathi, Deposition-induced residual stresses in plasma-sprayed coatings, Surface and Coatings Technology 187 (2–3) (2004) 307–319.
[19] F. Thummler, R. Oberacker, An Introduction to Powder Metallurgy, The University Press, Cambridge, London, 1993.
[20] S.S. Sih, J.W. Barlow, The prediction of the emissivity and thermal conductivity of powder beds, Particulate Science and Technology 22 (2004) 427–440.
[21] M. Rombouts, et al., Light extinction in metallic powder beds: correlation with powder structure, Journal of Applied Physics 98 (1) (2005) 013534 (12 pages).
[22] A.V. Gusarov, et al., Heat transfer modelling and stability analysis of selective laser melting, Applied Surface Science (2007).
[23] K.C. Mills, Recommended Values of Thermophysical Properties for Selected Commercial, Woodhead Publishing, 2002, p. 320.
[24] K. Dai, L. Shaw, Thermal and stress modeling of multi-material laser processing, Acta Materialia 49 (20) (2001) 4171–4181.
[25] Electrical Optical Systems, EOS M250Xtended, M270 Basic Operation Manual, 2005.
[26] P. Fischer, et al., Temperature measurements during selective laser sintering of titanium powder, International Journal of Machine Tools and Manufacture 44 (12–13) (2004) 1293–1296.
[27] K. Dai, L. Shaw, Distortion minimization of laser-processed components through control of laser scanning patterns, Rapid Prototyping Journal 8 (5) (2002) 270–276.
[28] X.-F. Shen, et al., Finite element simulation of thermal distribution in direct metal laser multi-track sintering, Journal of Sichuan University (Engineering Science Edition) 37 (1) (2005) 47–51.

Paper No: 1659 – 36th MATADOR Conference

Numerical and Experimental Studies on the Direct Laser Heating of Steel Plates in Laser Melting of Metal Powders

I.A. Roberts[1], C.J. Wang[1], K.A. Kibble[1], M. Stanford[1] and D.J. Mynors[1]

[1]Department of Engineering and Technology, University of Wolverhampton, Telford, TF2 9NT, United Kingdom

Abstract. A consequence of voids in a powder layer in laser melting of metal powders is the direct laser penetration through the pore structure and subsequent heating of the base platform on which it is laid – a steel base plate in many cases. As a result, thermal stresses develop due to high temperature gradients in a thin layer of the surface, which can result in undesired surface deformation of the steel platform used. This study investigates the residual stress profiles on the surface of a hot-rolled AISI 1015 steel plate used in the laser melting of metal powders in additive layer manufacturing of TiAl6V4 powder. A three-dimensional finite element simulation model is developed which considers the laser heating process as a sequentially coupled thermal elasto-plastic problem. Experiments using optical laser scanning microscopy to obtain surface topography of the melted surface are also presented showing reasonable agreement with the simulation results. The influence on the platform thickness is investigated. It shows that the thickness has an effect on the residual stress–depth profiles in the platform.

Keywords: Laser Melting, Surface Topography, Hardening, Additive Layer Manufacturing

1.1 Introduction

Laser processing is an invaluable tool used in manufacturing. The heating characteristics of lasers have been employed in many forming, sintering and melting processes as utilized in additive layer manufacturing (ALM). Laser melting in ALM produces three-dimensional parts by melting metal powders in layers according to numerically defined geometries to form fully dense parts with properties similar to those of the solid material [1]. One consequence of laser melting of metal powders on a platform is the direct heating of platform on which parts are built. This can have a number of undesirable effects on the accuracy of the finished components.

Physical processes including welding, hardening, alloying, cladding and bending can be effected by laser irradiation [2, 3]. These laser processes are associated with characteristic thermal cycles in small, highly localized regions on the surface of a workpiece. The thermal cycles result in physical and microstructural changes [4].

The transient temperature distribution in the irradiated material is a vital element for understanding the physical processes that occur. Yánez et al. [4] have studied the temperature distribution during laser heating of steel using both analytical and finite element models. The models used were limited to constant material properties. Wang et al. [5] developed a finite element model for simulating the temperature field in a line scan laser hardening of C45 steel using temperature dependent material properties. In addition to non-linearities introduced by temperature dependent properties, the laser scanning movement adds asymmetry to the problem; hence there is need for three-dimensional modelling. Chiang and Chen [2] studied the changes in microstructure with depth of H13 steel as a result of the laser melting of its surface. Selvan et al. [6] carried out experimental and analytical studies on CO2-laser treated En18 (medium carbon steel) and showed that quenching occurred at the scanned surface which resulted in a local increase in the hardness to about 950HV at the surface. The hardness decreased with depth to 250HV which is the material's original hardness value.

In this paper, a three-dimensional finite element model is developed to model the temperature and residual stress fields generated during the laser melting of the surface of a hot-rolled mild steel plate over a raster area. The model incorporates temperature dependent thermal, mechanical properties and latent heat during phase transitions.

1.2 Simulation Model

During laser melting of metal surfaces, complicated phenomena such as temperature dependency of material properties and laser absorption occur in very short time periods; hence, knowledge of the temperature field in and

around the melt region is essential for modelling for the laser heating process.

According to Shi *et al* [7], in order to simplify the calculation, the fundamental mode (TEM_{00}) Gaussian laser irradiance distribution can be replaced by a modified expression to calculate the average heat flux density as follows:

$$q = \frac{1}{A}\int_S IdA = \alpha \cdot \frac{1}{\pi R^2}\int_0^R \frac{2P}{\pi R^2} e^{-2r^2/R^2}.2\pi r dr \qquad (1.1)$$

Where q is heat flux, P is power, R is the spot radius, and α is the absorptance.

The variation of absorptance of materials is an important property that limits the amount of laser energy that is delivered into the material. The absorptance value from previous studies varies from the optical/radiative absorptance to the calorimetric absorptance and is known to depend on factors such as temperature, nature of surface, and wavelength of laser [8]. For this study, the calorimetric absorptance of steel as reported by Bertolotti [9] is used – 0.2 for the solid material and 0.1 for the molten material.

The temperature field can be represented as a quasi-steady state problem for the moving heat source using Fourier's heat transfer equation:

$$\rho\left(\frac{\partial H}{\partial t}\right) = \nabla\cdot(k\nabla T) + \dot{q} \qquad (1.2)$$

According to the specific problem additional terms must be included to reflect the particular loads and boundary conditions:

Preheat temperature $T = T_O$

Surface convection $(-k\nabla T)\cdot\hat{n} = h(T - T_O)$

Where ρ is density, k is thermal conductivity, H is enthalpy and h is convection coefficient.

The stress field can be modelled by determining the elastic component of the total strain [10];

$$\varepsilon = \varepsilon_{el} + \varepsilon_{ie} + \varepsilon_{th} \qquad (1.3)$$

The thermal strain component depends on the expansion coefficient, while the inelastic strain component depends on the stress deviation, strain hardening parameter and the temperature.

The stress field components are derived thus [11]:

$$\sigma = D\ \varepsilon - \varepsilon_{ie} - \varepsilon_{th} \qquad (1.4)$$

Where $[D]$ is the stress-strain matrix

1.2.1 Material Modelling

The temperature-dependent physical and mechanical properties of hot-rolled AISI 1015 have been taken from [12, 13]. Hardness tests conducted for the material gave a value of 143HV corresponding to an ultimate tensile strength of 400MPa and yield strength of 255MPa. For temperatures close to and above the melting point, the material loses all of its stiffness. To resolve numerical difficulties posed by zero matrices, very small values were used for the elastic and Engesser moduli and yield stress.

1.2.2 Finite Element Model

The laser heating of a 1mm × 2mm area on a 5mm × 5mm plate having a thickness of 1mm was modeled using ANSYS Mechanical, for which the general thermal and elasto-plastic algorithms used have been described [11].

The finite element mesh consists of 8-node brick elements for solving the temperature and structural field problems respectively. The same mesh was used for both field analyses. Because the powder layer has a height of 30μm and the laser beam size of 100μm, the element size had to be very small, in this case 25μm×25μm. Fine meshes were used in regions exposed to the laser scanning, and they become coarser the farther they were from the scanned zone as shown in Fig. 1.1.

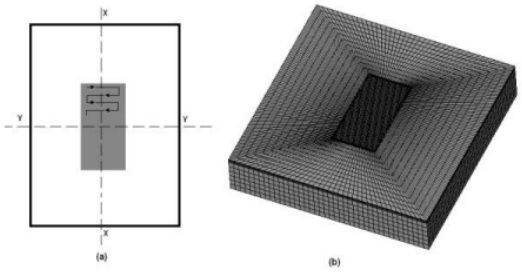

Fig. 1.1. Scanning pattern and finite element model

The movement heat source was considered to occur in discrete timesteps, irradiating a region equivalent to the size of the beam for a time period determined by the beam diameter and speed of travel [14]. The cooling down time was taken as 600s. The solidification process was modelled as a coupled thermal-structural field problem. The heat generated by plastic deformation of the material is negligible compared to the heat input of the laser beam [7]. Therefore, the problem is simulated as a sequential coupled field problem, using the transient temperature loads of the thermal model as input for the structural model [15]. To prevent rigid body movement, a zero displacement boundary condition is applied to one side of the plate model.

1.3 Experimental Set Up

An EOS M270 machine with a continuous wave Nd:YAG laser of wavelength, λ = 1.06μm and an output power reaching 200W, having a non-expanded beam size

of about 100µm was used to achieve laser melting. Stress-relieved test pieces with overhanging 5mm × 5mm × 1mm cantilever platforms shown in Fig. 1.2 are machined from hot-rolled steel blanks.

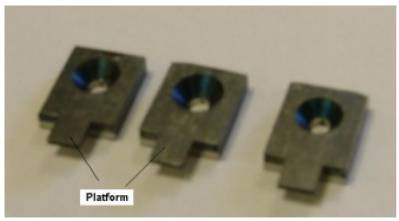

Fig. 1.2. Test samples

A central region 1mm × 2mm is mapped from a CAD model was laser scanned on the platform surface. Typical process parameters for building TiAl6V4 parts are used for this experiment – the laser power and speed were set to 195W and 1200mm/s respectively without overlaps specified. The raster scanning method (see Fig.1.1) as used with most laser prototyping systems was used.

The topography experiment involved capturing the surface state of the platform area before and after the laser scanning using an Olympus Confocal Laser Scanning microscope. The platform surface was divided into cells of 480µm × 640µm. A series of images taken at intervals were then knitted to form a 1024 × 768 pixel surface topography image of a 4800µm × 5120µm. Vertical displacements for designated paths *X* and *Y* were obtained as the difference between the height profiles before and after laser application. Due to visually evident splattering of molten material in the scanned zone, the displacement changes are measured for the regions outside the scanned zone. The entire process was repeated with three samples for which the average values were obtained.

1.4 Results and Discussion

Pilot studies were conducted with the simulation model. These were validated against the temperature measured experimentally and predicted analytically by [16] for the temperature field. The stress field analysis was validated against an analytical model used by [10].

1.4.1 Temperature Field Distribution on Steel Platform

The temperature distribution at various times is shown in Fig. 1.3. The results show that the different spots that make up a surface experience similar thermal cycles and that the heating and cooling cycles experienced by the spots occur within a few milliseconds. These rapid thermal cycles are associated with commensurate thermal stresses.

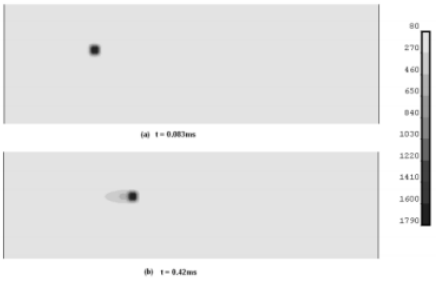

Fig. 1.3. Temperature field results

1.4.2 Surface Profilometry (Model Validation)

Fig. 1.4 compares the surface height profiles for the paths *X* and *Y* shown in Fig. 1.1. It can be seen that scanned zone forms a concave depression. This is due to the high tensile stresses that are generated at the surface of the plate. The resultant effect is a contraction in the scanned zone which tends to pull the surrounding undisturbed material to a new equilibrium position.

Several factors may have contributed to the discrepancy between the simulation and experimental results, including the absorptance of the material to the laser beam, which depends on a number of factors. In general, the simulation results show good agreement with the experimental results.

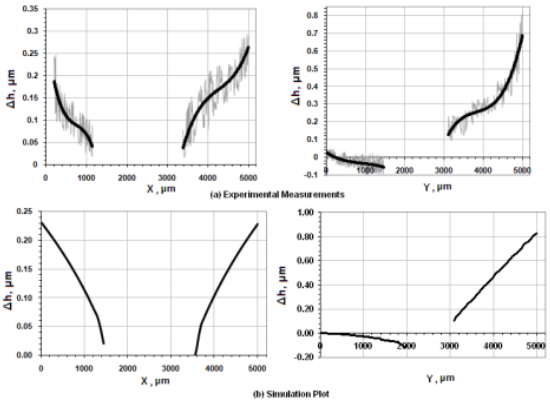

Fig. 1.4. Comparison between experiment and simulation model

1.4.3 Stress Field Results

The stress analysis was performed for a 1mm × 1mm region scanned on a 3mm × 3mm platform. Results for the transverse and longitudinal stresses are presented in Fig. 1.5. The longitudinal stresses are taken in the direction of travel of the laser while the transverse stresses are taken in the perpendicular direction.

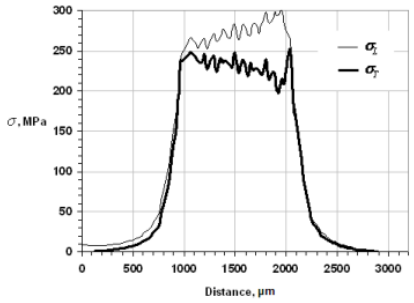

Fig. 1.5. Resiudal stress distribution

It can be seen that the longitudinal stresses are greater than the transverse stresses across the scanned zone.

1.4.4 Stress-Depth Profile

Grum and Sturm [17] studied the change in the residual stress states in the melt zone and were able to determine the depth of the hardened zone from this information. Fig. 1.6. shows that after laser melting, the residual stresses on the surface are tensile in nature, these however transform to compressive stresses with depth.

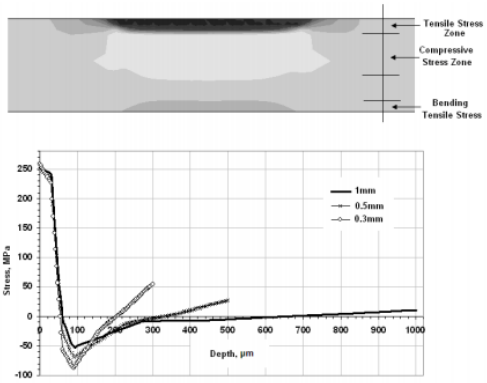

Fig. 1.6. Stress-depth profile

It can be seen from Fig. 1.6. that the depth at which the residual stress is zero is the same for all thickness cases analysed. The emergence of secondary tensile stresses towards the bottom of the platform is due to the deformation of its free end. This can result in accuracy issues if the thin platform is to be used for building parts using metal powders.

1.6 Conclusions

A three-dimensional finite element model has been developed to study the direct laser melting of a mild steel platform surface. The model has successfully predicted the temperature and stress fields associated with the process. After laser melting, tensile residual stresses develop on the surface which transform to compressive residual stresses with depth. Tensile stresses disappear at about the same distance in all thickness cases analysed.
The platform thickness did not affect the magnitude of surface residual stresses but affects the distribution with depth. Secondary tensile stresses emerge beyond the region of compressive stresses due to the deflection of the platform. These distortions could cause part accuracy for the conditions used in this work. The stress-depth profile can provide a robust means of determining the hardened zone depth.

1.6 References

[1] Noorani RI, (2006) Rapid Prototyping: Principles and Applications. New Jersey, USA: John Wiley & Sons Inc.

[2] Chiang K-A and Chen Y-C, (2005) Laser surface hardening of H13 steel in the melt case. Materials Letters, 59: p. 1919-1923.

[3] Zhang P, Guo B, Shan D-B, and Ji Z, (2007) FE simulation of laser curve bending of sheet metals. Journal of Materials Processing Technology, 184: p. 157-162.

[4] Yánez A, Álvarez JC, López AJ, Nicolás G, Pérez JA, Ramil A, and Saavedra E, (2002) Modelling of temperature evolution on metals during laser hardening process. Applied Surface Science, 186: p. 611-616.

[5] Wang XF, Lu XD, Chen GN, Hu SG, and Su YP, (2006) Research on the temperature field in laser hardening. Optics & Laser Technology, 38: p. 8-13.

[6] Selvan JS, Subramanian K, and Nath AK, (1999) Effect of laser surface hardening on En18 (AISI 5135) steel. Journal of Materials Processing Technology, 91: p. 29-36.

[7] Shi Y, Shen H, Yao Z, and Hu J, (2007) Temperature gradient mechanism in laser forming of thin plates. Optics & Laser Technology, 39: p. 858-863.

[8] Taylor CM,(2004) Direct Laser Sintering of Stainless Steel: Thermal Experiments and Numerical Modelling. Ph.D Thesis, University of Leeds.

[9] Bertolotti M, ed. Physical Processes in Laser-Materials Interactions. 1983, Plenum Press: New York.

[10] Masubuchi K, (1980) Analysis of Welded Structures. Vol. 33. Massachusetts, USA: Pergamon Press.

[11] ANSYS10.0, (2007) ANSYS Release 10.0 Documentation

[12] USDD, (1998) Military Handbook - MIL-HDBK-5H: Metallic Materials and Elements for Aerospace Vehicle Structures. U.S. Department of Defence.

[13] Mills KC, (2002) Recommended Values of Thermophysical Properties for Selected Commercial Woodhead Publishing. 320.

[14] Dai K and Shaw L, (2005) Finite element analysis of the effect of volume shrinkage during laser densification Acta Materialia, 53: p. 4743-4754.

[15] Dai K and Shaw L, (2004) Thermal and mechanical finite element modeling of laser forming from metal and ceramic powders. Acta Materialia, 52: p. 69-80.

[16] Yilbas BS, Sami M, and Shuja SZ, (1998) Laser-induced thermal stresses on steel surface. Optics and Lasers in Engineering, 30: p. 25-37.

[17] Grum J and Sturm R, (1998) Influence of laser surface melt-hardening conditions on residual stresses in thin plates. Surface and Coatings Technology, 100-101: p. 455-458.

Key Engineering Materials Vol. 450 (2011) pp 461-465
Online available since 2010/Nov/11 at www.scientific.net

doi:10.4028/www.scientific.net/KEM.450.461

Experimental and Numerical Analysis of Residual Stresses in Additive Layer Manufacturing by Laser Melting of Metal Powders

Ibiye A. Roberts[1, a], Chang J. Wang[1,b], Mark Stanford[1,c], Kevin A. Kibble[1,d] and Diane J. Mynors[1,e]

[1]Department of Engineering and Technology, University of Wolverhampton, Telford Campus, Telford, TF2 9NT, United Kingdom

[a]ibiye.roberts2@wlv.ac.uk, [b]c.j.wang@wlv.ac.uk, [c]m.stanford@wlv.ac.uk, [d]k.a.kibble@wlv.ac.uk, [e]d.j.mynors@wlv.ac.uk

Keywords: Laser melting, additive layer manufacturing, surface profilometry, element birth and death, residual stresses.

Abstract. Determining the three-dimensional residual stress fields and the associated distortions using numerical simulations for multi-layered parts has proved to be a challenge in additive layer manufacturing. This paper presents an innovative three-dimensional thermal-elasto-plastic finite element model for predicting the deformation and residual stress fields in $TiAl_6V_4$ parts built on steel platforms. The developed model utilises temperature dependent material physical and mechanical properties as well as latent heat of melting. Experiments conducted using surface profilometry showed good agreement with the simulation results. The finite element model was used to investigate the overall effect of the melting powder on the platform deformation and residual stresses for multiple layers of deposited powder.

Introduction

Laser melting (LM) of metal powders has been utilised in the additive layer manufacturing process for directly making complex functional parts from three-dimensional CAD models. In LM, the metal powders are completely melted and cooled to form fully dense parts. The LM process generates characteristic thermal cycles in small, highly localised regions on the top layer surface. The heat transfer mechanism in the LM process has been discussed in [1, 2]. These thermal cycles induce thermal stresses which accumulate over time to produce residual stresses in the finished parts. Residual stresses could result in undesired mechanical characteristics and visible part distortions and should be minimised. The mechanism of development of residual stresses in the laser heating processes has been discussed in [3, 4]. Mercelis and Kruth [3] used a theoretical method to predict the residual stress profiles in selective laser sintered (SLS) stainless steel powder for a number of layers, crack compliance experiments conducted supported the findings of their study. The theoretical method was idealised and limited to constant material properties.

Although studies by Shiomi *et al* [5] have attempted to calculate the residual stress fields from laser sintering processes, few have attempted to model the layer-wise building process due to the complexities introduced by the different states of the materials involved. In this study, a three-dimensional finite element model for predicting the temperature and stress fields is developed using temperature dependent material properties, latent heat and element birth and death simulation technique for modelling the addition of multiple layers.

Simulation Model

During laser melting of metal powders, complicated phenomena governed by the laser absorption and temperature dependency of the material properties occur in very short time periods; hence, knowledge of the temperature field is essential. The temperature field model for multiple layers has already been dealt with in a previous study [6]. The model developed employs the technique of element birth and death to simulate the addition of layers with time. Heat flux is applied to the

elements on the surface enclosed by a beam diameter for a time period determined by the scan speed and beam size. Within the irradiation time, the state of the elements are monitored (via nodal temperatures) to determine the state of the material and are updated accordingly (by linear interpolation where required). The process is repeated until the irradiation time is reached. On completion, the heat flux moves to the next spot in the scanning sequence defined by the raster scan strategy adopted. This routine is continued until all the regions defining the geometry on a layer have been treated. A new layer is then activated (via element birth) and the necessary boundary conditions and inputs applied. The elements before they are activated are visually present, however, they do not add to the overall stiffness matrix. The entire process is again repeated until the last layer is complete. A sequential coupled thermo-structural field problem using the transient temperature loads of the thermal analysis as input for the structural model was used for the simulation. To prevent rigid body movement, a zero displacement boundary condition is applied to one side of the platform. Fig. 1 shows the finite element model and scanning pattern. The model consists of two 30μm layers of $TiAl_6V_4$ lased on a hot-rolled steel platform.

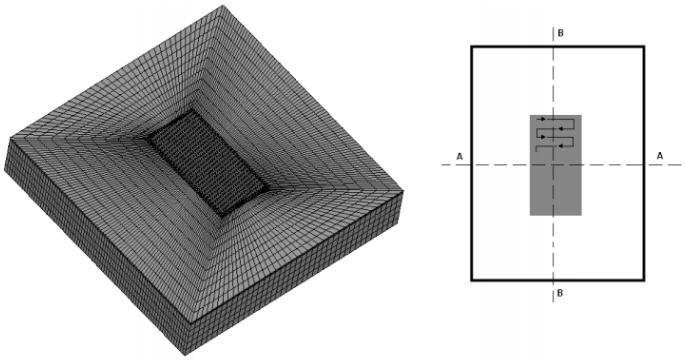

Fig. 1 Simulation model and raster scanning pattern

The material properties for $TiAl_6V_4$ and hot-rolled mild steel (AISI 1015) for the density, thermal conductivity, enthalpy and latent heat of fusion were taken from Mills [7] and Touloukian [8]. The thermal conductivity of the powder which is a field property was taken as 0.25W/mK for temperatures below the melting point [9]. Non-field properties which are dependent on the bulk density of a composition are computed based on measurements. The ratio of the measured bulk density to the solid density was 60.2%. The solidification of the molten material is modelled as a bilinear isotropic hardening problem with the von Mises yield stress criterion and associative flow rule. For temperatures close to and above the melting point, the material loses all of its stiffness. To resolve numerical difficulties posed by zero matrices, relatively small values were used for the elastic and Engesser moduli and yield stress. The simulation was carried out using ANSYS software, for which the thermal and elasto-plastic solution algorithms have been described [10].

Experiment Set Up

A detailed surface displacement experiment is conducted in this work. Limitations posed by the nature of the surfaces produced by LM and the fact that parts have to be built on solid platforms makes direct stress measurement difficult. Therefore, this work deals with measuring the deformation attributed to LM of metal powders on a steel platform. An EOSINT M270 machine [11] with a continuous wave Nd:YAG laser of wavelength, λ = 1.06μm and an output power reaching 200W, having a non-expanded beam size of 100μm was used to achieve laser melting. Stress-relieved test pieces with overhanging 5mm × 5mm × 1mm cantilever platforms were machined from hot-rolled

steel blanks. Two 30μm layers of $TiAl_6V_4$ mapped from a 1mm × 2mm CAD model were laser melted onto the platform surface. Typical process parameters for building $TiAl_6V_4$ parts were used for the experiment – the laser power and speed were set to 195W and 1200mm/s respectively with no scan track overlaps [11].

The topography experiment involved capturing the surface state of the platform area before and after the laser melting using an Olympus Confocal Laser Scanning microscope [12]. The platform surface was divided into cells of 480μm × 640μm. A series of images taken at intervals were then knitted to form a 4800μm × 5120μm surface topography plot. Vertical displacements for designated paths *A-A* and *B-B* (See Fig. 1) were obtained as the difference between the primary height profiles before and after laser application. The entire process was repeated for three samples, from which the average values were obtained.

Results and Discussion

Fig. 2 shows the surface topographic plots for the experiment. Due to visually evident splattering of molten material in the scanned zone, the displacement changes are measured for the regions outside the scanned zone.

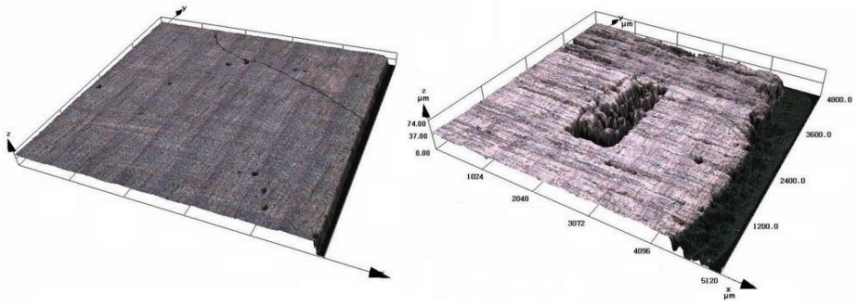

Fig. 2 Surface topographic pots before and after laser scanning

Fig. 3 compares the surface profile heights from experiments and the simulation model for the paths designated *A-A* (X-direction) and *B-B* (Y-direction). There is an evident concave depression formed as a result of the resultant contraction of the scanned zone. There are a few discrepancies between the simulation and experimental profile trends. In general, the simulation results show good agreement with the experimental results, suggesting that the assumptions and simulation method a sufficient. Deviations in the experimental results may have been caused by the molten material splattering during laser scanning.

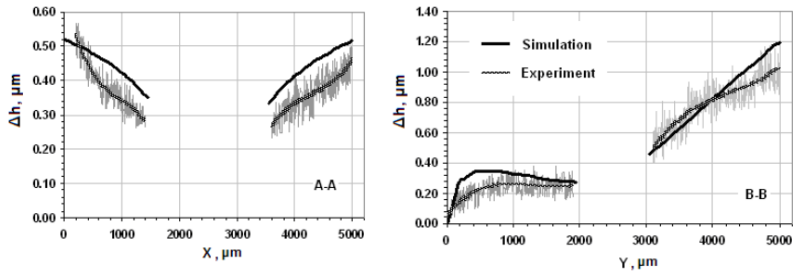

Fig. 3 Comparison between experiment and simulation model

Fig. 4(a)-(b) show the longitudinal and transverse residual stresses for a 1mm × 1mm two-layer part on a 3mm × 3mm ×1mm platform. The stresses start as compressive instantaneous stresses, but quickly transform to tensile stresses when it cools down as the laser heat flux moves to the next spot. It can be seen that the maximum longitudinal stress (868MPa) is greater than the maximum transverse stress (640MPa) in the scanned zone. The maximum platform deformation was 4.62μm for a one-layer part and 5.78μm for the two-layer part. There is also an increase in the maximum longitudinal stress from 776MPa for a one-layer part to 868MPa for a two-layer part, indicating an increase in the platform deformation and surface residual stresses as the number of layers increases. The increase in surface residual stresses could be attributed to the difference in structural mismatching (expansion coefficient and stiffness) between the first layer and the steel platform. The second layer of melted powder is effectively shielded from the platform.

Fig. 4(c) shows the variation of the maximum deformation with thickness of the platform for a two-layered part. It shows that the platform distortion increases as the thickness decreases.

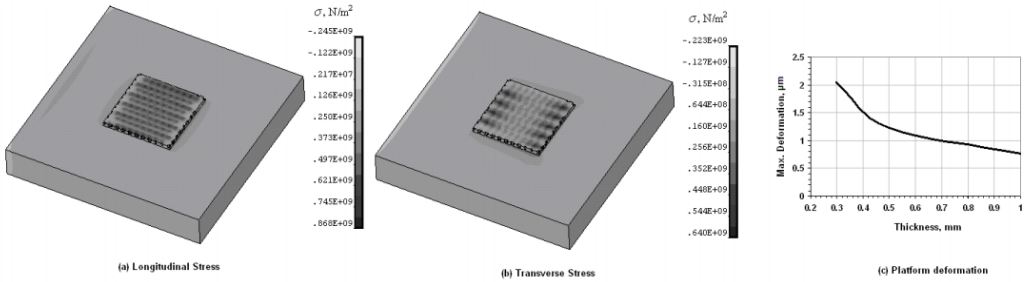

Fig. 4 Residual stress distribution and platform distortion

The stress-depth profile shows a region of tensile stress at the surface which changes to compressive stress with depth and the development of secondary tensile stresses at the base of the platform due to bending. This results in loss of accuracy when thin platforms are used for building parts.

Summary

A three-dimensional finite element model has been employed to model the residual stresses and deformation for the laser melting process of metal powders. The challenge posed by the addition of multiple layers of powder has been addressed by using an innovative simulation technique – element birth and death. The developed model has successfully predicted the distortions associated with the laser melting process showing good agreement with surface profilometry measurements. The addition of powder layers and subsequent laser melting increases the platform distortion.

References

[1] N.K. Tolochko, M.K. Arshinov, A.V. Gusarov, V.I. Titov, T. Laoui, and L. Froyen: Rapid Prototyping Journal Vol. 9 (2003), p.314-326.

[2] A. Simchi: Materials Science and Engineering A Vol. 428 (2006), p.148-158.

[3] P. Mercelis and J.-P. Kruth: Rapid Prototyping Journal Vol. 12 (2006), p.254-265.

[4] K. Masubuchi: *Analysis of Welded Structures*. Vol. 33.(Pergamon Press, USA 1980)

[5] M. Shiomi, K. Osakada, K. Nakamura, T. Yamashita, and F. Abe: International Journal of Machine Tools and Manufacture Vol. 46 (2004), p.1188-1193.

[6] I.A. Roberts, C.J. Wang, R. Esterlein, M. Stanford, and D.J. Mynors: International Journal of Machine Tools and Manufacture Vol. 49 (2009), p.916-923.

[7] K.C. Mills: Woodhead Publishing, 2002

[8] Y.S. Touloukian: *Thermal Expansion:* TPRC Data Series: Thermophysical Properties of Matter. Vol. 12.(IFI/Plenum, 1977)

[9] A.V. Gusarov, I. Yadroitsev, P. Bertrand, and I. Smurov: Applied Surface Science Vol. (2007),

[10] ANSYS10.0: ANSYS Release 10.0 Documentation (2007)

[11] Electrical Optical Systems: EOS M250Xtended, M270 Basic Operation Manual (2005)

[12] Olympus: Confocal Laser Scanning Microscope - LEXT OLS3000/3100 User's Manual (2008)